Global Wildland Fire Emission Modeling for Atmospheric Chemistry Studies

Judith Johanna Hoelzemann

Reports on Earth System Science

Global Wildland Fire Emission Modeling for Atmospheric Chemistry Studies

Judith Johanna Hoelzemann
aus Hannover

Hamburg 2006

Judith Johanna Hoelzemann
Max-Planck Institut für Meteorologie
Bundesstr. 53
20146 Hamburg
Germany

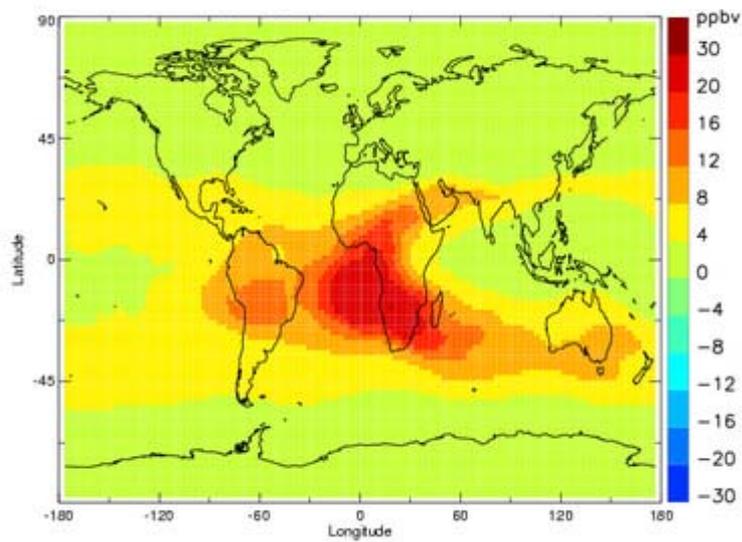# Global Wildland Fire Emission Modeling for Atmospheric Chemistry Studies

MOZART simulated ozone concentrations at 250 hPa resulting exclusively from fires, seasonal mean of January to March 2000

Judith Johanna Hoelzemann
Hamburg 2006

Contents

List of Acronyms

AATSR	Advanced Along Track Scanning Radiometer
ABBA	Automated Biomass Burning Algorithm
AFL	Available Fuel Load
AI	Aerosol Index
AMJ	April to June
AQUA	Earth Observing System (EOS) satellite from NASA
ATSR	Along Track Scanning Radiometer
AURA	Earth Observing System (EOS) satellite from NASA
AVHRR	Advanced Very High Resolution Radiometer
BB or bb	Biomass Burning
BC	Black Carbon
BIBEX	The Biomass Burning Experiment: Impact of Fire on the Atmosphere and Biosphere
BWEM	Boreal Wildland Fire Emission Model
C	Carbon
CACGP	Commission on Atmospheric Chemistry and Global Pollution
C-AM	Central America
CATT-BRAMS	Coupled Aerosol and Tracer Transport to the Brazilian developments on the Regional Atmospheric Modeling System
CASA	Carnegie Ames Stanford Approach
CC	Combustion Completeness
CCN	Cloud Condensation Nuclei
cg_scal	Global fire emission inventory based on Hao&Liu and scaled with ATSR fire pixels by Granier and Lamarque (pers. comm., 2004)
CH_4	Methane
CH_3Br	Methyl Bromide
CH_3Cl	Methyl Chloride
CMDL	Climate Monitoring and Diagnostics Laboratory
CO	Carbon Monoxide
CO_2	Carbon Dioxide
CMDL	Climate and Monitoring Diagnostic Laboratory
CPTEC	Centro de Previsão de Tempo e Estudos Climáticos in Brazil
CTM	Chemistry Transport Model
E-AS	Eastern Asia
ECMWF	European Centre for Medium Range Weather Forecast
EDGAR	Emission Database for Global Atmospheric Research
E-EU	Eastern Europe
EF	Emission Factor
ERS	European Remote Sensing
ESA	European Space Agency
FAO	Food and Agriculture Organization of the United Nations
FRP	Fire Radiative Power
GBA2000	Global Burnt Area of the year 2000 (JRC)
GEMS	Global and Regional Earth-System Monitoring using Satellite and In-Situ Data, EC 6th Framework Project
GFDL	General Fluid Dynamics Laboratory, Princeton, USA
GFED	Global Fire Emissions Database
GFMC	Global Fire Monitoring Center in Freiburg, Germany
GLC2000	Global Landcover Classification for the year 2000
Glob-FIRM	Global FIRe Model
GLOBSCAR	Global Burnt Scar (ESA)

GOES	Geostationary Operational Environmental Satellites from NOAA
GOME	Global Ozone Monitoring Experiment aboard ERS-2
GWEM	Global Wildland Fire Emission Model
Hao&Liu	Global climatological fire emission inventory produced in the 1990's based on Hao and Liu (1994) and Müller (1992)
IAMAS	International Association of Meteorology and Atmospheric Sciences
IFFN	International Forest Fire News
IGAC	International Global Atmospheric Chemistry Project
IGBP	International Geosphere-Biosphere Programme
IGBP-DIS	International Geosphere-Biosphere Programme - Data and Information System
IMPRS	International Max Planck Research School on Earth System Modelling
INPE	Instituto Nacional de Pesquisas Espacias in Brazil
ITCZ	Intertropical Convergence Zone
IPCC	Intergovernmental Panel on Climate Change
JAS	July to September
JFM	January to March
JRC	Joint Research Centre of the European Commission
LAI	Leaf Area Index
LBA	Large Scale Biosphere-Atmosphere Experiment in Amazonia
LFDB	Canadian Large Fire Database
LPJ-DGVM	Lund-Potsdam-Jena Global Dynamic Vegetation Model
mgs_scal	Global fire emission inventory based on Hao&Liu and scaled with ATSR fire pixels by Schultz(2002)
MODIS	Moderate Resolution Imaging Spectroradiometer aboard TERRA and AQUA
MOPITT	Measurements Of Pollution In The Troposphere, instrument aboard TERRA
MOZAIC	Measurement of Ozone And Water Vapor by Airbus In-Service Aircraft
MOZART	Model Of Ozone And Related Tracers
MPI-M	Max Planck Institute for Meteorology in Hamburg, Germany
N-AF	Northern Africa
N-AM	North America
NASA	National Aeronautics and Space Administration in USA
NCAR	National Center of Atmospheric Research in Boulder, USA
NC-AS	North-Central Asia
NDVI	Normalized Difference Vegetation Index
NMHC	Non-Methane Hydrocarbons
NOAA	National Oceanic and Atmospheric Administration
NPP	Net Primary Production
NO_x	Nitrogen Oxides (NO + NO2)
N_2O	Nitrous Oxides
NO	Nitrogen Oxide
NO_2	Nitrogen Dioxide
NRT	Near Real Time
O_3	Ozone
OC	Organic Carbon
OCE	Oceania
OH	Hydroxyl radical
OND	October to December
PBL	Planetary Boundary Layer
PFT	Plant Functional Type
$PM_{2.5}$	Particulate Matter with diameter up tp 2.5 micron
PM_{10}	Particulate Matter with diameter up tp 10 micron

POET	Precursors of Ozone and their Effects in the Troposphere, European Project
RETRO	REanalysis of the TROpospheric chemical composition over the past 40 years, European Project
S-AF	Southern Africa
SAFARI-92	Southern Africa Fire-Atmosphere Research Initiative by IGAC/BIBEX
SAFARI2000	Southern African Regional Science Initiative
S-AM	South America
S-AS	Southern Asia
SHADOZ	Southern Hemisphere ADitional OZonesondes
SeaWiFS	Sea-viewing Wide Field-of-view Sensor
SPOT	Satellite Earth Observation System, developed in France and by some other European Countries
TERRA	Earth Observing System (EOS) satellite from NASA
TOMS	Total Ozone Mapping Spectrometer
TRACE-A	Transport and Atmospheric Chemistry near the Equator-Atlantic: cooperative project between NASA and the Brazilian Space Agency (INPE)
TRMM	Tropical Rainfall Measuring Mission
VAS	Visible Infrared Spin Scan Radiometer
VEGETATION	Instrument system aboard SPOT
VIRS	Visible and Infrared Scanner aboard TRMM
W-EU	Western Europe
WFA	World Fire Atlas by ESA
WF_ABBA	Wildfire Automated Biomass Burning Algorithm product

Zusammenfassung

Der globale Einfluss von Feueremissionen auf den chemischen Zustand der Atmosphäre ist der internationalen Forschungsgemeinde seit längerem bekannt. Eine große Anzahl von Rodungsfeuern in Regenwäldern sowie Savannenfeuer, vor allem in den Tropen, führen immer wieder zu sehr hohen emittierten Schadstoffmengen in der Atmosphäre.

Vegetationsfeuer führen allerdings oftmals auch in außertropischen Regionen zu hohen Schadstoffbelastungen auf regionalen sowie interkontinentalen Skalen, da die Rauchwolken der Feuer über weite Entfernungen transportiert werden können.

Bis zum heutigen Tag werden in Chemie-Transport-Modellen zum Teil noch klimatologische Feueremissionskataster verwendet, um einen realistischen chemischen Zustand der Atmosphäre zu bestimmen. Da Emissionen von Feuern saisonal sowie inter-annuell stark variieren, ist die Information von diesen Katastern sowohl für mehrjährige klimatologische Studien, als auch auf der kürzeren chemischen Wetterskala, nur ungenügend.

In den letzten Jahren wurden Feuerpixel-Satellitenprodukte hergestellt, die eine objektivere und vollständigere Darstellung des globalen Feuervorkommens und damit auch ihrer Emissionen erlauben. Trotz dieses Fortschritts und den daraus gewonnenen Erkenntnissen anhand von Satellitendaten, die nur den Feuerort bestimmen, sind die erzielten quantitativen Informationen über verbrannte Flächen und folglich der Emissionen von Rauchaerosolen und Spurengasen, ihre Ausbreitung und ihr Einfluss, immer noch nicht ausreichend. Vor einiger Zeit wurden daraufhin globale Feuer-Satellitenprodukte entwickelt, die zur quantitativen Bestimmung von Feueremissionen beitragen sollen. Diese Produkte basieren auf komplexeren Algorithmen als die einfacheren Feuerpixel-Satellitenprodukte, und sind dadurch in der Lage, die Ausdehnung eines Feuers zu bestimmen, in dem seine verbrannte Fläche bestimmt wird. Diese Größe ist einer der ausschlaggebenden Parameter für die Modellierung von Feueremissionen.

In der vorliegenden Arbeit wurden diese neuen Produkte analysiert und zur Emissionsberechnung verwendet, um einen transparenten Ansatz mit reduzierten und geschätzten Unsicherheiten zu finden. In diesem Zusammenhang ist das globale Feueremissionsmodell (Global Wildland Fire Emission Model) GWEM neu entwickelt worden (Hoelzemann et al., 2004). Abgesehen von den verbrannten Flächendaten basiert dieses Modell auf dem Vegetationsmodell LPJ (Lund-Potsdam-Jena Global Dynamic Vegetation Model) und Satelliten-Vegetationskarten, um Feueremissionen auf globaler Skala zu bestimmen. GWEM ist zu einem Modul geworden, welches eine transparente Berechnung von Feueremissionen ermöglicht, unter Einbeziehung ihrer saisonalen und inter-annuellen Variabilität. Gleichzeitig wurden geeignete globale hoch-aufgelöste mehrjährige Feuer- und Vegetations-Satellitendaten fertiggestellt, die weitere Emissionsberechnungen ermöglichen. Verwendete Eingangsdaten und Ergebnisse von GWEM wurden sorgfältig mit anderen heute existierenden Katastern verglichen, die in der Forschungsgemeinde der Atmosphärenchemie weithin verwendet werden sowie mit kürzlich erschienenen Publikationen von regionalen Feueremissionsbestimmungen. Desweiteren wurde Wert auf die Untersuchung der Sensitivität von GWEM im Bezug auf Unsicherheiten in den Eingangsdaten gelegt.

Im Anschluss wurde das globale Chemie-Transport-Modell MOZART-2 verwendet, um den Einfluss der neuen GWEM-Feueremissionen auf die Atmosphärenchemie zu untersuchen. Eine Einflussstudie für das Jahr 2000 wurde mit dem Ziel durchgeführt, die Modellsensitivität gegenüber GWEM-Feueremissionen und im Vergleich mit anderen Feueremissionskatastern zu bestimmen. Die Ergebnisse dieser Modellstudie zeigen große Unterschiede in den Kohlenmonoxid- und Ozonkonzentrationen zwischen den verschiedenen Modelläufen. Die Unterschiede in den CO Hintergrundkonzentrationen am Boden über der Nordhemisphäre betragen um die 20-30%, während Unterschiede in feuer-beeinflussten Gebieten sich bis zu einem Faktor von 6 unterscheiden. Infolgedessen unterscheiden sich in diesen Regionen und deren Einflussgebieten die Ozonkonzentrationen um bis zu 30 ppbv.

Abstract

The impact of global fire emissions on the chemical state of the atmosphere has long been recognized by the international scientific community. Specifically in the tropics, a continuous issue related to air quality are numerous deforestation fires and savanna maintenance fires that emit vast amounts of pollutants into the atmosphere. But also in extratropical regions wildland fires can lead to pollution events on the regional and inter-continental scale, as their smoke-plumes are transported over long-range distances.

Until today, climatological fire emission inventories are used in Chemistry Transport Model to provide a realistic chemical state of the atmosphere. Since emissions from fires are highly seasonal and inter-annually variable processes, information from these inventories has proved to be insufficient both for climatological studies of various years and on the short-term chemical weather scale. In the last years, satellite fire pixel products have become available, providing a more objective and complete assessment of global fire occurrences and thus, emission estimates. However, despite all progress and evidence gained with satellite retrievals that provide only the location of a fire, quantitative information on burned area and thus on aerosol and trace gas release, their dispersion and their impact, remained insufficient.

Recently, new global fire satellite products have been developed to quantify fire emissions. These products use more complex algorithms than the simpler fire pixel products and are therefore able to quantify the extension of a fire by obtaining the area burned, which is a crucial parameter in wildland fire emission modeling.

In this work, these new products have been analyzed and applied for emission calculation in order to obtain a transparent approach with reduced and assessed uncertainties. For this purpose the new Global Wildland Fire Emission Model GWEM was developed (Hoelzemann et al., 2004). Apart from area burned data, this model is based on the Lund-Potsdam-Jena Global Dynamic Vegetation Model LPJ-DGVM (Sitch et al., 2003), and landcover maps to estimate fire emissions on the global scale. GWEM has become a tool, which allows for a transparent calculation of fire emissions including seasonal and inter-annual variations, as adequate global high-resolution multiyear satellite input data for monitoring fires and landcover are becoming available. Input data and results of GWEM were carefully compared to other present inventories that are still in use within the atmospheric chemistry community and to recent publications on regional fire emission estimates. Further, emphasis was laid on the sensitivity of GWEM in relation to uncertainties in the underlying input data.

The global Chemistry Transport Model MOZART-2 was in the following used to assess the influence of the new GWEM wildland fire emissions on atmospheric chemistry. An impact study in the year 2000 was performed with the goal to assess the sensitivity of the model towards wildland fire emissions, calculated with GWEM in comparison with other, presently used, fire emission inventories. MOZART results reveal significant differences of 20-30% in background surface CO concentrations in the northern hemisphere, while fire-prone areas can differ by up to a factor of 6. Consequently, the ozone production is altered significantly over fire activity regions and outflow areas resulting in surface ozone differences of up to 30 ppbv.

1 Introduction

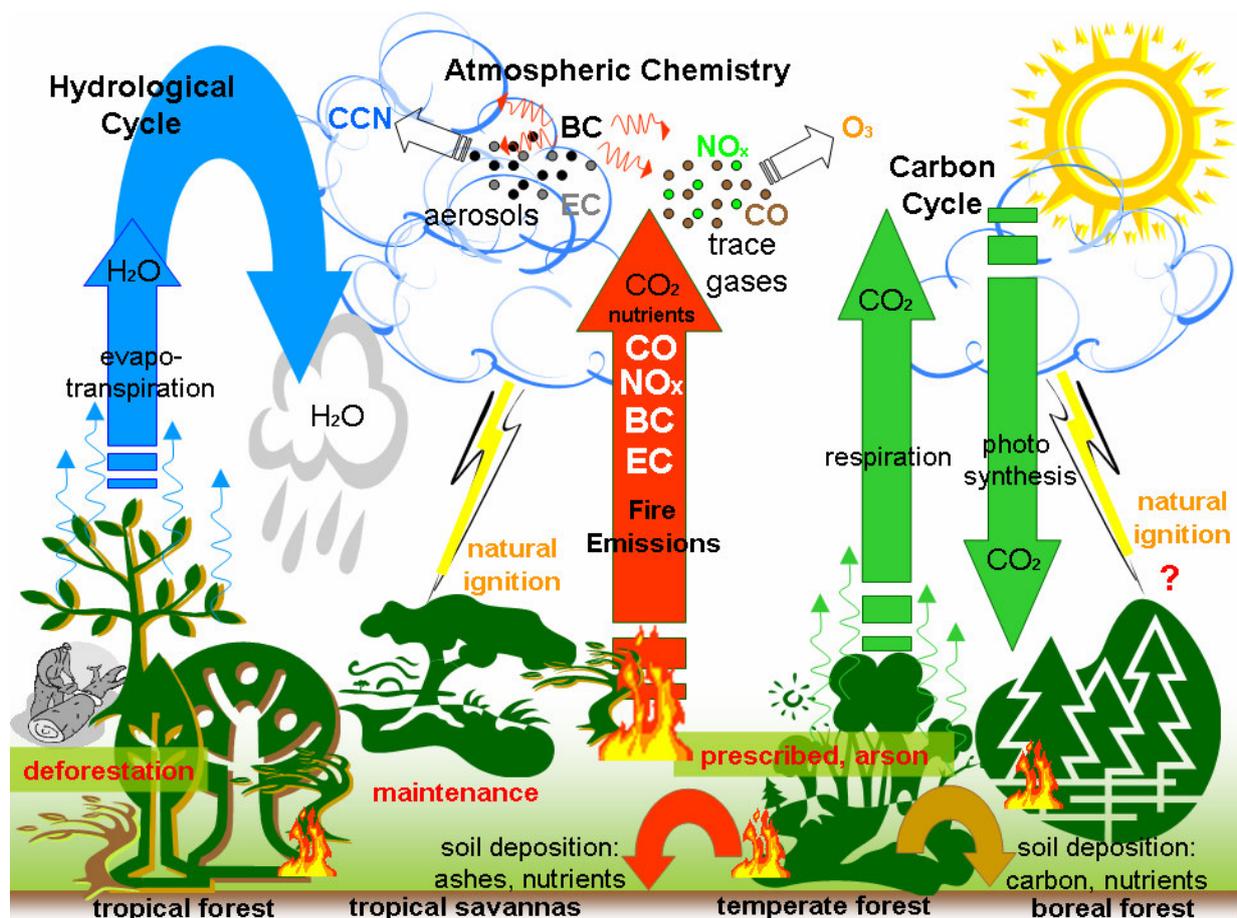## 1.1 Fires in the Earth System

Fires must have existed on Earth since the first land plants appeared to serve as fuel load (Andreae, 1991) during the Palaeozoic era. About 350-400 million years ago, vegetation started to expand around the same time as land masses on Earth began to build the super continent Pangaea. Naturally ignited fires at that time must have been triggered mainly by lightning associated to thunderstorms. Lightning frequency and its interplay with dry season length and intensity, plant (fuel) growth and its removal by mammals that consume vegetation, have ruled the natural fire regimes on Earth (Andreae, 1991).
It is the prehistoric human capture of fire that marks a profound event within the earth system (Pyne and Goldammer, 1997). Humans are the only species on Earth that control fire, which undoubtedly has made them leaders on the food chain. Ecological impact of anthropogenic fires in African savannas for example, can be identified already about 1.5-2 million years ago, when fire was used by humans for food preparation, hunting, and landscape control (James, 1989). Further, farming, pastoralism and production of ceramics, metallurgy (Pyne and Goldammer, 1997) and the burning of agricultural waste are well known anthropogenic activities making use of fire. More recently, prescribed burnings to control fuel accumulation in forests, deforestation processes for land clearing, pasture-land maintenance, pest-control, fertilization of soil, and lumbering in the tropics as well as charcoal production for industrial and domestic use and the combustion of biofuels as renewable energy source have considerably increased human related fire processes (Andreae, 1991; Pyne and Goldammer, 1997). All these fire processes can be subsumed under the term *biomass burning*. Today, humans are believed to be responsible for at least 90% of biomass burning on Earth. The remaining 10% of natural fires are still ignited by lightning activity in tropical savanna and some temperate and boreal forest ecosystems (Andreae, 1991). It is likely that annual biomass burning has strongly increased (30-50%) over the last century, due to the intense tropical deforestation and enhanced domestic fuel wood combustion (Scholes M. et al., 2003).

Wildland fires -that will in the following be defined as all natural and anthropogenic open vegetation fires occurring in savanna and forest ecosystems- have led to various transformations on Earth: fire continuously changes the vegetation cover on Earth and has significantly formed its present distribution. Fires are related to natural forest stand replacement, species competition, and conversion of tropical forests for agricultural or other purposes and they can lead to important ecosystem transitions (Mueller-Dombois and Goldammer, 1990; Geist and Lambin, 2001; Cochrane, 2003).
Natural fires in temperate and boreal forests reactivate the nutrient and carbon cycle of the ecosystem: In an aged forest stand, the cycling of nutrients and carbon slowly decrease, as fewer nutrients are available in the soil. A fire in such an environment can restart the cycle: nutrients and carbon are released to the atmosphere and return to the soil as ashes and decomposing on-site semi-burned dead plant material. The nutrient-enriched soils with enhanced microbial activity give rise to the regrowth of a new forest that will again uptake carbon from the atmosphere (Aber and Mellilo, 2001).
In savannas, natural fire regimes support the competition between grasses and trees: without fires in a grass-dominated savanna, tree species will potentially expand and convert the grassy savanna into a wooded savanna and further into woodland or even forest. In this scenario, trees will start to compete with the grass for light and slowly extinguish grass plants from the terrain (Daly et al. 2000). Natural fires are an important factor to maintain an equilibrium between both plant types: in contrast to trees, grassy vegetation has the ability to survive fire because the vital parts of the plants are located below the ground and thus are not affected by surface fire. As a consequence, in grass and tree shared savanna

Figure 1.1: Placement of wildland fires within the Earth System, fire reasons, fire interaction with the global carbon cycle and the hydrological cycle, and fire effects

environments that are affected by fire, the grass will survive while the mortality of the tree species will be significant. Some of the vegetation may also adapt to fire by creating resistance strategies.

Most anthropogenic wildland fires regularly take place in the tropics, either in tropical savannas for agricultural purposes or as deforestation fires in primary rain forest (Wuebbles, Brasseur and Rodhe et al., 2003). In Brazil alone from 2000 to 2005, fires were in the conversion of approximately 21800 km^2 per year of primary rain forests into pastures and agricultural lands (annual average estimate for the years 2000-2005 from the PRODES project at the Instituto Nacional de Pesquisas Espacias – INPE, Brazil). Other large deforestation regions with equal or even more intense deforestation activity are located in South East Asia and equatorial Africa. Tropical fires occur during the dry seasons, when potential plant material for burning is dry enough to serve as fuel. Deforestation fires are always a destructive process because they take place in biomes that would not burn under natural circumstances. This means that plants in such a biome are not adapted to survive fire and thus, present a high mortality rate. Selective logging and other anthropogenic disturbances make primary tropical forest more susceptible to fire. Widely used slash-and-burn techniques also allow the burning of naturally humid primary forest (Cochrane 2003).

During the northern hemispheric spring and summer, fires also occur in temperate and boreal regions. These fires are subject to a higher interannual variability than tropical fire activity (Kasischke et al, 2005). Outside the tropics, the forest lifecycle is slower and the forest ecosystem is more stable. Especially in the temperate zone, many forests are preserved reservoirs with low-impact fires taking place as prescribed-burnings to avoid litter accumulation and thus uncontrollable fire hazards. Temperate forests many times have the

form of scattered mosaics mixed with agricultural and urban landuse forms, and thus, fires are seen as an unwanted and dangerous threat to men. A large number of fire hazards in this ecosystem are a result of arson or accidental ignition, but they play a relatively small role from the global point of view. In remote, poorly-populated boreal forests still persists a high uncertainty as to the ratio of natural lightning-induced versus anthropogenic caused large fire occurrences. In favourable years for fire, low rainfall enables boreal fires that burn vast areas of forests.

The interactions of fires with the Earth's biosphere have significant implications on biogeochemical cycling (Crutzen and Andreae, 1990 and Hughes et al., 2000) (Figure 1.1). Fire alters the long-term dynamics of cycling and storage of carbon and other elements within the terrestrial ecosystems and thus changes their potential as sources and sinks for trace gases (Scholes M. et al., 2003). For example, fires destroy forests that are important carbon dioxide (CO_2) stocks. –In contrast to savanna fires, where vegetation and thus the CO_2 repository can be restored within a period of weeks to months, forests take decades for regrowth. Thus, the time scale of a fire (a few hours to days) is substantially lower than the time scale that vegetation requires to regrow (months to years) (Cardoso 2004). -A sudden release of all carbon stored within the plant to the atmosphere by a fire leads to an explosion of the normal CO_2 release rate reached by conventional plant respiration processes. Furthermore, CO_2 uptake by photosynthesis and thus its removal from the atmosphere ceases as the plant dies. Apart from direct CO_2 and other emissions into the air due to the combustion process, fires trigger emissions from the plants and the soil that take place during a few days after the burning. CO_2, NO and N_2O post-fire emissions may be more significant than their direct emissions. After a fire the soil changes its nutrient levels, pH and temperature (Scholes M. et al., 2003). Additionally, not all plant carbon is combusted and emitted into the air, but significant amount of carbon and nutrients remain on the ground as ashes (Figure 1.1), which affects and enriches the soil composition (Scholes M. et al., 2003).
Fires can also considerably affect the hydrological cycle (Figure 1.1). They indirectly reduce evapotranspiration due to plant removal (e.g. http://www.whrc.org/southamerica/fire_savann/FeedbackCycles.htm) and simultaneously augment the concentration of aerosol particles in the atmosphere, which are linked to cloud formation and their spatial distribution (e.g. Rosenfeld, 1999; Artaxo et al., 2002; and Artaxo et al. 2005).

Importance of Fires in the Climate System

The Kyoto protocol reinforced the importance of fires within the Climate System and has drawn the public attention to this topic. Today we know that fires potentially have a significant impact on global climate (e.g. Goldammer and Price, 1998; Stocks et al., 2000 and Nepstad et al., 1999). They enhance the greenhouse effect by emitting vast amounts of carbonaceous aerosols and trace gases to the atmosphere (e.g. Crutzen and Andreae, 1990; Brasseur et al., 1999; and Crutzen and Lelieveld, 2001), see also Figure 1.1). The aerosols, and to a minor extent as well the greenhouse gases, absorb and re-radiate solar UV radiation in the atmosphere. Fire aerosols modify precipitation patterns (e.g. Kaufman and Fraser, 1997; Ramanathan et al., 2001, and Andreae et al., 2002). Primary trace gas emissions such as carbon monoxide and nitrogen oxides lead to the formation of ozone (Figure 1.1). Ozone has recently been recognized as an important contributor to the enhanced greenhouse effect (contribution estimated to 20% since pre-industrial times) (Granier et al., 2003). Present annual carbonaceous fire emissions rival or may even exceed those from combustion of fossil fuels (Crutzen and Andreae, 1990). The emission of for example sulphur compounds (SO_2) however, are clearly more elevated during combustion of fossil fuels compared to those from biomass burning.
The deforestation of primary tropical rain forest is a permanent destruction of an important
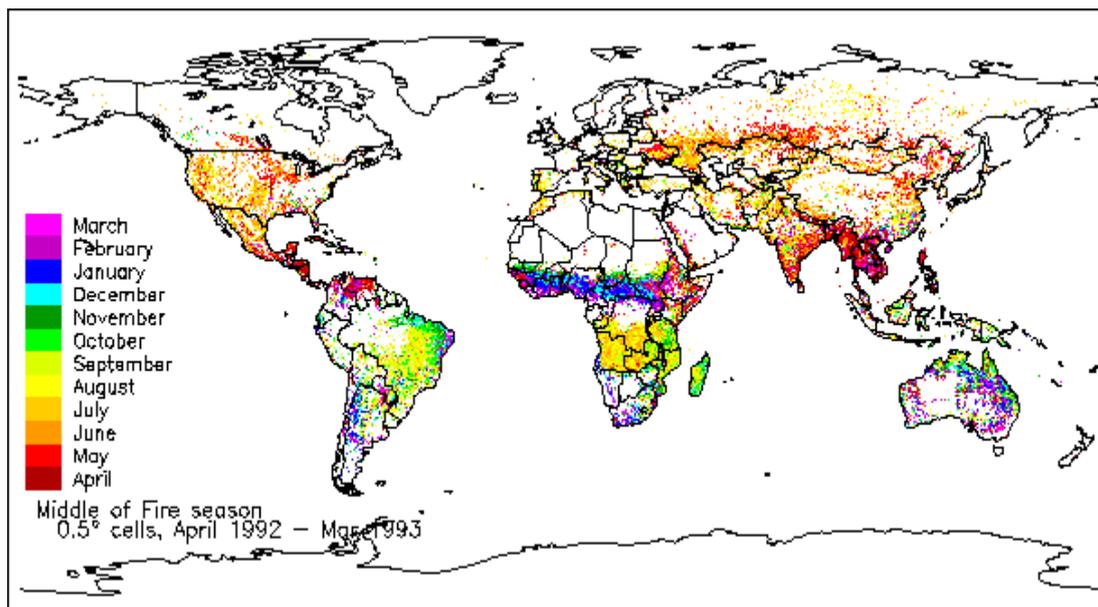
Figure 1.2: Monthly occurrence of global fire emissions from April 1992 to March 1993, source: Dwyer et al., 1999

CO_2 stock and also leads to microclimate change (e.g. Culf et al., 1996). On a shorter time scale, fire intensity controls the convective transport of fire emissions and thus their further horizontal transport. Fires change the albedo and other land surface properties of the Earth's surface, which can affect the transpiration and energy-balance on regional scales (Govaerts et al., 2002 and Beringer et al., 2003).

Vice versa, climate bears a considerable impact on fire: precipitation and temperature control fires by regulating soil and fuel moistures, fuel load growth (Net Primary Production NPP) and are also responsible for changes in fire regimes, which in turn has an influence on ecosystem changes (Goldammer, 1991). In both undisturbed and (men-)disturbed forest ecosystems that experience several years of low rainfall, fire susceptibility increases (Nepstad et al., 1994 and 1995). In disturbed forests however, the fire susceptibility will be higher (Uhl and Kauffman, 1990; Holdsworth and Uhl, 1997; and Cardoso et al., 2003).

On the weather time-scale, wind and humidity control fire properties such as flaming or smoldering combustion, spreading of the fire front, the injection height of the fire plume and thus its transport. Depending on the horizontal wind patterns in higher altitudes, fire emissions may be transported over long-range distances on regional to intercontinental scales (see e.g. studies by Forster et al., 2001; Andreae et al., 2001; and Stohl et al., 2002).

Importance of Fire Emissions for Modeling Atmospheric Chemistry Processes

Today, we are aware that emissions from wildland fires represent a large perturbation to global atmospheric chemistry. (Scholes M., et al., 2003). The abundant release of aerosols and chemical compounds into the atmosphere is one of the most direct effects of wildland fires. Fire emissions alter the air's chemical composition on local, regional and many times on inter-continental scales and thus have a strong impact on air quality. As a result this leads to considerable health effects on human population and reduced visibility in smoke and haze affected areas (e.g. Brimblecombe, 1987; Smith, 1987 and 1996; and Gupta et al. 1998). Cities in downwind location of fire-prone areas can be frequently affected by regional haze events during the burning season. Fine particular matter, (PM2.5 and PM10) but also carbon monoxide, methane, nitrogen oxides, benzene, formaldehyde and aromatics emitted by fires can then cause severe respiratory problems in the population, reaching

Figure 1.3: Picture of a fire with pyrocumulus injection into the atmosphere taken during the SMOCC campaign (Smoke Aerosols, Clouds, Rainfall and Climate: Aerosols from Biomass Burning Perturb Regional and Global Climate), courtesy of K. Longo and M. O. Andreae

from respiratory irritation over asthma to lung cancer, if exposure is frequent and over long periods (see for example a governmental web page of the "fire continent" Australia: http://www.deh.gov.au/atmosphere/airquality/_publications). Also the ambient use of fire is a cause of smoker's lungs and consequent diseases related to inhalation of smoke since ancient times (e.g. Brimblecombe, 1987). Another effect of regional fire haze is a strongly reduced visibility due to the aerosol load in the air, which repeatedly leads to the closure of airports in fire-prone regions for several days. For example, in Brazil, the airport of Rio Branco in the State of Acre that experiences large burning activities every year, had to be closed down repeatedly in September over the last years (A. Setzer in http://paginas.terra.com.br/servicos/vnw/ventonw/aero_queimadas.htm and LBA news: http://lba.cptec.inpe.br/lba/?p=11&lg=&op=74). Also the airport of Santarém, in the Amazon Basin, has to be closed down frequently during the burning season, due to poor visibility (Andreae, 1991).

The dominant fraction of emissions from fires contains carbon. Most of the carbon (about 90%) is emitted in the form of carbon dioxide (CO_2) or carbon monoxide (CO). Most of the remaining carbon splits into emission of methane (CH_4), non-methane hydrocarbons (NMHC), and oxygenated volatile organic compounds (O VOC) (Andreae and Merlet, 2001). Less than 5 % of the carbon is released as particulate matter (Reid et al., 2005a,b). Other relevant species released are nitrogen oxides ($NO_x = NO + NO_2$).

Every year an average of about 8200 Tg CO_2, 410 Tg CO, 19 Tg CH_4, 25 Tg NMHC, 16 NOx (as NO), 23 Tg OC, 3 Tg BC, and other species are emitted globally (estimates by Andreae and Merlet, 2001). These average values can vary considerably for individual years, as fire activity is highly interannually variable. Apart from strong year-to-year variations, wildland fires also have a highly seasonal distribution, driven by the regional dry seasons (Figure 1.2). If meteorological conditions are favorable, the smoke plumes can be injected into altitudes (Figure 1.3) above the Planetary Boundary Layer (PBL) (e.g. Lavoué, 2000; Andreae et al., 2001; Fromm and Servranckx, 2003; and Jost et al., 2004) reaching a degree of dispersion that would not be possible in lower levels. From there they can even be transported over

thousands of kilometers on an intercontinental scale. These processes are driven initially by fire heat and fuel moisture, depending later on meteorological conditions mainly (wind, temperature, precipitation). During these transport processes several of the chemical gases or particles are transformed by heterogeneous- and gas-phase chemistry as well as by aerosol microphysics and by thermodynamics.

- **Importance of Aerosols**

Carbonaceous aerosols, as released by wildland fires can be distinguished between Black Carbon (BC) and Organic Carbon (OC), and trace inorganic species such as potassium, chlorine, and calcium (Reid et al., 2005a,b). On average, wildland fires are responsible for 35% of all carbonaceous particle emissions (IPCC, 2001).

Aerosol particles in the atmosphere modify the radiative balance of the atmosphere on a regional and global scale: they reflect and disperse solar radiation back into space and thereby reduce the absorbed quantity by the earth's surface and absorb solar radiation and thereby heat the atmosphere (direct effects). Jacobson (2001) suggests that the atmospheric heating due to black carbon aerosols (BC) may compensate the cooling effect associated to sulfate aerosols and that the direct radiative forcing may exceed the one associated to methane (CH_4). In this case, aerosol particles are only outperformed by carbon dioxide (CO_2) in their contribution to atmospheric radiative heating. On the other side, photochemical production of tropospheric ozone (O_3) is severely reduced by an enhanced radiative actinic aerosol flux (Albuquerque et al., 2005).

The radiative balance and the hydrological cycle may also be indirectly affected by aerosols by microphysical and dynamical alterations in cloud formation (Kaufman, 1995). More cloud condensation nuclei (CCN) and ice are built in the atmosphere by enhanced aerosol concentration, that provoke changes in the cloud droplet spectrum (Warner and Twomey, 1967; Hobbs and Radke, 1969; Cotton and Pielke, 1996; Rosenfeld, 1999; Andreae et al., 2004 and Koren et al., 2004) and the thermodynamic stability (Longo et al., 2006). An augmented aerosol particle concentration leads to smaller and more cloud droplets and thus produces two effects: first, the higher droplet quantity reflects more solar radiation back into space (thus cooling the atmosphere). Second, the reduced size is less favorable to provoke precipitation, because small droplets tend not to coalesce into raindrops as efficiently as larger droplets. On the other hand, the thermodynamic stability imposed by direct interaction of aerosol particles with solar radiation (reduces heating in the lower atmosphere by solar radiation), restricts ascending convective cells that are generated close to the surface and thereby inhibits cloud formation.

The knowledge about aerosol particle properties and their role in atmospheric change is quite recent. Only in this last decade, the relevance of the inclusion of their effects in numerical atmospheric models for weather forecast, climate and air quality monitoring has been recognized. This change of attitude has brought an extraordinary increase, not only in complexity, but also in uncertainty to the scenario of climatic change (Andreae et al., 2005). For a long time, the well known effects of greenhouse gas heating were the actors in forecast climate models. Inclusion of aerosols in atmospheric models brings new challenges in terms of development of new parameterizations that properly represent the diverse processes of aerosol and other atmospheric elements interaction. And, before that, there is an increasing need for more accurate aerosol emission inventories.
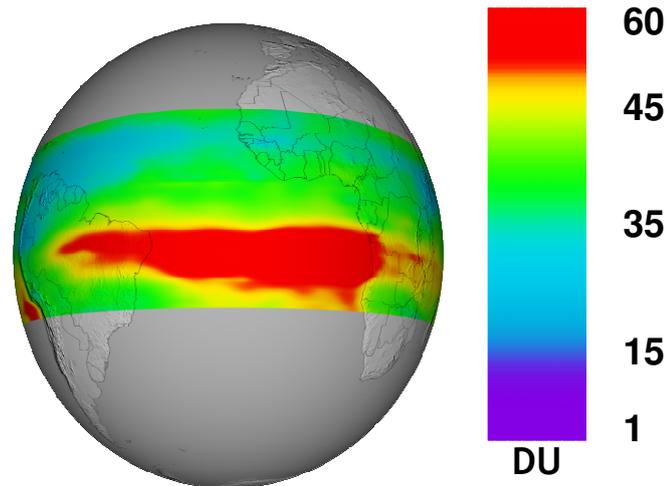
Figure 1.4: Tropospheric Ozone in Dobson Units [DU] measured by the Ozone Monitoring Instrument (OMI) aboard the NASA's AURA satellite over South America and Africa on October 12, 2004. Visualization by NASA/Goddard Space Flight Center, Scientific Visualization Studio, http://svs.gsfc.nasa.gov/search/ Keyword/Atmosphericscience.html

- **Importance of Chemical Gases**

Fires also emit important amounts of chemical species: apart from the most abundantly emitted gas, CO_2, trace gases such as carbon monoxide (CO), methane (CH_4), non-methane hydrocarbons (NMHC), nitrogen oxides (NO_x), nitrous oxides (N_2O), methyl chloride (CH_3Cl), methyl bromide (CH_3Br), etc. are released into the atmosphere.

The average annual contribution of fire emitted CO to the total abundance of its global budget is about 40% (IPCC, 2001). Fires contribute on average with about 20% to the global NO_x budget (IPCC, 2001). CO has a strong influence on the abundance of the hydroxyl radical (OH) and is part of a number of important chemical reactions in the atmosphere (e.g. Jacobson, 2001). Many of these fire emitted trace gases, but especially CO and NO_x, play an important role in the tropospheric ozone budget. Ozone photochemical production in the troposphere occurs by hydroxyl radical oxidation of CO, CH_4 and the NMHC's in the presence of NO_x (Penkett et al., 2003). According to a model study by Granier et al. (2000) about 25% of the global net chemical production of ozone results from biomass burning.

Elevated ozone concentrations can regularly be observed in considerable distance of fire sources (e.g. Fishman et al., 1996). For example Fishman and Brackett (1997) and Hudson and Thompson (1998) observed high tropospheric ozone abundances (see Figure 1.4) over the Southern Atlantic that are confirmed by various field campaign observations (e.g. Thompson et al., 1996a; and Browell et al., 1996). This ozone plume, its formation and transport and its biomass burning precursors have further been investigated in for example Thompson et al. (1996b) and more recently in Edwards et al. (2003) by the use of a number of satellite observations. These studies have helped considerably to understand the role of fires in the formation of tropospheric ozone. However, large uncertainties persist as to the quantitative estimate of ozone precursors from wildland fires.

1.2 State of the Art in Global Fire Emission Modeling

Wildland fires have gained the attention of the atmospheric chemistry modeling community since the 1980's (Seiler and Crutzen, 1980). When the first Chemistry Transport Models (CTM's) were developed, it was recognized that emissions from wildland fires should be included to realistically represent the distribution of ozone and its precursors. Similarly, realistic carbonaceous aerosol simulations are not possible without taking the burning of vegetation into account. As shown in Figure 1.1, the spatial, seasonal and interannual distribution of fires on the globe is highly variable, depending on the regions and ecosystems of the planet in which they occur. This variability turns global determination of fire occurrences into a challenge.

One of the first attempt to quantify global wildland fire emissions was performed by Seiler and Crutzen (1980), followed by Hao, Liu and Crutzen (1990), Hao and Liu (1994), Cooke and Wilson (1996), Galanter et al. (2000), Lobert et al. (1999), and Lavoué et al. (2000). These inventories typically represent climatological annual totals of wildland fire emissions (Hao and Liu, 1994; and Galanter et al., 2000). More recently, the considerable interannual variability of fire emissions has started to be investigated, for example by Wotawa et al. (2001), Schultz (2002), Duncan et al. (2003), Generoso et al. (2003), and Hély et al. (2003a). However, the above-mentioned inventories rely on incomplete and scattered input data. Errors are usually assumed to be very large and the data are of inconsistent quality on the global scale. For many regions, data from ground-based or airborne surveys is not available and, where available, they are often inconsistent, inaccurate or lack the necessary temporal resolution (at least monthly) to capture the highly variable wildland fire emission behavior.

A number of recent studies apply satellite data to improve the existing climatological emission inventories. Emissions are scaled to global active fire count (or: fire pixel) data from satellites such as the Along Track Scanning Radiometer (ATSR-2) of the European Space Agency (ESA) (Arino et al., 2001, Arino and Plummer, 2001). Duncan et al. (2003) determined an average seasonal variation of biomass burning out of four years of ATSR fire count data (1996-2000) based on the emission inventory by Yevich and Logan (Lobert et al, 1999) and derived the inter-annual variability of the wildland fire emissions from the Total Ozone Mapping Spectrometer (TOMS) Aerosol Index (AI) for several regions. Schultz (2002) applied the ATSR fire counts for both seasonal and inter-annual variability on the wildland fire emission inventory used in the MOZART-2 Chemistry Transport Model (described by Horowitz et al., 2003). Generoso et al. (2003) provided a climatological inventory for carbonaceous aerosols scaled by active fire counts from the Tropical Rainfall Measuring Mission TRMM-VIRS sensor.

Though a big step in the right direction from the global point of view, active fire counts alone have proofed not to be the appropriate product to make quantitative statements about global wildland fire emissions: the algorithms yield a noticeable number of false detections due to their simplicity (temperature threshold) (Mota et al., 2006; and see map of "spurious pixels" in Schultz, 2002). Fires have very different combustion behavior, depending on ecosystem, fuel moisture, and weather conditions they can evolve highly different intensities and thus temperatures, which feedback on the temperature signal they deliver. Therefore, even if a fire is spotted correctly it is still not possible to link this spot to the real spatial extension of the observed fire, and thus to the amount of emissions released. Further, Giglio and Kendall (2004) have highlighted in a comment with respect to the TRMM-VIRS fire counts, that the same hot spot retrievals are very sensitive to the algorithms applied, which can result in completely different products.

Van der Werf et al. (2003) developed a new fire emission inventory using a more elaborated approach with active fire counts from TRMM-VIRS for the period 1998-2001. The work complementarily relates fire counts to existing area burnt data from the USA and the Moderate Resolution Imaging Spectrometer (MODIS) for some regions. A modified version of

the Carnegie-Ames-Stanford-Approach (CASA) biogeochemical model is included in this approach to obtain a wildland fire emission inventory restricted to the tropics and subtropics. Also with this approach however, the uncertainty related to the burned area size still persists.

1.3 Objectives of this Study

The aim of this work has been to develop a new transparent, "bottom up" global wildland fire emission model, based on the most recent input data available for the calculation of emissions. Further, the impact of these newly derived emissions on atmospheric chemistry and specifically on tropospheric ozone was investigated.

Recently, new global fire satellite products have been developed to quantify fire emissions. These products use more complex algorithms than the simpler fire pixel products: first the GLObal Burnt SCAR (GLOBSCAR) data from the European Space Agency (Simon, 2002; and Simon et al., 2003) was released, shortly after followed by the Global Burnt Area Initiative GBA2000 from the Joint Research Centre of the European Commission (JRC), (Grégoire et al., 2003; and Tansey et al., 2004). These algorithms are able to quantify the extension of a fire by obtaining area burnt in a resolution of 1 km^2, which is a crucial parameter in wildland fire emission modeling.

In this work, these new products have been analyzed and applied for emission calculation in order to obtain a transparent approach with reduced and assessed uncertainties. For this purpose the new Global Wildland Fire Emission Model GWEM was developed (Hoelzemann et al., 2004). Apart from area burned data, this model is based on the Lund-Potsdam-Jena Global Dynamic Vegetation Model LPJ-DGVM (Sitch et al., 2003), and landcover maps to estimate fire emissions on the global scale. GWEM includes updated emission factors from Andreae and Merlet (2001) and Andreae (2003, pers. comm.). GWEM has become a tool, which allows for a transparent calculation of fire emissions including seasonal and inter-annual variations, as adequate global high-resolution multiyear satellite input data for monitoring fires and landcover are becoming available.

Input data and results of GWEM were carefully compared to other present inventories that are in use within the atmospheric chemistry community and to recent publications on regional fire emission estimates. Further, emphasis was laid on the sensitivity of GWEM in relation to uncertainties in the underlying input data.

First results of GWEM (Hoelzemann et al., 2004) are already used by the fire emission and atmospheric chemistry community. Some examples of such studies are: Chédin et al. (2005), Jaeglé et al. (2004 and 2005), Kasischke et al. (2005), Ito and Penner (2005), Jain et al. (2006), and Dentener et al. (2006).

Emission data from GWEM can further serve as a mean of calibration for mechanistically produced emissions that are needed for years of climatological studies where no satellite data is available. This has been the case for the work by Schultz et al. (2005).

The GWEM model will also serve as a basis for the development of a global assimilation of wildfire emissions scheme within the European GEMS project (Global and Regional Earth-System Monitoring using Satellite and In-Situ Data, EC 6th Framework Project) coordinated by the European Centre for Medium-range Weather Forecast (ECMWF), see http://www.ecmwf.int/research/EU_projects/GEMS).

The global Chemistry Transport Model MOZART-2 was in the following used to assess the influence of the new GWEM wildland fire emissions on atmospheric chemistry. An impact study in the year 2000 was performed with the goal to assess the sensitivity of the model towards wildland fire emissions, calculated with GWEM in comparison with other, presently used, fire emission inventories. The other global fire emission inventories comprise the old MOZART-2 standard fire emission data set, based on the climatological emission inventory

by Hao and Liu (1994) and Mueller (1992), further two emission inventories that are also based on this climatological data but are scaled with active fire counts from ATSR (Schultz, 2002; and Granier and Lamarque pers. comm., 2004), and finally the only other "bottom-up" fire emission inventory by Van der Werf et al., 2003) that has been extended to cover temperate and boreal ecosystems using also the ATSR fire pixels.

MOZART results reveal significant differences of 20-30% in background surface CO concentrations in the northern hemisphere, while fire-prone areas can differ by up to a factor of 6. Consequently, the ozone production is altered significantly over fire activity regions and adjacent areas resulting in surface ozone differences of up to 30 ppbv.

1.4 Outline

This study is organized as follows: Chapter 2 presents the Global Wildland Fire Emission Model (GWEM) that was developed in the framework of this study. GWEM presents the basic tool to estimate bottom-up fire emissions based on most recent available satellite- and other input data.

In Chapter 3 the resulting emissions from GWEM are compared for the year 2000 to other presently used global fire emission data sets. These data sets comprise one other newly built bottom-up approach, based on different input data, further, two methodologies that scaled a climatological fire emission inventory with fire count data for the year 2000, and finally the old climatological fire emission inventory that is still being used in many modeling studies using MOZART or other Chemistry Transport Models. In addition, other emission sources, apart from fires, used in the MOZART model are introduced.

The impact of these different wildland fire emission inventories on atmospheric chemistry is investigated in Chapter 4, using the global chemistry transport model MOZART-2. Results are compared and evaluated with CO satellite data from MOPITT, CO ground measurements from the CMDL network and ozone data from SHADOZ radio soundings and MOZAIC aircraft measurements. This chapter also provides an overview on the regional performances of the different inventories. The study closes in Chapter 5 with a summary of the approach and its main findings, main conclusions and with an outlook of desirable future developments in global fire emission modeling.

2 The Global Wildland Fire Emission Model GWEM

This chapter describes GWEM version 1.3 as used later in the Chemistry Transport Model MOZART-2. It is largely based on the paper of Hoelzemann et al. (2004), but with several improvements named in the outlook of this paper. Further, additions were made concerning the uncertainty of used data and resulting emissions.

2.1 Model Description

The Global Wildland Fire Emission Model GWEM is designed to provide global, monthly inventories for more than 40 different chemical trace gases and aerosols at $0.5° \times 0.5°$ spatial resolution. The resolution limit is imposed by the input of the LPJ vegetation model. GWEM includes the following data in its calculations: (i) monthly area burned to determine the spatial distribution of the fires and their extent within a gridbox, (ii) the amount of burnable plant material also known as the available fuel load (AFL), to determine the amount and exact location of carbon in the vegetation, (iii) a vegetation map which distinguishes ecosystems, (iv) emission factors as a function of chemical species or aerosols, and (v) the burning efficiency as a function of ecosystem, which determines how much of the available fuel load is burned.
Five ecosystems have been chosen for this global approach: (1) savanna and grasslands, (2) wooded savannas, (3) tropical forests, (4) temperate forests, and (5) boreal forests.
To adequately calculate the emissions for each gridbox in GWEM the very basic wildland fire emission equation $M_{BB} = A \times AFL \times \beta$ by Seiler and Crutzen (1980) (M_{BB} is the amount of biomass burned, A is the area burned, AFL is the available fuel load, and β is the burning efficiency) has been extended to:

$$M(X)_m = \sum_{k=1}^{n} EF_k(X) \times A_m \times \beta_k \times AFL_k.$$

$M(X)_m$ is the monthly total amount of species X emitted from wildland fires per gridbox. m is the number of months (m = 12), n is the number of considered ecosystems (n = 5). $Ef_k(X)$ is the emission factor for each species X for a typical fire in ecosystem k. $A_{i,k}$ represents the area burned per month and per ecosystem, while β_k is the burning efficiency in ecosystem k.
The model works on a subgrid-scale resolution of 1 km^2, predetermined by the area burned product used. This allows for a substantially higher resolution at area burned locations to determine the landcover related parameters (β and EF), before downscaling to the final $0.5° \times 0.5°$ resolution.
The information on area burned can be supplied by different products: in the first studies of GWEM the GLOBSCAR product from ESA on a 1 km^2 resolution has been used (Hoelzemann et al. 2004). It is based on the European Remote Sensing (ERS) ATSR-daytime satellite data. In later work and for the thesis at hand the GBA2000 by JRC was applied that yields a lesser under-detection bias than GLOBSCAR. The GBA2000 area burned product is derived from the VEGETATION instrument aboard the European SPOT-4 satellite, also on a 1 km^2 basis (see section 2.2.1). The AFL is compiled from an output of the LPJ vegetation model for the year 2000 that is divided in five different carbon pools, four of which further containing nine Plant Functional Types (PFT's) (see section 2.2.2). Many of the data shown in this chapter will be presented as regional totals or averages.
An overview of the geographical regions chosen for this purpose can be found in Figure 2.1. More detailed description and region acronyms used, are defined in Table 2.1.
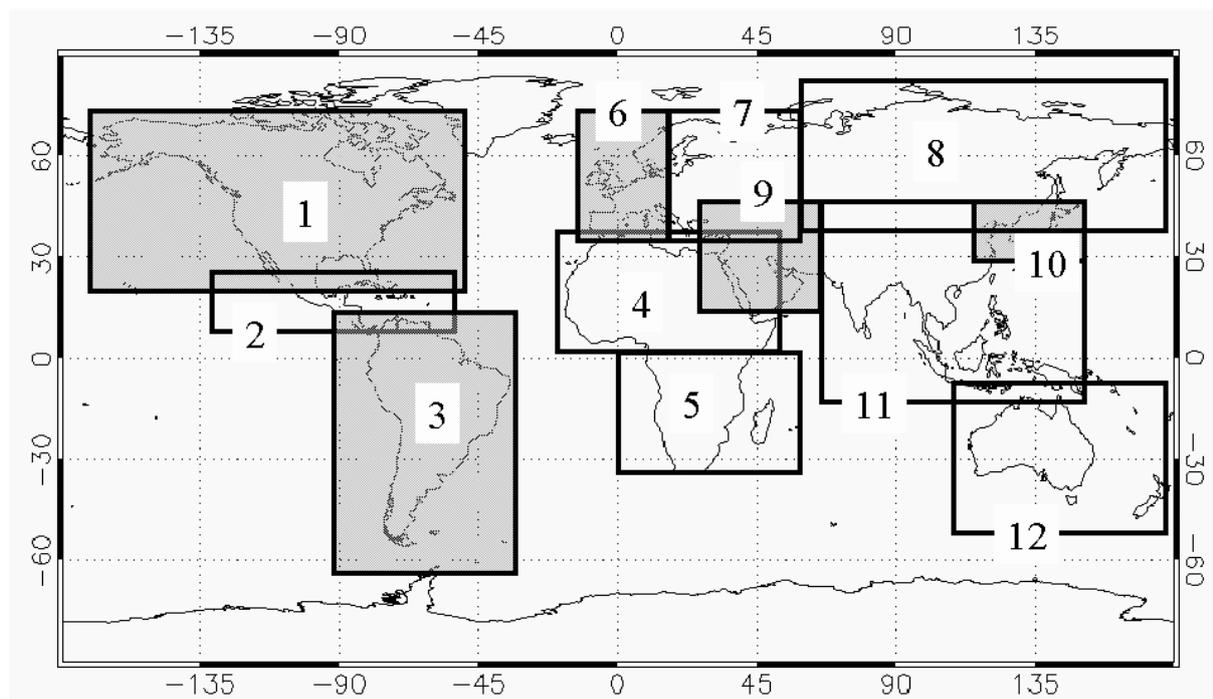
Figure 2.1: Geographical regions used for regional analyses in GWEM

Region number	Name of region	Abbreviation	Countries or geographical lat/lon describing region
1	North America	N-AM	Canada, United States of America
2	Central America	C-AM	Costa Rica, El Salvador, Grenada, Guatemala, Honduras, Mexico, Nicaragua, Panama
3	South America	S-AM	Argentina, Bolivia, Brazil, Chile, Colombia, Ecuador, French Guiana, Guyana, Paraguay, Peru, Suriname, Uruguay, Venezuela
4	Northern Africa	N-AF	All African countries north of the equator
5	Southern Africa	S-AF	All African countries south of the equator
6	Western Europe	W-EU	Austria, Belgium, Denmark, Finland, France, Germany, Greece, Ireland, Italy, Netherlands, Norway, Portugal, Spain, Sweden, Switzerland, United Kingdom
7	Eastern Europe	E-EU	Belarus, Bosnia-Herzegovina, Bulgaria, Croatia, Czech Republic, Hungary, Kazakhstan until $60°$ East, Macedonia, Poland, Romania, Russian Federation until $60°$ East, Slovakia, Slovenia, Ukraine, Yugoslavia
8	North/Central Asia	NC-AS	Russian Federation from $60°$ East, Kazakhstan, Mongolia
9	Near East	N-EA	Afghanistan, Armenia, Cyprus, Georgia, Iran, Iraq, Israel, Jordan, Kyrgyzstan, Lebanon, Pakistan, Saudi Arabia, Syrian Arab Republic, Turkey, Uzbekistan, Yemen
10	East Asia	E-AS	Japan, North Korea, South Korea
11	Southern Asia	S-AS	Bangladesh, Bhutan, Brunei, Cambodia, China, India, Indonesia, Hongkong, Malaysia, Myanmar, Nepal, Taiwan, Thailand, Vietnam
12	Oceania	OCE	Australia, New Zealand

Table 2.1: Geographical regions used for presentation of GWEM results. Only the main contributing countries are listed

2.2 Available Input Data for GWEM: Review and Choices

2.2.1 Area Burnt and Landcover Classification

Until recently, information on area burnt for global needs was based exclusively on country reports providing yearly amounts of hectares burned (e.g. the International Forest Fire News (IFFN reports) of the Food and Agriculture Organization (FAO)). The data exist only for some countries and are strongly variable in quality. This turns an application for global modeling into uncertain guesswork. Also, a countrywide approach does not allow for a sufficient resolution required for wildland fire emission modeling in terms of ecosystem distinction. Nevertheless, it was the best available for many years and has been used in several studies (e.g. Hao and Liu, 1994, Mueller, 1992, Lavoué et al., 2000).

Since then, more homogeneous and higher resolution quality data have become available and are used in regional-scale burned area assessment (e.g. Barbosa et al. 1999, Scholes et al., 1996, Pereira et al., 2000). However, these regional studies cannot be easily extended to the global scale, as regional data are patchy, follow different methodologies, and rely on different input.

In early 2003 two global satellite products for area burned, initially for the year 2000, became available: GBA2000 from the Joint Research Centre of the European Commission in Ispra, Italy (JRC) and used in this work, and GLOBSCAR from the European Space Agency (ESA) (Simon et al., 2003), which was applied in previous studies and is discussed in Hoelzemann et al. (2004). A brief sensitivity test of using the two different products has been performed in the input data discussion (section 2.4.1), as suggested in the paper by Tansey et al., 2004.

GBA2000 provides monthly areas burned globally at 1 km^2 resolution, in geographic coordinates. The product is derived from SPOT-VEGETATION (VGT) satellite data (Grégoire et al., 2003; and Tansey et al., 2004). The satellite has a daily coverage, except for the tropics, where the same area is only covered every 4-5 days. Overpass time is 10h30 AM. The VGT time series used for the global area burned product are of daily surface reflectance (S1) starting on December 1, 1999 to December 31, 2000. For best detection of burned scars, nine different algorithms are applied with respect to best performance in regional and ecosystem specific aspects (Tansey et al., 2004).

In this study a sub-selection of forest and savanna fires in the GBA2000 data set has been used, selected by help of a landcover map. Figure 2.2a (yellow dashed line) provides the monthly global burned area as given by GBA2000 for vegetated non-agricultural land cover classes according to the MODIS (Moderate Resolution Imaging Spectroradiometer) landcover map. This map was built by reprojection of mosaic exports from NASA TERRA/MODIS HDF-EOS MOD12Q1 V003 products by the Department of Geography, Boston University (http://duckwater.bu.edu/lc/ mod12q1.htm). To build the map, MODIS data was used from the period 10/15/00 to 10/15/01, based on the MODIS land cover classification algorithm (MLCCA) described by Friedl et al. (2002), and is therefore the closest available data for the year 2000. The MODIS lancdover map makes use of the International Geosphere-Biosphere Programme Data and Information Systems' (IGBP-DIS) system of units (Loveland & Belward, 1997) that is listed in Table 2.2.

Figure 2.2b presents regional area burnt abundances of the GBA2000 product according to the regions defined in Table 2.1. The other graphs in these two figures will be discussed in section 2.4.1 and 2.4.2. In total, a global area of 3.65 x 10^6 km^2 burned in forest and savanna fires in the year 2000. The MODIS landcover map is further used in GWEM to determine the emission factors and burning efficiencies, which vary between different vegetation types. GBA2000 records with IGBP classes 1-11 and 14 (see Table 2.2) were considered. Classes 12, 13, and 15-17 were eliminated due to their unburnable nature or inadequate biomass burning category, such as crops (class 12), which are not regarded here.

a)

b)
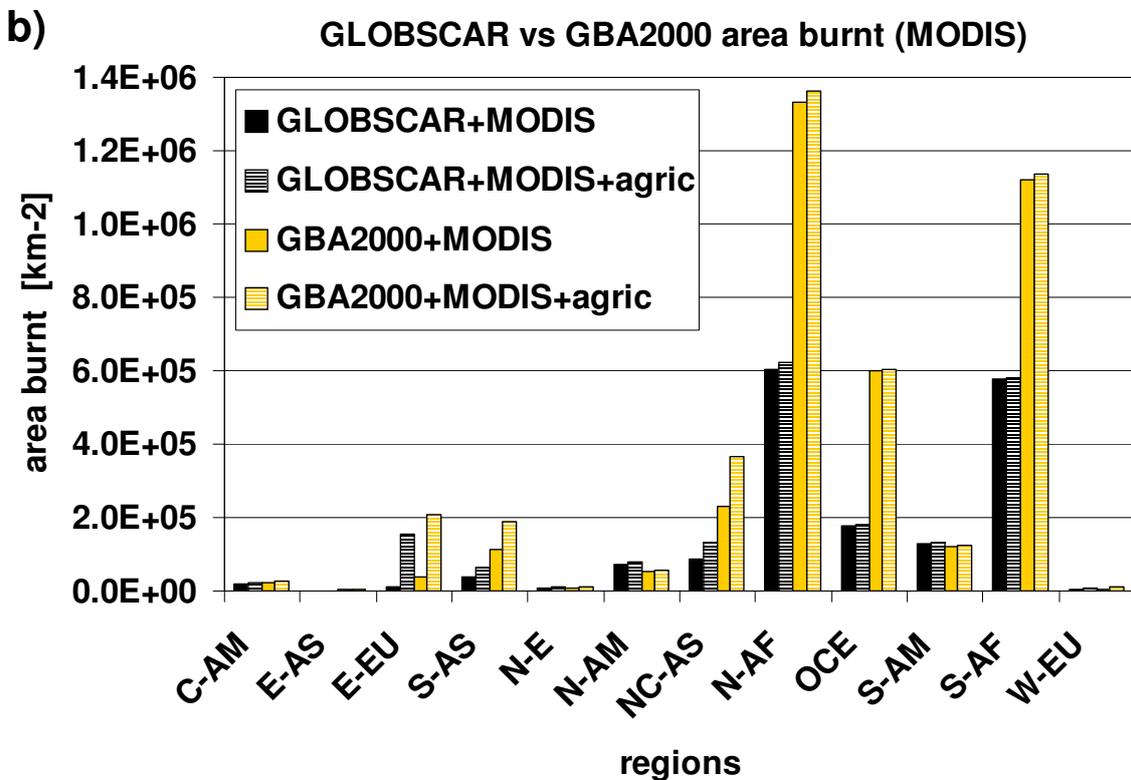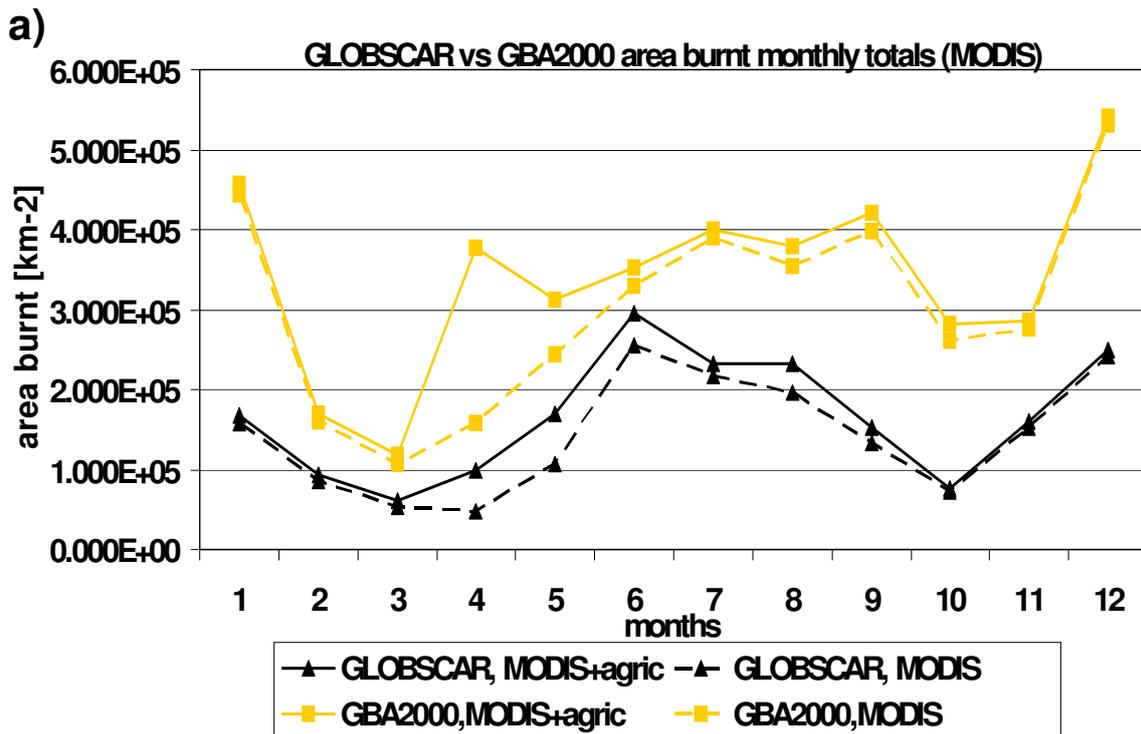
Figure 2.2: GBA 2000 (yellow) and GLOBSCAR (black) **a)** monthly area burned in km^2 with (continuous lines) and without (dashed lines) agricultural vegetation classes, and **b)** regional total area burned by wildland fires in km^2 for the year 2000. Full bars exclude burned areas in agricultural vegetation classes according to MODIS landcover map, while striped bars include all areas burned. Region acronyms are defined in Table 2.1

Value	Vegetations classes	Value	GWEM ecosystems	Value	Andreae and Merlet (2001) ecosystems
1	Evergreen Needleleaf Forest	4,5	Forest, latitude dependent [a] 3: tropical forest 4: temperate forest 5: boreal forest	2,3	Forest, latitude dependent [b]
2	Evergreen Broadleaf Forest	3,4			
3	Deciduous Needleleaf Forest	4,5			
4	Deciduous Broadleaf Forest	3,4			
5	Mixed Forest	3,4,5			
6	Closed Shrublands	2	Woody savanna	1	Savanna and grasslands
7	Open Shrublands	2			
8	Woody Savannas	2			
9	Savannas	1	Savanna and grasslands		
10	Grasslands	1			
11	Permanent Wetlands	2	Woody savanna		
12	Croplands	-	-	-	-
13	Urban and Built-Up	-	-	-	-
14	Cropland/Natural Vegetation Mosaic	2	Woody savanna	1	Savanna and grasslands
15	Snow and Ice	-	-	-	-
16	Barren or Sparsely Vegetated	1	Savanna and grasslands	1	Savanna and grasslands
17	Water Bodies	-	-	-	-
99	Interrupted Areas (Projection)	-	-	-	-
100	Missing Data	-	-	-	-

[a] 3: [-30°,+30°], 5: [< -60° and > +60°], 4: other, [b] 2: tropical forest, 3: extratropical forest

Table 2.2: International Geosphere Biosphere Programme (IGBP) landcover classification as described in Loveland and Belward (1997), GWEM ecosystem assignment and Andreae and Merlet (2001) ecosystem assignment

From the total of 4.10×10^6 km^2 detected GBA2000 area burned, 450000 km^2 of burned cropland (class 12) were eliminated from the record, according to the MODIS vegetation class map.

Please note that the totals of the GBA2000 numbers may vary in different studies, depending on the landcover map used to determine burnable vegetated areas and croplands. Further, the annual total GBA2000 values are lower than those of the monthly product (used here) because the annual product disregards areas that are burned twice a year, which frequently happens in many savanna type ecosystems with fast regrowth of fuel. More and online information on GBA2000 can be found at the Joint Research Centres' (JRC) website http://gvm.jrc.it/fire/gba2000/index.htm.

2.2.2 Available Fuel Load (AFL)

Equally crucial input data for wildland fire emission modeling is the information on potentially burnable vegetation (aka. available fuel load (AFL)). There are three different approaches pursued in the literature so far. Most common for wildland fire emission modeling, are compiled fuel load maps. (e.g. ECE-FAO's IFFN-reports or literature in e.g. Lavoué et al., 2000; Hao and Liu, 1994). These prescribed fuel load values are representative for ecosystems in a specific region, but cannot be applied on a global scale. To the authors' knowledge, there are currently no globally consistent and accurate data on
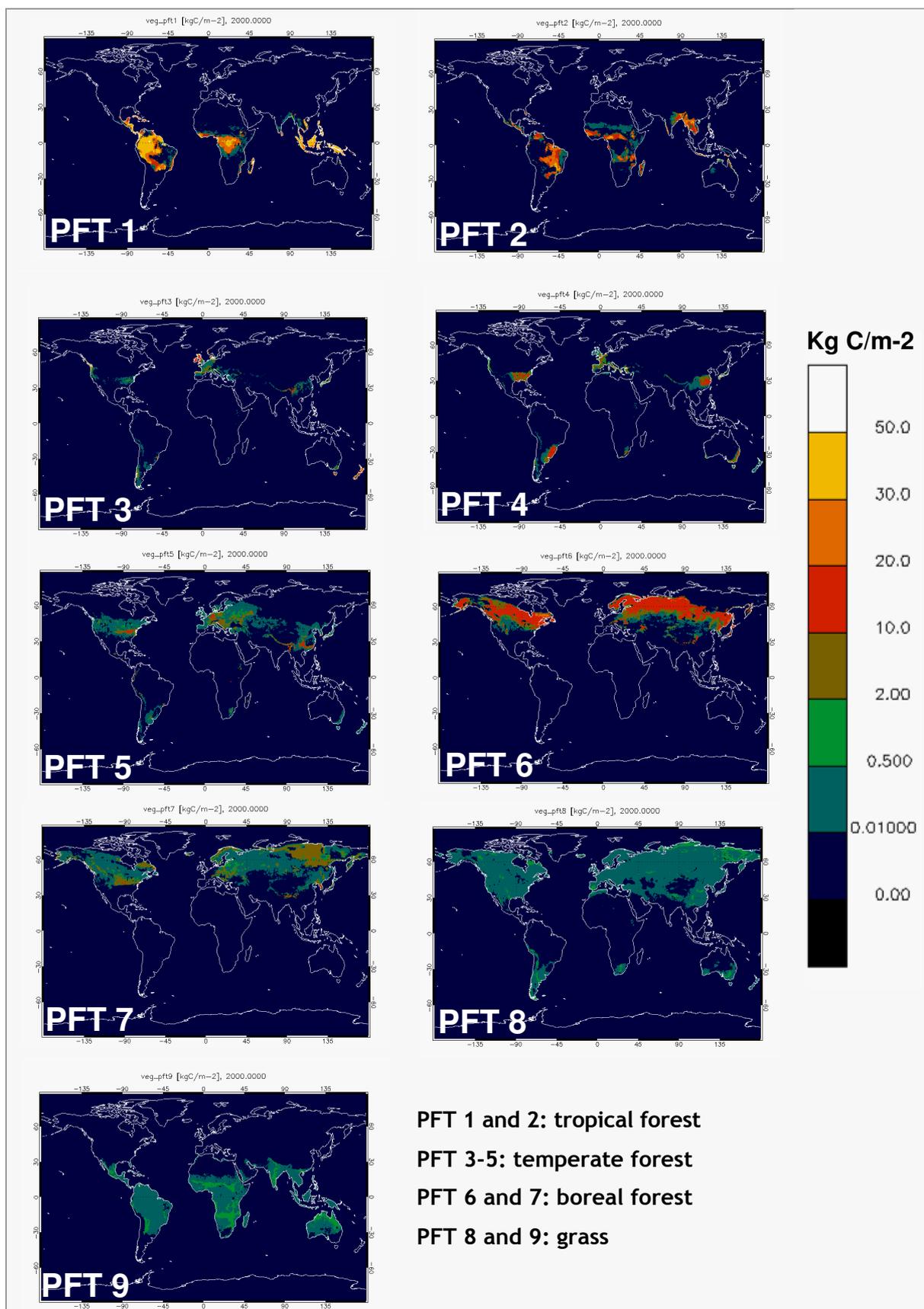
Figure 2.3: classification and distribution of the nine Plant Functional Types (PFT's) in the Lund-Potsdam-Jena Global Dynamic Vegetation Model (LPJ)

AFL in the literature, which can be used for emission modeling. In regional approaches, satellite retrieved vegetation specific parameters such as the NDVI (Normalized Difference Vegetation Index) for Africa have been used to compute the AFL (e.g. Barbosa et al. 1999). This remote sensing approach however, requires detailed background knowledge about each particular region under consideration. A third approach for estimating AFL is the use of vegetation models simulating the global carbon cycle within the terrestrial biosphere. These models calculate different carbon pools within the vegetation, and by choice of the essential ones, which are susceptible to fire, the AFL can be determined. On the regional scale, Hély et al. (2003b) have used a fuel load model for southern Africa, while Van der Werf et al. (2003) have applied the biogeochemical CASA model for emission modeling in the tropics and subtropics (38°S – 38°N).

In this work, a global output of the Lund-Potsdam-Jena Dynamic Global Vegetation Model (LPJ-DGVM) (Sitch et al., 2003) for the year 2000 is used for estimating the AFL. LPJ is considered a model of intermediate complexity, which can be applied to a broad range of global applications. LPJ simulates process-based large-scale terrestrial vegetation dynamics including the carbon exchange between land, atmosphere, and water. For a more detailed description see Sitch et al. (2003).

The LPJ model itself comprises a general fire model (Glob-FIRM: GLOBbal FIRe Model) (Thonicke et al., 2001) that annually constrains the amount of total biomass. Other constraining factors are tree mortality as a result of heat stress and light competition. Typical applications of LPJ are on climatological timescales. For this purpose a fully parameterized fire module that delivers burned areas based on information of biomass load, litter moisture, length of fire seasons, and PFT-dependent fire resistance is adequate. However, for the scope of best representing individual years as pretended in this work, this approach is too broad. In order not to create interferences of the two fire modules, the LPJ model was setup from the year 1901 to the year 2001. An annual output was produced for 1990 to 2001. GLOB-FIRM was switched on until end of December 1999 and then deactivated for the whole year 2000, to obtain a realistic potential biomass load of this specific year. To evaluate the sensitivity of LPJ towards its fire module two additional runs were performed: in one run the GLOB-FIRM model remained activated throughout the year 2000 and in another run GLOB-FIRM was switched off for the whole model run. This brief sensitivity study revealed that the run where GLOB-FIRM is totally switched off delivers abnormally elevated biomass densities, as biomass accumulates without the important disturbance of fire. The difference of the other two runs was minimal, but experienced a sudden jump in the temporal evolution of biomass from 1999 to 2000 in the case where GLOB-FIRM was deactivated for the year under consideration. Since only the year 2000 is regarded, the latter LPJ output was applied in GWEM to use the most realistic conditions for the year 2000.

LPJ delivers five global annual carbon pools of litter, leaf, heartwood, sapwood and fine roots at a 0.5°x 0.5° resolution. Except for the litter, these carbon pools are further sub-divided into nine Plant Functional Types (PFT's) that specify the type of vegetation inherent in one gridbox (Figure 2.3). Additionally, information of fractional cover of each PFT and the percentage of non-vegetated area per gridbox is delivered for each PFT-resolved carbon pool from LPJ. To arrive at values of AFL from the amount of total carbon given by the LPJ model, the PFT's in each carbon pool were summated according to Table 2.3:

$$AFL_{total} = \sum_{k=1}^{neco} AFL_k = \sum_{k=1}^{neco} \left[\sum_{t=1}^{npft} fc_t \times \sum_{p=1}^{ncp} \chi_{t,p,k} \times m_{t,p} \right],$$

where AFL$_{total}$ is the total available fuel load per grid box, AFL$_k$ are the AFL's for each

ecosystem in GWEM (neco=5), fc is the fractional cover of each of the PFT's (npft=9), χ is the susceptibility factor of each PFT and carbon pool per ecosystem (given as percentage in Table 2.3), and finally, m is the amount of carbon of each PFT per carbon pool. The susceptibility factors were defined in accordance with typical burning patterns of the individual ecosystems: in all ecosystems, litter is potentially fully available for burning. In forest ecosystems mainly the litter layer (dead needles and leaves, downed woody material) and small live and dead aerial fuels (foliage, twigs, small branches of understorey vegetation and trees) are consumed by fire; depending on dryness conditions the duff layer is also available for partial or complete combustion (FIRESCAN, 1996; Goldammer, pers. comm., 2002). However, there are differences for forests in different climatic zones and continents. In Eurasia, for example, less litter (only 70% of total) is available for fire because of the thickness and moisture content in raw humus layers during average fire-weather conditions (FIRESCAN, 1996; Goldammer, pers. comm., 2002). Also, the leaves in Eurasian forest are mostly not significantly consumed, since fires stick to the surface, and may also affect the ground layer (Thonicke, pers. comm., 2003, Goldammer, pers. comm., 2002).

An even more difficult case for generalization is the tropical forest: depending on its deforestation history it is variably susceptible to fire (Goldammer, 1999): if a tropical forest is undisturbed but dry and ready for a fire, the litter burns, but trees remain almost unaffected, only a minor percentage of the leafs can burn. If the tropical forest is moderately disturbed, half of the leaf and a small part of the wood pool can potentially burn in addition to the total litter, while in heavily disturbed tropical forest a considerable part of the leaf and decaying wood pool can be affected apart from the litter (Goldammer, pers. comm., 2002). It has been assumed that most of the present tropical forest fires are deforestation fires and can therefore be assigned to the third category.

For the sake of consistency it has been attempted to restrict the global model as little as possible with extra-rules for individual regions and biomes.

A best guess run was computed that includes the best estimate of AFL according to literature and input from various experts and is based on the information in Table 2.3 (numbers in black). Five additional GWEM runs with different AFL scenarios were performed in order to (i) extract the sensitivity of the model toward integration of different carbon pools and (ii) to illustrate the effect of idealized AFLs that are globally consistent and constant for each ecosystem based on data from Reid et al. (2005a,b). These five runs will also be further discussed in section 2.5.

The global distribution of the derived AFL for the best guess run can be found in Figure 2.4. The upper panel shows the AFL of fires in the GWEM ecosystems savanna and grasslands, and wooded savannas and on the bottom panel is the AFL for fires that burn in the GWEM ecosystems tropical forest, temperate forest and boreal forest.

A comparison of the AFL regional averages as used in GWEM and corresponding literature values of Table 2.4 for five major ecosystems can be found in Figure 2.5a   (savanna and grasslands, and wooded savanna) and Figure 2.5b (tropical, temperate and boreal forest). The errorbars denote a minimum and maximum assumption of AFL's induced by variation of the best guess percentages in Table 2.3 (minimum run: see blue entries, maximum run: see red entries). The striped bars on the right hand side of the diagrams show AFL literature values for each ecosystem as suggested by Zheng et al. (2003) and Palacios et al. (2002). The minimum and maximum values of the literature in Table 2.4 is shown by white and red circles, respectively.

	9	8	7	6	5	4	3	2	1	PFT´s No.
non-PFT-divided Carbon pools	C4 grass	C3 grass	boreal broadleaved summergreen	boreal needle-leaved evergreen	Temperate broadleaved summergreen	Temperate broadleaved evergreen	temperate needle-leaved evergreen	tropical broadleaved raingreen	tropical broadleaved evergreen	PFT name
LI[1]	LE - LE. 5% SW	LE - LE, 5% SW	-	-	-	-	-	-	-	**sav&grass**
LI[1]	LE	LE	5% SW, 5% HW - 50% SW, 50% HW	5% SW, 5% HW - 50% SW, 50% HW	5% SW, 5% HW - 50% SW, 50% HW	5% SW, 5% HW - 50% SW, 50% HW	5% SW, 5% HW - 50% SW, 50% HW	5% SW, 5% HW - 50% SW, 50% HW	5% SW, 5% HW - 50% SW, 50% HW	**Wooded sav**
LI	LE, SW, HW LE LE, SW, HW	-	-	-	-	-	-	LE, SW, HW LE LE, SW, HW	LE, SW, HW LE LE, SW, HW	**Tropical forest**
LI	-	LE, SW LE LE, SW, HW	LE, SW LE LE, SW, HW	-	LE, SW LE LE, SW, HW	LE, SW LE LE, SW, HW	LE, SW LE LE, SW, HW	-	-	**Temperate forest**
90 % LI 90 % LI LI	-	LE, SW, HW, FR LE, SW, FR LE, SW, HW, FR	LE, SW, HW, FR LE, SW, FR LE, SW, HW, FR	LE, SW, HW, FR LE, SW, FR LE, SW, HW, FR	-	-	-	-	-	**North America** (Boreal forest)
70 % LI 70 % LI LI	-	SW,HW, FR SW, FR SW, HW, FR	SW, HW, FR SW, FR SW, HW, FR	SW, HW, FR SW, FR SW, HW, FR	-	-	-	-	-	**Eurasia** (Boreal forest)

Table 2.3: Calculation of AFL from PFT´s in carbon pools of LPJ model; LI: litter, LE= leaf, HW: heartwood, SW: sapwood, FR: fine root, susceptibility factor χ of carbon pool is given in percentages (no percentage = 100%), black = best guess run, blue=minimum run, red=maximum run

[1] scaled to fractional cover of PFT 8+9

Name of region	Literature Average AFL [g/m²]
North America	$10,000^{4,d}$ -$38,000^{4,e}$; $2590^{5,g}$ – $3720^{5,g}$
South America	$710 – 6600^{1+2,a}$; $12,000 – 43,500^{3,c}$
Southern Africa	$250 – 734^{1+2,b}$
North Central Asia	$5000^{5,f}$

[1] savanna and grasslands, [2] wooded savanna, [3] tropical forest, [4] temperate forest, [5] boreal forest
[a] Brazil, Ward et al., 1992 and Guild et al., 1998
[b] South Africa, Stocks et al., 1996 and Trollope and Trollope 1996; Zambia, Shea et al. 1996
[c] Brazil, Ward et al., 1992, Kauffman et al., 1995 and Guild et al., 1998
[d] Oregon, USA, Hobbs et al., 1996; [e] Washington, USA, Hobbs et al., 1996,
[f] Siberia,Russia, FIRESCAN, 1996; [g] North America, Kasischke and Bruhweiler, 2003a

Table 2.4: Literature values of available fuel load (AFL) per ecosystem, in g dry matter / m², compilation by (Reid et al., 2005a,b)
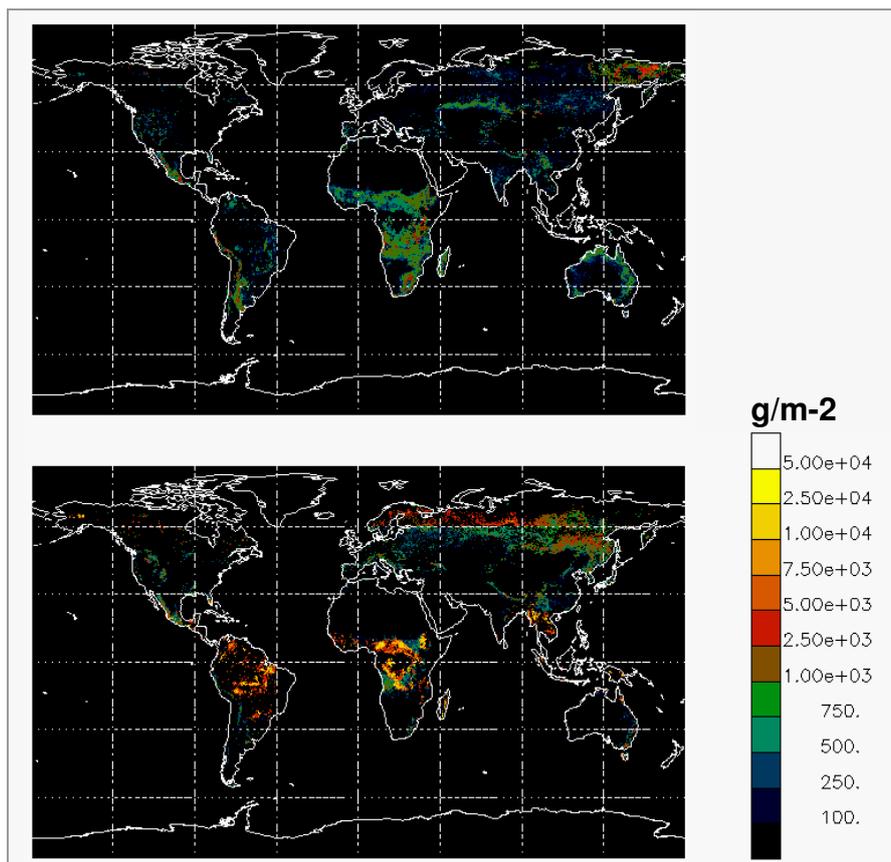
Figure 2.4: Global available fuel load (AFL) in [g/m²] for GWEM-1.3 based on data of the LPJ vegetation model for the year 2000 and the MODIS landcover scheme. Only AFL at GBA2000 area burnt locations is shown. Top: AFL for ecosystem savanna and grasslands, bottom: AFL for all forest ecosystems
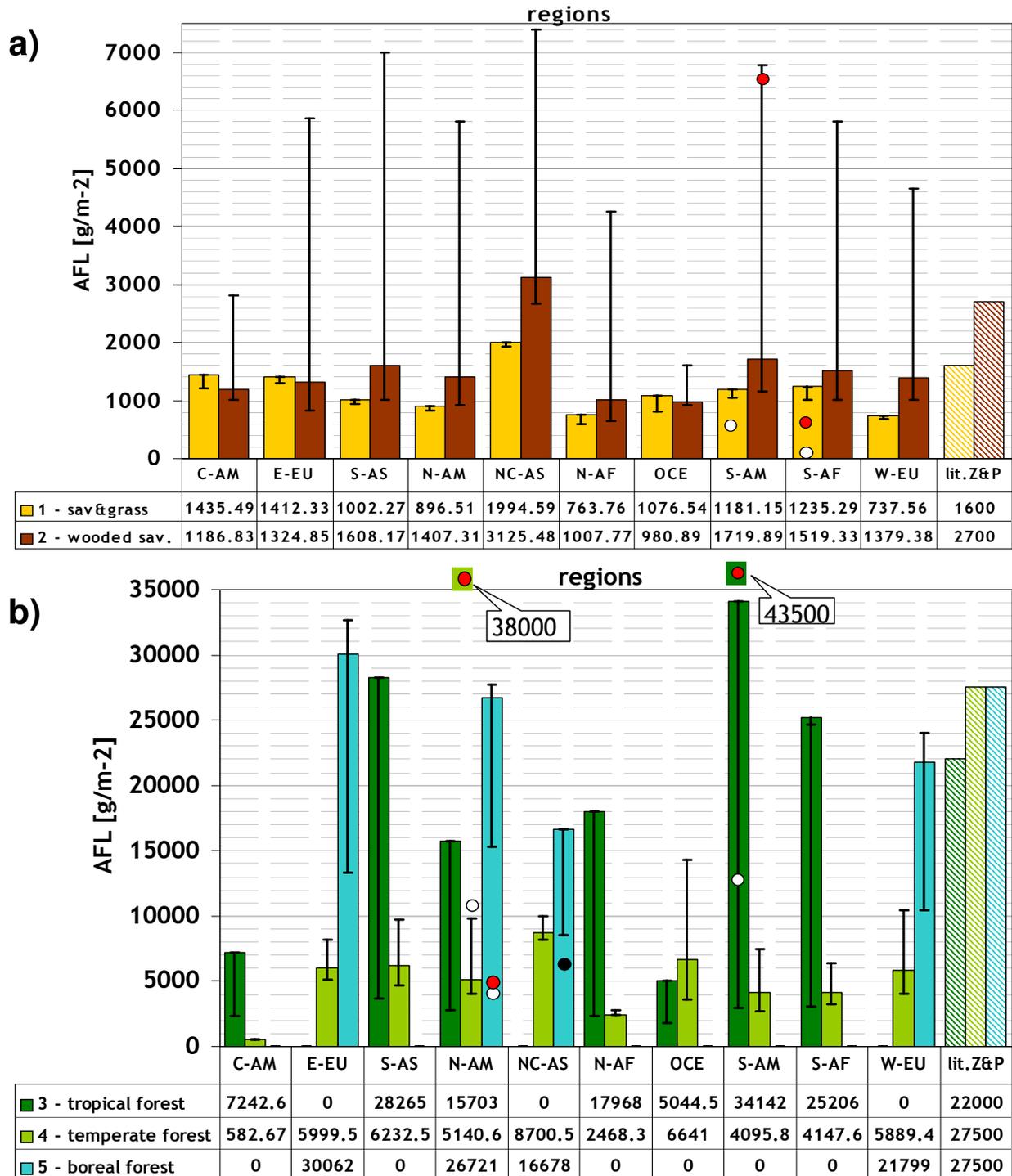
Figure 2.5: Regional averages of AFL in g/m² as calculated by GWEM-1.3 for
a) ecosystems savanna and grasslands and wooded savanna. The errorbars represent the numbers delivered by the AFL minimum- and maximum run. The striped bars on the right are values from literature by Zhengh et al. (2003) and by Palacios et al. (2002). The circles represent literature values as compiled by Reid et al. (2005a,b). White circles denote lowest published value per ecosystem found and red circles stand for highest numbers found.
b) same plot for tropical forest, temperate forest and boreal forest ecosystem

2.2.3 Emission Factors

A broad range of publications on emissions from biomass burning exists from various field campaigns and some laboratory studies. For a global approach, which includes many ecosystems, the use of average values based on many different sources seems to be the most appropriate way. In addition, emission factors vary as the fire season progresses due to changing moisture conditions. Unfortunately, information necessary to quantify this effect is only available for limited regions.

Emission factors in this paper are based on the publication of Andreae and Merlet (2001), with several updates (Andreae, pers. comm., 2003) (Table 2.5). Values and standard deviation are given based on a collection of emission factors for about 90 species from field campaigns in about 130 publications. Emission factors in this paper are given for the three different ecosystems (1) savanna and grasslands, (2) tropical forest, and (3) extratropical forest. The extension to the five ecosystems used in GWEM is listed in Table 2.2. Emission factors are averaged and constant throughout the year, independent of the wet (early) or dry (late) fire season. This with the exception of a regional study on southern hemispheric Africa (S-AF) emissions (section 2.5), where the impact of variable emission factors during the fires season has been tested.

Compound	Emission factor [g species / kg dry matter]			Standard deviation		
	1 Savanna and grasslands	2 Tropical forest	3 Extra-tropical forest	1	2	3
CO_2	1663	1580	1569	88	90	131
CO	61.6	103.2	106.7	16.2	18.9	37.1
CH_4	2.20	6.80	4.70	0.80	2.00	1.90
NMHC	3.40	8.10	5.70	1.00	3.00	4.60
NO_x	2.32	1.85	3.00	0.97	0.76	1.45
SO_2	0.71	0.57	1.00	0.82	0.23	- [a]
$PM_{2.5}$	4.90	9.10	12.99	1.50	1.50	6.95
TPM	9.20	8.50	17.62	3.90	2.90	6.36
TC	3.70	6.60	8.28	1.20	1.50	3.05
OC	3.30	5.20	9.14	1.30	1.50	0.83
BC	0.47	0.66	0.56	0.17	0.31	0.19

[a] only one value in literature for this species, therefore no standard deviation

Table 2.5: Emission factors for three different biomes used in GWEM, according to Andreae and Merlet, 2001, and Andreae, pers. comm. (2003)

2.2.4 Burning Efficiency

The burning efficiency or combustion fraction in GWEM is taken from Reid et al. (2005a,b) who have based their recommendations on several different publications for various regions and ecosystems (FIRESCAN, 1996; Guild et al., 1998; Hobbs et al., 1996; Kauffman et al. 1995; Kauffman et al. 1998; Shea et al, 1996; Stocks et al. 1996; Trollope and Trollope, 1996; Ward and Hao 1992; and Ward et al. 1996). The combustion fraction is kept invariant to changes in fuel moisture and does therefore not change during the annual cycle. Values are available for the five different ecosystems in Reid et al. (2005a,b), which are identical to those used in GWEM (Table 2.6). The uncertainties listed in this table are further discussed in section 2.5.

Ecosystem	Burning efficiency β	Uncertainty
Savanna and Grassland	0.85	0.1
Woody Savanna	0.6	0.1
Boreal Forest	0.5	0.1
Tropical Forest	0.5	0.1
Temperate Forest	0.5	0.1

Table 2.6: Burning efficiencies used in GWEM and uncertainties from a compilation of Reid et al. (2005a,b). For references see section 2.2.4 in text

2.2.5 Active Fire Counts

Active fire counts have only been used in this work for testing a complementary approach for monitoring deforestation fires in Southern America.

Available products on the global scale are for example, active fire detections by MODIS (since May 2001) and the ATSR World Fire Atlas (August 1996 – February 2002). In this work fire counts for the year 2000 were needed and therefore the ATSR data from ESA has been used. The ATSR fire counts are processed using nighttime data (approximately 10 pm local time) from the infrared channel (3.7 microns). If a threshold of 308 K or 312 K is exceeded (two different algorithms) the observed pixel is declared as burning. In this paper the product of the 308 K threshold algorithm is applied to the emission inventory for the year 2000 except for fire pixels which were declared as spurious, which means they are hot pixels, but not from wildland fires. These over-detections result from oil exploration gas flares and cities, but these can easily be eliminated: other than uncontrolled burning events, these kinds of fires are permanently seen by the sensors and can therefore be identified if the fire is located at the same spot during over 60% of the year (Schultz, 2002).

On the other hand, omission can occur for low temperature fires, such as peat fires, which are missed due to the temperature threshold of the product. For further information, see the Validation Report of the ATSR World Fire Atlas, by Arino and Plummer (2001).

2.3 Calculated Fire Emissions

Results of a "best guess" run with the Global Wildland fire Emission Model GWEM version 1.3 are shown here: Figure 2.6 presents the monthly integrated global emission flux of CO in g/m^2 for all months of the year 2000 at a $0.5°$ x $0.5°$ spatial resolution. A specific seasonality in each continental region can be observed.

In total, GWEM-1.3 computes 2289 (1403-5269) Tg C, 7488 (4581-17434) Tg CO_2, 347 (203-725) Tg CO, 15.64 (8.06-29.05) Tg CH_4, 21.06 (11.30-41.66) Tg C as NMHC (non-methane hydrocarbons), 10.65 (6.82-24.67) Tg NO_x (as NO), 31.58 (18.75-61.70) Tg $PM_{2.5}$, 20.73 (12.72-41.05) Tg OC, and 2.37 (1.38-5.20) Tg BC as wildland fire emissions for the year 2000. The uncertainty of the calculated values stems from a minimum- and a maximum AFL run (see section 2.5).

The ratio of NO_x/CO averaged over the year 2000 is shown in Figure 2.7. The NO_x/CO ratio varies from 0 to up to about 0.04 depending on the ecosystem. Lowest values can be observed in the tropical forest ecosystems (e.g. Africa, Brazil, South East Asia). The values of NO_x/CO in boreal forest are somewhat more elevated in the mid-range, while savannas and grasslands (e.g. Africa, Mongolia, Brazilian Cerrado, Australia etc.) show a high ratio of NO_x/CO. The ratio of the latter is higher, because of the more complete combustion in flaming fires, which reduces the amount of CO emitted relative to NO_x and CO_2.

To obtain a more detailed idea about regional emission behaviour 12 regions were defined (Figure 2.1) and the emissions in these regions were analyzed in terms of their amount, uncertainty, and seasonality. A more detailed description of the defined regions in Figure 2.1 is given in Table 2.1, where each regions' countries are listed. Figure 2.8 visualizes the seasonal variation of the wildland fire CO emissions for these 12 regions as computed by GWEM-1.3 for the year 2000. Due to the high variability of emissions, the figure is broken down in three diagrams: in Figure 2.8a the main emitter regions North Central Asia (NC-AS), Northern Africa (N-AF), and Southern Africa (S-AF) are shown together with the global graph. The region North Central Asia and Southern Africa show a pronounced peak in May and July, respectively. The respective fire seasons occur from April to September and May to October.

The Northern Africa fire season extends from October to March reaching its maximum in December. These three main regions account for most of the features of the global curve also shown in Figure 2.8a. In Figure 2.8b, a much smaller contribution is found for the regions Eastern Europe, Southern Asia, Oceania, Southern America, and Eastern Europe: the maximum monthly emissions for carbon monoxide are from Southern Asia in April 2000. The less significant contributor regions are shown in Figure 2.8c.

A look at the annual totals of CO and NO_x (as NO) is provided in Figure 2.9. Again, the values in the diagram are split up into the same regions. The highest contributors to the annual global amount of 347 Tg CO and 10.65 Tg NO_x are Northern Africa with 98 Tg CO and 2.96 Tg NO_x, and Southern Africa with 96 Tg CO and 3.17 Tg NOx. These emissions from whole Africa represent more than 55 % and 57% of the global numbers for CO and NO_x, respectively. All numbers can be found in Table 2.7 (CO) and Table 2.8 (NO_x) at the end of this section.

Total monthly emissions of CO for the three forest and two savanna ecosystems in GWEM can be found in Figure 2.10. A forest maximum can be observed in late spring of the northern hemisphere (temperate and boreal forests), followed by a late July/August peak of burning savanna and wooded savanna mainly in Southern Africa (see Figure 2.8a for comparison). The December maximum of CO emissions is a result of equal burning of savanna, wooded savanna and tropical forest in Northern Africa. A further discussion of the seasonality in GWEM is given in section 2.4.1.

Figure 2.11 depicts GWEM CO emissions in dependence of the regionally prevailing ecosystems. Most of savanna, wooded savanna and tropical forest CO was emitted in Africa, while the emissions from temperate and boreal forest dominated in North Central Asia.
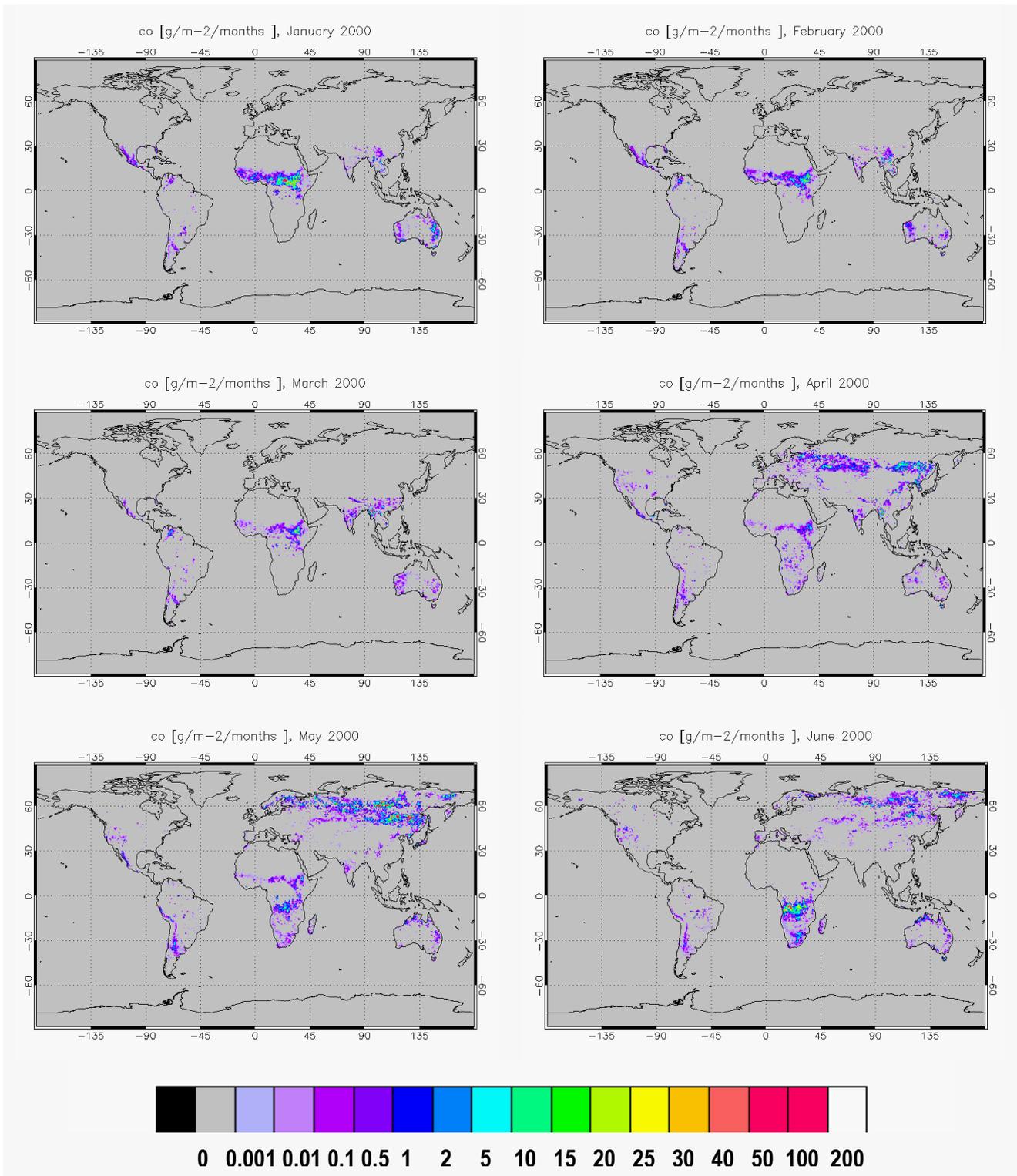
Figure 2.6: Global monthly CO wildland fire emissions in g/m^2 calculated by GWEM-1.3 for the months January – June 2000 based on MODIS landcover
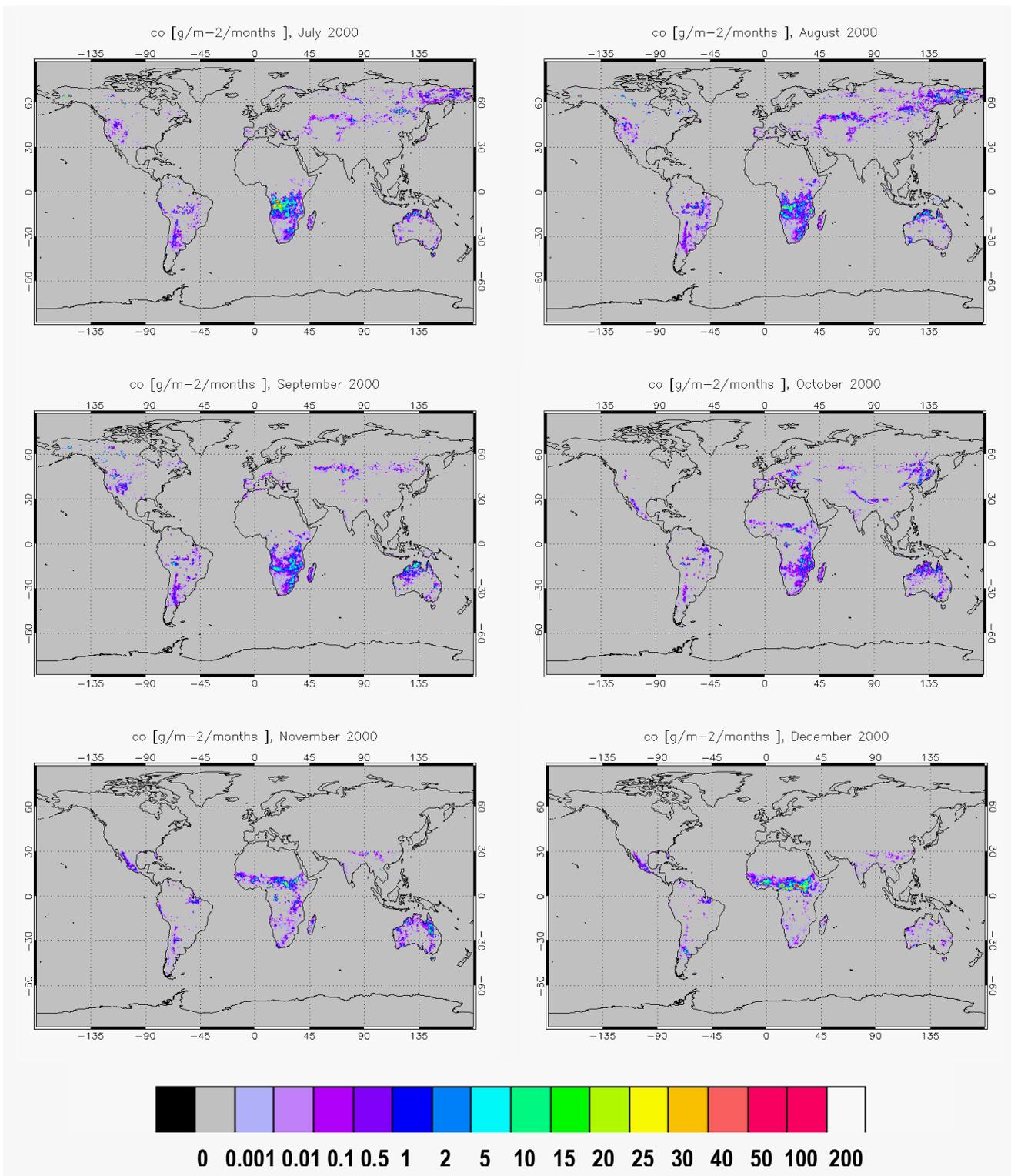
Figure 2.6 cont´d: Global monthly CO wildland fire emissions in g/m^2 calculated by GWEM-1.3 for the months July - December 2000 based on MODIS landcover
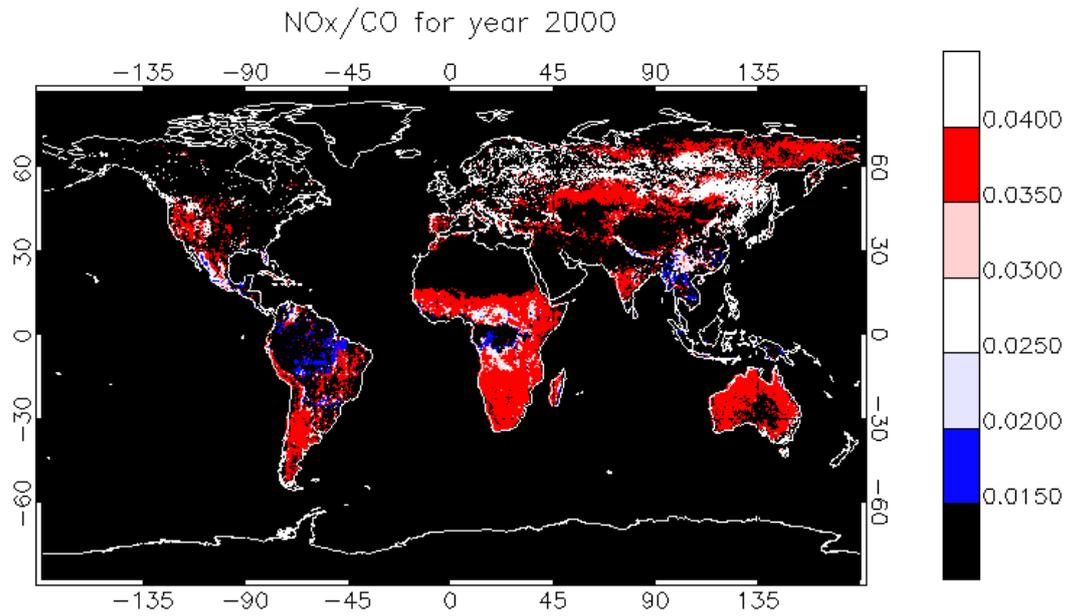
Figure 2.7: Global annual average NO_x/CO ratio of fire emissions calculated by GWEM-1.3 for the year 2000, based on MODIS landcover

Figure 2.8 a) CO monthly emissions from wildland fires in 2000 computed by GWEM-1.3 for the regional main contributors North Central Asi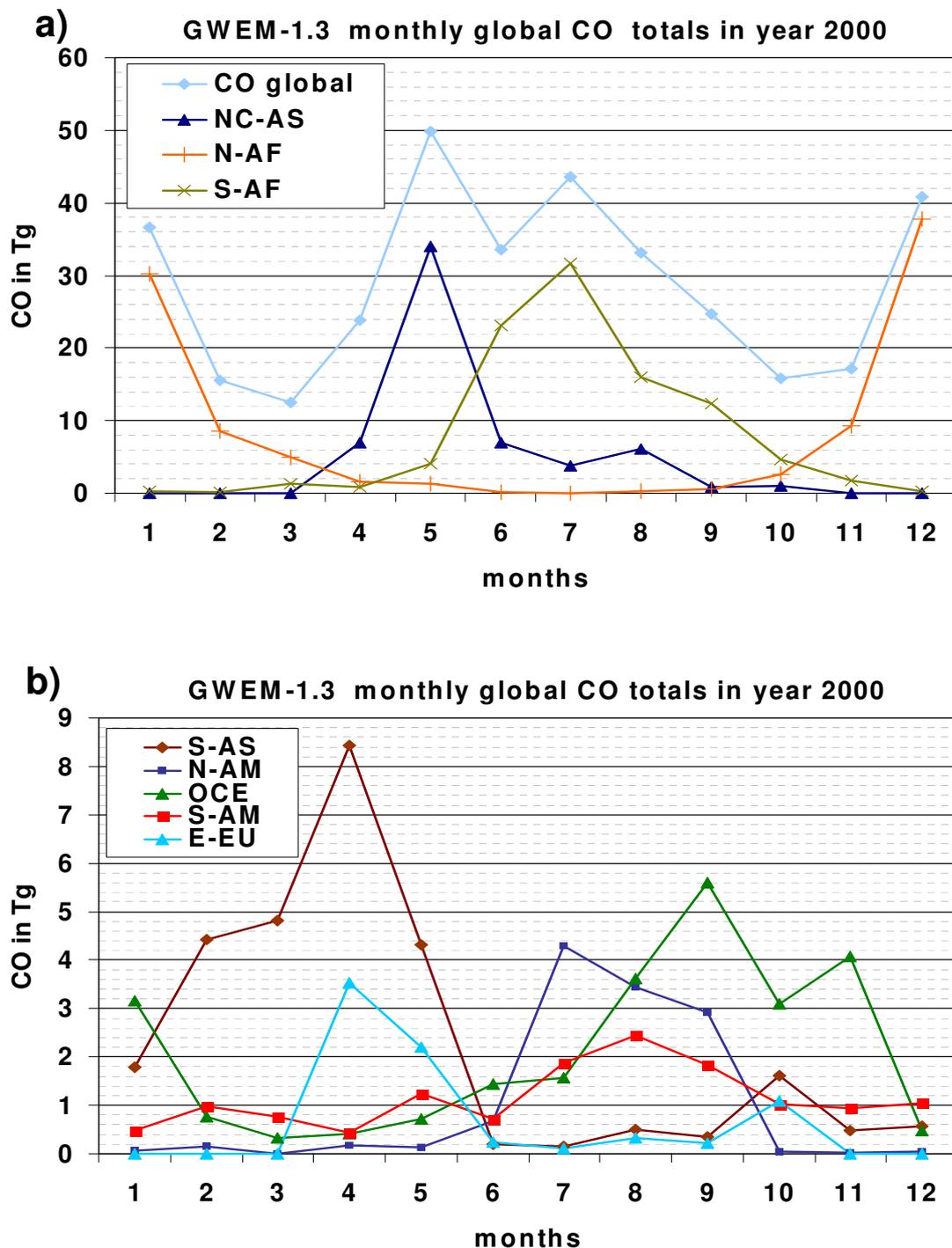a (NC-AS), Northern Africa (N-AF), and Southern Africa (S-AF). The blue line is the global graph for terms of comparison

b) CO monthly emissions from wildland fires in 2000 computed by GWEM-1.3 for the regional contributors Southern Asia (S-AS), North America (N-AM), Oceania (OCE), Southern America (S-AM), and Eastern Europe (E-EU)

c) (next page) CO monthly emissions from wildland fires in 2000 computed by GWEM-1.3 for the regional contributors Central America (C-AM), East Asia (E-AS), Near East (N-EA), and Western Europe (W-EU)
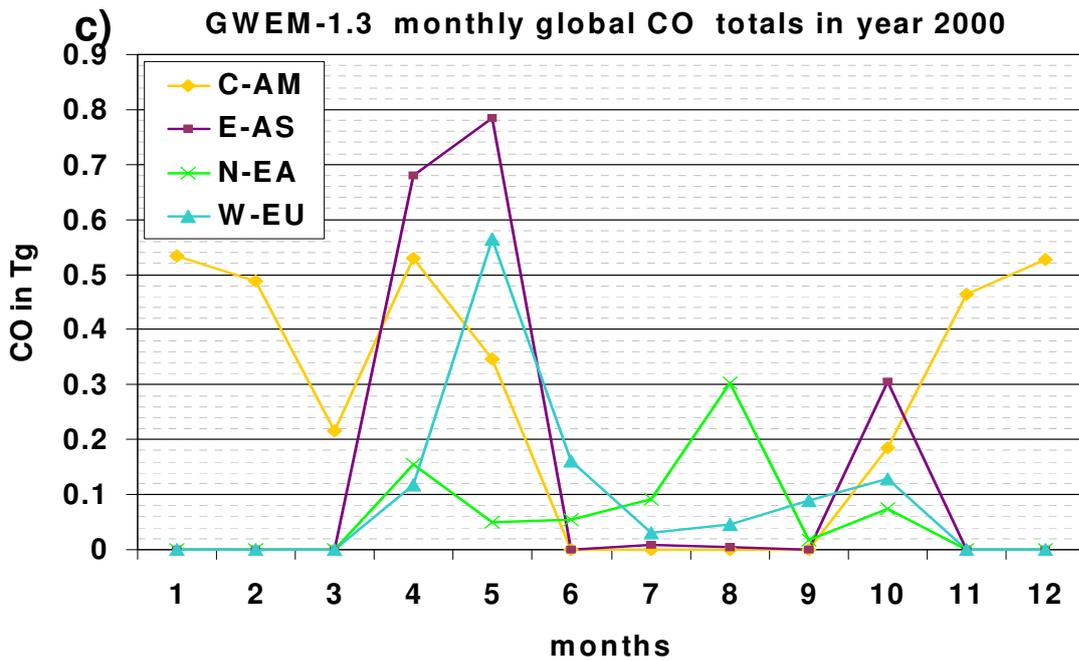
Figure 2.8: cont.'d
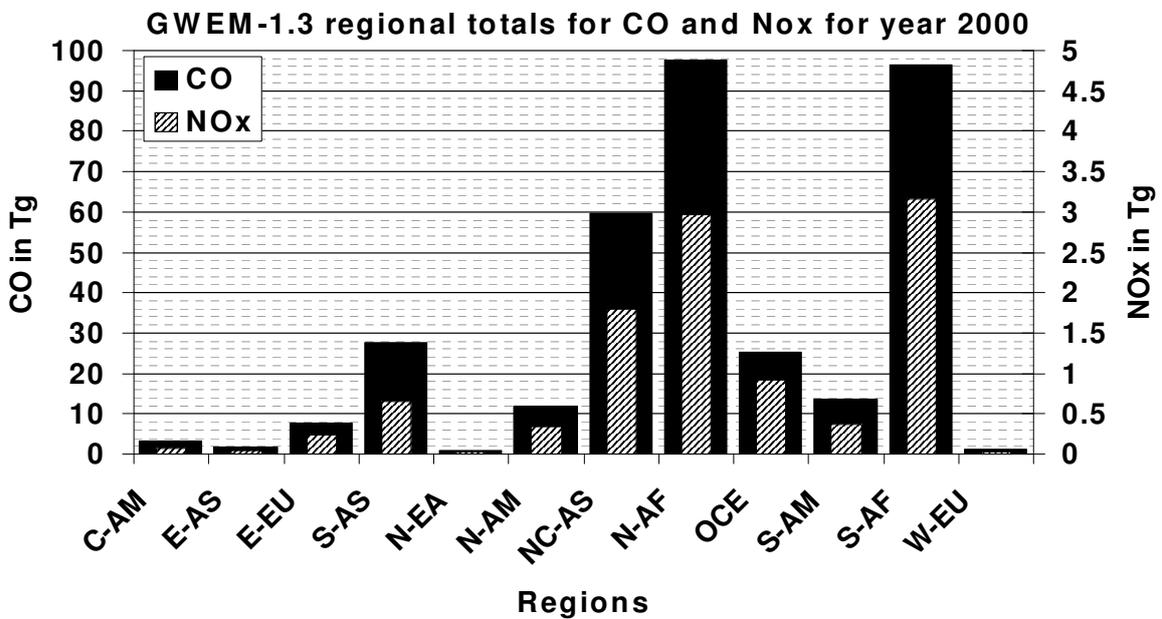
Figure 2.9: CO and NO$_x$ regional totals from wildland fires in 2000 computed by GWEM-1.3 for Central America, Eastern Asia, Eastern Europe, Southern Asia, Near East, North America, North Central Asia, Northern Africa, Oceania, Southern America, Southern Africa, and Western Europe. Regions are further specified in Figure 2.1 and Table 2.1
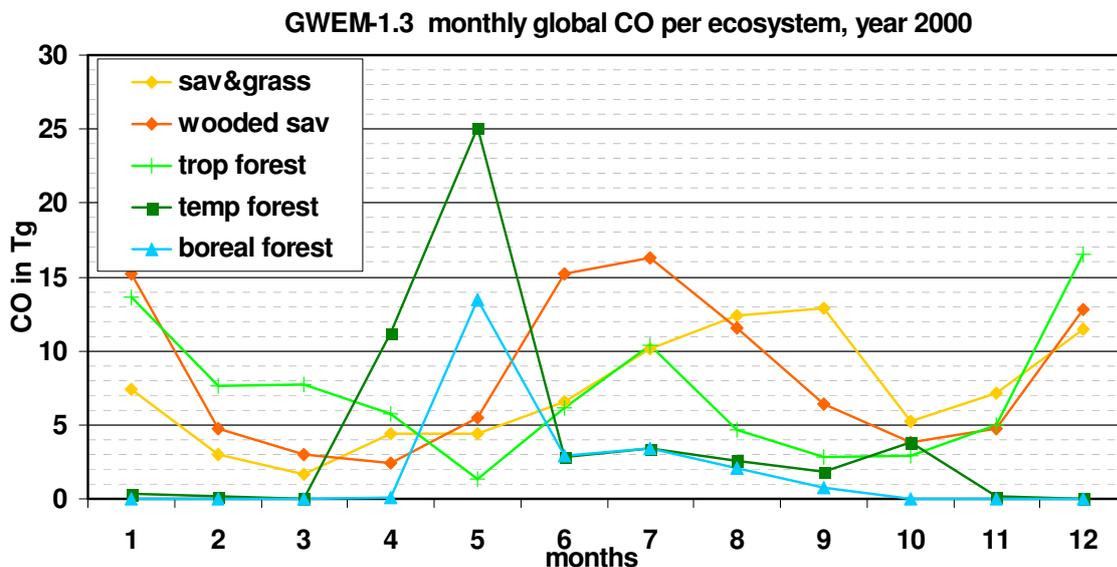
Figure 2.10: Global monthly CO emissions per ecosystem for the year 2000 of GWEM-1.3
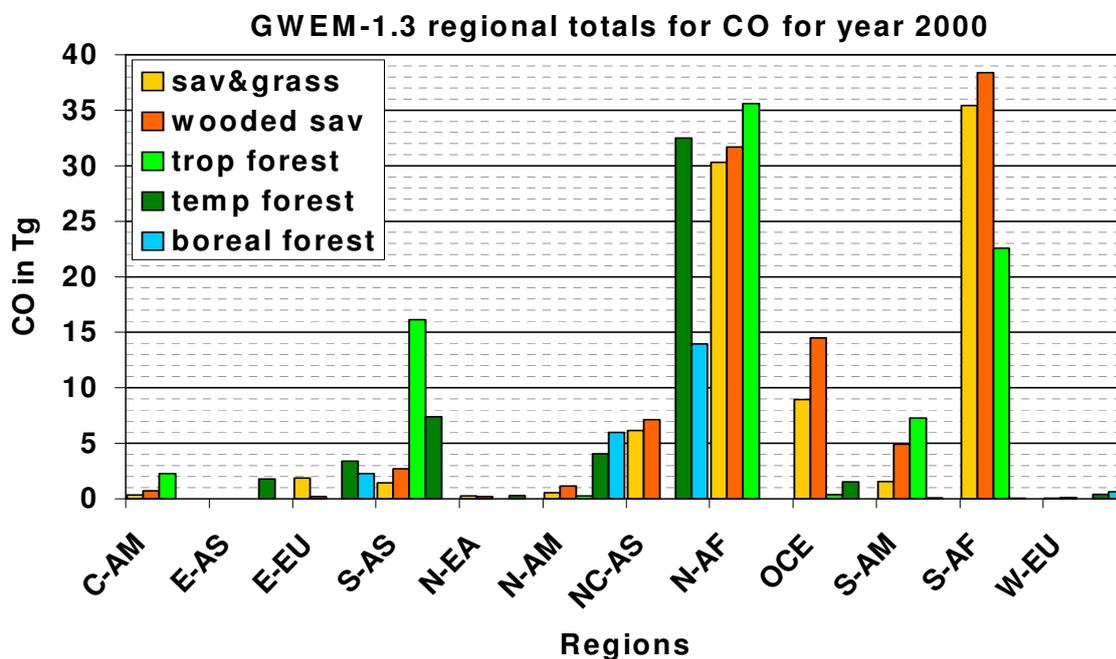
Figure 2.11: Regional total CO emissions per ecosystem for the year 2000 of GWEM-1.3

2.4 Discussion of GWEM-1.3 Emissions and Affecting Components

The results of GWEM are largely dependent on the validity and limitations of the input data used, which should therefore also be a topic of discussion. An attempt was made to gather data on sources and emissions of the year 2000 for terms of comparison. Data for other years than 2000 must be used with caution, because of the extremely high interannual variability of fire emission related data. Nevertheless, for many times it is the only available reference to obtain a first appraisal of results. The area burned and the available fuel load as principal input sources are regarded as well as the emissions of different species for different regions.

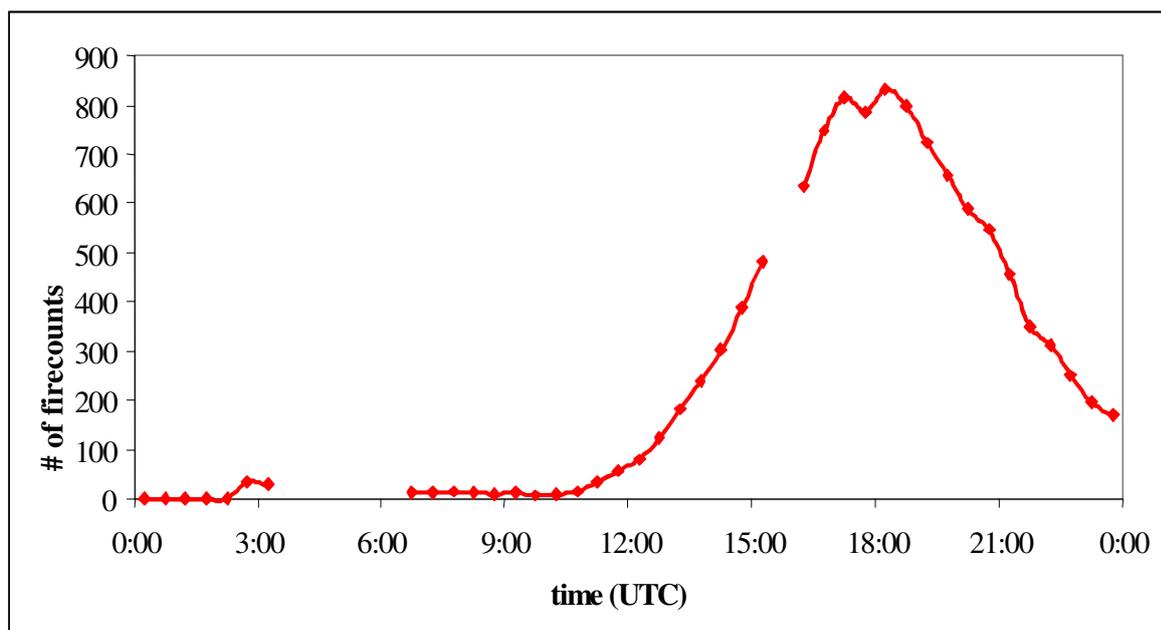**Figure 2.12:** Typical time series of diurnal evolution of biomass burning activity as detected by the GOES-8 WF_ABBA instrument in Amazonia, Brazil. Courtesy of Fernando Sampaio Recuero, CPTEC/INPE, Brazil

2.4.1 The Impact of Satellite Fire Products

Explicitly for the year 2000, there is only one global area burnt product for the purpose of intercomparison with the GBA2000 product used in GWEM-1.3: the GLOBSCAR product, released by the European Space Agency (ESA), yields 1.72×10^6 km^2 globally burnt area for the year 2000. GBA2000 presents the double of areas burnt with 3.65×10^6 km^2. These numbers are the subset of burnt area as used in GWEM-1.3, excluding agricultural fires.

The general lower amount of burned areas is a result of using two globally consistent algorithms that do not work equally well in different parts and biomes of the world. To avoid commission errors, a detected pixel in GLOBSCAR is only marked as burned if both of these global algorithms claim a burned pixel. For further description of the algorithms see Simon (2002) and Simon et al. (2004). The difference of the two products resulting from application of global (GLOBSCAR) versus regional algorithms (GBA2000) is further pronounced by an additional algorithm incorporated in GBA2000 that connects scattered burned areas thought to belong to the same burned scar. In individual regions, this ratio between GLOBSCAR and GBA2000 can be highly variable.

In the following, area burnt data have been compared to other published values in individual regions.

source	Northern Africa	Southern Africa AB
GLOBSCAR (in GWEM-1.3)[1]	0.60	0.58
GBA2000 (in GWEM-1.3)[1]	1.33	1.12
v. d. Werf et al., 2003[2]	1.67	1.16
Barbosa et al.,1999[3]	3.62 (3.04–3.91)	1.85 (0.54–2.93)
Scholes et al., 1996[4]	-	1.68

[1] estimate for the year 2000; [2] annual estimate from 1998 – 2001; [3] annual mean value of two different scenarios for 1981 – 1991; [4] satellite data derived estimate for the year 1989

Table 2.9a: Area burnt estimates intercomparison for Africa in 10^6 km^2 with GLOBSCAR and with different years available in the literature

Southern Africa is the region with most available data for comparisons due to campaigns such as the SAFARI 2000 initiative (Swap et al., 2002). An overview of published burnt area estimates is listed in Table 2.9a. The GLOBSCAR product represents in fact the only comparable global data set for the year 2000 that is publicly available. The GBA2000 product used in this work yields an area burned of 1.12 x10^6 km^2 for Southern Africa as used in GWEM-1.3 in the year 2000 and is more than a factor of 2 higher than the GLOBSCAR burnt areas. Due to the spatial resolution of 1 km^2 of these satellite products, they always provide lower values of area burned than other approaches that are able to monitor fires with smaller extensions. Furthermore, the year 2000 was a year with moderate to low fire occurrence for most regions and therefore yields lower estimates than averages over other years from the other studies. In the African northern hemisphere the GBA2000 burnt areas used in GWEM-1.3 are also almost a factor of 2 higher than in the GLOBSCAR product (Table 2.9a). Average figures by other studies are still higher, however discrepancies are not as pronounced as in the southern hemisphere.

In **South America** burnt areas from GBA2000 as well as GLOBSCAR are by a factor of 6 lower than the estimate by Van der Werf et al. (2003). Both products equally fail to represent a realistic dynamic pattern of the abundant deforestation fires in Amazonia. Fires considerably smaller than 1 km^2 can neither be detected by GLOBSCAR nor the GBA2000 algorithms. This has a big impact in regions where small fires dominate. This is mainly the case for deforestation fires in tropical rainforest, e.g. Brazil and Indonesia, but also to a lower extent for small savanna fires in Africa (Hély et al., 2003a). Therefore, it is expected that GWEM emissions are underestimated in these regions. The area burned data used in Van der Werf et al. (2003, 2004), for comparison, yields about 6 times more area burned for South America, compared to the GBA2000 product. However the area burnt for South America in these studies is highly uncertain as the method used to derive these numbers was not calibrated in this region but was derived from data from Africa and Australia (Van der Werf, pers. comm., 2004).

source	South America	Southern Asia	Australia
GLOBSCAR (in GWEM-1.3)[1]	0.13	0.04	0.18
GBA2000 (in GWEM-1.3)[1]	0.12	0.11	0.60
v. d. Werf et al., 2003[2]	0.74	0.39	1.18
Hurst et al., 1994[3]	-	-	0.87
Russel-Smith et al., 2003[4]	-	-	0.42

[1] estimate for the year 2000; [2] annual estimate from 1998 – 2001; [3] climatology; [4] 1999, only Northern Australian savanna

Table 2.9b: Area burnt estimates intercomparison for Southern America, Southern Asia, and Australia in 10^6 km^2 with GLOBSCAR and with different years available in the literature

Also, the GBA2000 product suffers from strong omission errors that are a combination of diverse circumstances that count also for other tropical deforestation areas:

- the size of the burned scar is mostly far below 1 km^2,
- frequent cloud coverage inhibits a remote sensing detection,
- the altered albedo signal cannot be distinguished from the surrounding living vegetation albedo,
- in some methods of tropical forest burning the canopy remains unaltered and hinders the detection of the burned surface,
- the overpass time is early at 10:30h, -the typical deforestation fires have their peak in the afternoon, around 15h PM, local time, as is illustrated by the Amazonian time series of the ABBA-GOES fire satellite in Figure 2.12,
- the overpass frequency of the SPOT satellite is 4-5 days in the tropics (see Tansey et al., 2004), which increase the omission probability related to cloud coverage

On the other hand, the few burnt areas that are detected are mainly commission errors related to false detections of the underlying algorithms. Mountain (in the Andes) and cloud shadows (see http://www-gvm.jrc.it/TEM/Disturbance%5Fby%5Ffire/products/burnt_ areas/global2000/gba2000_data.htm) and flooded wetlands (e.g. the Pantanal in Brazil) are in many cases mistaken for burnt scars in the landscape.

Deforestation fires are small in extent but intensive in fuel combustion, due to slash-and-burn techniques that expose the woody biomass to fire, which would not burn under natural forest fire conditions. Therefore, these sorts of fires are important to be included in emission studies. Currently, no other published global or regional area burned data is available to fill this gap. Active fire count data for South America exist from the GOES (Geostationary Operational Environmental Satellite) (Prins and Menzel, 1992 and Prins, et al. 1998; available at http://www.nrlmry.navy.mil/flambe/index.html) exists, as well as data from the Advanced High Resolution Radiometer/National Oceanic & Atmospheric Administration, US (AVHRR/NOAA) series received by CPTEC/INPE, Brazil (http://www.cptec.inpe.br/queimadas), from MODIS (http://modis-land. gsfc.nasa. gov/fire.htm), from the Visible and Infrared Scanner (VIRS), onboard the Tropical Rainfall Measuring Mission (TRMM) satellite (TRMM-VIRS, available at http://daac.gsfc.nasa.gov/ precipitation/trmmVirsFire.shtml), and data from ESAs' Along Track Scanning Radiometer (ATSR and AATSR, available at http://dup.esrin.esa.int/ionia/wfa/index.asp). However, these data are solely hot spot detections without an extension of the burned scars, which leads to further assumptions. Each of the sources provides specific but not all-embracing information on deforestation fires: The GOES satellite for example, monitors fires every 30 minutes, but only on a 4 km^2 resolution. In future studies it will have to be investigated to what extent these data serve the purpose of substituting GBA2000 data in South America. A similar evaluation will be needed for the higher resolved AVHRR/NOAA data (resolution of 1.1 km to about 5 km, depending on angle) and MODIS (1 km resolution) fire pixels. TRMM-VIRS data have been used by Van der Werf et al. (2004), however the attributed area burned size for South America in this work is currently being refined in light of overestimated emissions (Van der Werf, pers. comm., 2004). Finally, there is ATSR fire count data that is retrieved at night, when most of the deforestation fires are extinguished. (Figure 2.12). An early test with GWEM confirmed that in fact the ATSR data only add a negligible amount of around 20% to the already detected area burned by GBA2000, when in fact a number in the order of 5 times the amount of GBA2000 detected burned areas is expected. In summary, active fire counts on one hand have the advantage of

- being more easily retrieved (temperature threshold, one algorithm, therefore more and higher resolved products available)
- capturing small fires

- having a high temporal resolution.

On the other side, it is a non-trivial task to use these data, because

- of occurrence of many false detections due to algorithm simplicity
- of the distinction whether a new fire is detected or an old fire is double counted (this requires knowledge of typical fire regimes)
- of required additional knowledge on typical burned scar sizes (depending on region and fire type) to translate the signal into area burned, which is a prerequisite to calculate the fuel load and thus estimating emissions
- the time in which small active fires can be monitored is very limited. Typical time frames are a couple of hours for an active and small controlled fire compared to a minimum of two weeks for burned scars in fast regrowing savannas (e.g. Africa) and up to three years of recognizable burned areas such as in Canada

A new area burnt data set recently published by Giglio et al. (2005), based on MODIS (Moderate Resolution Imaging Spectroradiometer) satellite fire pixels and attributed burnt area extensions derived from MODIS selected burnt area tiles may bring more light into the real extension of burnt areas in South America.

In **Southeast Asia** and **Australia** GBA2000 yields around a factor of 3 higher burnt area estimates than the GLOBSCAR product. Burnt areas used by Van der Werf et al. (2003) are still 3 and 2 times larger than the GBA2000 values for Southeast Asia and Australia, respectively. Published climatological estimates and values for the year 1999 yield Australian area burnt totals that lie in-between the afore mentioned values (see Table 2.9b).

source	North Central Asia	Europe	North America
GLOBSCAR (in GWEM-1.3)[1]	0.09	0.01	0.07
GBA2000 (in GWEM-1.3)[1]	0.23	0.04	0.05
v. d. Werf et al., 2003[2]	-	-	0.30
Soja et al., 2004[3]	0.09	-	-
Sukhinin et al., 2004[4]	0.10	-	-
Barbosa (2002)[1]	-	0.04	-

[1] estimate for the year 2000; [2] annual estimate from 1998 – 2001; [3] Siberia only; [4] Russia and Mongolia only

Table 2.9c: Area burnt estimates intercomparison for Southern Africa in 10^6 km^2 with GLOBSCAR and with different years available in the literature

In **North Central Asia** the GBA2000 product also delivers burnt areas that are by a factor of 2 higher than those from the GLOBSCAR product (Table 2.9c). Recently published estimates differ highly for this region. The values in Table 2.9c account for different regions: areas burnt from Soja et al. (2004) are only for Siberia.

Tables 2.9a and 2.9c yield an interesting comparison for Northern African and North Central Asian burnt areas: the GBA2000 area burned in Northern Africa is over 5 times higher than in North Central Asia (GLOBSCAR: almost 7 times higher). Nevertheless, the resulting emissions differ only by a factor of about 1.6 in both regions for GBA2000, and also for GLOBSCAR) (Tables 2.7a and Table 2.10a). The explanation is given by the much lower fuel loads in the predominant savanna ecosystem in Northern Africa compared to North Central Asia. Fires in Northern Africa are more frequent, but emit much less than the boreal forest fire dominated North Central Asia region.

Figure 2.2a reflects the numbers of Tables 2.9 with additional information on the total area burnt including the agricultural landcover class both for the GLOBSCAR and the GBA2000 product. The biggest discrepancies are the areas burnt on agricultural land in Eurasia, in particular those in Eastern Europe. These fires occur in northern hemispheric spring with a

maximum in April, which is strongly depicted by the GBA2000 data, and to a much lesser extent by the GLOBSCAR data (Figure 2.2a).

A regional study in **Western Europe** for the year 2000 has been performed by Barbosa (2002) for the main Mediterranean countries (Portugal, Spain, France, Italy, and Greece). Burned area estimates from this work are derived from the IRS (Indian Remote Sensing Satellite), which detects burned scars bigger than 0.5 km^2. The total amount of area burned in the year 2000 was 3867 km^2. GBA2000 detected about 15% more area burned at 4707 km^2 but for the whole of Western Europe, which includes UK, Scandinavia, and Germany in addition.

Finally, in **North America** GLOBSCAR burnt areas are somewhat higher than in the GBA2000 product, which may be related to false detections in Canada by the GLOBSCAR product. Areas burnt as used in Van der Werf et al. (2003) are by a factor of 6 higher than the satellite area burnt products (see Table 2.9c).
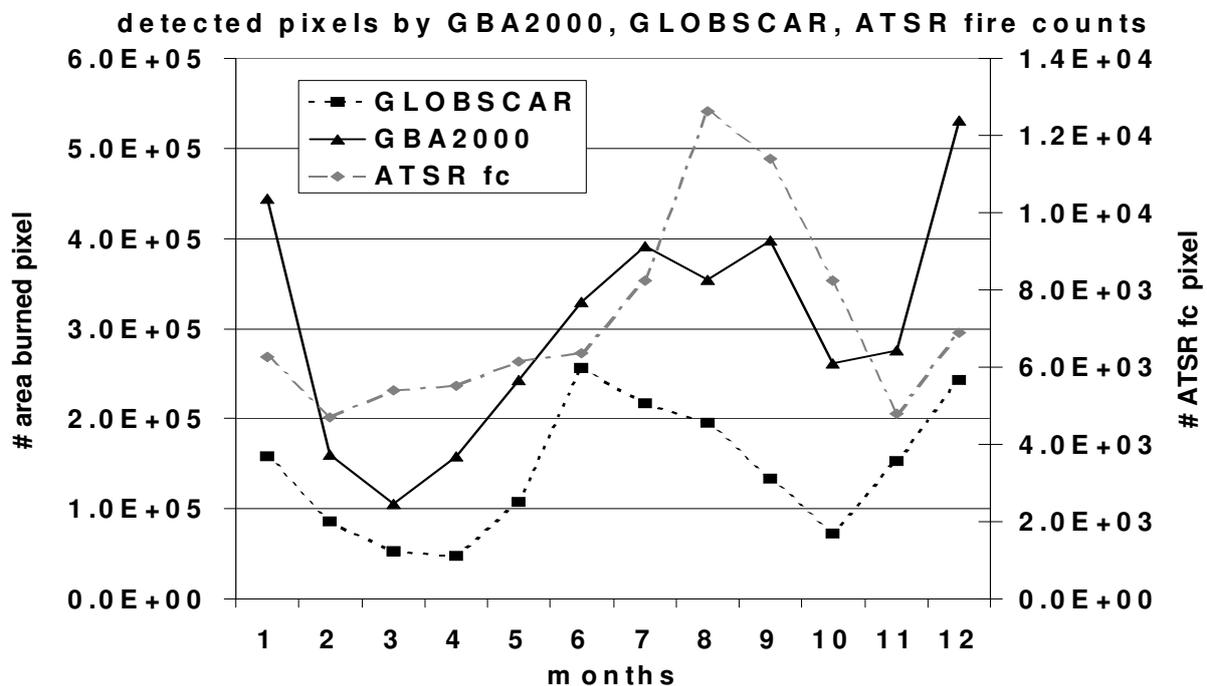
Figure 2.13: Number of 1x1 km^2 area burnt detections by GBA2000 and GLOBSCAR versus number of detected ATSR active fire counts in the year 2000

Seasonality
The seasonality in GWEM arises solely from the monthly area burned provided by GBA2000. The basic seasonal behaviour as shown and described in section 2.3 agrees with the generally known patterns of regional burning seasons. However, one of the two maxima occurs about one month earlier than in other global wildland fire emission inventories (e.g. Galanter et al., 2000, Duncan et al. 2003, Schultz, 2002).
A qualitative comparison of the monthly number of area burned records from GBA2000 with ATSR active fire counts (Figure 2.13) shows that the maxima of GBA2000 occur in July and December, while for the ATSR fire counts the maxima is observed in August and December. Also AVHRR data of fire counts (World Fire Web, JRC, Ispra, published in Dwyer et al., 2000) from the 1992/1993 period show distinct maxima in these two months. The differences can be reconciled in light of the different quantities observed. Active fire counts do not reveal information about the associated burned scar size. Therefore, the different maxima in Figure 2.13 may imply that the maximum of the ATSR active fire counts in August results

from many small fires with small burned scars, while the GBA2000 peak in July takes place because of a reduced number of larger fires. -During the course of the burning season the ratio between the number of fires and their extension (burnt area) may be subject to changes. This is reinforced by the fact that according to the GLOBSCAR Products Qualification Report (Simon, 2002), the GBA2000 product is in qualitative agreement with GLOBSCAR results concerning regional seasonalities.

For the Southern Africa region, the maximum is also observed in July resulting from wet miombo fires in the northern countries (e.g. Democratic Republic of Congo). This peak is a determining factor on the progression of the global seasonality (both graphs in Figure 2.8a). The lack of a distinct peak later in the season results from the strict exclusion of burned scars on agricultural landcover classes, which typically occur in late summer in the northern hemisphere as well as in Southern Africa. Further, there may also be a superposition of omission effects in some regions, such as Southern Africas' southern countries, where many typical small one-day fires in the burning season are undetected by satellites due to their small extension in addition to the above mentioned South America omissions that also peak in October. These assertions need to be verified in a careful multi-sensor data analysis.

Synthesis

In summary, the findings on the GBA2000 product were the following: apart from the seasonality, there is a general underestimation of burned areas in GBA2000 resulting from (i) the spatial resolution of the data set, which cannot reliably detect small fires, (ii) cloud coverage which renders a representative assessment of burned areas impossible in regions like northern Brazil, equatorial Africa, and Indonesia, and (iii) understorey peat fires mainly in Russia and Indonesia, which are not detected due to a lack of change in the surface albedo after a fire and low temperature fire properties. Other satellite area burned products on the same resolution, such as GLOBSCAR, reveal similar omission problems and are therefore not an alternative for these kinds of fires.

Integration of ground fires require an individual approach, based on different information such as peat resources, burning depth, soil moisture and specific emission factors. Recent studies have shown that in some ecosystems emissions from burning soil organic material, notably peat, may equal or even exceed the emissions produced from burning surface vegetation. For instance, Kasischke et al. (2005) estimated that burning of ground-layer organic matter contributed between 46% and 72% of all emissions from wildland fires in the boreal regions. Page et al. (2001) found that burning peat soil contributed 79-84% of all carbon emitted (in total 0.48 -2.57 GtC) during the 1997 Indonesian wildland fire event.

There is a good performance of GWEM-1.3 in the temperate and boreal areas and for larger fires e.g. in Africa. More investigation is needed to further improve and evaluate the remote sensing detection of burned areas on the global scale. For further discussion of the GBA2000 product, see Tansey et al. (2004) and Boschetti et al. (2004).

2.4.2 Calculated Available Fuel Load (AFL)

The output from the LPJ vegetation model available for this study is broken down in five different carbon pools: litter, leaf, heartwood, sapwood, and fine roots. Four of these five carbon pools (all but the litter) are further divided into nine Plant Functional Types (PFT's). From these PFT's the AFL's for the different ecosystems were derived as described in section 2.2.2.

An attempt was made to evaluate the AFL's presented in Figure 2.5a and b. Literature values for these essential data are, if existent, highly diverse and difficult to compare: often it remains unclear if the values denote (i) the total biomass load, (ii) the aboveground biomass density, (iii) a tree mortality rate, which denotes only the percentage of the trees

that die as an effect of the fire, or (iv) the available fuel load, which is the part of the vegetation that can potentially burn in a natural wildland fire. Sometimes even, the percentages are directly merged with the burning efficiency numbers, and a separation is therefore impossible without further knowledge.

Nevertheless, some information could be gathered: Reid et al. (2005a,b) compiled a variety of literature values for AFL in different ecosystems and regions. A comparison of these numbers to the corresponding AFL values used in GWEM is presented in Figure 2.5.

In Figure 2.5a the GWEM AFL's for savanna and grasslands in South America are up to 2 times higher than the available literature values in Reid et al. (2005a,b). However, the average value by Palacios et al. (2002) and Zhengh et al. (2003) is higher than the GWEM AFL for all regions but North Central Asia.

For the ecosystem wooded savanna the errorbars are large in the GWEM AFL calculation, because a large uncertainty persists to what extent wooded biomass is involved in an occurring fire. Also, wooded savanna is highly diverse in terms of woody biomass. The literature value for South America is at the upper end of the range. Again the values by Palacios et al. (2002) and Zhengh et al. (2003) are higher than the best guess of the GWEM AFL, except for North Central Asia. All ranges except for Oceania cover the literature value of Palacios et al. (2002) and Zhengh et al. (2003).

Figure 2.5b presents the forest ecosystems. The errorbars for tropical forests are very large, again due to the uncertainty of consumption of woody biomass that is directly linked with the burning motive: slash and burn techniques include the woody biomass in the fire, because the trees are lumbered, cut into smaller pieces, and exposed to the sun in order to dry out for some time prior to burning. Where part of the wood is utilized for industrial purposes (paper industry, other wood products, fuel wood), it is removed from the area set on fire and in consequence much less biomass is susceptible to burning and thus less carbon is emitted into the atmosphere. Finally, in case of a natural fire kindled by lightning most of the woody biomass and the canopy will remain, the latter due to moister conditions in tropical forests. The GWEM best guess assumptions on AFL in tropical forest considers most of the fires as deforestation fires and therefore agree with the AFL maximum end of the range. The maximum literature value available for South America (Figure 2.5b) is still above the used GWEM AFL value. The lower of two literature values found in North America for temperate forest is a little above the AFL range of GWEM. The difference of AFL reported for the two different sites however are huge (Figure 2.5 b). Values suggested by Palacios et al. (2002) and Zhengh et al. (2003) are between 2-10 times higher than the GWEM AFL values, depending on the region.

Finally, the literature estimates for boreal forest have a small range that is about 1/3 lower than GWEM AFL average values. The Palacios et al. (2002) and Zhengh et al. (2003) values are within the range of GWEM AFL estimates for Northern Africa and North America, but 15%-30% higher than the AFL calculated by the LPJ model in other regions.

Some of the discrepancies may be a result of the incoherent terminology (see above). In addition, the literature values may be biased, because only trees above a certain diameter are counted in forestry statistics. This implies that in particular the most fire susceptible parts of the vegetation are not taken into account in these studies.

Generally, the original AFL in GWEM would be systematically underestimated for forest ecosystems and exceed the published values for savannas ecosystems in mixed gridboxes, which contain both types of ecosystems. This discrepancy arises from the coarser $0.5° \times 0.5°$ resolution of the LPJ model compared to the 1 km^2 resolution of the GBA2000 area burned product. In the mixed gridboxes, the amount of wood provided by LPJ is given for the whole gridbox, which is either too elevated for a pure savanna or grassland fire of 1 km^2 extension or too low, if the burned pixel is located in a forest.

This systematic error (see Figure 2.14 for illustration) is mostly removed by the new partitioning into PFTs for all carbon pools but the litter. In former GWEM versions this lead to a strong overestimation of AFL of savanna fires and an underestimation of AFL of forest fires in these kinds of gridboxes (see Hoelzemann et al., 2004). In GWEM-1.3 (used here)

savanna-type fires only use the fraction of litter of PFTs 8 and 9 (C3 and C4 grasses) and discard most of the woody PFTs. On the other hand, forest-type fires make use of all litter available in the gridbox plus the woody PFTs susceptible to fire. A small systematic tendency may persist however, due to the litter that remains undivided in the LPJ model. Current efforts of LPJ improvement focus on further partitioning of the litter pool (separation of coarse and fine litter), improving the presentation of fire behaviour and fire effects in the fire model (Thonicke, Spessa, Prentice, Reg-FIRMv2.0, manuscript in prep.) and inclusion of crops in the current natural vegetation regime of LPJ (Bondeau et al., 2003) and Criscuolo, 2006, PhD thesis of the Max Planck Research School on Earth System Modeling (IMPRS-ESM) in Hamburg, Germany).

Another factor affecting the AFL data may be the fire history: primary tropical rainforest for example, has a very different susceptibility to fire and burning characteristics compared to secondary rainforest which has already burned before. This is due to the stepwise conversion into savanna or pasture land during each consecutive fire event (Goldammer, 1999). Finally, in some savanna regions AFL may have to be reduced due to grazing cattle.
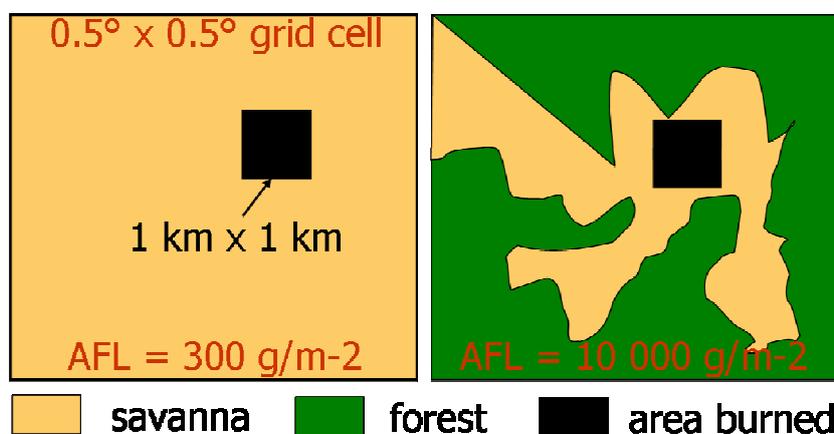
Figure 2.14: Illustration of possible overestimate of the Available Fuel Load (AFL) in GWEM, due to the spatial resolution of 0.5° x 0.5°: The LPJ vegetation model delivers an AFL value for each grid cell. On the left, the AFL within an area burned of 1 km^2, will be well represented because it is located within a uniform savanna grid cell. On the right, another area burned with the same size is located in a mixed ecosystem grid cell. The AFL that has been consumed should be the same as on the left (300 g/m^2), since the fire also took place in a savanna. However, the LPJ model yields a considerably higher AFL of 10000 g/m^2) due to the forest that is also inherent in this grid cell

In summary, the LPJ model output as used for this work is the best possible data to be used from this model for the purpose of deriving AFL for a specific year. Inclusion of more anthropogenic disturbances and a finer litter pool partitioning in this model will further optimize data for this purpose. A higher than annual temporal resolution would be desirable, to improve performance in regions where fast regrowing and changing biomes (savanna and grasslands, litter pools) dominate the fire susceptible vegetation. Finally, the derivation of AFL from the LPJ data possibly inserts errors that can only be avoided by more detailed investigation of interrelationships during measurement campaigns and its transparent mediacy to users in an interdisciplinary environment.

2.4.3 The Impact of Emission Factors

The global average emission factors compiled by Andreae and Merlet (2001) provide a useful reference for global emission estimates. A lot of effort has been placed into the determination of emission factors during the past decade. Thus, they are currently not the main source of uncertainties in global wildland fire emission modeling. Nevertheless, there is still room for further improvement in terms of the number of ecosystems (currently three

categories for wildland fires) and for some species for which less data is available. In addition, there have been discussions whether to distinguish between emission factors from smoldering and flaming fires. Each fire has a flaming and a smoldering phase. Depending on the fuel type and its moisture content the smoldering combustion phase may be prolonged. Measurements taken from particular fires in these two phases differ considerably. On the global scale though, it is not necessary to consider this distinction and average values should suffice (Andreae and Merlet, 2001).

The trace gases CO_2, CO and CH_4 have the most reliable emission factors due to many verified published measurements, whereas trustworthy quality aerosol emission estimates from biomass burning are more difficult to obtain. Still, there seems to exist good and consistent information on the latter as well, taken from slightly aged smoke plumes (approximately 1-2 hours). For further details, see Andreae and Merlet (2001).

2.4.4 Evaluation of GWEM-1.3 Fire Emissions

Tables 2.7a-c and Tables 2.8a-c (end of section) list the monthly and regional total emissions of CO and NO_x obtained in GWEM-1.3. The total numbers in GWEM-1.3 are somewhat lower with 347 Tg CO, and 10.65 Tg NO_x compared to most other inventories. The climatological emission inventory by Galanter et al. (2000), for example, yields 554 Tg CO, and 14.12 Tg NO_x for annual savanna and forest fire emissions, Duncan et al. (2003) present 437 Tg CO annual mean emissions from biomass burning (1979-July 2000), including agricultural waste burning (excluded in GWEM-1.3).

Three of the four other inventories that were used in the MOZART model study in Chapter 4 also deliver emissions that are 14% to 34% higher for CO and 29% to 56% higher for NO_x. These inventories will be described and compared in more detail in Chapter 3.

Climatological studies on carbonaceous aerosol emissions from fires derive annually 5.98 Tg BC (Cooke and Wilson, 1996), 32.1 Tg OC and 4.1 Tg BC (Liousse et al., 1996). These values are within the large ranges calculated by GWEM-1.3. Generoso et al. (2003) estimate 29.15 Tg OC and 3.36 Tg BC for the year 2000. The best guess of GWEM-1.3 is 20.73 Tg OC and 2.73 Tg BC, which is lower than the published values. It should be noted that these numbers are subjected to a higher uncertainty than those from chemical species, due to difficulty of accurately measuring emission factors of fire aerosols.

source	Northern Africa	Southern Africa	Whole African continent
GWEM-1.3, this study[1]	679	714	1393
Ito and Penner (2004)[1]	-	-	932
v. d. Werf et al., (2003)[2]	510	520	1030
v. d. Werf et al., (2004)[1]	870	1010	1880
Palacios-Orueta et al. (2004)[1]	-	-	1702
Barbosa et al. (1999)[3]	-	205	647
Duncan et al. (2003)[4]	-	-	887
Scholes et al. (1996)	-	80	-

[1] estimate for the year 2000; [2] annual mean estimate from 1998 – 2001; [3] annual mean estimate for the years 1985/6 and 1987-1991, mean of 2 scenarios taken; [4] 1980-July/2000

Table 2.10a: Carbon emission estimates intercomparison for Africa in Tg ($=10^{12}$g)

On the regional scale, there are more studies for terms of comparison: most data is available for **Africa**, the continent with most fire occurrence. For the entire African

continent, GWEM lies somewhat below the average carbon emissions of the other studies that refer to the year 2000 (Table 2.10a). Carbon emissions calculated by Ito and Penner (2004), also based on the GBA2000 area burnt product are about 30% lower than those of GWEM. Compared with Ito and Penner (2004), the Available Fuel Load (AFL) used in GWEM is higher and thus leads to higher carbon emission estimates. In contrast, emissions by Palacios-Orueta et al. (2004), also based on GBA2000 area burnt and by Van der Werf et al. (2004) are by 18% (26%) higher than in GWEM.

In **Northern Africa**, GWEM carbon emission estimates are of the same order as in the southern hemisphere of this continent (Table 2.10a). Compared to other studies, the GWEM estimate is 25% higher than the first estimate by Van der Werf et al. (2003), but about 20% lower than in Van der Werf et al. (2004), which may partly be traced back to higher estimates in fuel load of GWEM and a lower number in burnt areas.

Specifically in the southern hemisphere extensive data are available from diverse measurement campaigns, for example SAFARI-92 (Andreae et al., 1996), SAFARI2000 (Swap et al., 2002), and TRACE-A (Fishman et al., 1996). Table 2.10a shows a number of published studies that allow for a direct comparison of carbon emissions, however only 3 of them are specifically for the year 2000. Due to the high interannual variability a quantitative comparison with other years is questionable but it allows at least an evaluation of the order of magnitude in regions that have a regular fire behaviour.

Emissions in **Southern Africa** are somewhat higher than north of the equator, both for the studies of Van der Werf et al. (2003, 2004) and in this study. Earlier studies of the 1990's clearly show lower carbon emission estimates than the more recent ones based on modern fire satellite products.

Some carbon monoxide (CO) emission estimates are also available in literature, such as the one by Hély et al. (2003b), who calculated CO emissions for August and September 2000 (Table 2.11a) also based on the GBA2000 product. The average AFL used in GWEM is more than a factor of 3 higher than in Hély et al. (2003b). These discrepancies highlight the importance of a correct landcover classification: In GWEM-1.3 using the MODIS landcover map, more of the fires occur in wooded savanna, or even in tropical forest, while the Hély et al. (2003b) study apparently attributes most fires to savannas. In addition, there are likely differences in the emission factors used.

a)	GWEM-1.3		Hély et al. (2003b)	
Data	August 2000	September 2000	August 2000	September 2000
AFL[1] [g/m^2]	1323 (1 - 5061)		351 (3 – 1311)	
CO [Tg]	16.00	12.33	2.89	1.72

b)	GWEM-1.3 May to October 2000		Sinha et al. (2004) May to October 2000	
	Savanna&grasslands	Wooded savanna	Savanna&grasslands	Wooded savanna
AFL[1] [g/m^2]	1296 (1 - 5061)	1532 (1-5367)	870 (840-900)	340 (330-350)
CO [Tg]	34.10	37.59	0.99	25.10

[1] mean value of this area and range

Table 2.11: a) Mean Available Fuel Load (AFL) in g/m^2 and emissions of CO in Tg for August and September 2000 in subequatorial Africa. GWEM-1.3 results in comparison with data from Hély et al. (2003b)
b): Mean Available Fuel Load (AFL) in g/m^2 and CO emissions in Tg from May to October 2000 in Southern Africa. GWEM-1.3 results in comparison with data from Sinha et al. (2004)

The same can be stated for the intercomparison with another published study: Sinha et al. (2004) calculated fire emissions in the year 2000 in Southern African savannas and wooded

savannas (i.e. dambo grassland savannas and miombo woodlands) (Table 2.11b). Again, GWEM CO emissions from May to October are in total a factor of 3.5 higher than in Sinha et al. (2004). In particular, the estimates for savanna and grasslands in GWEM are of the same order as CO emissions in wooded savanna, while in Sinha et al. (2004) CO emissions from savanna and grasslands account for less than 4% of the total CO emissions. The LPJ model derived AFL is still considerably higher in GWEM than in the Sinha et al. (2004) study (a factor of 1.5 for savanna fires and a factor of 4.5 for wooded savanna fires), however the discrepancy is not as pronounced as in the comparison with Hély et al. (2003b).

GWEM presents African CO emissions for the year 2000 with 98 (35-299) Tg CO in the northern hemisphere and 96 (57-221) Tg CO in the southern hemisphere (see Table 2.7a). Annual mean estimates by Duncan et al. (2003) are only marginally smaller with 87 Tg CO/yr north of the equator and 86 Tg CO/yr in the south. For the whole African continent Barbosa et al. (1999) have estimated an emitted mean amount of 40 – 151 Tg CO. GWEM's best guess result for carbon monoxide emissions in Africa is somewhat higher with 194 Tg CO (range: 92 - 520). The area burnt values in the different studies (discussed in section in 2.4.1) are not linearly related to the emissions. This leads to the conclusion that the available fuel load must also differ substantially between the various estimates.

Seasonally all studies agree that the burning season in Northern Africa occurs from November-February with a maximum in December (see GWEM seasonality in Figure 2.8a). The average seasonality estimated by Duncan et al. (2003) yields the maximum in January. In the southern hemisphere all studies show a burning season from June through October with a maximum in July. The average seasonality by Duncan et al. (2003) shows highest CO emissions in September followed by August and October. This maximum shift of two months later is related to the inclusion of fires due to agricultural activity that are explicitly excluded in other inventories.

source	South America	Southern Asia	Australia
GWEM-1.3, this study[1]	87	144	200
Ito and Penner (2004)[1]	-	-	109
v. d. Werf et al., 2003[2]	500	220	150
v. d. Werf et al., 2004[3]	590	230	-
Hurst et al. (1994)[4]	-	-	132
Russel-Smith et al. (2003)[5]	-	-	≤106

[1] estimate for the year 2000; [2] annual mean estimate from 1998 – 2001, South America south of equator only, Southern Asia excludes China; [3] year 2000, South America south of equator only, Southern Asia excludes China; [4] climatology; [5] year 1999

Table 2.10b: Carbon emission estimates intercomparison for South America, Southern Asia, and Australia in Tg (=10^{12}g)

In **South America** all studies agree that fire emissions are abundant, however estimates still remain highly uncertain, due to the still scarcely known variable of burnt area by deforestation fires in the Amazon basin and savanna maintenance fires. Carbon emission estimates by GWEM-1.3 are fairly low, while estimates in both Van der Werf studies are more than 5 times higher (Table 2.10b). Carbon monoxide estimates from other studies reinforce the high variability in the different calculations: GWEM -1.3 yield 14 Tg CO for the year 2000, which compares with 75 Tg CO/yr by Duncan et al. (2003) (annual mean estimate), and 102 Tg CO/yr by Potter et al. (2002) (annual mean estimate for 1992/1993).

As reported in section 2.4.1, the GBA2000 area burnt product has a major flaw in South America and GWEM-1.3 is therefore not able to provide correct fire emission estimates for this region. Recently, a new GWEM version (version 1.4) has been released that includes a corrected burnt area set for South America based on 3 different fire satellite products. This area burnt has been made available by the Brazilian Center of Weather Forecast and

Climate Studies at the National Institute for Space Research (INPE/CPTEC, K. M. Longo, pers. comm. 2005). This new product almost doubled the burnt area in South America for the year 2000 from 119100 km^2 (GWEM-1.3) to 213 021 km^2 (GWEM1.4). CO emissions however, are only enhanced by 30% to the amount of 20 Tg CO. GWEM-1.4 is further described in Appendix A.

This emission estimate compares somewhat better with a recent study by Freitas et al. (2005a) from CPTEC/INPE (for the year 2002), who calculate annual fire emissions of 30 Tg CO. The year 2002 was a year with high fire occurrence compared to the year 2000. This study assumes a representative average burnt area for each fire pixel. Qualitative results (temporal evolution) are quite satisfactory, albeit with some systematic underestimation in quantities, resulting partly from the coarse resolution of the GOES fire satellite data that provides the area burnt location and extension. The latest version of the CPTEC/INPE emission model, used on an operational basis for Chemical Weather Forecast, already includes additional data from the AVHRR/NOAA series and AQUA/TERRA-MODIS fire counts with a higher resolution (1 km^2) (see section 2.4.1 for details). This multi-tier approach has further improved the emission fluxes (Longo and Freitas, pers. comm., 2005) and is presented on a daily operational basis on the web (http://www.cptec.inpe.br/ meio_ambiente). The remaining small underestimation is believed to be also an issue of measurement representativeness, not only the emission calculation (Longo and Freitas, pers. comm., 2005). However, the derivation of burnt area extension from fire pixel data remains a source of uncertainty: depending on the viewing angle, but also "due to the strong thermal energy emitted by the vegetation fires, even a fire front with about 30 m by 0.5 m will be detected. Thus, a fire pixel may correspond, to a small vegetation fire, to many and close small fires, or to a single large fire with 1 km^2" Longo and Freitas, pers. comm. (2005), http://www.cptec.inpe.br/queimadas/ info_mapa.htm).

There are also two inverse modeling studies that have used MOPITT CO satellite data and a Chemistry Transport Model to investigate the skill of CO a priori emission estimates. An analysis by Arellano et al. (2004) concludes that the fire emissions by Van der Werf et al. (2003) were in good agreement with satellite observations from MOPITT (Measurement Of Pollution In The Troposphere; http://www.eos.ucar.edu/mopitt) instrument taken from April 2000 to March 2001. On the other hand an inverse CO modeling study by Pétron et al. (2004) arrives at about 30% less a posteriori CO emissions for this region during the same time span. This intercomparison highlights the still persisting uncertainty of the different data for inventory assessment but apparently also in inverse modeling techniques (Pétron et al., 2004).

The seasonality of fire emissions in South America has its maximum during August-October. All different inventories agree that highest emissions are observed in the month of September, regularly for different years. The erroneous estimates for South America of GWEM-1.3 present an earlier maximum in August, however the corrected GWEM version 1.4 strongly improves the seasonality and shifts the maximum to September (see Appendix A), as according to the other studies.

In **Southern Asia**, GWEM yields over 35% less carbon emissions than estimates by both Van der Werf studies (Table 2.10b), although these studies exclude China from their defined Southern Asian region.

GWEM yields 28 Tg CO in the year 2000 for Southern Asia. Compared to studies who also calculated carbon monoxide emissions for this region this estimate is considerably lower, partly because agricultural activity related fires are not taken in to account. Streets et al. (2003) calculated 64 Tg CO of biomass burning for a typical year of fire activity, Duncan et al. (2003) estimated an average CO emission of 82 Tg CO/yr, and Heald et al. (2003) scaled this latter inventory with an approach based on AVHRR derived active fire counts of the World Fire Web (WFW, available at http://www.gvm.sai.jrc.it/fire/wfw/ wfw.htm) and reached an amount 69 Tg CO only for the biomass burning season months February to March of the year 2001.

Indonesian fire emissions are no explicitly regarded for the year 2000. Due to their very high interannual variability and in contrast to other years such as the El Niño episode in 1997/98, fires did not play an important role in Indonesia during the year 2000.

While GWEM emissions yield highest estimates for the month of April (see Figure 2.8b), followed by March and May, the other studies show their emission maxima somewhat earlier in March.

Studies on **Australian** fire emissions yield more homogeneous results than for other regions (Table 2.10b). GWEM-1.3 annual carbon emissions are at the upper end with 200 Tg C for the year 2000. Most fires occur in North Australia from August to November and to a lesser extent in East Australia from September to December. GWEM emissions show a maximum in September and November which corresponds to the seasonality presented by Van der Werf et al. (2003) and to the typical Australian burning activity reported in Russell-Smith et al. (2003).

source	North Central Asia	Europe	North America
GWEM-1.3, this study[1]	322	49	61
v. d. Werf et al., 2003[2]	-	-	180
Kasischke et al. (2005)	178 (110-212)[3]	-	58 (35-64)[4]
Soja et al. (2004)	253 (153-413)[3]	-	-

[1] estimate for the year 2000; [2] annual mean estimate from 1998 – 2001; [3] average from 1998-2002 for boreal Eastern Russia only, [4] Canada only, average from 1995-1998

Table 2.10c: Carbon emission estimates intercomparison for North Central Asia, Europe, and North America in Tg ($=10^{12}$g)

A number of recent studies exist on fire emission calculation within North **Central Asia**, however, the sub-regions they refer to differ considerably. While North Central Asia in this study refers to Europe from 60° eastward, Russia Mongolia and Kazakhstan (see Figure 2.1 and Table 2.1), other studies refer either to the whole boreal regions on the globe, to the boreal East Russia, defined as "Russia east of the Ural Mountains" (Kasischke et al., 2005) or Siberia only (Soja et al., 2004).

The carbon emission estimate by GWEM (Table 2.10c) is higher than the estimates of Van der Werf et al. (2004) for the complete boreal northern hemisphere for the year 2000 (130 Tg C) and Kasischke et al. (2005) for the period of 1992 and 1995-2003 (106-209 Tg C/yr). Kasischke et al. (2005) estimate an amount of 178 Tg C/yr emitted by fires in boreal Eastern Russia, while Soja et al. (2004) estimate about 30% more (Table 2.10c) for this region. It is assumed that the study of Van der Werf et al. (2004) underestimates boreal carbon emissions related to omissions in the ATSR fire counts that were used in this study to estimate burnt areas above 38°N.

Estimates of carbon monoxide compare as follows: Kasischke et al. (2005) estimate a range from 33-77 Tg CO/yr in the boreal northern hemisphere for the period of 1992 and 1995-2003 and 66 (35-81) Tg CO/yr for boreal Eastern Russia (1998-2002 average). The latter value compares well with Soja et al. (2004), who estimated 63-104 Tg CO/yr for the same region and period. GWEM-1.3 yields 60 Tg CO for the year 2000 in the large North Central Asian region. The year 2000 was a year with low fire emissions in this region and a comparison with an average annual emission estimate that includes high emission years due to El Niño episodes (1997/98) is therefore questionable. It is interesting to note that GWEM carbon emission estimates are higher than those of Kasischke et al. (2005), whereas the carbon monoxide estimates agree reasonably well. On one side, it has been shown in section 2.4.2 that GWEM uses high fuel load estimates from the LPJ vegetation model, which leads to enhanced carbon emission estimates. On the other hand the Boreal Wildland Fire Emission Model BWEM developed by Kasischke et al. (2005) is specifically designed for

boreal ecosystems and thus takes into account more of the details concerning burning characteristics of boreal fires. This includes the burning of organic soil layers that are characterized by smoldering combustion, which releases a higher amount of CO into the atmosphere. In the Global Wildland Fire Emission Model GWEM no enhanced CO emission factor has been used in this region for the sake of global consistency.

Fire activity in North Central Asia is observed during the boreal spring and summer months from May to August. The maximum activity month can be highly variable (Soja et al. 2004), but for the year 2000 the GWEM model calculates highest CO emissions for the month of May, followed by June and April, in accordance with the study of Kasischke et al. (2005).

In **Europe** fire emissions are not as important as in many other parts of the world. Only a marginal influence of fire emissions on the atmospheric chemical composition can be observed. The dominant emission sources are related to fossil fuel combustion.

Barbosa et al. (2002) calculated wildland fire emissions from the five Mediterranean countries in Europe and estimated that 0.46 Tg CO and 0.024 Tg NO_x were emitted. GWEM results yield 1.14 Tg CO (0.63-1.70) and 0.033 Tg NO_x (0.019-0.051), for all of Western Europe, respectively. Since the five Mediterranean countries in Barbosa et al. (2002) are the main contributors for Europe, a comparison of these numbers appears reasonable. The results are higher than the Barbosa estimates for CO but within in the range for NO_x. This suggests that ecosystems with a higher degree of smoldering combustion (forests) that favour the emission of CO probably overestimate their AFL in GWEM. The LPJ-DGVM used in GWEM has few anthropogenic processes included and therefore assumes high forest coverage for Europe, which leads to a higher CO combustion when burning.

It should be noted that agricultural fires have explicitly been excluded from GWEM, in order to avoid an overlap with agricultural waste fire emissions in chemistry transport modeling. To illustrate the potential impact of agricultural fires (i.e. the subset of fires seen from space), we have performed an additional run based on the MODIS landcover map, which includes the IGBP vegetation class 12. The available fuel load has been assumed to be similar to that of wooded savanna and emission factors were taken from Andreae and Merlet (2001). The inclusion of fires in pixels marked as agricultural land leads to the additional global release of 16 Tg CO and 0.59 Tg NO_x in GWEM-1.3. This compares to 23 Tg CO and 0.47 Tg NO_x (also released as NO) per year estimated by Yevich and Logan (2003).

Fires in Europe occur mainly in the Mediterranean Western European countries but also in continental Eastern Europe. GWEM CO emissions for the year 2000 peak in the month of May and June and again later in the year in October in Western Europe. The same counts for Eastern Europe with the early burning season starting somewhat earlier in April.

For **North America**, GWEM-1.3 carbon estimates compare well with those of Kasischke et al. (2005) (Table 2.10c), although the latter refer to Canada only. Average carbon emissions for whole North America presented in Van der Werf et al. (2003) are about a factor of 3 higher than those of GWEM. In GWEM fire activity peaks in July, followed by August and September (Figure 2.8b). Kasischke show a maximum somewhat earlier in June, although not explicitly for the year 2000 only. Van der Werf et al. (2003) show the highest activity as early as May however, this estimate is based on nighttime ATSR fire counts only.

a.)

months	C-AM	E-AS	E-EU	S-AS	N-EA	N-AM	NC-AS	N-AF	OCE	S-AM	S-AF	W-EU	monthly totals
1	0.53	0.00	0.00	1.79	0.00	0.06	0.00	30.26	3.15	0.47	0.32	0.00	36.59
2	0.49	0.00	0.00	4.43	0.00	0.14	0.00	8.55	0.76	0.98	0.17	0.00	15.52
3	0.22	0.00	0.00	4.81	0.00	0.00	0.00	4.97	0.33	0.76	1.34	0.00	12.44
4	0.53	0.68	3.53	8.44	0.15	0.18	6.91	1.62	0.40	0.43	0.81	0.12	23.81
5	0.35	0.78	2.20	4.31	0.05	0.12	34.05	1.31	0.73	1.25	4.06	0.56	49.77
6	0.00	0.00	0.24	0.19	0.06	0.68	6.91	0.13	1.43	0.73	23.05	0.16	33.57
7	0.00	0.01	0.10	0.16	0.09	4.30	3.76	0.07	1.58	1.87	31.63	0.03	43.59
8	0.00	0.00	0.32	0.50	0.30	3.44	6.14	0.35	3.63	2.43	16.00	0.05	33.17
9	0.00	0.00	0.21	0.35	0.02	2.92	0.83	0.57	5.60	1.82	12.33	0.09	24.74
10	0.19	0.30	1.08	1.62	0.07	0.03	1.08	2.61	3.10	1.03	4.60	0.13	15.85
11	0.46	0.00	0.00	0.48	0.00	0.03	0.00	9.35	4.07	0.94	1.78	0.00	17.11
12	0.53	0.00	0.00	0.57	0.00	0.05	0.00	37.83	0.49	1.05	0.30	0.00	40.82
Regional totals	3.29	1.78	7.68	27.65	0.75	11.95	59.68	97.63	25.28	13.77	96.39	1.14	**346.99**

b.)

months	C-AM	E-AS	E-EU	S-AS	N-EA	N-AM	NC-AS	N-AF	OCE	S-AM	S-AF	W-EU	monthly totals
1	0.29	0.00	0.00	0.31	0.00	0.01	0.00	8.65	2.95	0.22	0.14	0.00	12.58
2	0.30	0.00	0.00	0.64	0.00	0.05	0.00	3.30	0.68	0.30	0.10	0.00	5.36
3	0.10	0.00	0.00	0.97	0.00	0.00	0.00	2.09	0.31	0.25	0.22	0.00	3.95
4	0.18	0.46	3.25	3.54	0.15	0.12	6.67	1.05	0.29	0.32	0.54	0.06	16.63
5	0.25	0.55	1.09	4.04	0.04	0.12	28.48	1.07	0.58	1.11	2.52	0.27	40.13
6	0.00	0.00	0.13	0.14	0.05	0.56	5.39	0.11	1.12	0.36	12.75	0.09	20.71
7	0.00	0.00	0.09	0.10	0.08	2.81	3.39	0.05	1.25	0.90	17.24	0.03	25.94
8	0.00	0.00	0.27	0.15	0.29	2.44	5.69	0.32	2.94	0.63	10.73	0.03	23.51
9	0.00	0.00	0.19	0.16	0.02	2.45	0.77	0.26	4.68	0.61	8.61	0.06	17.81
10	0.18	0.26	0.95	1.43	0.05	0.03	1.05	1.18	2.52	0.22	2.85	0.09	10.81
11	0.38	0.00	0.00	0.15	0.00	0.01	0.00	4.71	3.57	0.43	0.83	0.00	10.08
12	0.36	0.00	0.00	0.12	0.00	0.01	0.00	12.67	0.46	0.68	0.12	0.00	14.42
Regional totals	2.02	1.27	5.97	11.75	0.69	8.60	51.46	35.47	21.36	6.05	56.65	0.63	201.91

Table 2.7: Regional total and global monthly CO emissions for the year 2000 as calculated by **a.)** the best guess run of GWEM-1.3, **b.)** the minimum run of GWEM-1.3, and **c.)** the maximum run of GWEM-1.3

c.)

months	C-AM	E-AS	E-EU	S-AS	N-EA	N-AM	NC-AS	N-AF	OCE	S-AM	S-AF	W-EU	monthly totals
1	0.63	0.00	0.00	3.15	0.00	0.08	0.00	117.32	3.51	0.96	0.38	0.00	126.02
2	0.59	0.00	0.00	5.45	0.00	0.24	0.00	29.54	1.04	2.07	0.27	0.00	39.20
3	0.26	0.00	0.00	7.17	0.00	0.01	0.00	13.09	0.39	1.53	1.58	0.00	24.03
4	0.64	1.22	4.14	11.77	0.17	0.49	8.13	3.18	0.74	0.56	1.34	0.24	32.62
5	0.38	1.42	2.44	5.42	0.07	0.15	41.09	1.56	1.00	1.52	9.88	0.64	65.56
6	0.00	0.00	0.38	0.24	0.07	0.74	10.20	0.15	2.01	1.50	64.27	0.21	79.77
7	0.00	0.03	0.13	0.21	0.14	5.18	4.86	0.08	2.21	3.01	79.15	0.05	95.05
8	0.00	0.02	0.35	0.57	0.41	4.73	7.76	0.37	4.33	5.21	31.51	0.12	55.38
9	0.00	0.00	0.23	0.47	0.03	3.60	0.92	0.68	6.48	2.74	19.76	0.21	35.13
10	0.19	0.41	1.51	2.45	0.14	0.05	1.21	3.06	3.90	1.97	9.44	0.23	24.56
11	0.50	0.00	0.00	0.80	0.00	0.04	0.00	13.89	4.58	1.03	2.60	0.00	23.43
12	0.62	0.00	0.00	0.95	0.00	0.08	0.00	116.04	0.53	1.23	0.70	0.00	120.15
Regional totals	**3.80**	**3.09**	**9.19**	**38.66**	**1.03**	**15.38**	**74.16**	**298.95**	**30.73**	**23.34**	**220.88**	**1.70**	**720.91**

Table 2.7: cont.'d

a.)

months	C-AM	E-AS	E-EU	S-AS	N-EA	N-AM	NC-AS	N-AF	OCE	S-AM	S-AF	W-EU	monthly totals
1	0.0126	0.0000	0.0000	0.0377	0.0000	0.0011	0.0000	0.9136	0.1143	0.0135	0.0085	0.0000	1.1012
2	0.0116	0.0000	0.0000	0.0869	0.0000	0.0029	0.0000	0.2722	0.0271	0.0251	0.0051	0.0000	0.4309
3	0.0050	0.0000	0.0000	0.1005	0.0000	0.0001	0.0000	0.1515	0.0122	0.0197	0.0262	0.0000	0.3152
4	0.0116	0.0191	0.1118	0.1970	0.0046	0.0059	0.2107	0.0555	0.0136	0.0141	0.0269	0.0033	0.6738
5	0.0077	0.0220	0.0624	0.1296	0.0017	0.0040	0.9764	0.0481	0.0269	0.0446	0.1360	0.0158	1.4752
6	0.0000	0.0000	0.0073	0.0056	0.0019	0.0197	0.2159	0.0049	0.0518	0.0214	0.7499	0.0050	1.0835
7	0.0000	0.0002	0.0036	0.0041	0.0032	0.1229	0.1185	0.0023	0.0568	0.0499	1.0030	0.0010	1.3656
8	0.0000	0.0002	0.0115	0.0111	0.0109	0.1009	0.2161	0.0128	0.1332	0.0588	0.5506	0.0015	1.1075
9	0.0000	0.0000	0.0078	0.0090	0.0006	0.0883	0.0292	0.0151	0.2073	0.0447	0.4409	0.0028	0.8457
10	0.0048	0.0085	0.0304	0.0469	0.0022	0.0009	0.0310	0.0736	0.1133	0.0238	0.1611	0.0037	0.5002
11	0.0125	0.0000	0.0000	0.0108	0.0000	0.0005	0.0000	0.2913	0.1504	0.0251	0.0508	0.0000	0.5414
12	0.0135	0.0000	0.0000	0.0121	0.0000	0.0011	0.0000	1.1193	0.0182	0.0325	0.0085	0.0000	1.2052
Reg. totals	**0.0792**	**0.0500**	**0.2348**	**0.6513**	**0.0252**	**0.3483**	**1.7977**	**2.9602**	**0.9249**	**0.3733**	**3.1673**	**0.0331**	**10.6453**

Table 2.8: Regional total and global monthly NO_x emissions for the year 2000 as calculated **a.)** by the best guess run of GWEM-1.3 **b.)** the minimum run of GWEM-1.3, and **c.)** the maximum run of GWEM-1.3

b.)

months	C-AM	E-AS	E-EU	S-AS	N-EA	N-AM	NC-AS	N-AF	OCE	S-AM	S-AF	W-EU	monthly totals
1	0.0077	0.0000	0.0000	0.0082	0.0000	0.0002	0.0000	0.3050	0.1076	0.0079	0.0049	0.0000	0.4415
2	0.0077	0.0000	0.0000	0.0165	0.0000	0.0010	0.0000	0.1179	0.0246	0.0104	0.0034	0.0000	0.1815
3	0.0027	0.0000	0.0000	0.0263	0.0000	0.0000	0.0000	0.0738	0.0116	0.0089	0.0054	0.0000	0.1287
4	0.0050	0.0128	0.1024	0.1003	0.0044	0.0041	0.2022	0.0387	0.0102	0.0116	0.0195	0.0017	0.5130
5	0.0058	0.0155	0.0312	0.1213	0.0015	0.0037	0.8153	0.0396	0.0217	0.0410	0.0920	0.0076	1.1964
6	0.0000	0.0000	0.0041	0.0045	0.0018	0.0162	0.1706	0.0042	0.0410	0.0130	0.4603	0.0031	0.7188
7	0.0000	0.0001	0.0031	0.0029	0.0030	0.0803	0.1072	0.0019	0.0456	0.0294	0.6144	0.0009	0.8887
8	0.0000	0.0001	0.0100	0.0046	0.0102	0.0715	0.2010	0.0119	0.1097	0.0202	0.3917	0.0010	0.8319
9	0.0000	0.0000	0.0069	0.0052	0.0005	0.0746	0.0273	0.0091	0.1746	0.0205	0.3172	0.0018	0.6379
10	0.0046	0.0073	0.0267	0.0413	0.0016	0.0008	0.0300	0.0419	0.0932	0.0071	0.1056	0.0025	0.3627
11	0.0106	0.0000	0.0000	0.0042	0.0000	0.0002	0.0000	0.1712	0.1326	0.0153	0.0295	0.0000	0.3637
12	0.0100	0.0000	0.0000	0.0030	0.0000	0.0003	0.0000	0.4496	0.0173	0.0251	0.0042	0.0000	0.5095
Reg. totals	**0.0542**	**0.0358**	**0.1844**	**0.3384**	**0.0231**	**0.2531**	**1.5536**	**1.2649**	**0.7897**	**0.2103**	**2.0481**	**0.0187**	**6.7743**

c.)

months	C-AM	E-AS	E-EU	S-AS	N-EA	N-AM	NC-AS	N-AF	OCE	S-AM	S-AF	W-EU	monthly totals
1	0.0160	0.0000	0.0000	0.0884	0.0000	0.0020	0.0000	4.1711	0.1255	0.0319	0.0108	0.0000	4.4456
2	0.0154	0.0000	0.0000	0.1253	0.0000	0.0062	0.0000	1.0577	0.0358	0.0660	0.0088	0.0000	1.3151
3	0.0066	0.0000	0.0000	0.1886	0.0000	0.0005	0.0000	0.4551	0.0142	0.0487	0.0351	0.0000	0.7488
4	0.0157	0.0345	0.1328	0.3146	0.0051	0.0172	0.2554	0.1137	0.0242	0.0186	0.0465	0.0069	0.9852
5	0.0089	0.0400	0.0700	0.1670	0.0025	0.0047	1.2176	0.0577	0.0370	0.0547	0.3537	0.0180	2.0318
6	0.0000	0.0000	0.0124	0.0073	0.0027	0.0218	0.3319	0.0056	0.0717	0.0503	2.2926	0.0067	2.8029
7	0.0000	0.0008	0.0045	0.0062	0.0050	0.1547	0.1564	0.0027	0.0779	0.0926	2.7812	0.0017	3.2837
8	0.0000	0.0007	0.0128	0.0137	0.0146	0.1480	0.2736	0.0133	0.1593	0.1627	1.1311	0.0041	1.9338
9	0.0000	0.0000	0.0084	0.0135	0.0008	0.1119	0.0323	0.0193	0.2397	0.0791	0.7191	0.0067	1.2311
10	0.0049	0.0114	0.0428	0.0765	0.0043	0.0014	0.0355	0.0903	0.1407	0.0588	0.3420	0.0068	0.8155
11	0.0137	0.0000	0.0000	0.0230	0.0000	0.0009	0.0000	0.4612	0.1672	0.0285	0.0815	0.0000	0.7760
12	0.0168	0.0000	0.0000	0.0263	0.0000	0.0021	0.0000	4.0457	0.0197	0.0391	0.0234	0.0000	4.1732
Reg. totals	**0.0981**	**0.0873**	**0.2837**	**1.0504**	**0.0351**	**0.4713**	**2.3028**	**10.494**	**1.1129**	**0.7309**	**7.8257**	**0.0510**	**24.5426**

Table 2.8: cont'd.

2.5 Uncertainties

The uncertainties of the GWEM input data have been reported for the emission factors (Table 2.5) and the burning efficiencies (Table 2.6). The uncertainty for the latter varies considerably for different species. While emission factors of species such as CO_2, CO, and CH_4 for example, are quite well known due to the broad availability of measurements in literature, others rely on one documented measurement only (see Andreae and Merlet, 2001). Typically, the uncertainty of emission factors is in the order of 20-30 %. For the burning efficiency, uncertainty ranges between 12 % in savanna and grasslands and 20% in the forests. A first simple approach to uncertainty assessment in terms of the AFL input was integrated in GWEM by attributing a minimum-maximum range to the AFL data.

The uncertainty assessment for the burned area from satellites, such as GBA2000, is a difficult task. Several questions arise which are not yet possible to answer on a quantitative basis: How much of a 1 km^2 area burned record is really burned? How much of the areas burned remains unseen due to almost permanent cloud coverage, especially during the burning season? How much of dark rocks or soil is mistaken for burned area? How many small and patchy areas burned are ignored by the satellite? How many peat fires are omitted due to their low temperature and invisibility in terms of reflectance?
It is far beyond the framework of this study to answer these questions, which are currently being investigated by the fire remote sensing community. Here, it is only feasible to show up the difference of available global area burned, namely the GBA2000 versus the GLOBSCAR product, as suggested in Tansey et al. (2004). In total, using GLOBSCAR in GWEM-1.3 delivers a total of 223 Tg CO, or 36 % less global CO emissions. Largest discrepancies are observed in Africa and Eastern Russia, and Australia according to the difference plot in Figure 2.14. In these regions GBA2000 observes significant more burned area than the GLOBSCAR product and emission fluxes of e.g. CO thus are more elevated.

The AFL used in GWEM-1.3 is also subject to major uncertainties: Figure 2.15 illustrates the bandwidth of CO monthly total emission throughout the year 2000, resulting from different AFL assumptions. The constant AFL values suggested by Reid et al. (2005a,b) are 500 (100 – 800) g/m^2, 2000 (500 – 10000) g/m^2, 30000 (10000 – 50000) g/m^2, 20000 (8000 – 40000) g/m^2, and 8000 (2500 – 20000) g/m^2 for savanna and grasslands, wooded savanna, tropical forest, temperate forest, and boreal forest, respectively. The values are based on the literature values in Table 2.4. "Fuel loads are considered reasonable but may be highly uncertain -the mean value given is for illustrative purposes. Given in parentheses are commonly reported ranges of values" (Reid et al., 2005a,b). Two of these runs include both minimum and maximum assumptions of AFL and the emission factors ("all min" and "all max" runs). The range of global CO emissions that result from the runs that solely incorporate a change in AFL is 203 – 725 Tg CO. If emission factors are additionally set to their lower and upper deviation, the global CO emissions range from 137 – 945 Tg CO (i.e. 40% - 270% of best guess (=347 Tg CO)). The difference between the GWEM best guess run with AFL from the LPJ model and the run with best guess globally constant AFL numbers is small, except for a higher peak of the latter in April and May. Average temperate forest AFLs in the northern hemisphere as calculated from the LPJ model are considerably lower than the from Reid et al. (2005a,b) suggested constant AFL values (see Figure 2.5b) and explains the absence of this northern hemispheric spring peak.

The selection of a landcover map can also have considerable impact on emission results. The difference in GWEM CO emissions by using either the widely used IGBP-DIS landcover map (Loveland and Belward, 1997 and Loveland et al., 2000) or the default MODIS landcover map produces the differences shown in Figure 2.16. The most remarkable differences between these two runs are found in Africa and Eastern Europe. The GWEM run that is based
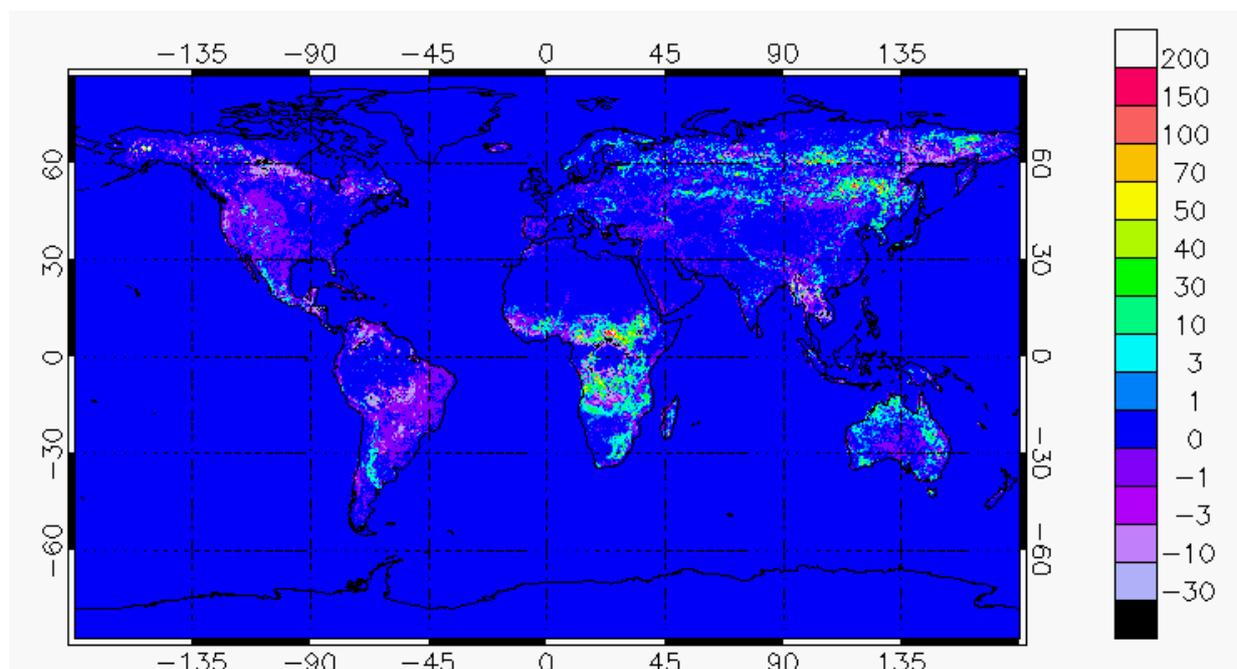
Figure 2.14: CO difference in g/m-2 of GWEM-1.3 using GBA2000 area burned minus GWEM-1.3 using GLOBSCAR in the year 2000

on the IGBP landcover map calculates about four times as much CO in June as the GWEM run based on the MODIS landcover map. This is solely caused by the highly differing ecosystem assignments between these two maps. In total the IGBP based GWEM run produces 913 Tg CO, over 260 % more than the best guess GWEM run based on the MODIS map.

There is also a remarkable difference in seasonality and CO emissions in Eastern Europe between the two model runs. This is explained by the incorrect assignment of agricultural areas as wooded savannas in the IGBP data set: the MODIS map contains many pixels associated with the vegetation class 12 "Croplands", which are removed from the analysis in this study. In case of the IGBP-DIS map, these pixels are assigned to other vegetation classes (6,8,9,11, and 14), which are part of the ecosystems savanna and grasslands, and woody savannas (see Table 2.2) and are counted as burned areas. Similar explanations hold for some other regions as well. In all remaining regions, no striking differences in the monthly totals can be observed. However, major differences may exist, although not in the areas where the GBA2000 product yields detections of burned area.

With regard to the extent of present deforestation and because of improved methodology and data sets, the MODIS landcover map is believed to be closer to the truth. Another new vegetation map (GLC2000, Bartholomé et al., 2002) shows only minor differences to the MODIS data set, at least as far as this study is concerned. The landcover in GWEM decides on emission factors and burning efficiencies and even the area burned selection. Therefore, a careful choice at this point is important. In Hoelzemann et al. (2004), the effect of using different landcover maps has been investigated in more detail. These first three sources of uncertainty will have an effect on the same scale on emission fluxes of other species than CO that are calculated by GWEM.

The compiled emission factors from Andreae and Merlet (2001) used in GWEM have standard deviations or ranges, depending on the amount of measurements found in literature. These ranges have been applied to perform a minimum alias maximum run, where only the emission factors are modified. CO emissions resulting from GWEM runs with variable emission factor range between 246 – 453 Tg CO. This represents 70 % or 130% of the best guess run of GWEM using the mean emission factors in Andreae and Merlet (2001).
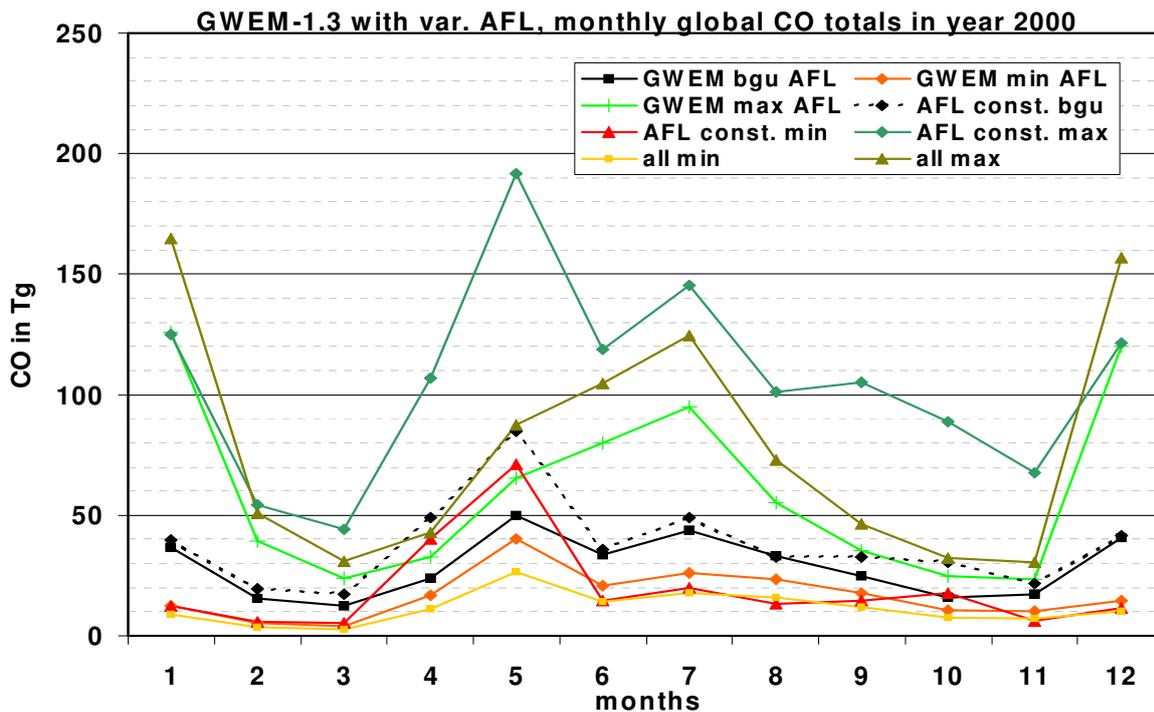
Figure 2.15: CO seasonality in Tg of the year 2000 for an ensemble of GWEM-1.3 runs based on different AFL. The solid black line is the standard GWEM best guess run with AFL from the LPJ model, as used for all shown results in Chapter 2. The light green and dark orange lines are the respective AFL-LPJ minimum and maximum runs used as a range on the GWEM results. The dotted black line comprises constant AFL for each ecosystem as suggested by Reid et al., 2005a,b. The red and dark green lines are the respective minimum and maximum values. Yellow and olive green lines result from a minimum/maximum AFL run of GWEM with additional use of the lower/upper range (standard deviation) of emission factors from Andreae and Merlet (2001)
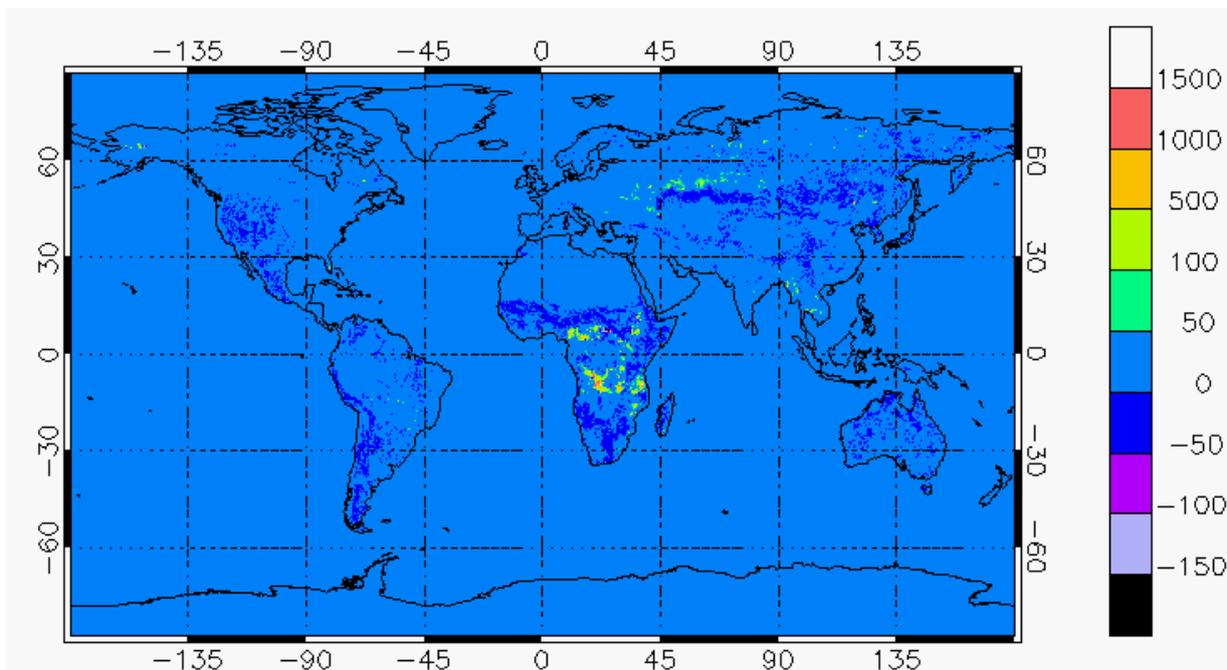
Figure 2.16: CO difference in g/m-2 of GWEM-1.3 using the IGBP-DIS landcover map minus GWEM-1.3 using the MODIS landcover in the year 2000
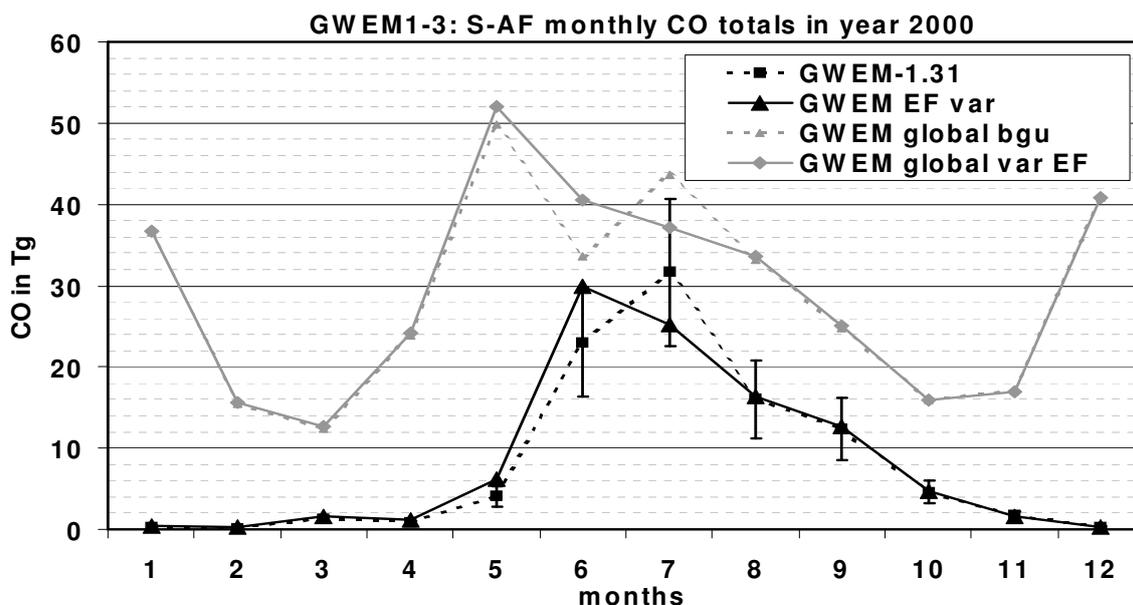
Figure 2.17: CO monthly totals in g/m-2 of GWEM-1.3 of Southern Africa in the year 2000 (black lines) and CO global monthly totals (gray lines). The dotted lines are the standard best guess of GWEM-1.3. The full lines are a GWEM-1.3 run, where variable emission factors have been used in Southern Africa, adapted from values of Korontzi et al. (2003)

Other than for the previous uncertainty sources, the variety of an emission factor is related to the species specific accuracy with which it can be measured. CO is a species relatively easy to be assessed. One aspect is the stable lifetime until it is measured. This is in contrast to aerosols such as black carbon (BC): at the time it is measured, it is already mixed with secondary aerosol components that were not directly emitted by the fire, or partially deposited. Also it remains unclear, whether what is measured is always pure BC, or mixed with organic not completely combusted components (Andreae and Merlet, 2001). Therefore, the standard deviation of BC und thus the induced uncertainty in the emission fluxes are larger than for CO: GWEM calculates a range of 60 % or 140% of the GWEM best guess run (= 2.375 Tg BC).

Further, a test was performed of how much seasonal varying emission factors influence emission fluxes. The region chosen for this test is Southern Africa as only region with available data for this purpose. Korontzi et al. (2003) deliver measured emission factors in the months from August to September that were extrapolated to the earlier and later burning season (May to October). The early burning season is characterized by higher emission factors for species that are favoured by smoldering combustion, because the fuel moisture is higher. The later the season, the drier the fuel, the smaller the emission factors for CO. Figure 2.17 presents the changed CO seasonality in Southern Africa (black line) and its effect on the global seasonality of CO from wildland fire emissions. The maximum emission flux is shifted from July to June 2000, solely by introduction of seasonal emission factors.

After assessing the individual uncertainties, the question arises about how they interact.

The validation of a global product such as GWEM can only be performed in a multi-tier approach: comparisons and uncertainty estimates must be made both for the individual input data sets as well as for the final product. Likewise, scales from local (e.g. a few GBA2000 pixels) to global must be considered. An assessment of the impact of the emission factors uncertainty on the model results can be performed by following for example the approach of van Aardenne (2002).

2.6 Synthesis

The Global Wildland Fire Emission Model was developed and has been presented in its most recent version 1.3. This version is based on (i) global area burnt data from the GBA2000 data set, (ii) carbon pool content data of the LPJ global dynamic vegetation model to estimate the Available Fuel Load (AFL) of the vegetation, (iii) a MODIS landcover map based on data from October 2000 to October 2001, (iv) burning efficiencies from Reid et al. (2005a,b), and (v) emission factor from Andreae and Merlet (2001) and updates from Andreae (pers. comm., 2003). Globally, the resulting emissions are somewhat lower than previous estimates. A detailed inspection of the individual factors contributing to the emission estimates indicates that there is some underestimation in the GBA2000 burned areas, in particular for regions with many small but intense fires related to deforestation processes, such as in South America. Thus, applications in global modeling must consider additional data for calculating emissions of the small but intense deforestation fires, especially in South America. For South America, a Brazilian data set of satellite fire pixels from CPTEC/INPE was recently applied to improve regional emissions in GWEM (see Appendix A, GWEM-1.4 description). Future satellite derived fire products should be based on multiple sensors and combine burned area information with hot spot detection in order to increase the completeness of the product and allow emission estimates for other years.

Also it was found that estimated fuel loads in some regions based on data from the LPJ-model are more elevated compared to values from published literature. However, it should be noted that high uncertainties persist to the validity of attributing published fuel load estimates of an ecosystem to the same ecosystems in another region, which is a well-established procedure in global studies due to the scarcity of available data.

The LPJ-model operates only on the basis of natural vegetation and does not include major anthropogenic changes induced by human agricultural activities (e.g. crop plantations) that substitute natural vegetation in many parts of the world. Crop Plant Functional Types (CFT's) have recently been implemented in the LPJ-model (e.g. PhD thesis by Luca Criscuolo, MPI-M/IMPRS, 2006) and will allow for more accurate estimates of the AFL in the future for the purpose of fire emission modeling.

Further, the derivation of fuel load from the total biomass density relies to a high extent on guesswork that could be avoided in the future, if values of fuel loads/biomass and burning efficiencies in literature would be more consistently and transparently defined, bearing an interdisciplinary user community in mind. More campaigns in different ecosystems that derive burning efficiencies directly from the on-site biomass by assessment of pre-burning and post-burning biomass amounts would avoid the interim step of calculating the available fuel load from the total biomass.

The aim of the discussion section has been to put GWEM emissions into relation to other emission data sets. This allowed an insight on how GWEM-1.3 emissions behave quantitatively and qualitatively compared to other published emission inventories.

Generally it can be said that in some regions the various fire emission estimates differ substantially and that it is not possible to determine, which study yields the most accurate results. For the purpose of quantitative intercomparison, fire emissions need to be converted into a measurable quantity that can be evaluated against observations. -Emission intercomparison does not deliver a final answer as other inventories also contain uncertainties and flaws in the same order as GWEM. Section 2.5 permitted a qualitative investigation of uncertainties of individual GWEM components, which did not reduce the uncertainties in numbers, but helped to better define their origins and inter-relations.

Further studies with a tropospheric global Chemistry Transport Model are a prerequisite to allow a quantitative evaluation of fire emission estimates and derive final conclusions of their skill.

3   Fire and Other Emission Data Sets for MOZART-2

The Global Wildland Fire Emission Model GWEM presented in Chapter 2 was designed to improve fire emissions for use in atmospheric chemistry modeling. To investigate the achieved improvements of GWEM and its intercomparison with other available global fire emission data sets, the GWEM emissions and other fire emission data sets were applied to the global tropospheric Chemistry Transport Model MOZART-2. Resulting tropospheric trace gas concentrations of e.g. ozone precursors CO and NO_x and consequent ozone enhancement can then be validated with atmospheric trace measurements.
This chapter presents the different vegetation fire emission inventories that were utilized in this study using MOZART-2 and the other emissions i.e. biogenic, anthropogenic, biofuel, agricultural waste burning, ocean, and soil emissions that are needed to cover the complete ensemble of emission sources.

3.1 Wildland Fire Emissions

Five wildland fire emission inventories were considered for the year 2000: The GWEM-1.3 inventory (**GWEM**), the inventory by Van der Werf et al. (2003) (**gfed**), the climatological inventory of MOZART-2 developed several years ago by Hao and Liu (1994) (**Hao&Liu**), and two versions of the ATSR fire count scaled climatological inventories: Schultz (2002) (**mgs_scal**) and Granier and Lamarque (pers. comm., 2004) (**cg_scal**). The text in parentheses is the corresponding shortcut name used throughout this and forthcoming chapters. CO and NO_x regional total emissions from all inventories and sources (burning and non-burning) are given in Figure 3.1 and Figure 3.2, respectively. The global seasonalities of these emissions are reflected in Figure 3.3. This latter figure highlights the importance of global CO emissions from wildland fires: although highly variable, all fire emission graphs are in average of the order of global anthropogenic emissions. Further, all figures highlight the remarkable differences between the five wildland fire emissions inventories. Table 3.1 lists the global total annual wildland fire emissions for the year 2000 from each inventory. All inventories made use of the Andreae and Merlet (2001) published emission factor compilation. GWEM-1.3 and gfed additionally used the corrected lower NO_x average emission factor (Andreae, pers. comm., 2003; Table 2.5).

species	source Hao&Liu	mgs_scal	cg_scal	gfed	GWEM-1.3
NOx (as NO)	16.2	14.4	13.7	13.7	10.7
CO	465	395	292	445	347
C2H6	3.8	3.1	1.9	3.1	2.3
C3H8	0.73	0.61	0.42	1.78	1.31
C2H4	6.89	5.78	3.94	6.58	4.99
C3H6	2.23	1.87	1.30	2.26	1.80
CH3OH	14.69	12.54	8.53	10.08	7.76
Acetone	2.37	1.98	1.88	3.33	2.53

Table 3.1: Annual total emissions in Tg of the year 2000 for the five wildland fire emission inventories applied to MOZART-2.
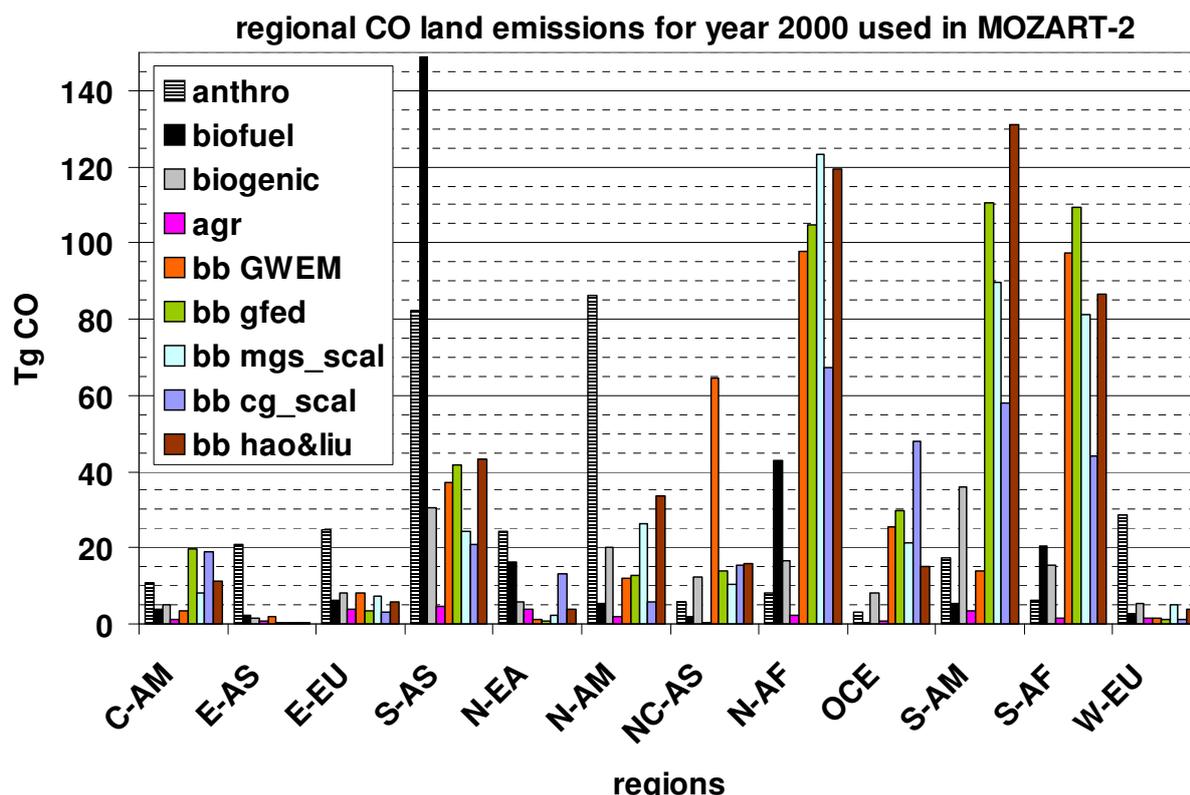
Figure 3.1: Regional total POET CO emissions from anthropogenic sources, biofuel, biogenic, and agricultural-waste burning, together with all five wildland fire emission inventories (bb) yielding emissions from forest and savanna fires

3.1.1 A Climatological Emission Inventory

The climatological biomass burning emission inventory for the tropics by Hao and Liu (1994) has been widely used in global Chemistry Transport Models (CTM's). This 5° x 5° inventory is based on FAO statistics from the 1970's, global vegetation maps and published data on biomass density and emission factors from a variety of different publications and geographical regions (see Table 1 of Hao and Liu, 1994). The seasonality in this inventory is derived from the variation of ozone surface concentrations in each grid cell. In the MOZART-2 model that will be presented in Chapter 4, the inventory of Hao and Liu (1994) has until recently been used for forest and savanna fires in the tropics and corresponding emissions by Müller (1992) in the extratropics. The latter is based on area burned data from statistics of the U.S. Forest Service, the Organization for Economic Cooperation and Development (OECD) and the United Nations of the 1980's. Biomass density, carbon content and emission factors for the calculation of fire emissions are derived from published scientific literature of the 1970's and 1980's.

These inventories are part of the standard MOZART-2 description by Horowitz et al. (2003). The amount of species emitted is derived from the biomass burned using the compilation of emission factors by Andreae and Merlet (2001).

Due to the strong regional seasonality, high inter-annual variability, and decadal trends of wildland fire emissions, this long-used inventory needed to be updated and refined, as soon as more recent and better resolved global active fire count data became available.
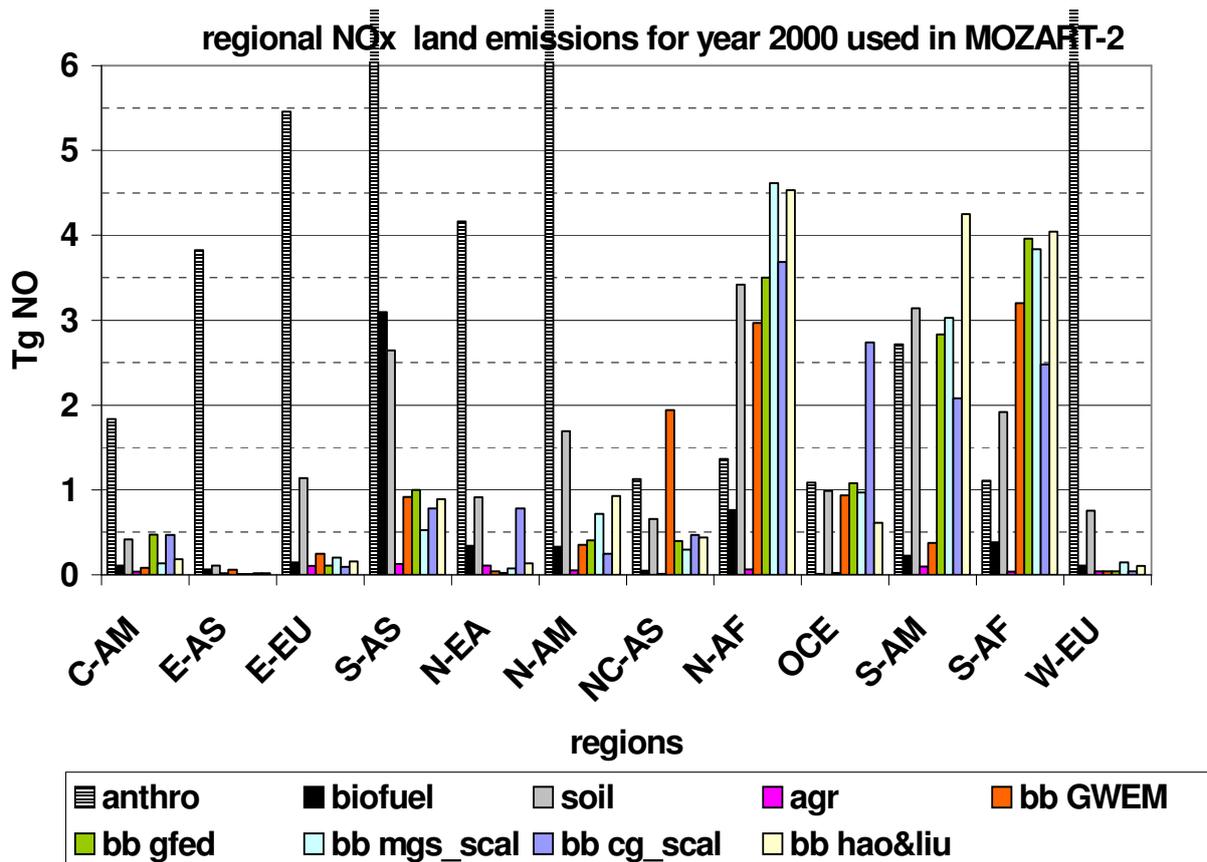
Figure 3.2: Regional total NO$_X$ emissions from POET for anthropogenic, biofuel, biogenic, and agricultural-waste burning sources, together with all five wildland fire emission inventories (bb) yielding emissions from forest and savanna fires

3.1.2 Scaled Climatological Emissions

With the availability of high-resolution remote sensing fire count data, the climatological inventory of MOZART-2 (see previous section 3.1.1) could be seasonally and inter-annually redistributed, to better represent the emission patterns of the late 1990's and the beginning of the new millennium. This interim solution was performed in two different approaches, one by Schultz (2002) and the other by Granier and Lamarque (pers. comm., 2004). The two studies comprise the same underlying base-inventory of MOZART-2 (see section 3.1.1) scaled with active ATSR nighttime fire count data of the ESA World Fire Atlas (WFA) from 1997-2001.

The method by Schultz (2002) applies ATSR nighttime fire count data above a 308 K threshold. Fire counts are gridded to a 1°x1° grid and normalized per year over the whole period of available ATSR data from August 1996 – 2001. The resulting scale factors are then multiplied with the climatological Hao and Liu (1994) data set. Hot spots in the ATSR data sets that are obviously not a result of large vegetation fires (so-called "spurious pixels") were removed from the data set prior to calculation of emissions (Schultz, 2002). ATSR scaled emissions by Granier and Lamarque (pers. comm. 2004), represent a quick preliminary estimate of the use of fire counts for estimating biomass burning emissions, without removal of false detections and based on the ATSR fire counts above a threshold of 312 K. This scaling approach assumes that the total emitted over the ATSR observation period of 1997-2001 is similar to the total evaluated by Hao and Liu (1994) in their climatological study. The distribution of a conversion factor is then defined, and applied annually to the ATSR observations.

Results are also gridded on a 1°x1° grid from 1997 – 2001. These forest and savanna fire

emissions are used in the European project POET (Present and future surface emissions of atmospheric compounds, EU project EVK2-1999-00011), see POET report (Olivier et al., 2003). In total, the latter approach yields 26% less global total CO and interestingly only 5% less NO_x emissions than the Schultz (2002) inventory. The reason for these differences seem to be superposing impacts from different input data. The emission ratios applied to both inventories to derive other species' estimates from CO_2 emissions are slightly lower in the forest ecosystems of the cg_scal inventory (4-5%), both for CO and for NO_x. For savanna ecosystems the difference is 1% (NO_x) and 2% (CO) (Schultz and Granier, pers. comm., 2004). The discrepancies in emission ratios cannot fully explain the different amounts of emitted CO. Likely, the application of two different algorithms (308 K (mgs_scal) versus 312K (cg_scal) temperature threshold) of the ATSR fire counts is responsible for the discrepancies in emissions.

3.1.3 Gfed Emissions

Van der Werf et al. (2003) developed an active fire count dataset from the Tropical Rainfall Measuring Mission (TRMM) only for the tropics and subtropics (38°S – 38°N) for 1998 - 2002. They related these fire counts to existing area burned data from the USA and the Moderate Resolution Imaging Spectrometer (MODIS) for some regions. The attribution of area burned per fire count are ecosystem-resolved averages. A modified version of the Carnegie-Ames-Stanford-Approach (CASA) biogeochemical model is included in this approach to obtain biomass densities. The latest version of the global fire emission database (gfed), updated from Van der Werf et al. (2003), currently delivers 1°x1° gridded monthly fire emissions from January 1998 – December 2002. The estimates of average area burned per fire count were updated by additional MODIS area burned tiles across Africa, South America, and Australia.

In the extratropics, where no TRMM-VIRS fire counts are available, the approach was extrapolated using ATSR data with a temperature threshold of 312 K. In the Russian Far East, a combination of country-level fire statistics and AVHRR-derived estimates was applied. The area burned for the year 1997 is calculated by a linear relationship of ATSR data to TRMM-VIRS fire counts. This dataset is described in Randerson et al. (2004), with the exception that the extratropical ATSR data is calculated in a way that preserves the seasonality and inter-annual variability of the ATSR fire counts (v. d. Werf, pers. comm., 2003).

3.1.4 GWEM-1.3 Emissions

The Global Wildland Fire Emission Model version 1.3 (GWEM-1.3), developed at the Max Planck Institute for Meteorology, was extensively described and discussed in Chapter 2.
It is the updated version based on the publication by Hoelzemann et al. (2004).
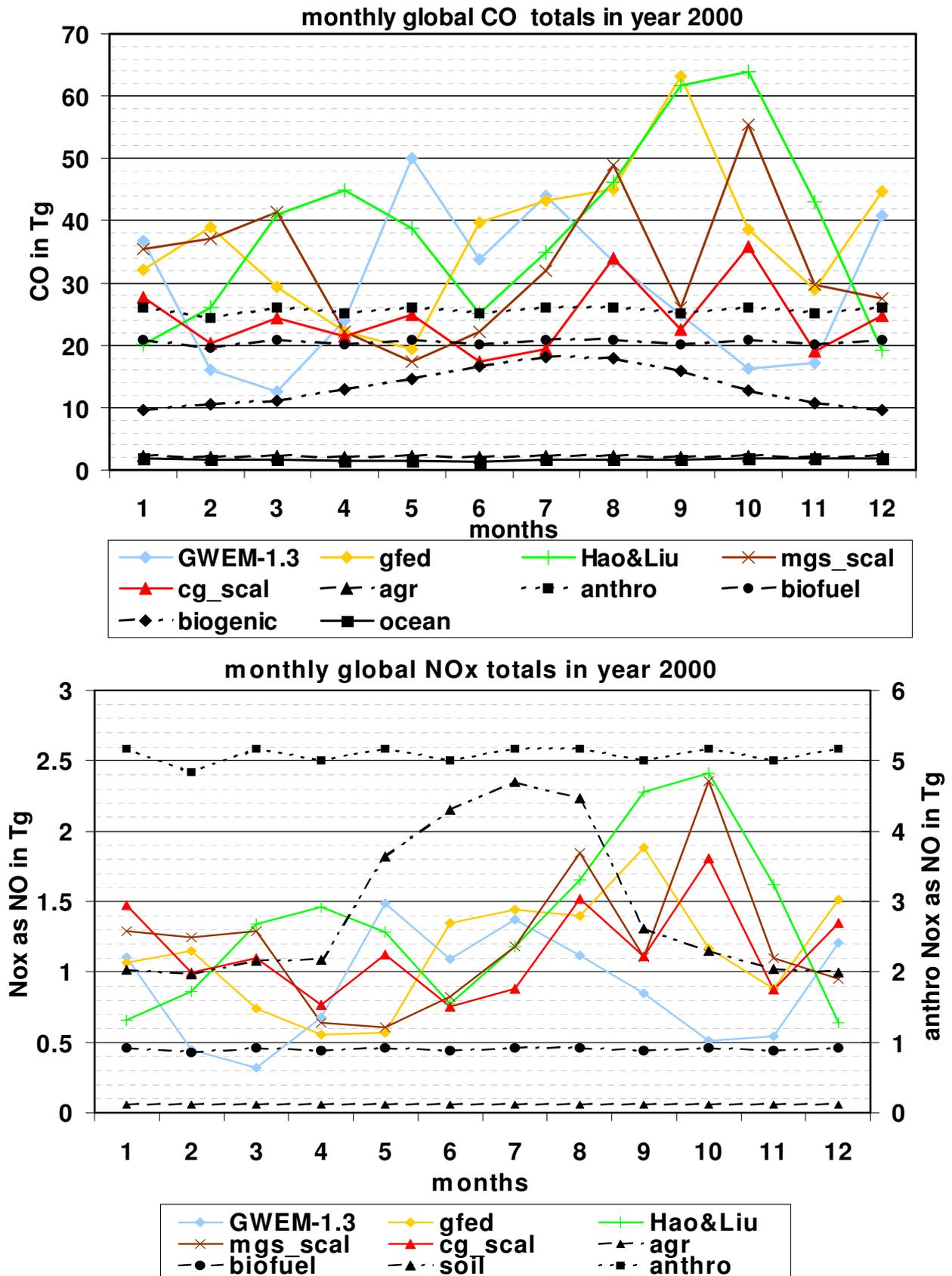
Figure 3.3: Seasonality of year 2000 global total CO (top) and NO_X (bottom) emissions from POET for anthropogenic, biofuel, biogenic, and agricultural-waste burning sources, together with all five wildland fire emission inventories yielding emissions from forest and savanna fires

3.2 Other Emission Sources

All emissions other than from forest and savanna fires are taken from the POET (EU project EVK2-1999-00011) database (Olivier et. al., 2003) for the year 2000. The sources are divided into anthropogenic, biogenic, ocean, soil (NO_x only), agricultural-waste burning emissions, and emissions from biofuels.
Anthropogenic emissions include the combustion of fossil fuels for power production or residential use, road and non-road transport, international shipping, oil production, coal fires, iron, steel and aluminium production, pulp and paper production and waste incineration. Biogenic emissions are those from living vegetation. The combustion of biofuels takes place in the industrial, power, residential and transport sectors.

The emission inventories are based on the EDGAR-3 data base and are typical for the years 1990, 1995 and 1997 (Olivier and Berdowski, 2001 and Olivier et al., 2001, available at http://arch.rivm.nl/env/int/coredata/ edgar/). POET is a European project that developed emission distributions over the 1990-2000 period. Estimates for other years than the EDGAR base years, rely on interpolation and extrapolation. For further details see the POET report, by Olivier et al. (2003). Table 3.2 lists the global total POET emissions for the year 2000.

species	agricultural waste burning	anthropogenic	biofuels	biogenic	ocean	soil
NOx (as NO)	0.7	61.0	5.4	-	-	17.2
CO	25.5	306.7	246.7	160.3	20.0	-
NMHC (as C)	0.6	23.5	5.3	-	1.7	-
C2H6	0.3	5.2	1.7	-	1.0	-
C3H8	0.14	-	-	-	1.29	-
C2H4	0.39	1.32	3.26	-	1.40	-
C3H6	0.28	0.59	1.59	-	1.52	-
CH3OH	0.87	2.95	-	-	-	-
Acetone	0.18	0.29	0.03	24.33	-	-

Table 3.2: Annual total emissions in Tg of the year 2000 for non-wildland fire emission sources applied to MOZART-2

3.3 Evaluation and Intercomparison of Emission Data Sets

The emission inventories of section 3.1 and 3.2 are compared for CO and NO_x, highlighting their global relevance (Figure 3.4 and 3.5, respectively). Their global contribution by individual sources is in the following set into relation with regional emission patterns that can have a very different scenario of source contributions. A small emission case study is performed for Southern Africa, one of the most important and most studied regions in terms of fire emissions.

3.3.1 Global Emissions

The global CO emission contribution from wildland fire emissions in Figure 3.4 lies between 30 – 38 % among the different fire emission inventories. The relative share of anthropogenic emissions, biofuels and biogenic emissions on the global scale consequently varies between 25 – 29%, 20 – 24%, and 13 – 19%, respectively. The total values for these sources are kept invariant however (see Table 3.2), since the focus is an investigation of the sensitivity towards wildland fire emissions.

While the emissions from forest versus savanna fires is very similar in the GWEM-1.3 emissions and the mgs_scal emissions (15% CO from forest fires versus 17% (GWEM-1.3) and 19% (mgs_scal) from savanna fires), the cg_scal fire emissions differ with only 9% of the CO being released from forest fires and 19% from savanna fires. This difference is the effect of using the ATSR nighttime fire count product with the higher threshold of 312 K (instead of 308 K) that misses many forest fires in the temperate and boreal regions (Arino and Plummer, 2001) in case of the cg_scal inventory. The global seasonality, depicted in Figure 3.3, reflects very different scenarios for the five inventories: the mgs_scal and cg_scal emissions evolute similarly in the second half of the year, albeit with more elevated emissions from the mgs_scal inventory. From January to March the difference in the mgs_scal and cg_scal emissions are even more pronounced and in May the mgs_scal CO emission totals drop below the estimates of cg_scal. The gfed inventory shows very low emissions during the northern hemispheric spring and has a distinct peak in September as a result of the elevated emissions from deforestation fires in South America. The GWEM-1.3 fire emissions yield highest emission in the boreal spring and summer with a maximum in May from temperate and boreal fires and a later peak with maximum in July from Southern African/South American fires. Also, a distinct boreal winter peak with a maximum in December, as a result from Northern African fires can be observed. The GWEM-1.3 seasonality is discussed in more detail in Chapter 2. In case of NO_x (Figure 3.5), the global scenario looks quite different, with anthropogenic emissions ranging from 61 – 64 % clearly dominating the other sources. The next major source are emissions from soil. Wildland fire emission are only responsible for 14 - 18 % of global NO_x emissions. The seasonality is very similar to the one of CO (Figure 3.3), however anthropogenic and soil emissions (the latter in the northern hemispheric summer months) play a major role in the overall emission scenario.
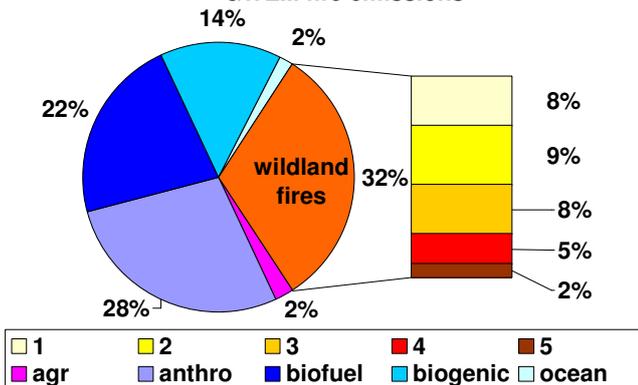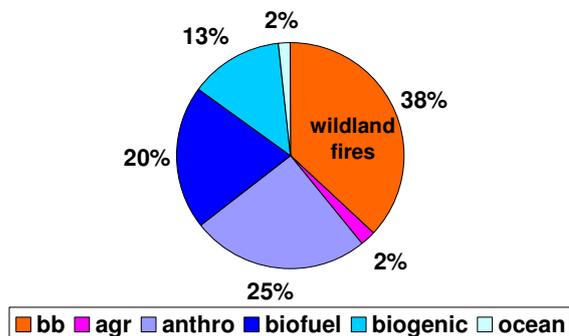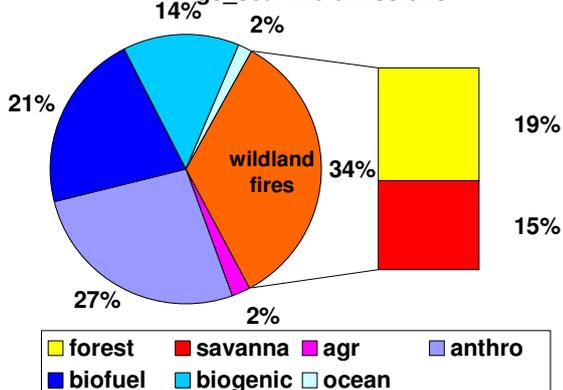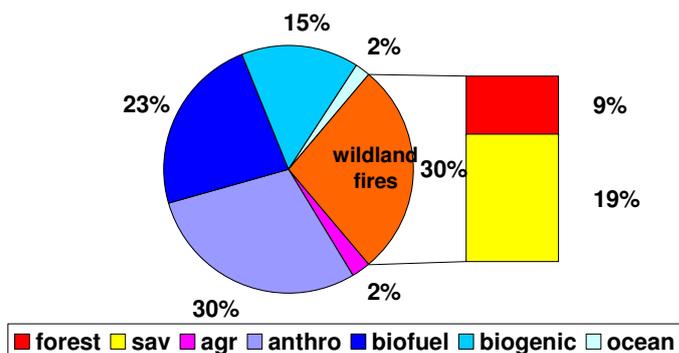
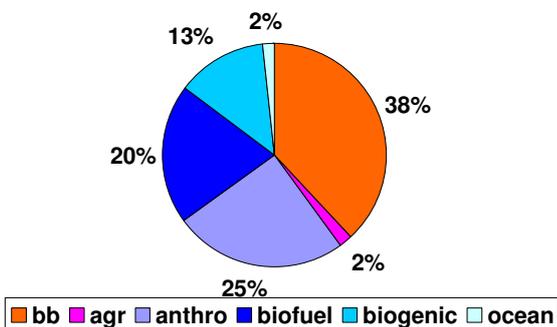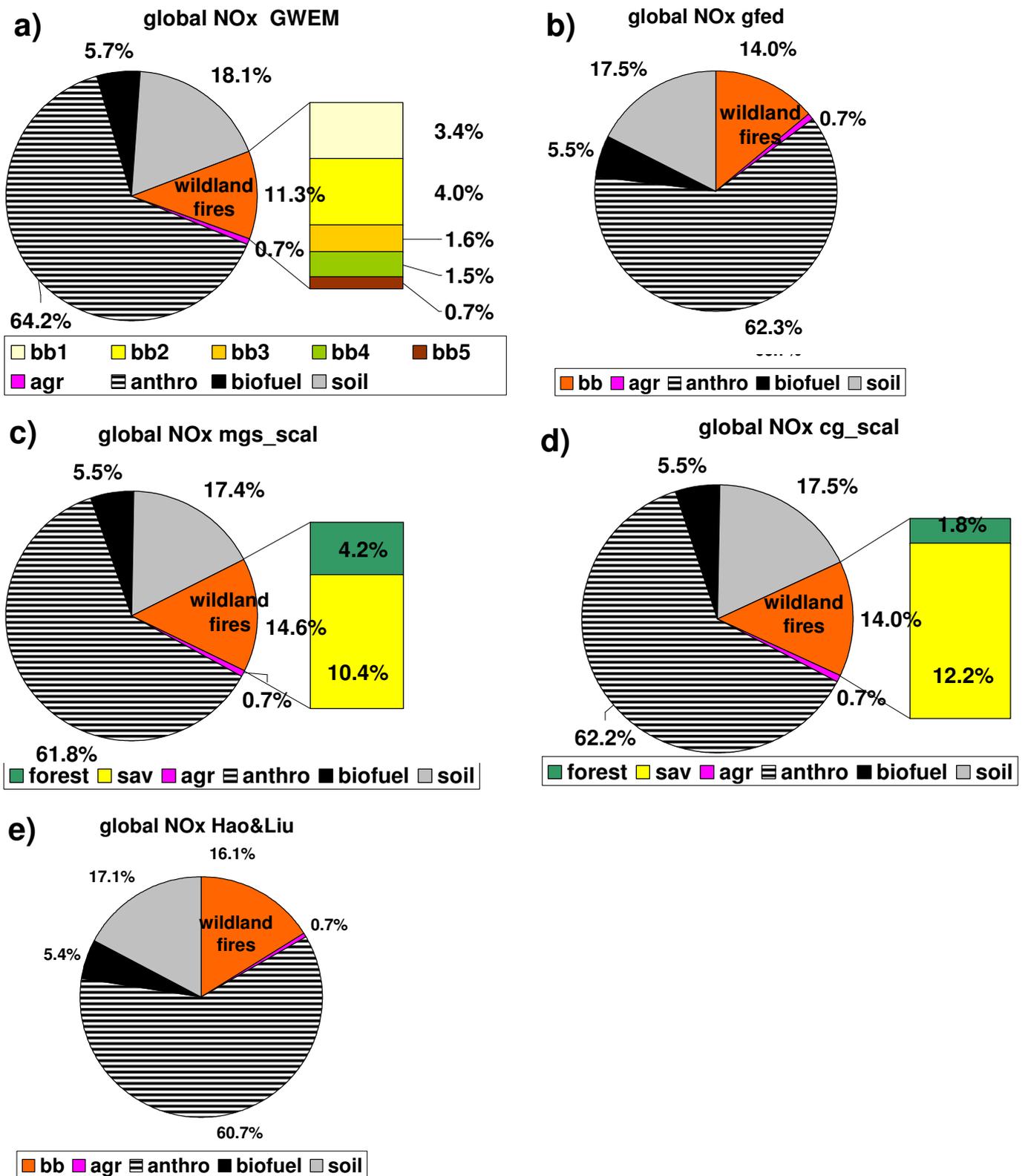**Figure 3.4:** Global relative contributions of all CO emission sources. a) with GWEM-1.3 wildland fire emissions sub-divided into savanna&grassland (bb1), wooded savanna (bb2), tropical forest (bb3), temperate forest (bb4), and boreal forest (bb5) fire emission contributions, b) the gfed fire emissions (bb), c) mgs_scal and d) cg_scal fire emissions, both sub-divided into contributions from forest and savanna (sav) fires, and e) the Hao&Liu climatological fire emissions

Figure 3.5: Global relative contributions of all NO$_x$ emission sources. a) with GWEM-1.3 wildland fire emissions sub-divided into savanna&grassland (bb1), wooded savanna (bb2), tropical forest (bb3), temperate forest (bb4), and boreal forest (bb5) fire emission contributions, b) the gfed fire emissions (bb), c) mgs_scal and d) cg_scal fire emissions, both sub-divided into contributions from forest and savanna (sav) fires, and d) the Hao&Liu climatological fire emissions

3.3.2 Emissions in Southern Africa

Savanna, and to a lesser extent forest fire emissions, play a significant role in Southern Africa. Figure 3.6 reflects that through all inventories the CO emission contribution from fires is over 50%, ranging from 50 – 72% between the different data sets. Again, the forest emission in cg_scal are substantially lower than in the GWEM-1.3 and the mgs_scal inventory. This suggests that the failure of the ATSR 312 K threshold discussed in 3.3.1 apparently also holds for tropical forest. Another explanation could be the application of a different landcover map with a lesser forest occurrence. The seasonality of the different wildland fire emission inventories in Southern Africa (Figure 3.7 bottom right) proceed quite differently. While the scaled Hao and Liu (1994) emissions (cg_scal and mgs_scal) have their peaks in August and October, the inventories that were built up from recent fire satellite data and vegetation models (GWEM and gfed), yield a large peak in June/July and a smaller one in September. As noted for the global scale, the cg_scal emissions are lower than the mgs_scal emissions, despite of their identical climatological emission source data.
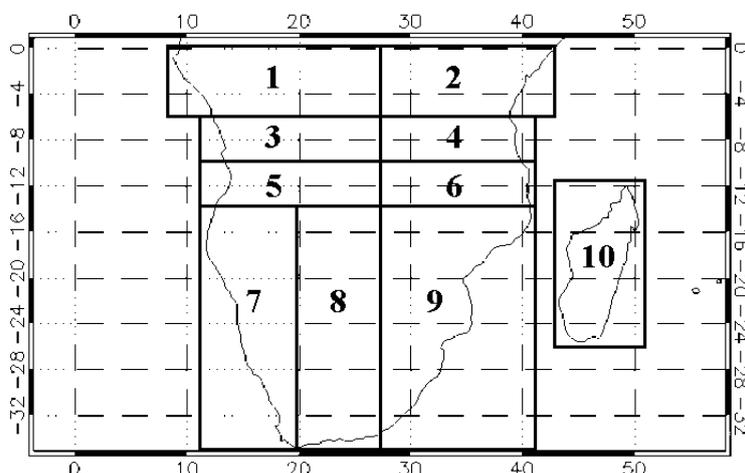
Figure 3.8: Ten Southern African subregions

The Southern African region has been further sub-divided to allow a more detailed analysis of the behavior in different subregions (Figure 3.8): the emission source distribution is quite differently shaped in those ten subregions, as can be seen in Figure 3.9. The lowest continental CO relative share by wildland fire emissions is 40% in the north eastern-most subregion 2 (over southern Kenya and northern Tanzania) and mainly covered by savanna and grasslands vegetation type. The highest relative contributors are subregions 3 and 5 with 92% and 89% of the CO respectively, being a result of fires in predominantly wooded savanna ecosystems. These regions cover the south of the Democratic Republic of Congo and Angola with large areas of open and closed deciduous tropical forest. Also in total numbers, the highest share from wildland fires originates from these regions, emitting 27 Tg CO and 24 Tg CO annually, according to GWEM-1.3. In Figure 3.10, 85% of the CO is emitted in June and July in the Southern African subregion 3 and 88% of the CO emissions in subregion 5 are released from May to July (strong peak in June). In general, the Hao and Liu (1994) emissions disagree strongly in seasonality, especially for the equator-near regions. The cg_scal and mgs_scal emissions mainly agree in seasonality but disagree in magnitude for most regions, for reasons already explained above. Systematically, GWEM and gfed yield earlier peaks than the other inventories for all Southern African subregions.

3.3.3 Other Regions

There is reasonable agreement between GWEM and the gfed inventory for Northern Africa. All inventories show a similar pattern in this region (Figure 3.7), however there are differences of the magnitude in the northern hemispheric spring months. In December, there is a large difference in magnitude between the scaled climatological inventories on one side and the newly built gfed and GWEM inventories: the latter provide the double CO emissions in December.

In Southern America, CO emissions are underdetected by GWEM and may be overdetected by the old Hao&Liu and thus by the two scaled inventories mgs_scal and cg_scal. As discussed in Chapter 2, the gfed emissions may also overestimate in this area. All inventories agree on an increase in CO emissions between August and October (S-AM, Figure 3.7), which is in agreement with the South American burning season.

In Southern Asia (S-AS, Figure 3.7) all inventories show a spring CO peak between February and May. GWEM and the gfed yield highest CO emissions, all other inventories are about 1/3 lower. Later in the year the inventories show another peak in fall that is most pronounced in the gfed inventory. All Australian emission inventories agree on a maximum of CO emissions from wildland fires in September. Only the cg_scal data presents a very elevated peak in October (OCE, Figure 3.7).

Remarkable for the North Central Asia region is a very high peak of GWEM CO emissions in May (NC-AS, Figure 3.7). All other inventories emit about 6 times less CO (see Figure 3.1) throughout the year 2000. The old Hao&Liu inventory is also very low in this area and all other 3 inventories rely on the same ATSR nighttime fire count data that strongly underdetects fires in this region. An additional explanation may be that fuel loads in GWEM-1.3 are considerably higher in some ecosystems compared to published literature, as discussed in Chapter 2.
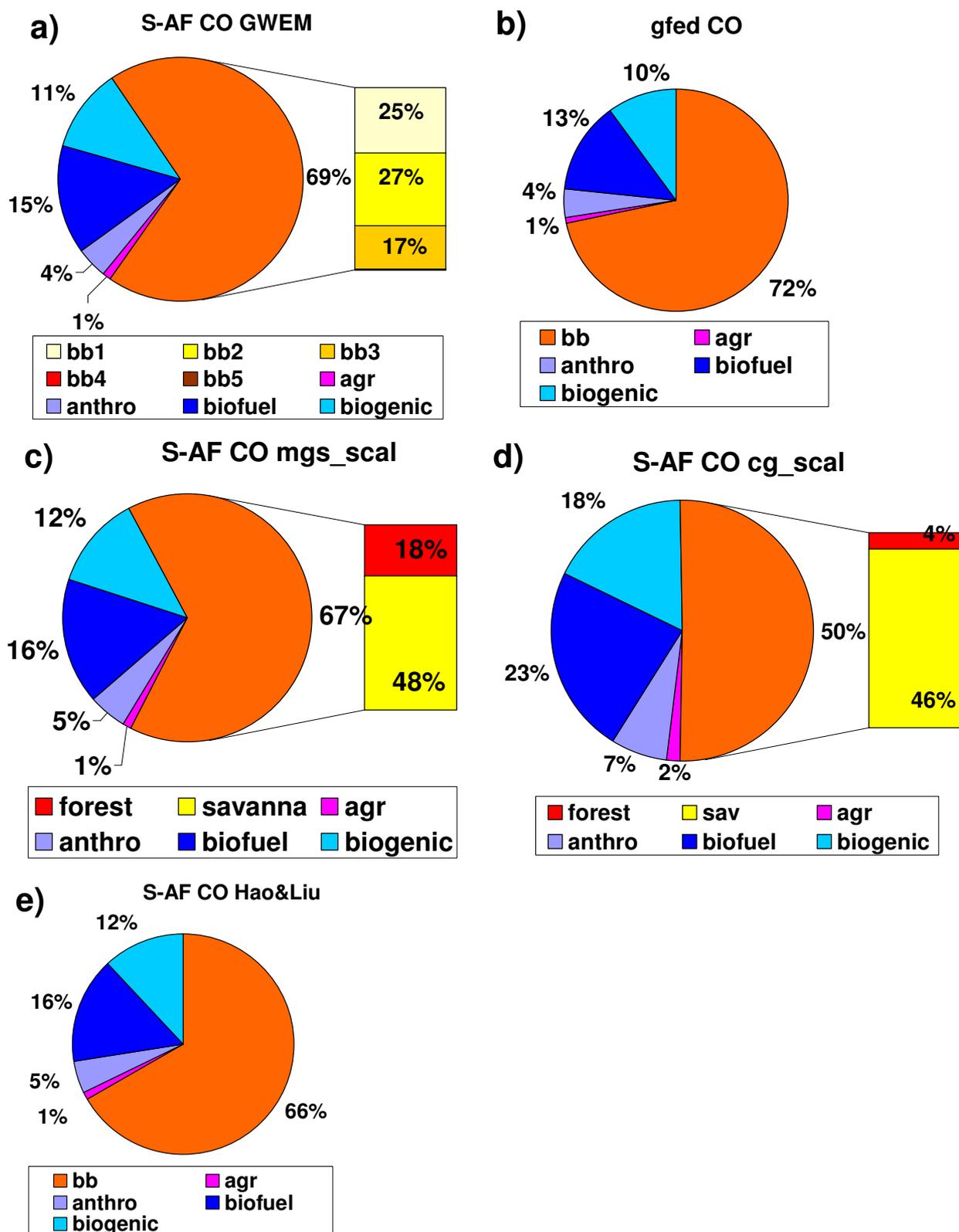
Figure 3.6: Southern African relative contributions of all CO emission sources. a) with GWEM-1.3 wildland fire emissions sub-divided into savanna&grassland (bb1), wooded savanna (bb2), and tropical forest (bb3) fire emission contributions, b) the gfed fire emissions (bb), c) mgs_scal and d) the cg_scal fire emissions, both sub-divided into contributions from forest and savanna (sav) fires, and e) the Hao&Liu climatological fire emissions (also bb)
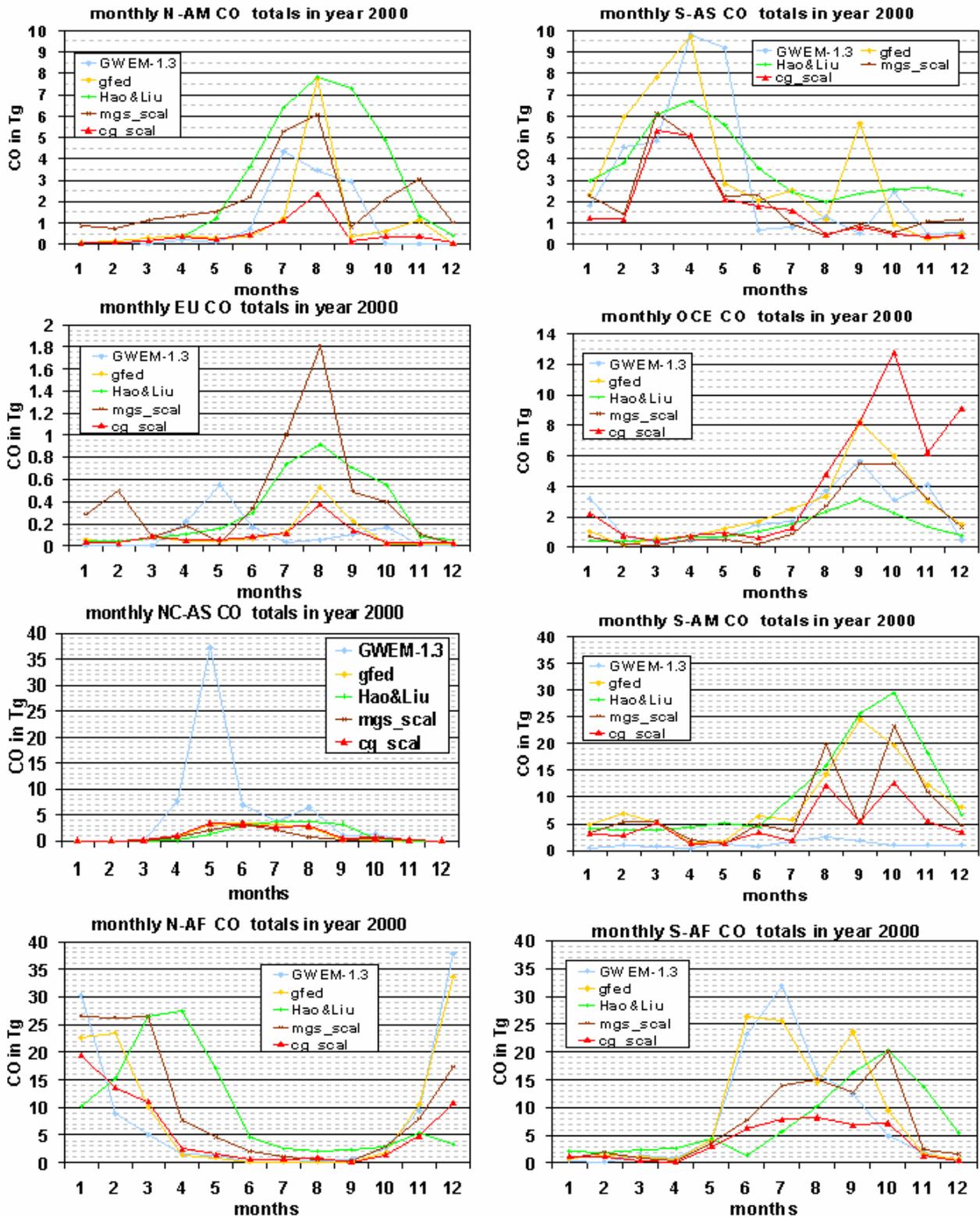
Figure 3.7: Regional seasonality of CO emissions from all five wildland fire emissions inventories in eight regions (from top left to bottom right): North America (N-AM), Southern Asia (S-AS), European Union (EU), Oceania (OCE), North Central Asia (NC-AS), South America (S-AM), Northern Africa (N-AF), and Southern Africa (S-AF). These regions are further specified in Table 2.1 and Figure 2.1 of Chapter 2
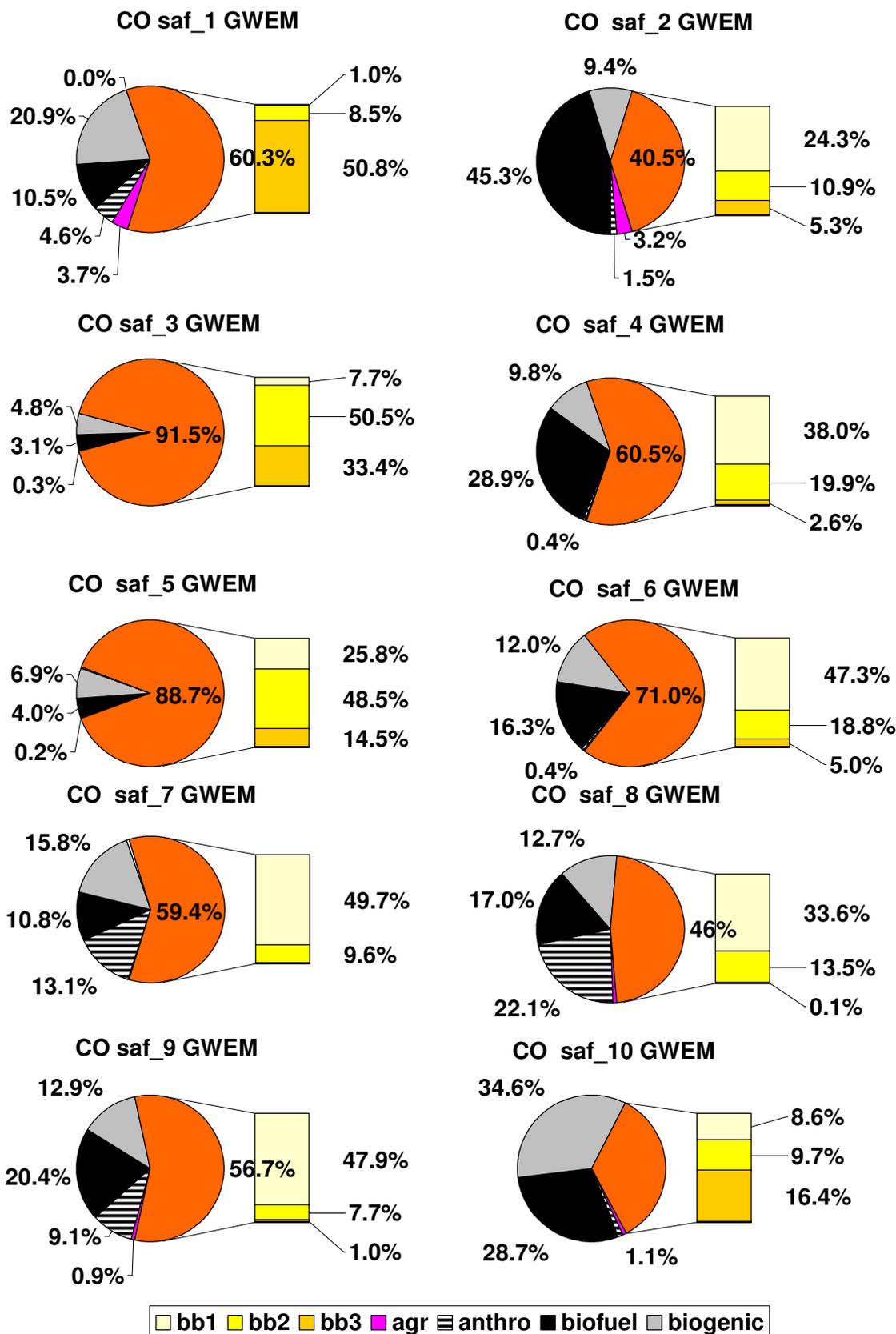
Figure 3.9: Sub-division of Southern African relative contributions of all CO emission sources with GWEM-1.3 wildland fire emissions sub-divided into savanna&grassland (bb1), wooded savanna (bb2), and tropical forest (bb3) fire emission contributions. Region numbers are according to map in Figure 3.8
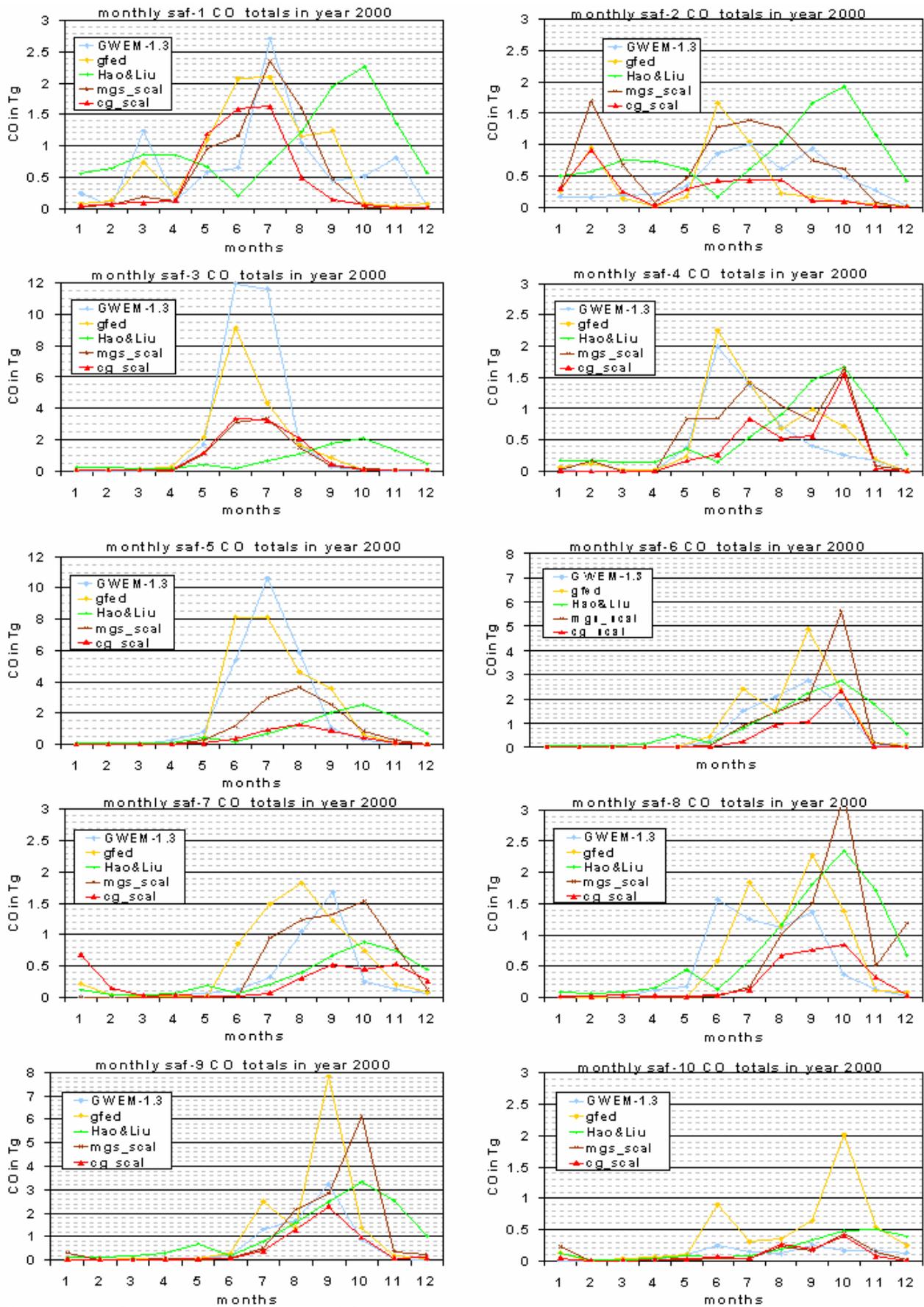
Figure 3.10: Regional seasonality of CO emissions from all five wildland fire emissions inventories in the Southern African subregions. The regions saf-1-10 are specified in Figure 3.8

4 Impact of Wildland Fire Emission Modeling onTropospheric Carbon Monoxide and Ozone

The five wildland fire emission data sets described in Chapter 3 were compared in a year 2000 sensitivity study with MOZART-2, the global Model of OZone And Related Tracers, version 2 (Horowitz et al., 2003). Two of these five inventories were calculated by new global bottom-up emission models. One of the models is the Global Wildland Fire Emission Model GWEM, developed at the Max Planck Institute for Meteorology in Hamburg, presented in Chapter 2 of this work and published in Hoelzemann et al. (2004), the other is the Global Fire Emission Database GFED, published in Van der Werf et al. (2003). The other inventories are based on the climatological fire emissions inventory used in previous MOZART studies by Hao and Liu (1994), and Müller (1992). Two approaches are based on this climatological inventory but rescaled with a global active fire satellite product (ATSR - World Fire Atlas of the European Space Agency). This scaling provided an inter-annual variability and a new seasonality of the climatological fire emission data set by redistributing the emissions in time and space. Table 4.1 lists the different inventories and their shortcuts for further use in this chapter:

Name	Description	References
GWEM-1.3	Global Wildland Fire Emission Model, Max Planck Institute for Meteorology in Hamburg	Hoelzemann et al. (2004), Version 1.3; fully described in Chapter 2 of this thesis
gfed	Global Fire Emission Database (GFED)	Van der Werf et al. (2003)
hao&liu	Climatological emissions used in former MOZART studies	Hao and Liu (1994) and Müller (1992)
mgs_scal	Scaled climatological emissions with a global active fire satellite product, (ATSR - World Fire Atlas of the European Space Agency)	Schultz (2002)
cg_scal	Scaled climatological emissions with a global active fire satellite product, (ATSR – World Fire Atlas of the European Space Agency)	C. Granier and J.-F. Lamarque, personal communication, 2004

Table 4.1: Overview of different fire emission inventories used in MOZART

The different wildland fire emission inventories were merged with other emission sources for the year 2000 from the POET database (Precursors of Ozone and their Effects in the Troposphere, European Project, NO EVK2-1999-00011, project report by Olivier et al. (2003)).

The main objectives for this modeling work are, (i) to determine which fire emission inventory yields best results, (ii) to show, where model performance is improved by using inventories based on satellite observations of active fires or burned area, (iii) to show, where model deficiencies persist regardless of the choice of the emission inventories, (iv) to assess the importance of choosing adequate fire emissions in global chemistry transport modeling, and (v) to highlight the differences in impact of new bottom-up inventories versus fire count scaled climatological inventories. This study also contributes to the evaluation of recent satellite fire products and the way these were used in the different inventories. Large differences between such products were found e.g. by Boschetti et al. (2004), and it remains to be seen if these discrepancies are also reflected in trace gas concentrations resulting from fire emissions based on these data sets.
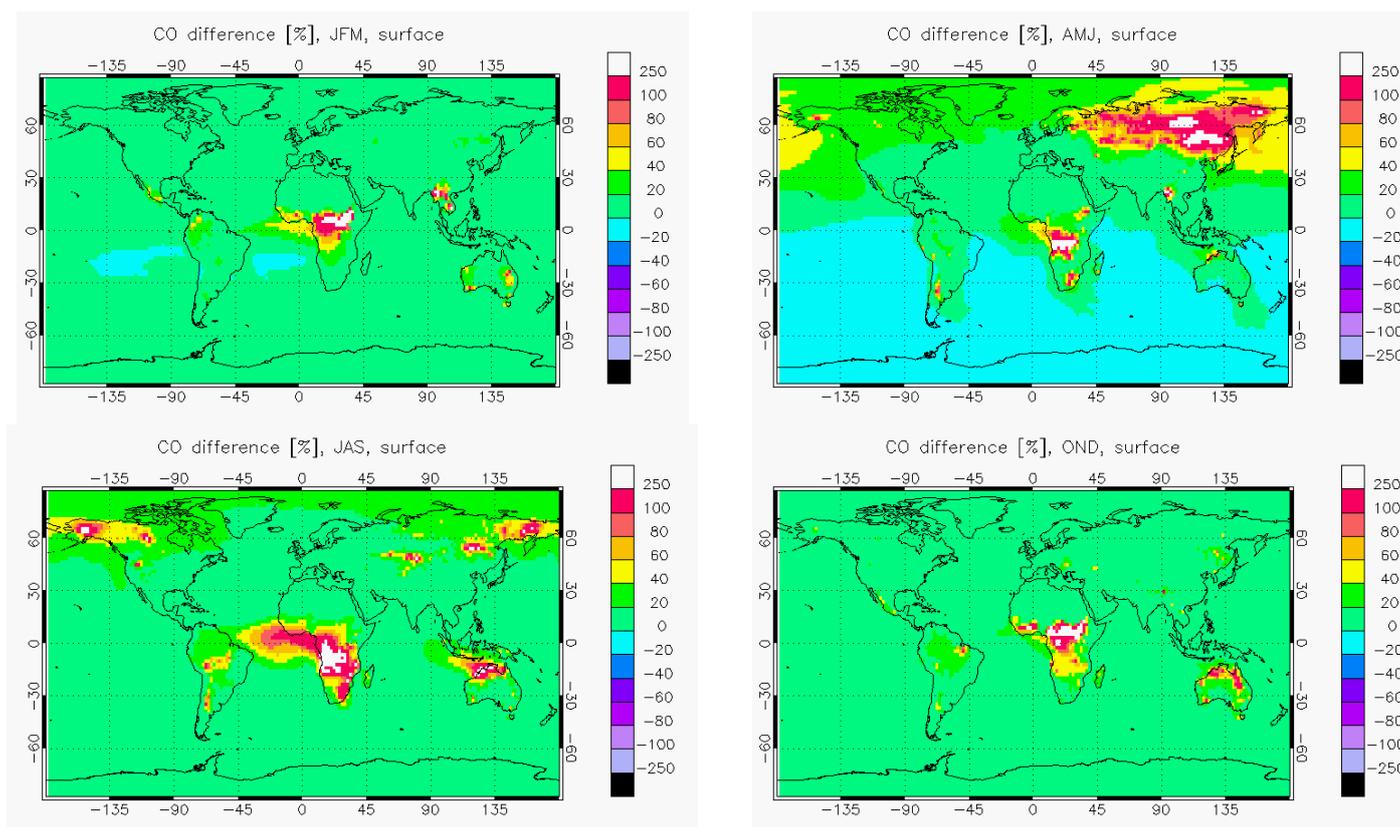
Figure 4.1: Difference plot in percentage of seasonal surface CO concentrations in MOZART-2 resulting exclusively from biomass burning (base-run A minus run D, see Table 4.2)

In the following, a brief description of the model and set-up of the simulations are given. Then, the model simulations are evaluated with CO satellite data from the Terra/MOPITT instrument (Terra Measurement Of Pollution In The Troposphere) (http://www. eos.ucar.edu/mopitt) and with the NOAA Climate and Monitoring Diagnostic Laboratory (CMDL) surface CO measurements (http://www.cmdl.noaa.gov). Effects on the ozone distribution are analysed with ozone sounding data from SHADOZ (Southern Hemisphere ADditional OZonesondes) and with MOZAIC data (Measurement of Ozone And Water Vapor by Airbus In-Service Aircraft).

According to IPCC (2001), the tropospheric ozone burden is currently about 370 Tg O_3, which corresponds to a mean abundance of about 50 ppbv. The ozone sources are photochemical production associated to pollution precursors mainly from biomass burning, urban plumes, aircraft corridors and convective outflows and the stratospheric influx of ozone loaded air that is around 475 Tg O_3/yr (IPCC, 2001). The main sinks are associated with photochemical reaction with other species ($HO_2 + O_3$) and photodissociation as well as deposition related to vegetation. Uncertainties of these source and sink terms are large and can therefore not be globally well quantified in global CTM's (IPCC, 2001).

CO is directly emitted by fires (~40% of global direct emissions (IPCC, 2001)) and in some regions fires are the main contributing factor for high CO abundances during the fire season. The lifetime of CO is in the order of a few months, which allows this species to be transported over long-range distances. Generally, fire emissions remain within the planetary boundary layer or are vertically lifted to higher levels by convection downwind of the emission source. Some fires however, burn very intensely and trigger a strong convection (e.g. Folkins et al., 1997; Andreae et al., 2001; Fromm and Servranckx, 2003). In combination with favorable meteorological conditions, these fire emissions can then be transported vertically into regimes with stronger horizontal wind, thus allowing for intercontinental transport (e.g. Fromm and Servranckx, 2003 or Andreae et al., 2001). The

strength of pyroconvection is of course highly dependent on fire temperature and size development (which in turn are dependent on fuel composition and moisture) and local meteorological patterns (stability of horizontal air layers and synoptic scale patterns).

In the presence of NO_x, which is also emitted by fires (10-18% of global direct emissions (WMO, 1999)), CO but also methane (CH_4) and other hydrocarbons (NMHC) are converted into ozone by oxidation with OH (hydroxyl radical) in a photochemically active troposphere. Since ozone also has a lifetime in the order of some weeks, it can either be produced close to the fire source and then be transported into other regions of the globe, or it is produced in remote regions were the short-lived NO_x is present from other sources (e.g. lightning, aircrafts, or energy use).

To obtain an overview about the major global biomass burning regions, Figure 4.1 presents seasonal surface CO concentrations resulting exclusively from wildland fires. Figure 4.1 is a difference plot of a MOZART run using GWEM-1.3 fire emissions minus a MOZART run excluding all fire emissions. Fires have an important share on CO concentrations over the African continent (40% to over 250% more CO than without fires), North Central Asia (40% to over 250%), boreal North America (20% to 100%), Northern Australia (20% -100%) and South America (20% to 80%). South America yields relatively low fire emissions in the year 2000 and is additionally underestimated by the GWEM-1.3 inventory, as mentioned earlier in Chapter 2. The slightly negative CO concentrations (-2 parts per billion by volume (ppbv) at maximum)in the southern hemisphere of the difference plots in Figure 4.1 are a result of a chemistry feedback in the model: the fires in run A produce OH that leads to an enhanced CH_4 depletion in the fire emission outflow regions. Therefore, less CH_4 is transported to remote regions in the southern hemisphere, which in turn leads to slightly lower CO in those regions (CO is mainly produced by CH_4 in remote areas).

Generally, and as will be demonstrated later in section 4.5, the overall amplitude of the CO seasonal cycle stemming exclusively from fires is much higher than the amplitude of CO from a "no-fire" MOZART run. Sometimes differences can be in the same order as the discrepancies resulting from the use of different inventories.

4.1 MOZART-2: Model Description and Setup of Experiment

The global Model of OZone And Related Tracers, version 2 (MOZART-2) is described in detail by Horowitz et al. (2003). The original model was developed at the National Center of Atmospheric Research (NCAR) in Boulder, USA (Brasseur et al., 1998). Current versions are jointly developed at NCAR, the General Fluid Dynamics Laboratory (GFDL) in Princeton, New Jersey, USA, and the Max Planck Institute for Meteorology (MPI-M) in Hamburg, Germany. MOZART is driven by 6-hourly meteorological fields and it contains a detailed chemistry scheme that is optimized on the global simulation of ozone and its precursors. The MOZART chemical scheme is solved for 63 species and 170 chemical reactions for the O_3-NO_x-CO-CH_4-NMVOC system. The solver for the chemical scheme is an Euler-backward method with Newton Raphson iteration with a time step of 15 minutes. The advection of tracers is calculated using the semi Lagrangian advection scheme of Lin and Rood (1996). The horizontal spectral resolution is T63, which corresponds to approximately 1.9° x 1.9°. The model contains 47 vertical levels, with the uppermost located at 10 hPa. NO_x produced by lightning is parameterized depending on the location of convective clouds as diagnosed by the Zhang et al. (1995) scheme in MOZART. The lightning flash frequency calculation follows Price and Rind (1993).

In this study MOZART version ham2.4.2 of the Max Planck Institute for Meteorology was applied, which contains an updated dry deposition velocity table (J.-F. Lamarque pers. comm., 2002). In the following, this version will be referred to as MOZART. In contrast to the standard configuration of Horowitz et al. (2003), the MOZART model in this study was

MOZART run	Fire Inventory	Modifications
A	GWEM-1.3	-
B	dto.	global lightning emissions are set to 0
C	dto.	lightning emissions in southern hemispheric Africa are set to 0
D	none	global wildland fire emissions are set to 0
E	as in A	wildland fire emissions in southern hemispheric Africa are set to 0
G	cg_scal (ATSR scaled)	-
H	mgs_scal (ATSR scaled)	-
J	gfed	-
K	climatological Hao&Liu	-

Table 4.2: MOZART run descriptions and abbreviations

run with meteorological data from the European Centre of Medium Range Weather Forecast (ECMWF), using the operational analysis data of the year 2000. The simulation started on January 1999, with a spin-up period of one year and was run until January 1, 2001.

The wildland fire emission inventories of the species CO, C_2H_4, C_2H_6, C_3H_6, C_3H_8, other NMHC (non-methane hydrocarbons), NO_x, and acetone are taken from the five emission inventories listed above in Table 4.1. These emissions explicitly exclude those from agricultural burning activities. Fossil fuel combustion, agricultural waste burning, biogenic emissions from vegetation, emissions from soils, and oceanic emissions of the above named species, as well as all emissions for the chemical compounds CH_2O, isoprene and terpenes, are taken from the POET (Precursors of Ozone and their Effects in the Troposphere, European Project, contract EVK2-1999-00011) data base for the year 2000 (Olivier et al., 2003). Emissions of H_2 and aircraft emissions were used from the MOZART standard emission pool, as described in Horowitz et al. (2003).

Ten MOZART runs were performed for the year 2000. These runs will from here on be referred to as simulations A-K, as defined in Table 4.2. Five simulations using the five different fire emission inventories as described in Chapter 3 (MOZART runs A, G, H, J, and K), can be regarded as base runs, to allow for a comparison and evaluation of GWEM-1.3 emissions with others. In addition to these simulations, a number of sensitivity runs were performed to test the effect of interplay between fire and lightning emissions. A run with wildland fire emissions set globally to 0 (zero) was set up (run D). The same was done in MOZART run B but for lightning emissions. Further, wildland fire (run E) and lightning (run C) emissions were set to 0 (zero) in southern hemispheric Africa, to enable an investigation of emissions and outflow specifically for that region. At last, lightning emissions in Indonesia were doubled (run F) to determine, to what extent NO_x emissions from this area contribute to the chemical environment over Africa. As no significant impacts on ozone, NOx, or CO was found in this simulation, it will not be further considered in the following.

4.2 Evaluation of Simulated CO Concentrations

According to the NOAA CMDL surface measurements (see http://www.cmdl.noaa.gov/ccgg) of several years, the seasonality of CO is anticorrelated in the northern and southern hemisphere (out of phase by six months) (Novelli et al. 1998). CO abundances are driven by distribution and seasonality of their sources and sinks. Main primary sources are emissions from fossil fuel combustion and biomass burning. Secondary sources are oxidation of methane (CH_4) and non methane hydrocarbons (NMHC's). The only relevant sink of CO is oxidation with OH (OH + CO $\rightarrow$ H + CO2) (Penkett et al., 2003). Deposition at the surface accounts for about 10% of the total loss. CO maxima in the northern hemisphere are found in winter, owing to wide-spread use of wood and coal for cooking and heating, where incomplete combustion leads to CO emissions. The reduced solar radiation in the winter troposphere and reduced vertical mixing processes in the planetary boundary layer in winter lead to a reduced availability of OH and thus let CO concentrations accumulate.

Calculated MOZART carbon monoxide concentrations of base-run A (see Table 4.2) are compared to other MOZART simulations published elsewhere, as well as to MOPITT (Measurement Of The Pollution in The Troposphere) satellite CO data and CO ground observations from the NOAA Climate Monitoring and Diagnostics Laboratory (CMDL) flask measurement network. Figure 4.2 shows seasonal mean CO concentrations of base-run A. On the left hand side (from top to bottom) are surface CO concentrations for January to March (JFM), April to June (AMJ), July to September (JAS), and from October to December (OND). On the right hand side are corresponding zonal mean vertical cross sections.
The different biomass burning seasonalities and fossil fuel combustion dominated areas can well be observed in the CO surface plots. Northern Africa CO concentrations from biomass burning peak in December and January (see JFM and OND plots), Southern African biomass burning starts in May and peaks in July (see AMJ and JAS figures). The Eurasia burning season occurs in northern hemispheric spring (March to June).

### 4.2.1 Comparison of Modeled CO Concentrations with Measurements

MOPITT – Carbon Monoxide Satellite Data
The MOPITT (Measurement Of The Pollution in The Troposphere) instrument (Drummond, 1992, Pan et al., 1998, and Edwards et al. 1999) aboard the NASA EOS TERRA satellite retrieves vertically resolved column densities of carbon monoxide (CO) in the troposphere since March 2000. MOPITT data are reported at seven levels (surface, 850, 700, 500, 350, 250, and 150 hPa) for global clear sky measurements. Data coverage is global (approximately every 3 days) at a resolution of 22 km x 22 km. A variety of comparisons to validation CO data showed an average absolute bias of 4.2 $\pm$ 14.5 ppbv CO for the 700 hPa level used in this study (Emmons et al., 2004). Further information on validation aspects of MOPITT CO and evaluation of its underlying radiances can be found in Emmons et al. (2004) and Deeter et al. (2004).
In this study, MOPITT level 2, phase 1 (Emmons et al., 2004) monthly averaged CO data at 700 hPa are used from March to December 2000 to evaluate CO concentrations as simulated by MOZART. The MOPITT CO mixing ratios at a certain level reflect the vertical resolution of the measurement as defined by the reported averaging kernels. These averaging kernels are applied to the raw MOPITT data to account for the vertical resolution of retrievals and correlations between retrieval levels (Emmons et al., 2004). The MOPITT CO profiles and averaging kernels are binned onto the MOZART horizontal grid (T63 i.e. approx. 1.9° x 1.9°). High latitude data of MOPITT should be used with caution because of its high a priori profile component (http://www.eos.ucar.edu/mopitt/data). Therefore, only MOPITT data from 65°S to 65°N is used in this study.
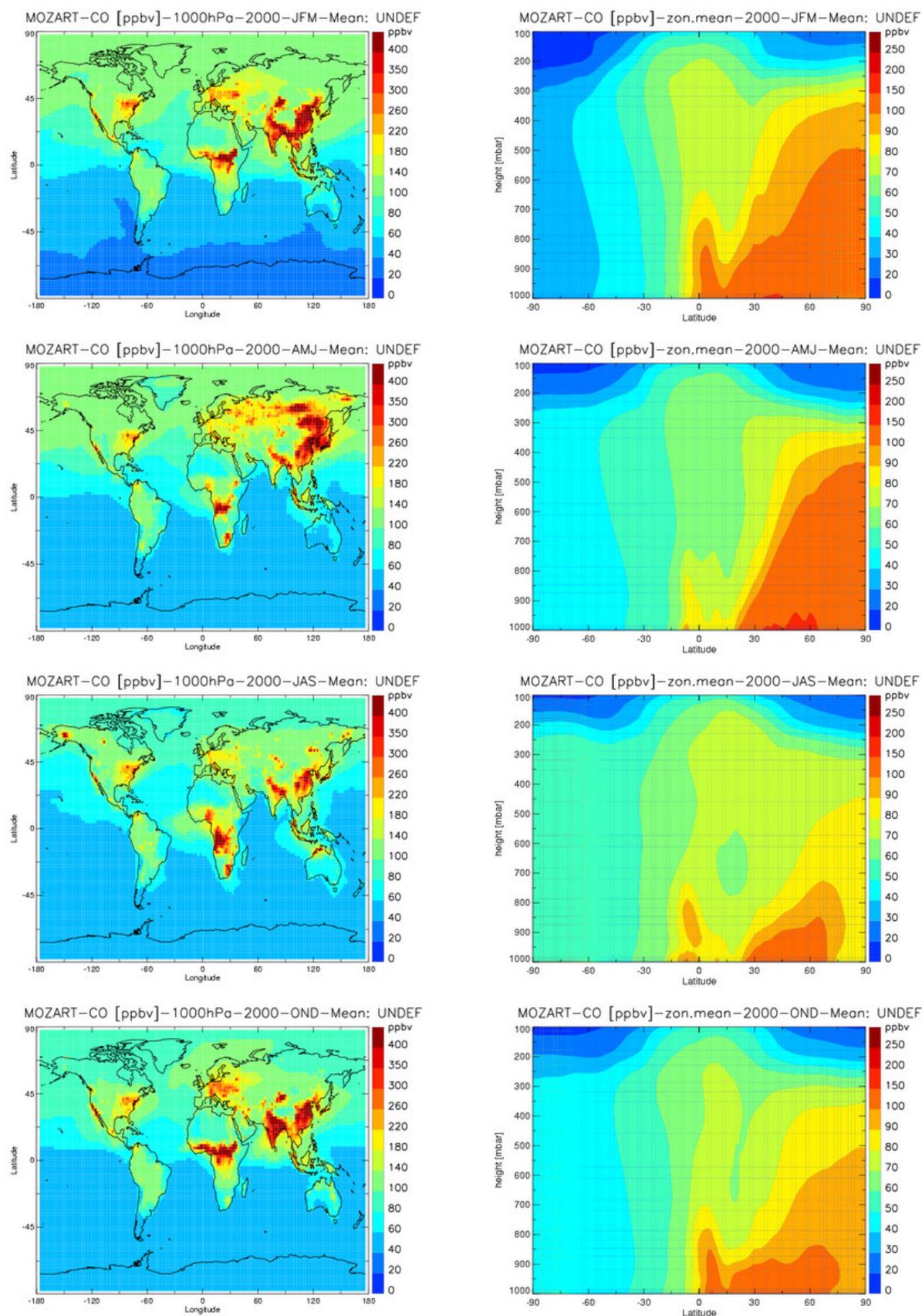
Figure 4.2: Global MOZART-2 seasonal carbon monoxide (CO) in ppbv of the year 2000. Results of run A, using GWEM-1.3 fire emissions. On the left hand side are seasonal CO concentrations at surface level, on the right hand side seasonal zonal means (different scale!)
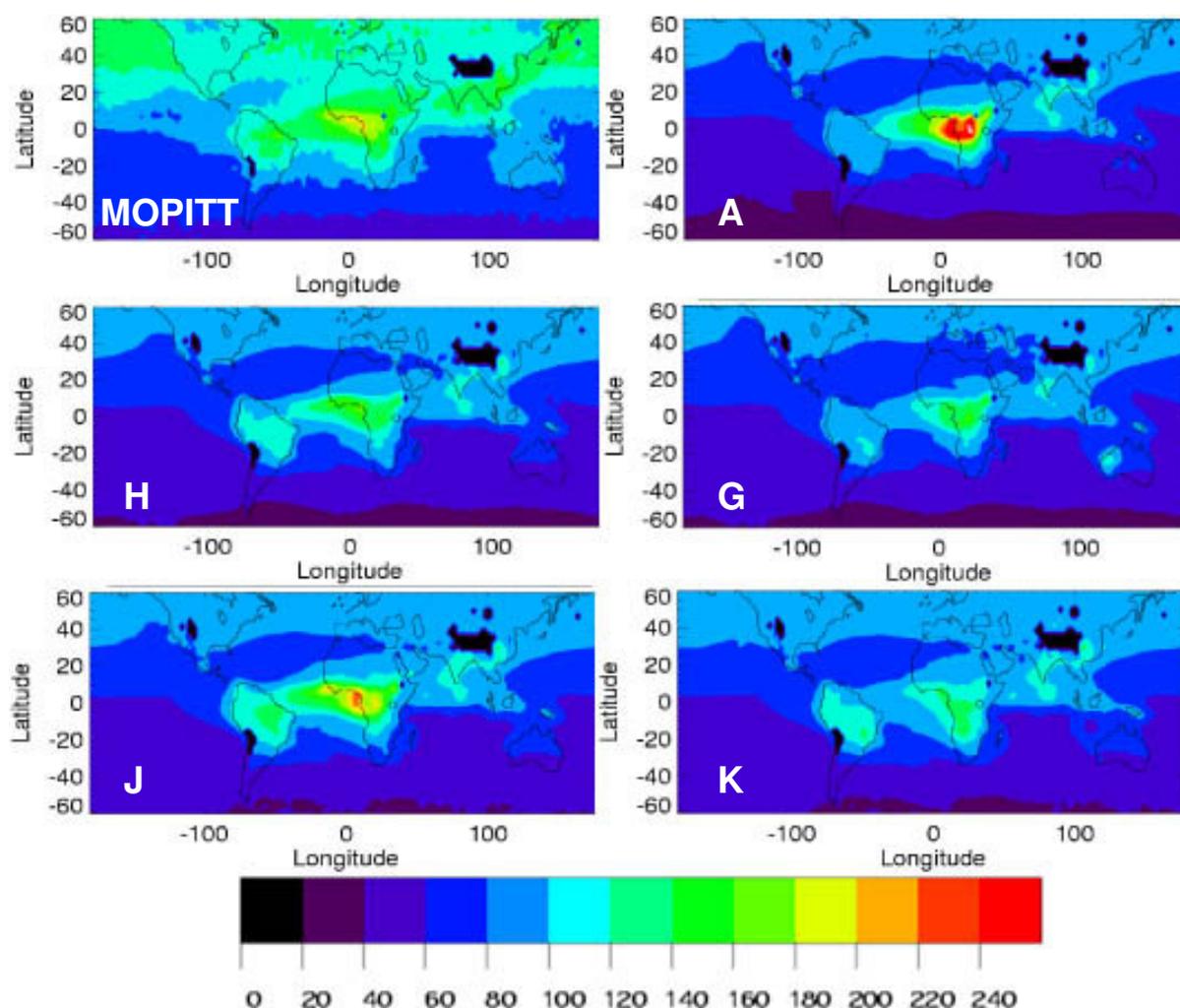
Figure 4.3: December 2000 monthly MOPITT CO concentrations (upper left panel) in ppbv at 700 hPa, compared to corresponding monthly mean CO concentrations of MOZART runs A,H,G,J, and K (see Table 4.2 for specification of different MOZART runs).

Figure 4.3 presents global monthly mean MOPITT CO observations in ppbv for the month of December 2000. MOZART runs A, J, H, G, and K with different wildland fire emission inventories are shown in comparison to MOPITT observations.

Overall, low CO concentrations in the northern hemisphere can be noted for all months and in all MOZART runs (Figure 4.3). A detailed evaluation of the differences between the various simulations is presented in section 4.5. Base-run A reproduces the enhanced CO observed by MOPITT over Africa resulting from fires, but seems to overestimate emissions for June and December. South American MOZART CO from deforestation fires is 40 - 60 ppbv lower than what is seen by MOPITT in the same area. In this area fires play a dominant role, while further south in Asia, there is a strong interplay with CO from fossil fuel combustion.
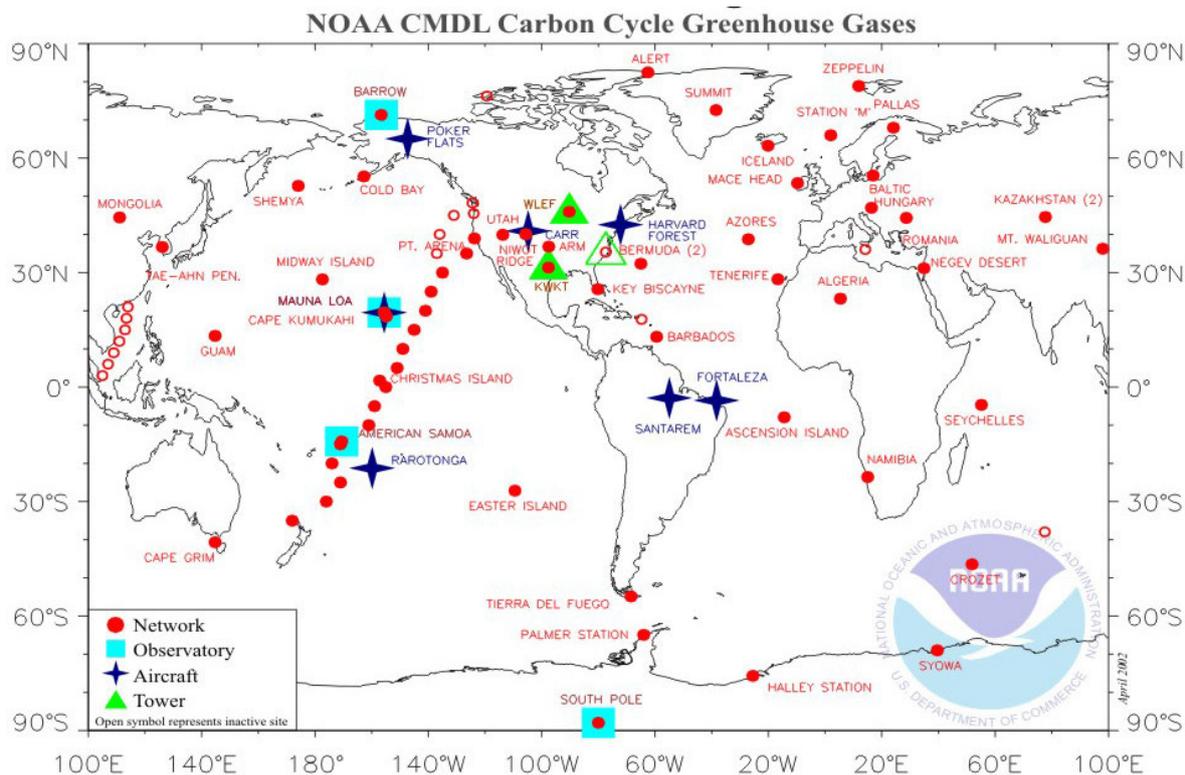
Figure 4.4: CMDL carbon monoxide measurement network, stations with measurements for the year 2000 are listed in Table C1.

CMDL Carbon Monoxide Surface Measurements

Atmospheric carbon monoxide ground observations from the NOAA Climate Monitoring and Diagnostics Laboratory (CMDL) co-operative sampling network (Novelli et al., 1992; Novelli et al., 1998; and Novelli et al., 2003, data available at: http://www.cmdl.noaa.gov) were compared to simulated MOZART carbon monoxide concentrations. The geographical distribution of CMDL measurement sites is shown in Figure 4.4. The subset of stations with observations in the year 2000 is listed in Table C1 in Appendix C.

Figures 4.5 presents an example of monthly mean seasonalities of CMDL CO measurements compared to MOZART simulations. Two panels are shown: in the upper panel the CO variability is shown for all available years of CO measurements. The lower panel presents the measured CO seasonality of the year 2000 as red dots and corresponding MOZART simulations (runs A, J, H, G, and K) as solid lines. Black dots are the monthly mean concentrations of other years to provide a measure of variability.

More selected monthly mean seasonalities of CMDL CO measurements are shown in the regional discussion (section 4.5 (Figures 4.24ff). Generally, the MOZART simulations yield a low-bias in the northern hemisphere, as in the comparison to MOPITT. In high latitudes MOZART is about 20–50 ppbv lower than the CMDL observations, in mid latitudes the low-bias is 20–30 ppbv, and at low northern latitudes (subtropics) 10 – 30 ppbv. In the southern hemisphere however, there is an excellent agreement between simulated and observed CO concentrations.

Run A (red line) shows enhanced CO concentrations in northern hemispheric spring and early summer at northern mid- and high latitudes, which improves the MOZART performance at several stations for these months (e.g. Shemya Islands, Sary Taukum, and Ny-Alesund).
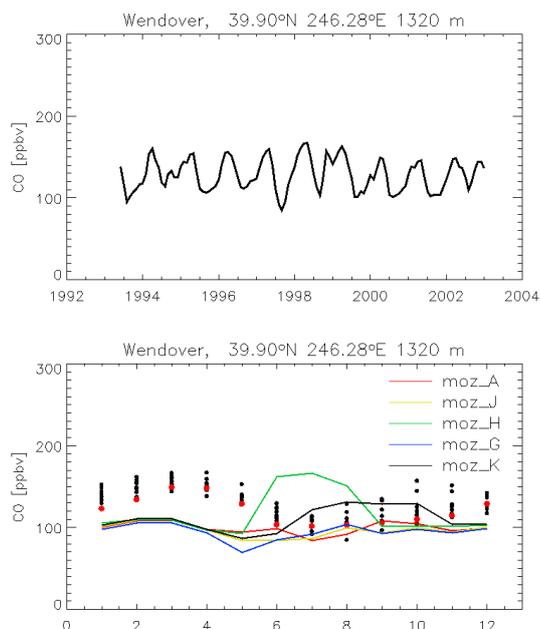
Figure 4.5: CMDL CO measurements in the year 2000 (red dots) and available other years (black spots) at Wendover, Utah, USA. Interannual variability is shown in the upper panel, year 2000 seasonality in the lower panel. The lower panel also shows MOZART-2 results for the main runs A, J, H, G, K (solid lines) as described in Table 4.2

4.2.2 Comparison of CO Concentrations with Other MOZART Experiments

The seasonal CO surface concentration features (Figure 4.2) in the northern hemispheric summer (JAS) are similar to those of Horowitz et al. (2003) and Brasseur et al. (2005), though about 50 ppbv or more (Africa) higher in their maxima. The same can be observed for African CO concentrations from January to March. From July to September, CO concentrations of base-run A are considerably lower over Southern America, compared to Horowitz et al. (2003). In comparison with the Brasseur et al. (2005) MOZART simulations, differences in this region are substantially lower.

General zonal mean features compare well with the ones found in Brasseur et al. (2005) for the year 2000. However, CO concentrations are generally lower by about 10 to 20 ppbv in northern hemispheric mid latitudes compared to both the Horowitz et al. (2003) and Brasseur et al. (2005) simulations. In northern hemispheric winter, typical values of run A are around 140 ppbv, while in summer concentrations are about 100 ppbv. Additionally, northern hemispheric background CO concentrations are generally lower by 20-30 ppbv in run A at surface and also still at 500 hPa.

This basic feature can be observed in all performed MOZART runs (A to K) of this series, which can both be verified in the difference plots discussed in section 4.5 and in seasonal surface and zonal mean figures in Appendix B. The observed low northern hemispheric winter CO concentrations can be traced back to low emissions in the residential fossil fuel inventory for Asia in the underlying POET emission data base (Olivier et al. 2003). This feature is also observed in other currently available emission inventories. Streets (pers. comm., 2003) concluded that East Asian emission factors for residential fossil fuel are highly uncertain and that emissions may be higher by a factor of 2 in reality. In fact, an experiment with emission data compiled in the framework of the European RETRO project (project number: EVK2-CT-2002-00170, http://retro.enes.org) shows that enhanced Asian residential fossil fuel emissions by a factor of 2 correct the monthly totals of the inventory in the northern hemispheric winter months. (Figure 4.6). The emission enhancement is in
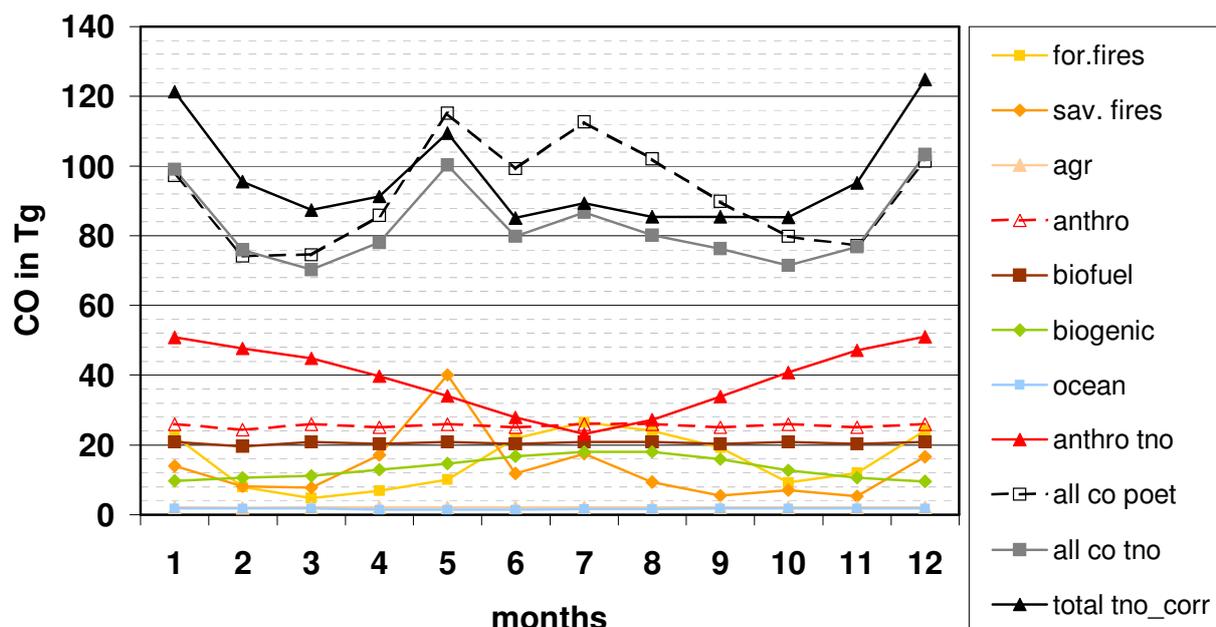
Figure 4.6: CO emission seasonality in the year 2000 from POET and RETRO emission data for individual sources and totals. Emission sources, as in order of the legend, are: forest fires, savanna fires, agricultural waste burning, anthropogenic, biofuel, and biogenic emissions, and emissions from the ocean. Those sources form a total shown as a black dashed line ("all co poet"). The grey line shows the total of CO emissions as used within the RETRO project from TNO ("all co tno"). The black line shows the correction of these emission totals, by enhancing Asian residential fossil fuel emissions by a factor of 2 ("total tno_corr")

the order of 20-30% by this correction for winter and between 1-10% for the summer months. Assuming a linear relationship, the use of enhanced Asian residential fossil fuel emissions in the MOZART model would correct the CO winter low bias in the northern hemisphere, without yielding much higher concentrations in the summer months. The comparisons between the MOZART runs and CMDL observations show that for boreal latitudes, a correction in the order of 40% would be needed for winter (Figures 4.7 and 4.10), while in lower northern latitudes the required winter correction is indeed in the order of 20-30%.

To investigate why low CO concentrations in the northern hemisphere are not so pronounced in Horowitz et al. (2003) and Brasseur et al. (2005), the lifetimes of CH_4 were compared. The CH_4 lifetime is an indicator of the OH abundance in the atmosphere, as CH_4 competes with CO concerning chemical reaction with the hydroxyl radical OH (see e.g. Penkett et al., 2003). Therefore, if the lifetime of CH_4 is shorter, this implies that more OH is in the atmosphere that will serve as a sink to CO and thus lead to lower CO concentrations. All MOZART simulations in this study yield an average CH_4 net lifetime of 7.8 years. Horowitz et al. (2003) state a CH_4 lifetime of 9.4 years in their MOZART version, with respect to the loss rate provoked by OH depletion only. The net lifetime (including all loss rates) is reported in the same order as the CH_4 lifetime reported by the 2001 Intergovernmental Panel on Climate Change (IPCC) report, and is 8.4 years. Brasseur et al. (2005) obtained a CH_4 net lifetime of 9.1 years in their MOZART study. In fact, this intercomparison explains the lower CO concentrations and its origins in present MOZART simulations as a result of its shorter CH_4 lifetime.

It should be noted that although CO concentrations are low in the present MOZART runs, simulations can still yield reasonable ozone concentrations. According to Prather et al. (2003) and Schultz et al. (2003) for example, the precursor species NO_x has a stronger impact on the ozone budget than CO.

## 4.3 Evaluation of Simulated Ozone Concentrations

Here, MOZART results from base-run A are presented for ozone and compared to other MOZART simulations in previous publications. Further, vertical profiles from ozone radio soundings of the Southern Hemisphere Additional Ozonesondes (SHADOZ) network and ozone aircraft measurements of the MOZAIC program (Measurement of Ozone and Water Vapor by Airbus In-Service Aircraft) are presented that will be used for intercomparison in the regional discussion of the model results (see section 4.5).

Global ozone concentrations of base-run A are shown at 850 hPa (Figure 4.7) to highlight ozone maxima resulting from biomass burning (for example over Africa). Ozone is not directly emitted by burning processes but produced by photochemical reaction of CO and NO_x. Maximum concentrations can occur several hundred kilometers downwind of pollution sources or in the free troposphere if convection or synoptic-scale processes lift ozone and its precursor species upwards. Generally, ozone concentrations above the boundary layer increase with height due to subsidence of upper tropospheric and lower stratospheric ozone-rich air masses and a longer lifetime of ozone in the upper troposphere (see zonal plots, Appendix B).

The general distribution of ozone maxima shown in Figure 4.7 are in good agreement with previous MOZART simulations. Background concentrations of base-run A are about 10 ppbv lower in the northern hemisphere than in Horowitz et al. (2003). This feature may be attributed to the low CO emissions from residential fossil fuel in Asia, as discussed in the
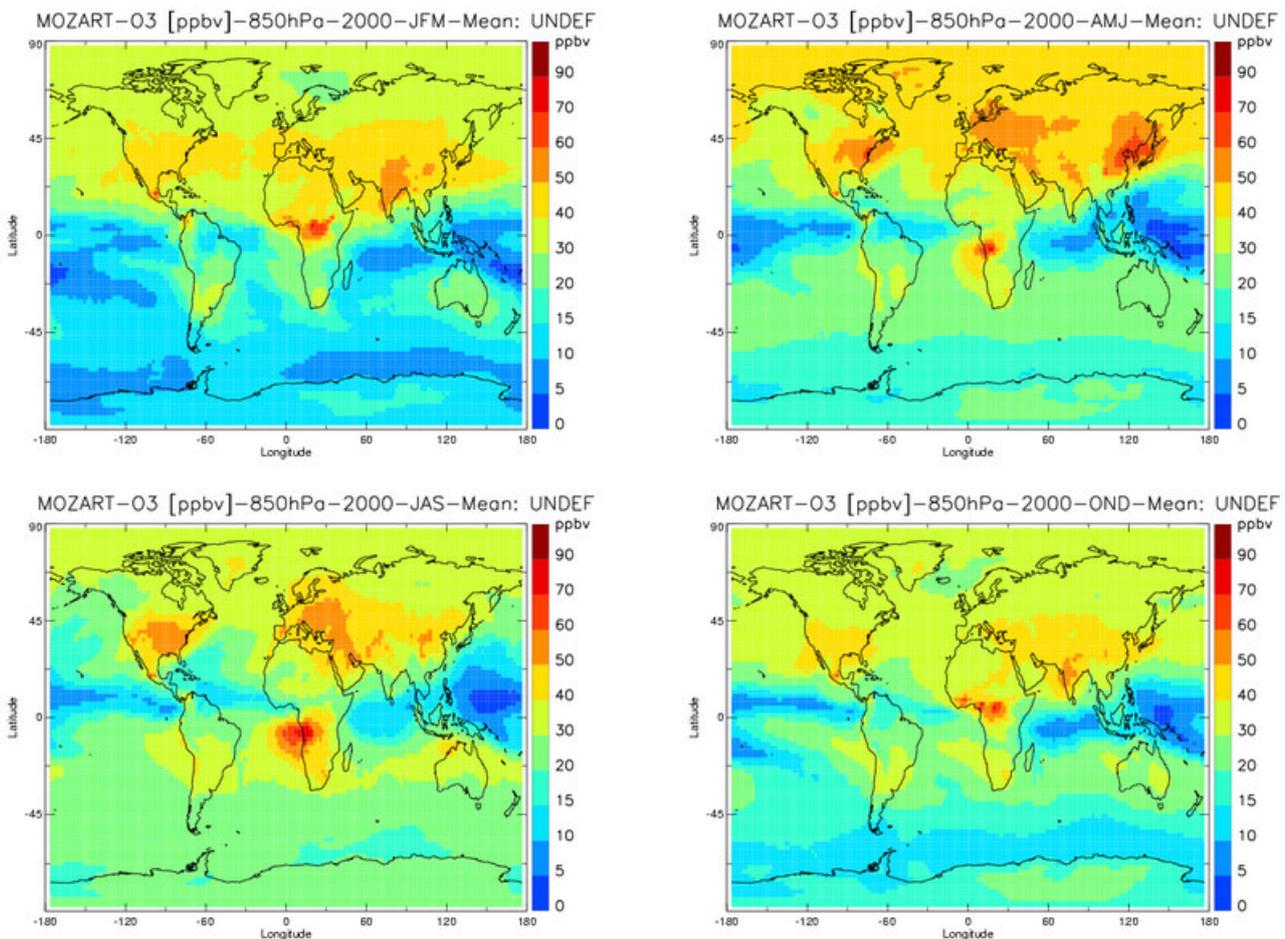
Figure 4.7: Global MOZART-2 seasonal ozone concentrations in ppbv at 850 hPa of the year 2000. Results of run A, using GWEM-1.3 fire emissions
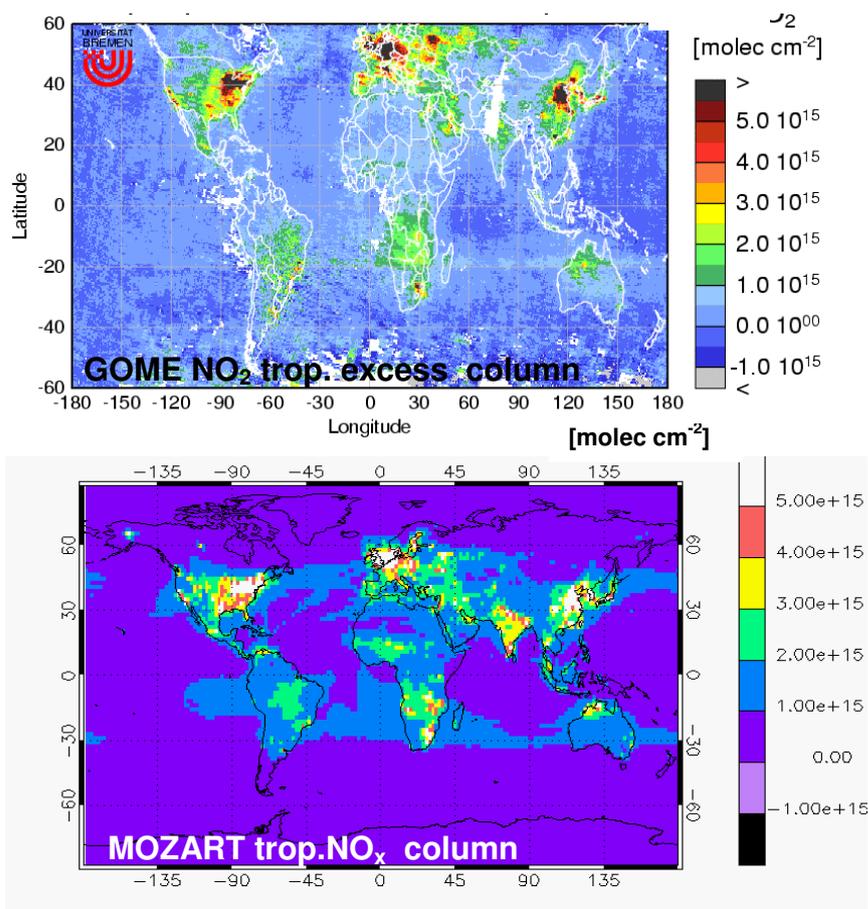
Figure 4.8: qualitative intercomparison of GOME NO_2 tropospheric excess column measurements (top) and modeled MOZART tropospheric NO_x column (bottom) in molecules/cm^2 for September 2000

previous section, but it might also be related to the use of different meteorological fields (M. Schultz, pers. comm., 2004) Also, the South Atlantic maximum in January is lower by about 10 ppbv, which may have its origin in the low-bias from missing fire emissions in South America, where fires occur north of the equator at this time of the year. Surface ozone concentrations in North America are 10 to 20 ppbv lower than in Brasseur et al. (2005), while zonal mean concentrations are in good agreement. Seasonal plots for various altitudes of all MOZART runs (A, J, G, H, and K) can be found in Appendix B.

In general, a clear impact from fires on ozone distribution and concentration can be observed from the patterns in Figure 4.7 over areas where fires play a predominant role.

A qualitative comparison of global satellite derived NO_2 measurements from GOME (the Global Ozone Monitoring Experiment aboard the second European Remote Sensing satellite (ERS-2 launched by the European Space Agency (ESA)) (Figure 4.8) show a good agreement with the ozone locations related to fires mainly in the southern hemisphere (Figure 4.7). Also the industrially related NO_2 concentrations in the northern hemisphere are well mirrored by the MOZART. Figure 4.8 also shows that the MOZART tropospheric NO_x column is well correlated with the GOME measurements, which is a prerequisite to successful ozone modeling.

SHADOZ Ozone Radio Soundings
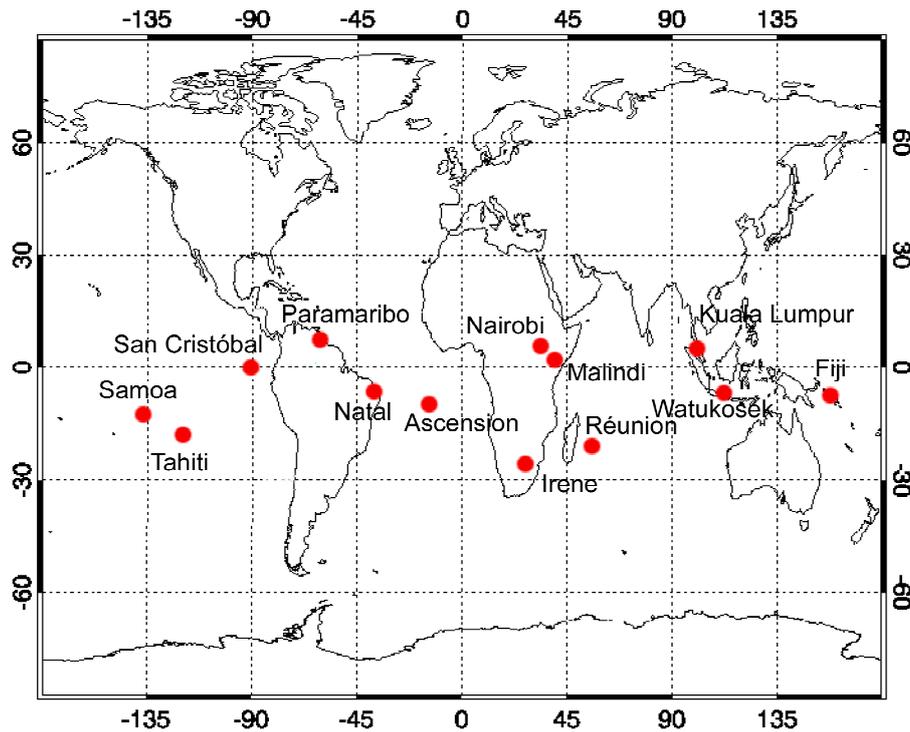
Figure 4.9: SHADOZ ozone sounding locations with data of the year 2000. For detailed information see Table C2 in Appendix C
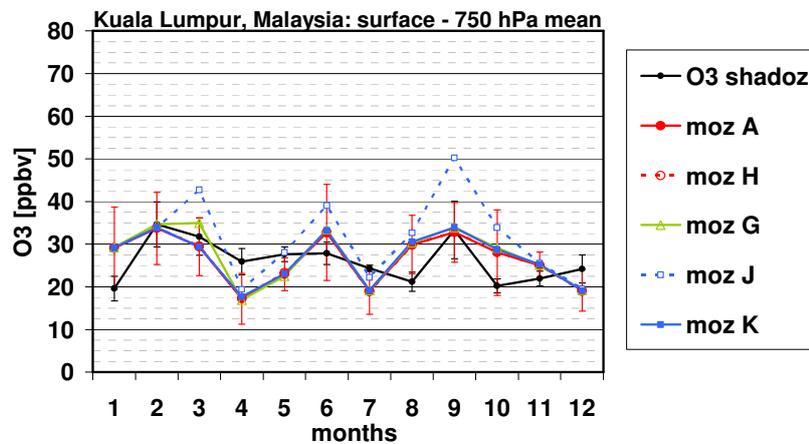
Figure 4.10: SHADOZ ozone measurements from radio soundings at Kuala Lumpur, Malaysia in the year 2000 and corresponding MOZART-2 graphs of the five main runs A, J, H, G, and K. Seasonalities of monthly mean ozone are averaged from the surface level to 750 hPa. Error bars are standard deviations

In the year 2000, the Southern Hemisphere Additional Ozonesondes (SHADOZ) network consisted of 12 tropical and subtropical stations located in the southern hemisphere (see Figure 4.9 and Table C2). The archived data are available at http://croc.gsfc.nasa.gov/shadoz. In Thompson et al. (2003a) the ozone sonde precision is given with 5%. A detailed description and evaluation of uncertainties and accuracies of the data is reported in Thompson et al. (2003a and 2003b). The monthly number of ozone soundings per station in the year 2000 varies from 0 to 9 with an average of 3 soundings per month (Table C3). Malindi in Kenya is the station with the lowest number of ozone soundings (only 8 throughout the whole year of 2000), while San Cristóbal counts the most

soundings with 48 releases and an average of 4 per month (Table C3).

Figure 4.10 shows an example of the ozone seasonality as derived from the SHADOZ ozone soundings at Kuala Lumpur, Malaysia in the year 2000, compared to MOZART simulations. Mean values are calculated for a near surface layer (from surface to 750 hPa). Further figures will be presented in the regional discussion in section 4.5 (Figures 4.21ff).

The comparison to SHADOZ ozone seasonality provides a highly variable picture that cannot be easily resumed. Table C4a and C4b in Appendix C confirm that in fact base-run A only has significant R^2-correlations (i.e. > 0.7) with observations for 3 stations out of 12 at the near-surface layer and only at 1 station for the upper layer (750 – 500 hPa). However, ozone simulations by MOZART match the SHADOZ observations within the sometimes large range of their standard deviation at 10 out of 12 stations (83%) for more than 6 months at the lowest 2 km of the troposphere. At the layer above, reaching up to 500 hPa (~5 km), only 4 stations (33%) agree with regard to this criterion. 3 of the stations (25%) systematically underestimate ozone concentrations close to the surface for at least one season. In the upper layer (750 hPa – 500 hPa) this is the case for 6 stations (50%). Overestimates by the model are less frequent in the upper layer (3 of 12 stations). At the surface there are 4 stations with this feature. The seasonal pattern provided by the SHADOZ measurements is qualitatively captured by the model for 9 out of 12 stations (75%) close to surface and by 7 stations (58%) in the upper layer, however correlation is weak.

Largest discrepancies are found for Paramaribo in Suriname, San Cristóbal situated west from Southern America at the equator, and at Pago Pago, Samoa. At these stations, MOZART systematically overestimates the measured SHADOZ ozone concentrations by up to 30 ppbv. Specifically San Cristóbal and Paramaribo show a pronounced maximum in July for all MOZART runs that is not mirrored with this shape in the SHADOZ ozone data. In the years prior to 2000, there were no pronounced peaks in ozone. (Thompson et al. 2003b, Figure 5). Since all MOZART runs show this same pattern, this may either indicate that sampling problems exist for these stations or that there is a systematic high-bias in the model. Both hypotheses will have to be further investigated in the regional discussion in section 4.5.

MOZAIC Aircraft Ozone Measurements

Vertical profiles from selected airports serviced by MOZAIC aircraft were used to complement the southern hemispheric ozone picture provided by the SHADOZ data.

The MOZAIC program (Measurement of Ozone and Water Vapor by Airbus In-Service Aircraft) uses regular Airbus A340 passenger aircraft flights since 1994 to collect ozone and water vapor data all over the world. For more detailed information see Marenco et al. (1998) or http://www.aero.obs-mip.fr/mozaic. MOZAIC airports with profiles in the year 2000 used in this study are shown in Figure 4.11. An airport list with further information is given in Annex C, Table C1. Measurements are taken every 4 seconds which leads to ascending and descending profiles at a vertical resolution of 20-28m close to the airports. These are in good agreement with near-by in-situ ozone soundings (Marenco et al., 1998; Thouret et al., 1998). The measurement accuracy is estimated to be ±2 ppbv + 2% (Thouret et al., 1998).

Figure 4.12 presents an example of a monthly mean ozone vertical profile as measured by ascending and descending MOZAIC aircrafts from and to the airport of Brazzaville, Congo in August 2000. In the regional discussion more of these MOZAIC profiles from airports all over the world will be compared to MOZART simulations (see Figures 4.22ff). The same as observed in the SHADOZ data holds for MOZAIC ozone profiles. In several cases the simulations predict an ozone plume with roughly the right enhancement above background, but they underestimate the altitude of the plume. This could be explained by the circumstance that in MOZART all emissions are injected into the surface layer, whereas the actual injection height of fire emissions is often higher. Alternatively one can suspect systematic errors in the parameterizations of boundary layer venting and convection.

Figure 4.11: MOZAIC airports with ozone aircraft measurement data of the year 2000. For detailed information see Table C1

Figure 4.12: MOZAIC monthly mean ozone aircraft measurements (black) and corresponding MOZART simulations at Brazzaville, Congo airport from May to August 2000

4.4 Impact of Fire Emissions and Lightning on NO$_x$ and Ozone

High NO$_x$ concentrations exist close to the surface where industrial pollution (Europe, North America) and strong biomass burning emissions (e.g. Africa, South America, South Asia) occur. Concentrations are highest in winter when reduced mixing and slower chemical degradation lead to accumulation of NO$_x$ in the boundary layer. During northern hemispheric summer, convective transport from surface to the mid-troposphere and NO$_x$ production from lightning lead to a mid latitudinal maximum of NO$_x$ concentrations in the free troposphere. The geographical distribution of NO$_x$ maxima agrees with Brasseur et al. (2005), but they tend to be 2-10 times higher in base-run A. Zonal mean cross sections of NO$_x$ are in good agreement (not shown). Figure 4.13 instead, shows seasonal global NO$_x$ concentrations of base-run A at 850 hPa, which allows to better distinguish the biomass burning emissions that are transported to higher altitudes.
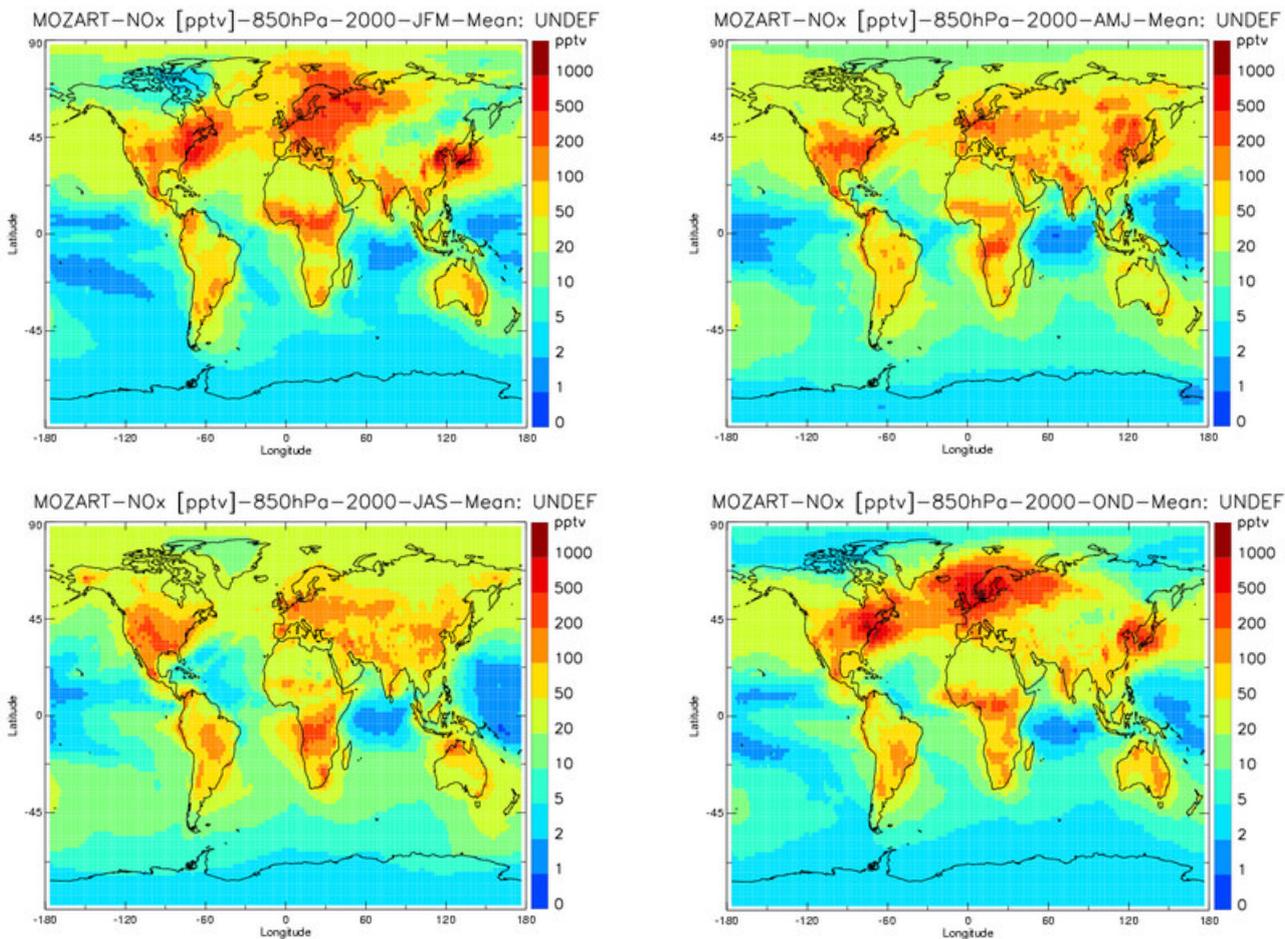
Figure 4.13: Global MOZART-2 seasonal nitrogen oxide concentrations in ppbv at 850 hPa of the year 2000. Results of run A, using GWEM-1.3 fire emissions
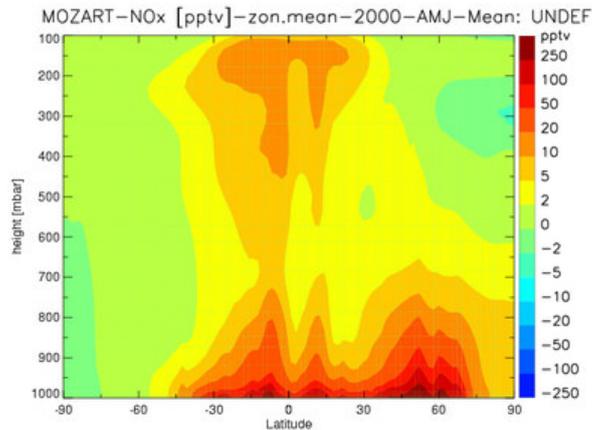
Figure 4.14a: MOZART zonal mean of April, May, and June 2000, base-run A minus run D shows global impact exclusively from fire emissions on NOx concentrations

Impact of Fire Emissions

The global impact of fire emissions on simulated NO_x concentrations is shown in a northern hemispheric spring (April-July) zonal mean plot in Figure 4.14a. It is a difference plot of base-run A with GWEM-1.3 fire emissions, and run D, without fire emissions. Close to the sources, NO_x concentrations as a result of fires can be as high as 250 pptv. In higher altitudes around 850 hPa, zonal mean NO_x resulting from fires, still reaches over 20 pptv. The same is true for air masses over the equator around 200 hPa and less. In this height, NO_x concentrations from fires reach their maximum from January to March (Figure 4.14b), when strong convection patterns transport air from northern African fires high up.

The impact of fires on ozone is also most pronounced in this period over Africa: a zonal mean maximum in January-March of about 8 ppbv extends from 600 – 150 hPa altitude centered at 20° S (Figure 4.14b). In the zonal mean of July-September two ozone maxima with the same amplitude are observed further down, centered at about 850 hPa at 10°S and northward of 60°N (Figure 4.14c). Conferring the individual monthly means reveals that the southern hemispheric maximum peaks in July, while the one in the northern hemisphere peaks one month earlier. Altogether, fires increase the annual tropospheric ozone burden significantly.
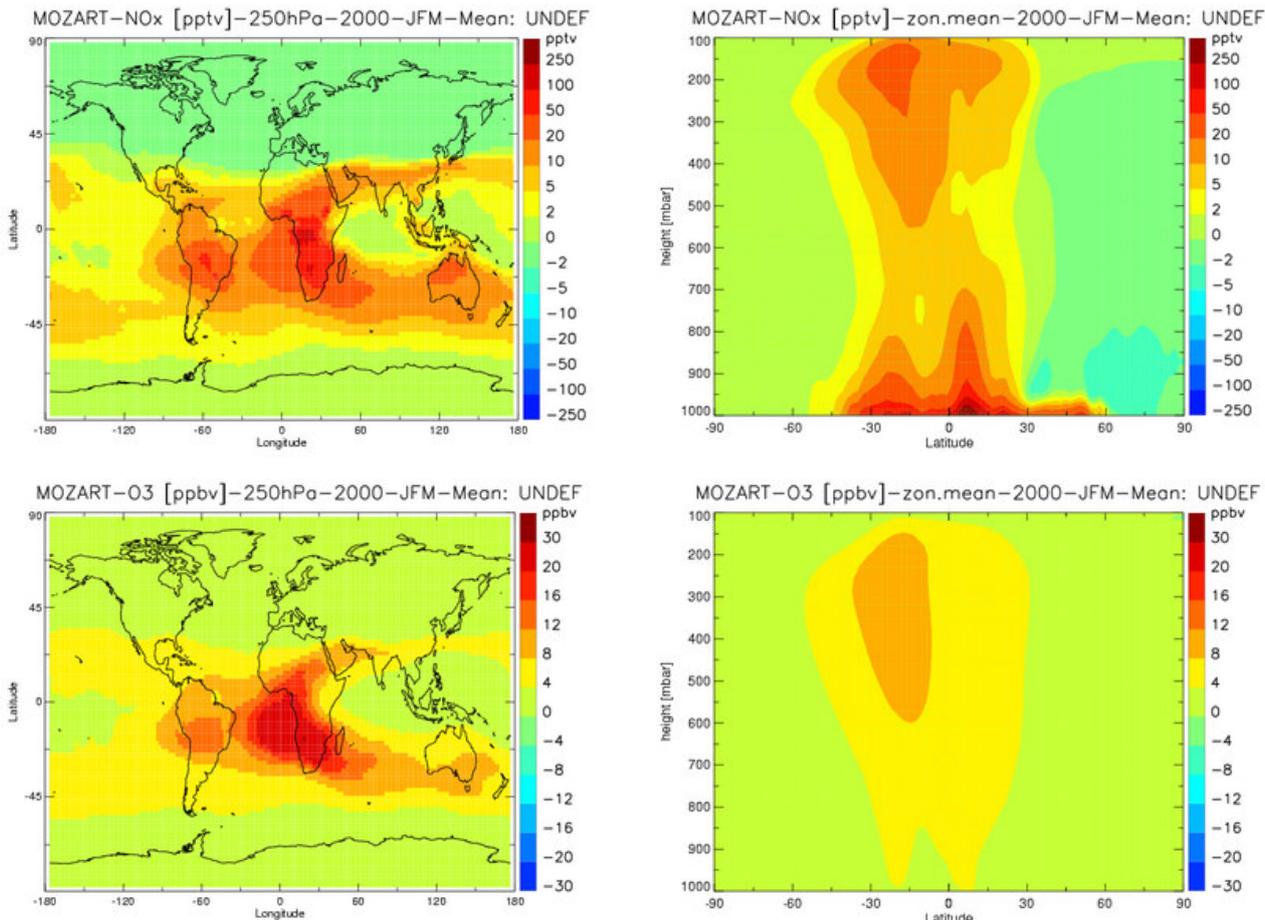
Figure 4.14b: MOZART NOx (top) and ozone (bottom) resulting exclusively from fires, base-run A minus run D, on the left: seasonal mean of January-March 2000 at 250 hPa, on the right: corresponding zonal means
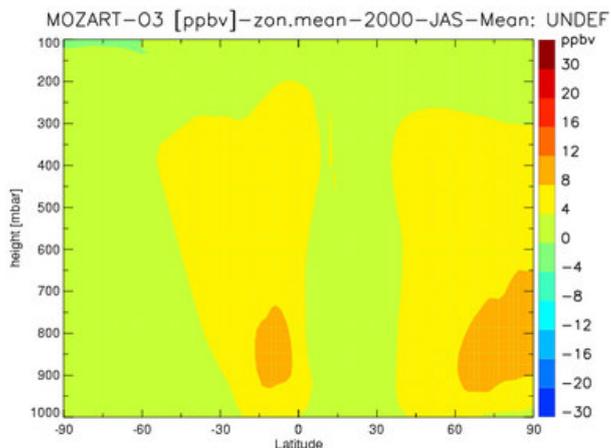
Figure 4.14c: MOZART ozone zonal mean of July-September 2000, base-run A minus run D shows global impact exclusively from fire emissions on ozone concentrations
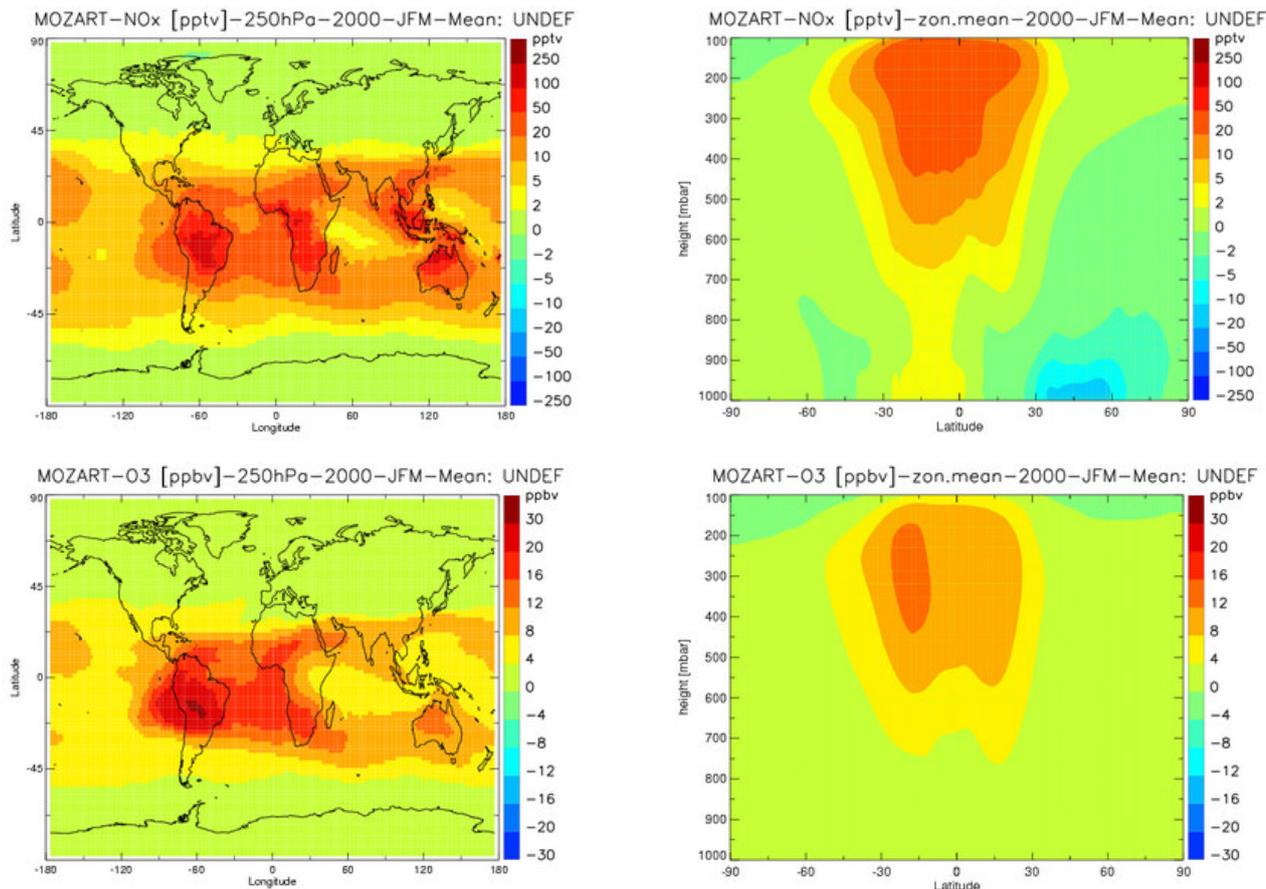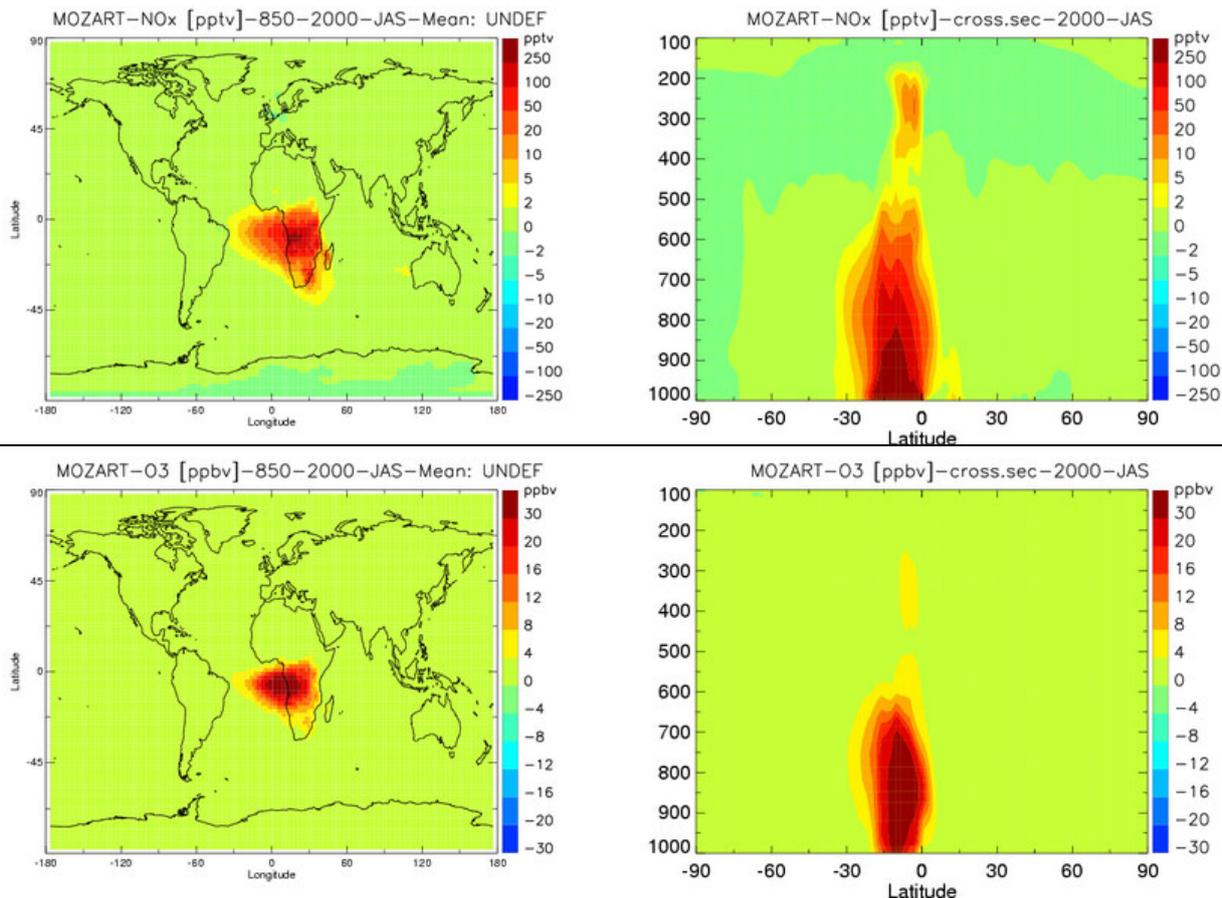
Figure 4.15: MOZART NOx (top) and ozone (bottom) resulting exclusively from lightning, base-run A minus run B, on the left: seasonal mean of January-March 2000 at 250 hPa, on the right: according zonal means

Impact of NOx Lightning Emissions

Figure 4.15 highlights the impact from NOx lightning emissions, on the NO_x and ozone distribution in MOZART in January, February and March 2000. The NO_x zonal mean plot at the top right shows a NO_x maximum induced by lightning activities of over 20 pptv centered at 250 hPa and reaching from 450-100 hPa at approximately 10°S. The global distribution at 250 hPa on the top left-hand side of Figure 4.15 delivers more information on the geographical distribution of lightning activities: in early 2000 there is a large area over the Amazonian region with NO_x concentrations over 100 pptv. Another lightning-active region is over northern Australia at the same latitude, also yielding values over 100 pptv. The bottom panels of Figure 4.15 give a similar picture of ozone distributions. The JFM zonal mean shows an ozone enhancement resulting from NO_x lightning emissions of 12 ppbv reaching from 450 hPa to 170 hPa and also at 10°S. On the global distribution the largest ozone enhancement is again observed over Amazonia with seasonal mean concentrations of 20-30 ppbv, followed by an enhancement of over 16 ppbv over the African west coast. Over Australia the ozone increase is still more than 12 ppbv.

Compared to the impact from fires (Figures 4.14a-c), NO_x and ozone maxima resulting from lightning are more widely spread in the tropical belt with more enhanced concentrations over Southern America, Northern Australia and South-East Asia. NO_x concentrations from lightning in higher altitudes are stronger and distributed over a larger area than those from fires. However, and as can be expected from the location of sources, the close-to-surface

Figure 4.16: MOZART seasonal mean NOx (top) and ozone (bottom) concentrations from fires in July-September 2000 in southern hemispheric Africa. Difference of base-run A minus run E. On the left: seasonal means at 850 hPa, on the right: according cross section at 15° E longitude

levels NO_x concentrations as a result from fires are considerably higher than those from lightning. Concerning ozone concentrations, lightning yields more ozone over Southern America than fires (at least for base-run A with few deforestation fires in South America). Fires in turn produce much more ozone over Africa for lower altitudes, which is reverted in higher levels where lightning takes place.

Impact of Fire and Lightning NO_x Emissions in Southern Hemispheric Africa
Two further MOZART experiments were set up to investigate the impact of fires and lightning specifically in southern hemispheric Africa on tracer distribution and concentrations. In run E (Table 4.2), all fire emissions in southern hemispheric Africa were set to 0. Computing the difference of base-run A and this run E, will provide the distribution of species resulting exclusively from fires in southern hemispheric Africa. The same sort of experiment was performed for lightning emissions. Run C (Table 4.2) excludes NO_x lightning emissions over southern hemispheric Africa.

Figure 4.16 shows the impact of southern hemispheric Africa fires on MOZART NO_x and ozone concentrations, which is strongest in July through September. NO_x enhancements from fires are confined to the lowermost model levels and the large majority do not exceed the 500 hPa level (see Figure 4.16 vertical distribution at top right). The global distribution at 850 hPa on the left-hand side show that fire emission-prone air masses with enhancements of over 50 pptv move more towards the southern Atlantic westward, than eastwards over the Indian Ocean. This is also related to the fact that more of the fires in the southern

hemispheric region take place in the western countries of Africa. Maximum NO_x concentrations close to the sources exceed 250 pptv. Without fires in MOZART (run D) NO_x concentrations from July to August 2000 remain between 10 and 25 pptv on the African continent as well as over the Southern Atlantic Ocean. Thus, Southern African fires lead to a NO_x enhancement with a factor of 2-5.

The two bottom panels of Figure 4.16 show the impact of fire emissions on ozone, which has a similar, although spatially a somewhat more restricted, distribution. From the sources up to a pressure level of 700 hPa the ozone enhancement exceeds 30 ppbv. In MOZART "no-fire" run D, ozone concentrations close to the surface remain between 1 and 5 ppbv, while in more elevated levels ozone ranges between 10 -25 ppbv. This means that because of fire activity in southern hemispheric Africa, ozone close to the surface is more than 6 times higher than without fires, and up to 700 hPa ozone is more than doubled compared to MOZART run D.

Figure 4.17 depicts the lightning impact in southern hemispheric Africa. The highest lightning activity over southern hemispheric Africa can be observed from January through March at an altitude above 500 hPa (maximum at about 350 hPa, according to MOZART). The global distribution of NO_x from southern hemispheric Africa lightning on the left-hand side shows that the northernmost air is transported over the ITCZ over the sahelian zone and from there over the Saudi-Arabian peninsula and India. In the south, lightning NO_x loaded air is driven by the southern hemispheric African high and taken over the Indian Ocean and even over Australia. Close to the source, NO_x concentrations are in the order of over 50 pptv.

The impact of lightning in southern hemispheric Africa on ozone can be found in the bottom panels of Figure 4.17. The maximum of ozone built by lightning precursors lies at 350 hPa over southern hemispheric Africa. It yields seasonal mean concentrations of up to 16 ppbv in the first months of the year (left panel), while ozone due to fires peaks considerably closer to the surface with concentrations of over 30 ppbv (Figure 4.16).
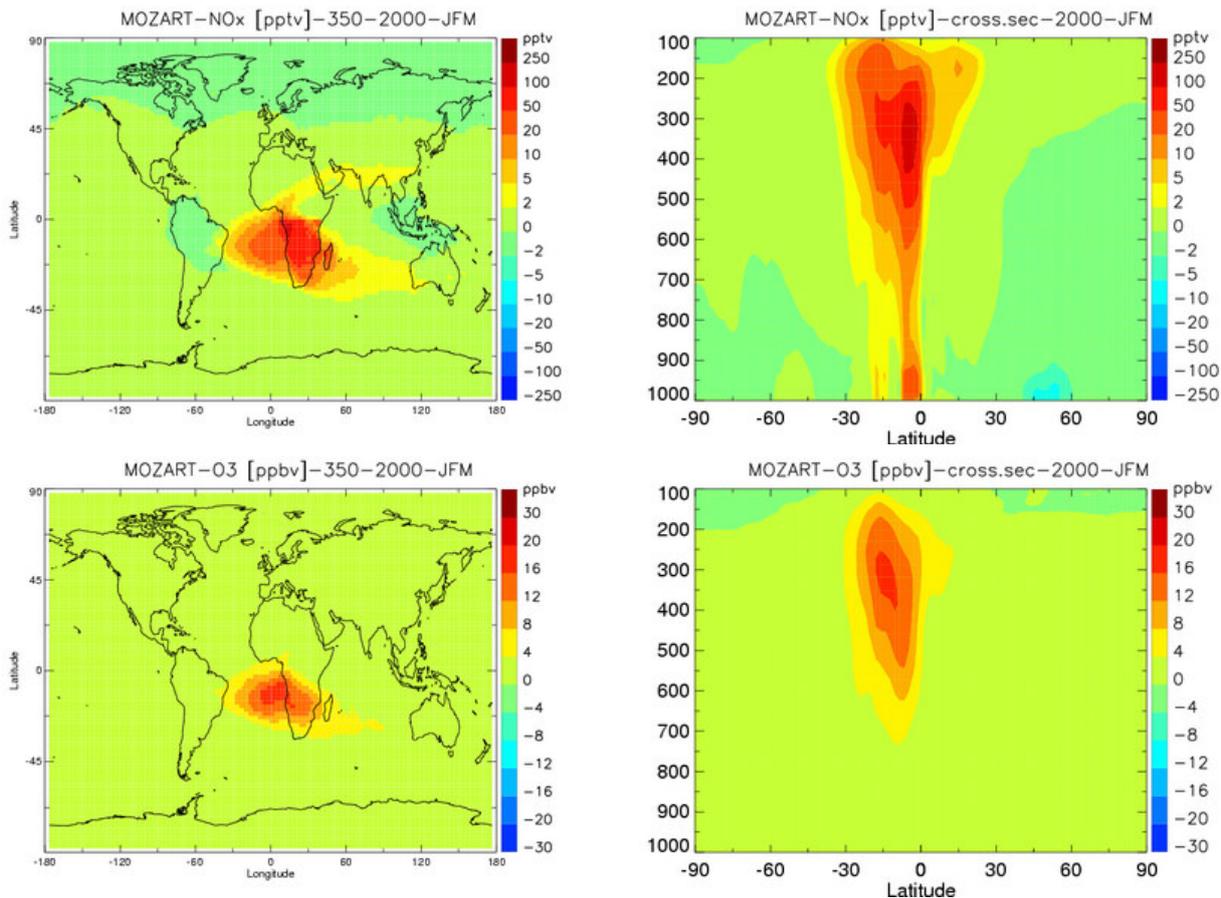
Figure 4.17: MOZART seasonal mean NO$_x$ (top) and ozone (bottom) in pptv from lightning in January-March 2000 in southern hemispheric Africa. Difference of base-run A minus run C. On the left: seasonal means at 350 hPa, on the right: according seasonal cross section at 15 E longitude

4.5 The Impact of Using Different Fire Emission Inventories

Figures 4.18 and 4.19 highlight the differences between MOZART runs A and run J (difference plots of run A minus the remaining runs H, G, and K can be found in Appendix D, Figures D1-3). Figure 4.18 shows the global seasonal surface CO difference in ppbv of run A minus run J. The two most evident features in Figure 4.18 are (i) the difference in the temperate and boreal northern hemisphere in April-June where CO is larger in MOZART run A (using GWEM-1.3 fire emissions), and (ii) the clear discrepancy between small Southern American CO concentrations in run A from August-December that result from low biased fire emissions in the GWEM-1.3 inventory and high-biased fire emissions in the gfed inventory used in run J (see Chapter 2). In the northern hemisphere large areas show between 20-120% more elevated CO abundances at surface level for run A, while in very active burning regions an increase of up to a factor of 3 can be observed, with peaks of up to a factor of 6 for individual gridboxes in Russia. The difference between run A and J in the zonal mean of Figure 4.19a in northern hemispheric spring (April-June) is also seen in the comparison with all other runs (G, H, and K) with run A. It reveals the impact of enhanced mid- and high latitude fire emissions on higher altitude atmospheric CO concentrations. According to Figure 4.19a, CO concentrations in run A are enhanced by 20 ppbv in an altitude up to 550 hPa (over 5 km), compared to the other runs. The main reason for this discrepancy in northern hemispheric CO abundances is the different satellite fire products that were used to compile the underlying fire emission inventories. In these latitudes all inventories used in run G, H, and J rely on the active fire count product from ATSR. This product is known to have strong omissions in North Central Asia (see Chapter 2). Another superposing effect might be high estimates of fuel loads from the LPJ vegetation model that are required for fire emission calculation in the GWEM-1.3 inventory (run A).

In South America there are contrary trends in the two MOZART runs, with run A yielding 20-80% less CO mainly in the Amazonian region as a result of failure of the satellite area burnt product GBA2000 to capture small deforestation fires.

Additionally, there is a geographical shift in minima and maxima of CO concentrations over the African continent. In the northern hemisphere, seasonal mean plots from January-March and from October-December show that maximum CO abundances in run J are located over western Africa, while CO in run A is concentrated more in the east/southeast of the northern hemisphere. South of the equator, CO of run J results mainly from savanna fires in the south, while CO of run A is more evident further north, where wooded savanna and tropical forest ecosystems dominate.

NO_x concentrations also differ substantially in the northern hemispheric summer (July-September) between run A and J (Figure 4.19b): at up to 700 hPa still, there is 20-50% (20-50 pptv) less NO_x abundance in Southern America for run A, but 10-40% (2-20 pptv) more CO in high northern latitudes.

Strongest surface ozone impacts can be observed in northern hemispheric spring (April-June) over a large area in Eastern Russia (Figure 4.19c). The higher CO and NO_x fire emissions of GWEM-1.3 in Eurasia have a strong impact on ozone photochemical production in the lower troposphere. Over the whole region mean ozone levels of run A are 4-12 ppbv (20-80%) higher.

Difference plots of carbon monoxide of run A minus the remaining runs H, G, and K can be found in Appendix D as Figures D1-3, respectively. All of these are based on the same climatological inventory and are therefore expected to share similar features. However, in spite of using the same ATSR fire count data set, the two scaling approaches (runs G and H) show some differences. For example, Figure 4.19d that presents a direct comparison of the two similar runs H and G in the October-December season, reveals four features worth to be highlighted: (i) run H yields clearly higher CO concentrations (20-60%) in a north-to-south
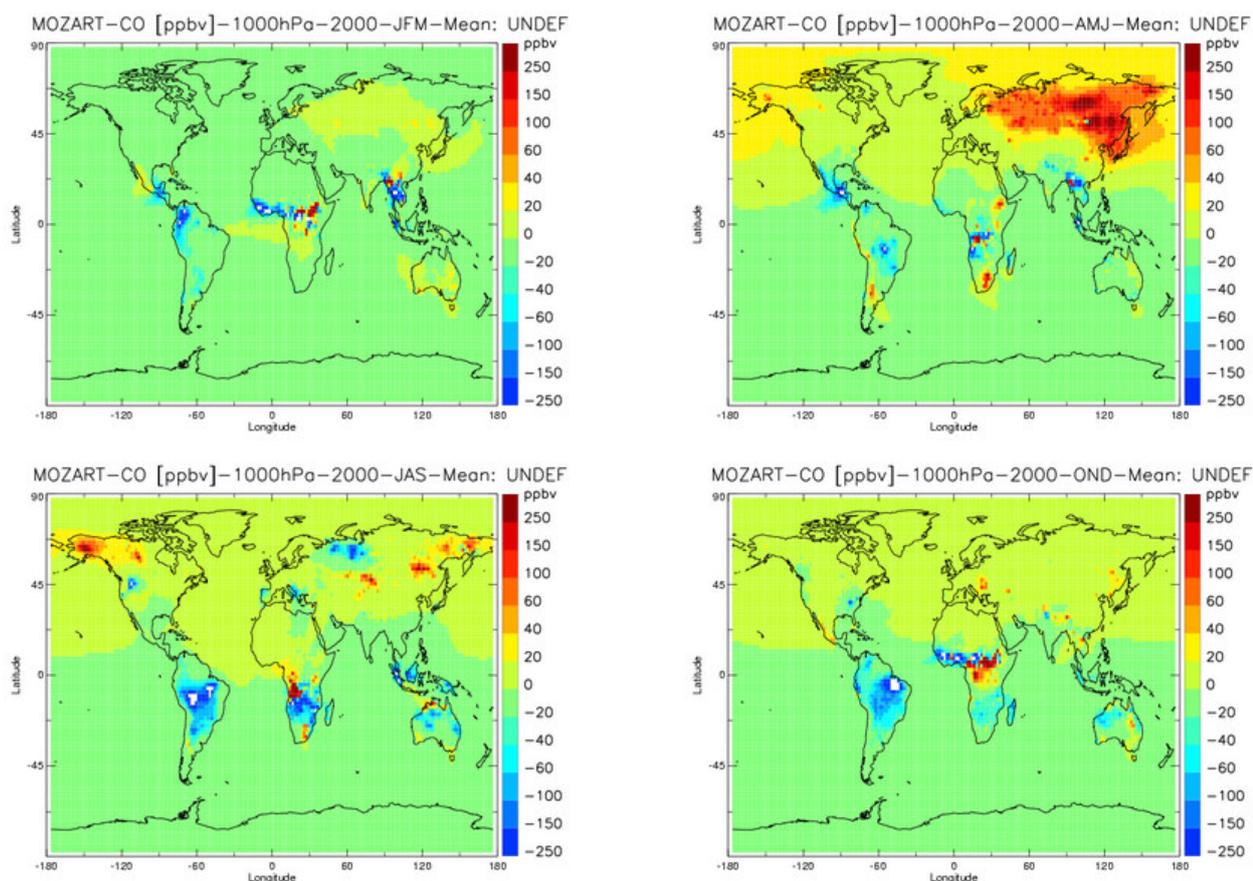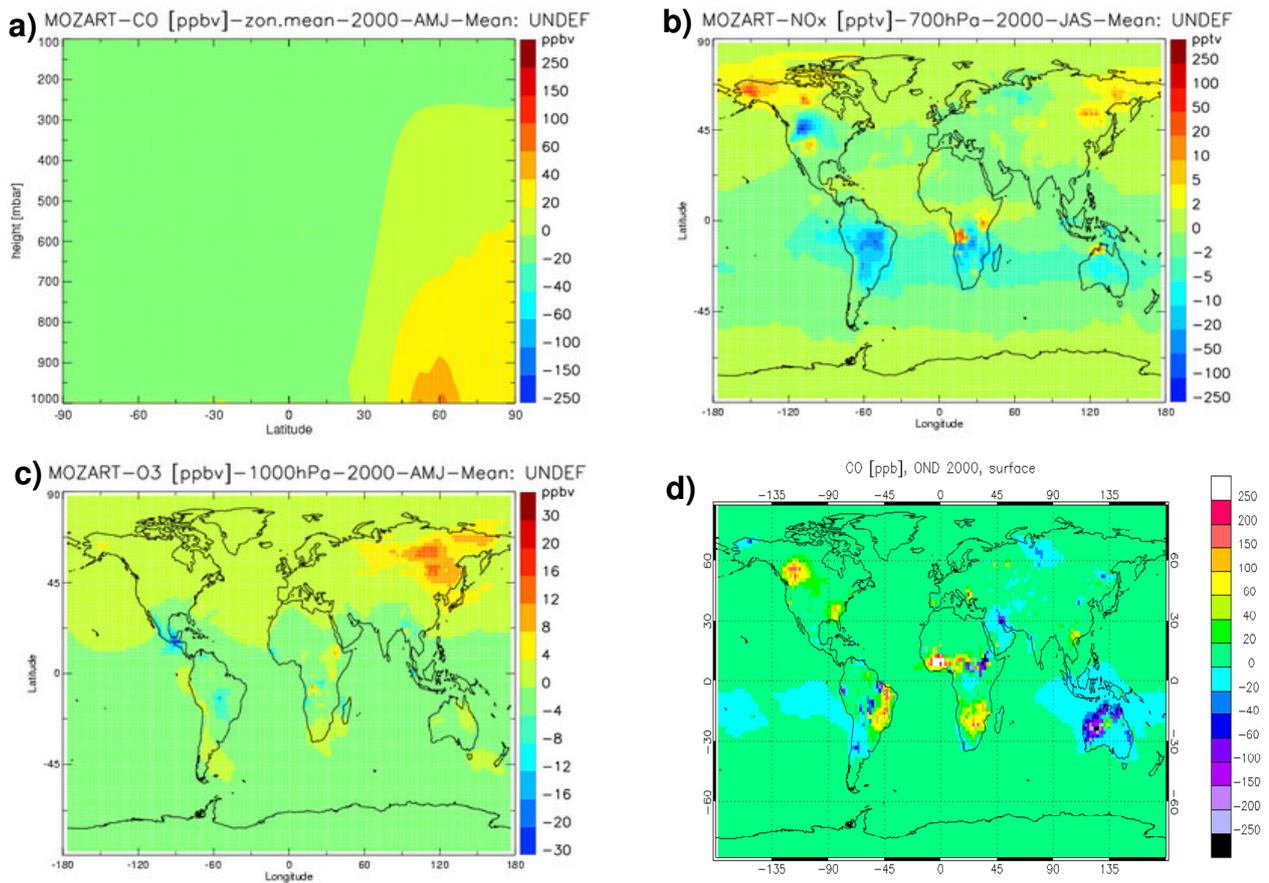
Figure 4.18: MOZART run A - J: difference of global seasonal surface carbon monoxide concentrations in ppbv in year 2000. Run A uses GWEM-1.3 fire emissions and run J uses gfed fire emissions

course along the Brazilian coast, which is absent in run G. (ii) run G has more fire emitted CO in western Africa (80-140%)and over savannas in southern Africa (40-80%). (iii) Australian CO concentrations are much higher in run G, especially on the north-northwest coast (50-80%), and (iv) run H has local CO concentrations at about 50°N (ranging 60-150 ppbv) in the north west of North America, this maximum is absent in run G. Very local minima in the difference plots (e.g. 48°E 31°N at the Persian Gulf or 78°E 64°N in Russia), mainly in the northern hemisphere in run J and G are the result of so-called spurious pixels (see Schultz, 2002) in the underlying ATSR satellite fire product used for estimating fire emissions. In a new version of the run G underlying cg_scal fire emission inventory, these pixels have been removed.

The northern hemispheric CO enhancement of run A in Eurasia is prevalent in all difference plots of the MOZART runs, with unaltered strength. Southern American CO is considerably low in run A compared to all other runs. Run K features the strongest discrepancy in this area (30-90 % more CO), which is similar to run J, although with a location that is different from that of run J (further to the south-east). Run H has 30-70 % higher CO concentrations in South America than run A, followed by run G with 30-50 %) (Figures D1 and D2).

Run H (Figure D1) has higher CO concentrations in Northern Africa than run A. In sub-equatorial Africa, less CO is found for run H over tropical forest and wooded savanna ecosystems (JAS), than in runs A and J. Southern African CO surface concentrations of run G over savanna ecosystems are in better agreement with run A (difference of about 10 %), than run H (20-30 %) and run J (10-30%). Run G yields more CO over Australia compared to the remaining runs. In the following the individual fire regions will be discussed and evaluated.

Figure 4.19: **a)** MOZART run A - J: difference of global seasonal (April-June 2000) zonal mean carbon monoxide concentrations in ppbv in year 2000. Run A uses GWEM-1.3 fire emissions and run J uses gfed fire emissions,

b) MOZART run A – J: difference of global seasonal mean (July-September 2000) nitrogen oxide concentrations in pptv at 700 hPa. Run A uses GWEM-1.3 fire emissions and run J uses gfed fire emissions,

c) MOZART run A - J: difference of seasonal (April-June 2000) zonal mean surface ozone concentrations in ppbv. Results of run A, (using GWEM-1.3 fire emissions) minus run J (using gfed fire emissions),

d) MOZART run H - G: difference of global mean seasonal (October, November and December) surface carbon monoxide concentrations in ppbv in year 2000. Run H uses mgs_scal fire emissions and run G uses cg_scal fire emissions, both are ATSR scaled climatological emissions as of Hao&Liu

4.5.1 Africa
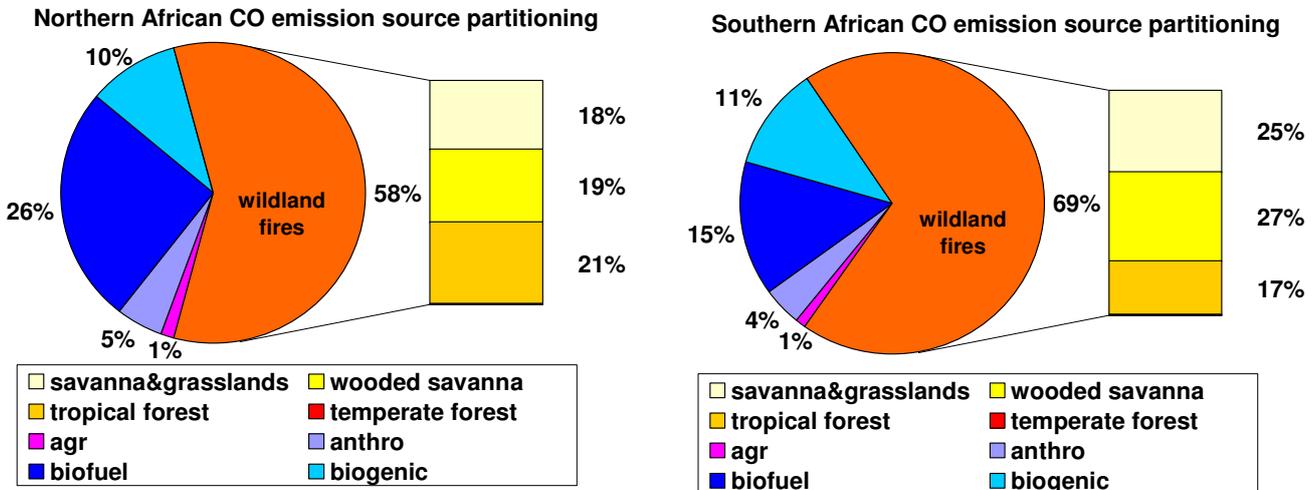
Figure 4.20: CO emission source partitioning in MOZART run A for Northern and Southern Africa. Sub-categories as in Chapter 3

Africa is the continent with most fire activity (e.g. Andreae, 1991; Barbosa et al., 1999; Boschetti et al., 2004) and will therefore be discussed first. In Africa, fires occur on a regularly basis, compared to other regions of the world. Fire occurrence in Africa mainly has its origins in human controlled burnings related to land-use change, which is a broader expression for land management practices. Most fires in Africa occur in savanna and wooded savanna biomes (e.g. Barbosa et al. 1999). In these ecosystems the purpose can either be the stimulation of grass regrowth to feed cattle or provocation of rapid nutrient release, before start of the new growth season. In forest ecosystems deforestation with subsequent burning takes place for agricultural use of land, and also creating areas of cattle pasture. In northern hemispheric Africa, the fire season takes place from October through March, with a maximum in December or January. In the southern hemisphere, fires are most active during late July to September, with fewer fires occurring in May, June, and October.

All fire emission inventories used in this study show abundant CO emissions in Africa similar to MOZART run A in Figure 4.20 (see also Chapter 3). Fires are clearly the most dominant source of CO emissions. A distinct seasonal shift from the northern to the southern hemisphere as described above could also be observed in all inventories for the year 2000 and is thus well reflected by all MOZART runs (e.g. Figures 4.1 and 4.2).

Northern Hemispheric Africa

In boreal winter, MOPITT CO shows a maximum a little south of the fire emission sources, already located over the gulf of Guinea (Figure 4.21). The ozone precursors emitted by fires in northern hemispheric Africa are convected into mid-tropospheric altitudes and then transported by south-easterly winds over the South Atlantic. During this process they are partly transformed into ozone. This feature is part of explanation of the "ozone paradoxon" as described in Thompson et al. (2000), and further investigated for example in Martin et al. (2002), Edwards et al. (2003) and Sauvage et al. (2005).

The general features of MOPITT CO data over and in the vicinity of northern Africa at 700 hPa are reflected by all MOZART runs. All runs reflect a maximum of CO concentrations in December in agreement with the MOPITT CO, except for run K, where no distinct maximum is simulated in this period. Figure 4.21 reveals that for the month of December, run A and J reflect the qualitative and quantitative features displayed by MOPITT very well, with a wide
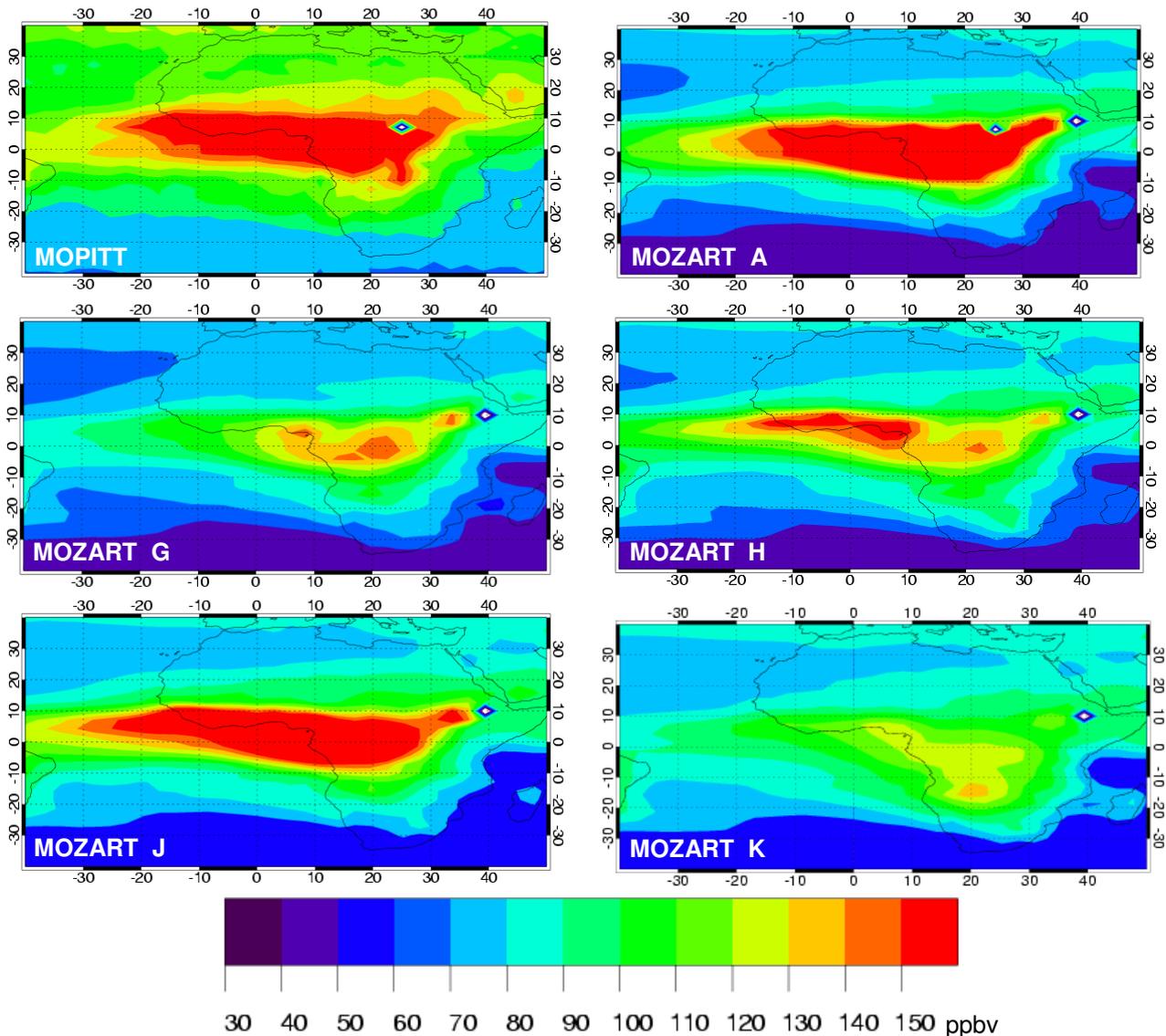
Figure 4.21: African MOPITT and MOZART CO in ppbv for simulations A, G, H, J, and K in December 2000 at 700 hPa

 area over western Africa and the gulf of Guinea yielding CO concentrations of over 150 ppbv. Run H shows a similar feature, but with lower concentrations (100-150 ppbv) over the Equatorial Atlantic. Compared to MOPITT, run H underestimates CO concentrations in northern hemispheric Africa by about 40 ppbv (up to 30%). Run G and K in turn, show even far lower CO concentrations and do not develop a similar feature of CO as can be seen for MOPITT. Additionally, run K shows a CO maximum too far in the south, in Southern Africa instead of in the northern hemisphere. The seasonal behavior of run K with its climatological fire emissions is less distinct for Africa and the distribution of CO concentrations is somewhat diffuse (see Figure 4.21) compared to all other runs that are based on fire products from satellites (see also Chapter 3). No in-situ measurement site of the CMDL network with CO surface data is located in or close to the biomass burning region in northern hemispheric Africa.

There are only two sites on the northern hemispheric African continent, where ozone soundings are carried out for SHADOZ. They are located in the equatorial region in Kenya, at Nairobi and Malindi (Figure 4.22). These stations are situated off the main regions of fires, in east Africa. Generally, all MOZART runs (A, J, H, G, and K) follow the SHADOZ ozone monthly mean observations at these stations reasonably well and are within the, although
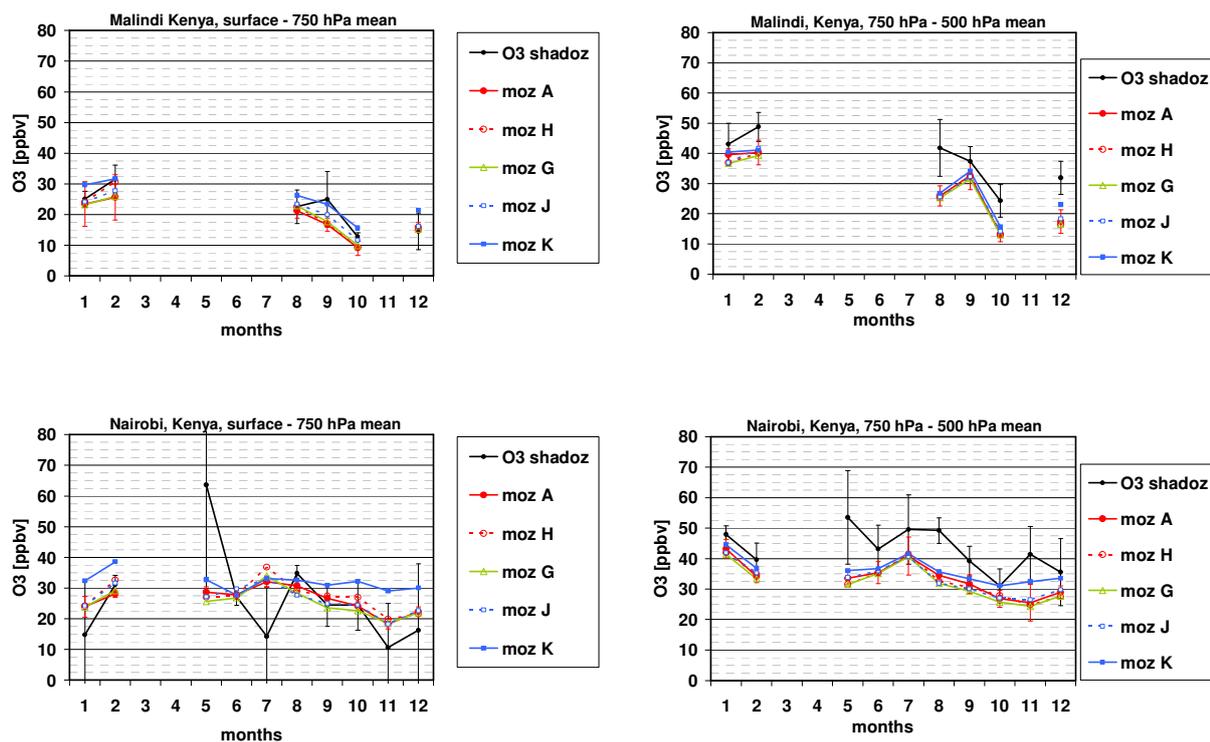
Figure 4.22: Northern African SHADOZ ozone measurements in ppbv from radio soundings at Malindi and Nairobi, Kenya in the year 2000 and corresponding MOZART-2 graphs of the five main runs A, J, H, G, and K. Seasonalities of monthly mean ozone are averaged from the surface level to 750 hPa on the left-hand side and for 750 - 450 hPa on the right-hand. Error bars are standard deviations.

sometimes large, error bars. This is the case both for mean values of the lower level from surface to 750 hPa, as well as for ozone in the level above from 750 hPa to 500 hPa (Figure 4.22). For Malindi data are only available for half of the year (September to February). For January, August and December MOZART simulations are improved by the new fire emission inventories (A, J, H, and G) compared to the old climatological fire emissions used in run K. However, for February, September, and October the performance is worse, compared to run K. This observation holds both for average values from surface to 750 hPa (approx. 2 km) and for the 750 hPa to 500 hPa (approx. 5 km) layer (Figure 4.22). Altogether, Table C4a and Table C4b show high R^2 correlations between model and observations for almost all runs, with run J performing best in both layers (R^2 = 0.88 (surface) and R^2 = 0.84 (at 750 hPa layer).

At Nairobi, SHADOZ data is missing for March and April. There are no significant differences in the new inventory runs (A, J, H, and G) in the boundary layer. All of these runs improve the MOZART model performance from September to December and January by reducing ozone concentrations by 20-30% compared to the overestimating run K with climatological fire emissions. At the upper layer from 750 hPa – 500 hPa however, the constellation is inverted. From September to December run K shows the best simulation performance. At Nairobi, as a total and including performances of all months, no significant R^2 correlations (Table C4a, b) are found.

Run K, based on the climatological fire emissions, yields higher ozone concentrations at those two locations than all other MOZART runs, especially in the lower levels. This is contrary to the findings in comparison with MOPITT CO data at 700 hPa, where run K showed the lowest CO concentrations over northern Africa.

While the GBA2000 area burnt based emission data set used in MOZART run A shows a few burned areas in eastern Africa for December (see http://www.grid.unep.ch/activities/ earlywarning/preview/ims/gba), these are absent in the underlying area burnt data sets of

emissions used in MOZART run J (TRMM-VIRS fire counts) and MOZART run G and H (ATSR fire counts). According to the Joint Research Centre's web-site, commission errors "are present in the burnt area products, these are mainly caused by flooding of non-permanent water features and hot dark rocks in the East of Africa. Compared with the magnitude of burning in Africa, these false detections are insignificant." (see http://www-gvm.jrc.it/TEM/Disturbance%5Fby%5Ffire/products/burnt_areas/global2000/gba2000_data.htm). The large CO plume over Northern Africa in higher altitudes as seen in the MOPITT data comparison (Figure 4.21) is produced by fires that are located a little westwards from Kenya, while the somewhat higher ozone concentrations yielded by MOZART run K are a result of the diffuse fire emission scenario projected by the underlying climatological emissions used in this model simulation. A moderate amount of fire emissions are equally distributed over northern hemispheric Africa instead of accumulating in central and western Africa of the northern hemisphere, and the overall African maximum is located in the southern hemisphere.

MOZAIC ozone aircraft measurements are complementary to the SHADOZ ozone radio soundings. MOZAIC data for the year 2000 in Northern Africa is available for a number of airports, mainly in western Africa. For many airports, no data is available in the main fire season for a specific year. Sauvage et al. (2005) have produced a MOZAIC climatology from 1997-2003 that was also used for terms of comparison in this work.

In Abidjan, (Côte d'Ivoir), Accra (Ghana), and Lagos (Nigeria), but also further south at Brazzaville (Republic of the Congo) and Libreville (Gabon), MOZAIC ozone data in 2000 show a clear plume in varying heights from approximately 1-3 km (Figure 4.23a,b,c,d). Also the simulated MOZART ozone reflects these features, although regularly in lower altitudes of 0.5-2 km and different amplitudes between the different model runs. According to Sauvage et al. (2005) the climatological MOZAIC plumes are also generally located higher up around 2 km in average (1.2-3.1 km), which agrees with the pattern of the year 2000 MOZAIC data. Since in most cases the MOZART model runs underestimate the height of the measured ozone plume. This seems to be caused by a transport-related issue in the model. The uniform injection height at surface level of fires into the MOZART model also plays a significant role. For certain fire types in some ecosystems this might not be the adequate treatment, as in reality injection heights of several kilometers can be quite common, if meteorological conditions are favorable. In Abidjan (Figure 4.23d) in November, all MOZART simulations behave similar and no strong influence from fire emissions can be observed. For all other months with MOZAIC measurements (January – March), MOZART base-run A is closest to the observations, all other model runs overestimate ozone. The other runs in Abidjan in February (Figure 4.23d) show a distinct peak that is not reflected in the MOZAIC measurements. An inspection of the simulated monthly concentrations of those runs over Abidjan reveals that this peak is already evident in the fire-generated CO and NO_x concentrations over western Africa (not shown), which are the precursors of ozone. This pattern in Figure 4.23d can be traced back to the geographical distribution of the underlying satellite fire products that were used to calculate the different fire emissions: as mentioned above, the TRMM-VIRS fire pixels and the ATSR fire counts show more fire activity during February and March in westernmost Africa than the GBA2000 product. This results in higher fire emissions of CO, NO_x and other compounds emitted by fires in this region. The more elevated CO from fires is already mirrored by the regional CO fire emission seasonality in Figure 3.7 in Chapter 3: in contrast to all other inventories, the GWEM-1.3 fire emission inventory drops to a third of its monthly emissions from January to February and further decreases in March. All other inventories start the decrease one or two months later. In Libreville, there are only MOZAIC flights for the month of January 2000. All runs but run K reflect the distinct ozone plume. However, base-run A and run G clearly overestimate the ozone maximum of about 75 ppbv by 15-20 ppbv (over 17-21%), while the maximum in run J is by 10 ppbv too low, which corresponds to an underestimate of about 13%.

a)

b)
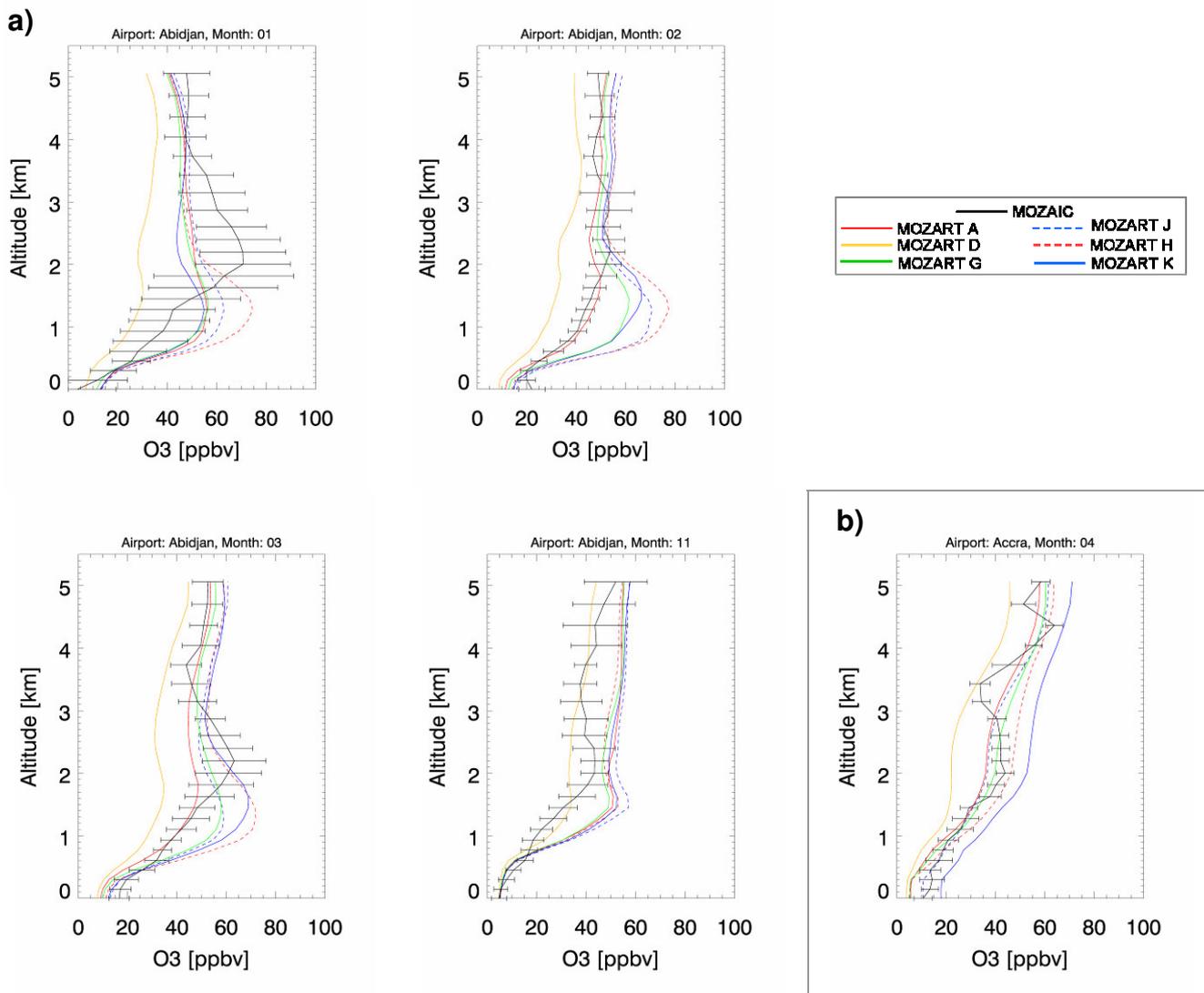
Figure 4.23a,b: MOZAIC monthly mean ozone aircraft measurements (black) and corresponding MOZART simulations at a) Abidjan, Ivory Coast airport from January to March and November 2000, and b) at Accra, Ghana airport in January 2000

Generally, run A yields higher surface CO concentrations due to different fire emissions in east and central Northern Africa (western Ethiopia and southern Sudan) than run J (Figure 4.18). On the other hand, run J yields higher CO concentrations in western Africa (from Senegal, over Guinea, Ivory Coast, Ghana, Nigeria, southern Chad, Central African Republic, and to Cameroon). Also in the early burning season (October-December), more CO from fires is observed in run A at equatorial western Africa (Cameroon, Central African Republic, Southern Sudan, Congo, and Democratic Republic of the Congo) (Figure 4.18). In Figures D1, D2, and D3 (Appendix D) run A also yields a similar pattern for Northern Africa, compared to runs H, G, and K, respectively.

An inspection of the fire products used to estimate the underlying fire emissions of those MOZART runs do not entirely explain these discrepancies: in January and February 2000 ATSR and TRMM-VIRS (used in fire emission calculations of run G, H, and J respectively) do not show a clearly higher amount of active fire counts compared to the areas burnt from GBA2000 (used for the calculation of fire emissions in run A). In March however, ATSR shows a somewhat higher fire activity in westernmost Africa than GBA2000. The same is the case for TRMM-VIRS fire pixels in February. The TRMM-VIRS sensor generally captures more active
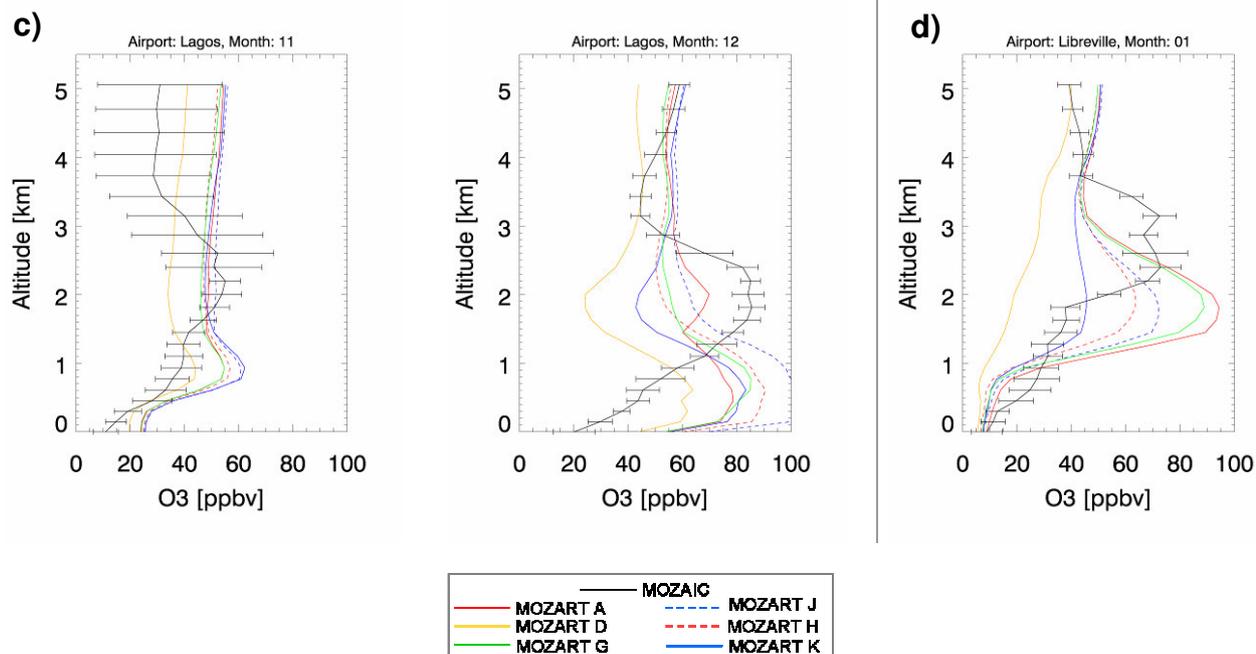
Figure 4.23c, d: MOZAIC monthly mean ozone aircraft measurements (black) and corresponding MOZART simulations at **c)** Lagos, Nigeria airport in November and December 2000 and **d)** Libreville, Democratic Republic of Congo airport in January 2000

fires in regions where small fires of short duration during the day are predominant, compared to the ATSR instrument operating at night.

From October to December, run A yields more elevated CO concentrations at the equator (mainly Congo), which can also not be traced back to differences in fire locations of the underlying fire emission inventories, but can rather be attributed to differences in the biomass loads of the individual emission sources. In case of the ATSR-scaled fire emissions the direct attribution of emissions to each fire pixel does not allow a conclusion of a specific source inducing the differences, but the amount of emissions attributed to each fire occurrence is clearly lower than the emissions per area burnt of GBA2000 in the GWEM-1.3 inventory used in run A. The main biome burned in this region is wooded savanna. This biome has rather high biomass loads in GWEM-1.3 (see Chapter 2) and will therefore produce elevated emission fluxes of CO and NO_x which in turn can lead to ozone enhancements.

Synthesis for Northern Hemispheric Africa
In summary, the chemical composition of the atmosphere over Northern Africa in the year 2000 was highly influenced by emissions over a large part of the year. All fire emission inventories under investigation reinforce that fires are the predominant source of pollution on this continent. According to an evaluation of the performed MOZART simulations with carbon monoxide satellite measurements by the MOPITT instrument and SHADOZ radio soundings, CO and ozone concentrations are best represented by the new bottom-up inventories used in MOZART run A (GWEM-1.3 fire emissions) and run J (gfed fire emissions). Both the GBA2000 Global Burnt Area Product and the TRMM-VIRS fire pixels with attributed area burned sizes in run A and run J, respectively, work generally well for northern Africa in terms of their seasonality and the consequently derived CO abundances emitted by fires. MOZART simulations based on ATSR-scaled fire emissions (run G and H) follow the seasonal behaviour as of the bottom-up inventory-based simulations (run A and J), but fail to reach the quantitative CO abundances expected according to MOPITT observations.

Compared to the former climatological fire emission inventory used in MOZART (hao&liu fire emissions) all new fire emission inventories clearly improved the MOZART model

performance in Northern Africa. A large part of the differences found between the MOZART runs is related to the fire emissions. However, discrepancies in the new inventories are not mainly due to the underlying fire products but to attribution of fire emissions to each fire or area burnt occurrence.

The comparison of MOZART simulations to MOZAIC aircraft ozone data yielded no clear favorite of the different simulations but highlighted the need of the introduction of adequate fire injection heights into the atmosphere: the modeled ozone plume heights were systematically lower than those of the measured profiles. However, compared to MOZART run D without any fire emissions, all fire emission inventories (with exception of run K in some cases) improved the model ozone simulations (see Figures 4.23a-d).

Southern Hemispheric Africa

All MOZART simulations show an earlier maximum of CO concentrations in the burning season than the MOPITT instrument. MOPITT shows the most enhanced CO concentrations in September/October, while MOZART run A and J show a maximum in July and run G even in June. Run H peaks in August and October. Only the climatological simulation yields an seasonality in agreement with MOPITT measurements. Enhanced CO concentrations in run J are maintained also for the months of September and October, while CO concentrations in run A drop already considerably after August.

In July 2000, fires in the southern hemispheric African tropical region yield CO concentrations of about 160-180 ppbv according to MOPITT and are qualitatively and quantitatively well reflected by run A and run J (Figure 4.24). The CO maximum in run A extends a little more to the west than MOPITT. The same counts for run J, but to the south, which can be attributed to the fact that emissions sources of run A are more abundant in the northern part of Southern Africa and are therefore transported more over the Southern Atlantic. More fire emission sources of run J in turn, are situated in the southern part of Southern Africa and lead to more elevated in-situ CO concentrations over this region. This is in agreement with the prevailing wind systems over Southern Africa with generally eastern winds in a northern latitude band between approximately 0°-20°S, a transition zone with no or southward transport of air masses and a westward transport zone south from 20°S. According to Garstang et al. (1996) the transport westwards or eastward can either be direct or occur in 3 different ways within an anticyclonic circulation: either westward, eastward, or by anticyclonic recirculation). For further details on typical meteorological situations during the dry season in southern hemispheric Africa see Garstang et al (1996) or Sinha et al. (2004).

Also Figure 3.10 in Chapter 3 displaying the seasonality of the different fire emission data used in MOZART for 10 different Southern African regions, shows higher CO emissions of GWEM-1.3 (used in run A) for the northwestern regions of Southern Africa in July 2000, while run J yield more elevated CO emissions in the southern and southeastern regions.

The MOPITT comparison with run G, H and K yields a considerable low-bias in July, reaching from about 20 ppbv (run H) to over 40 ppbv (run K) (Figure 4.24). Run K, using the climatological fire emission inventory, generally shows dispersed CO concentrations, which is also reflected in Figure 3.10.

The only measurement site from the CMDL network that is located on the southern hemispheric African continent is Gobabeb in Namibia (Figure 4.25), but unfortunately measurements of the year 2000 are not available for the period July to November. However, for these months measurements of other years are shown to provide a rough estimate on the CO variability that may be expected. In months May and June runs A and J perform slightly better than the other model simulations. No clear statement can be made about other months of this year, except that all runs are largely within the range of other year observations.
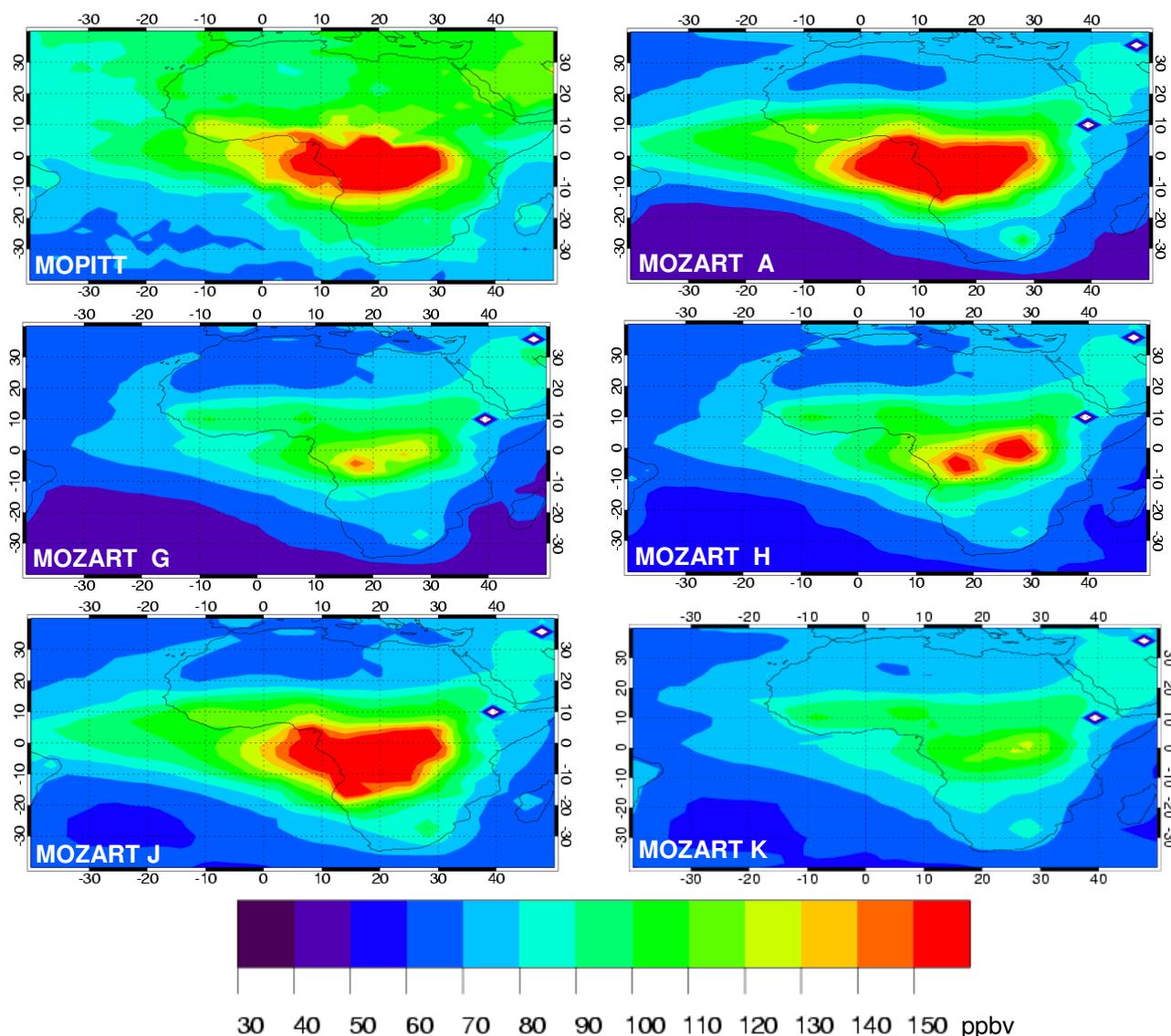
Figure 4.24: African MOPITT and MOZART CO in ppbv for simulations A, G, H, J, and K in July 2000 at 700 hPa

Off the southern Atlantic coast, there is another CMDL site on Ascension Island (Figure 4.25), that is regularly influenced by fire polluted air masses from the southern African continent. MOZART runs A and J show a clear biomass burning signal from June to August in contrast to the other three simulations. The graphs of run A and J are almost identical and improve the model performance in June by enhancing CO concentrations by 20 ppbv to match the monthly mean CMDL observations at 80 ppbv. However, they overestimate the months of July and August by 10 and 5 ppbv, respectively. September to December CO concentrations are underestimated by all runs by 5 to 30 ppbv. Offshore the east coast of equatorial southern hemispheric Africa, on Mahe Island, Seychelles, no impact from fire emissions can be observed.

The only SHADOZ site on the Southern Hemispheric African continent is situated at Irene in South Africa (Figure 4.25). In the first half of the year (January to June) MOZART simulations are not influenced by biomass burning and uniformly overestimate measured SHADOZ ozone by up to 60%. An ozone maximum in October is matched by run K and H. Run J and G are somewhat lower (about 30%) but still within the standard deviation range. Run A underestimates SHADOZ ozone by about 25%. December ozone (observed 30 ppbv) is strongly overestimated by all MOZART runs. All simulated December ozone is doubled, in case of run
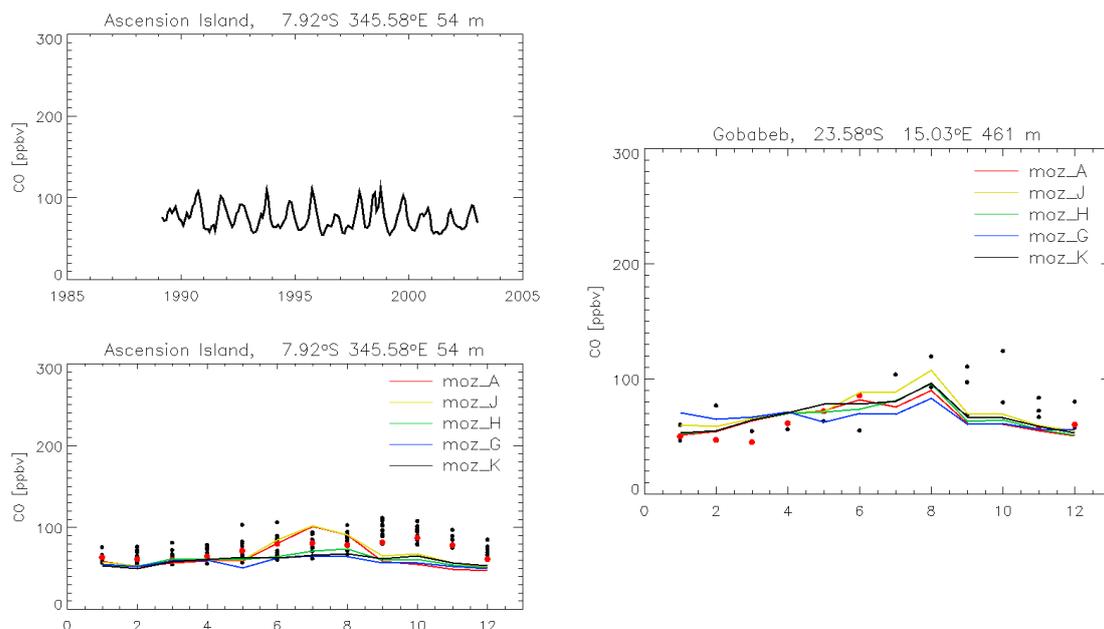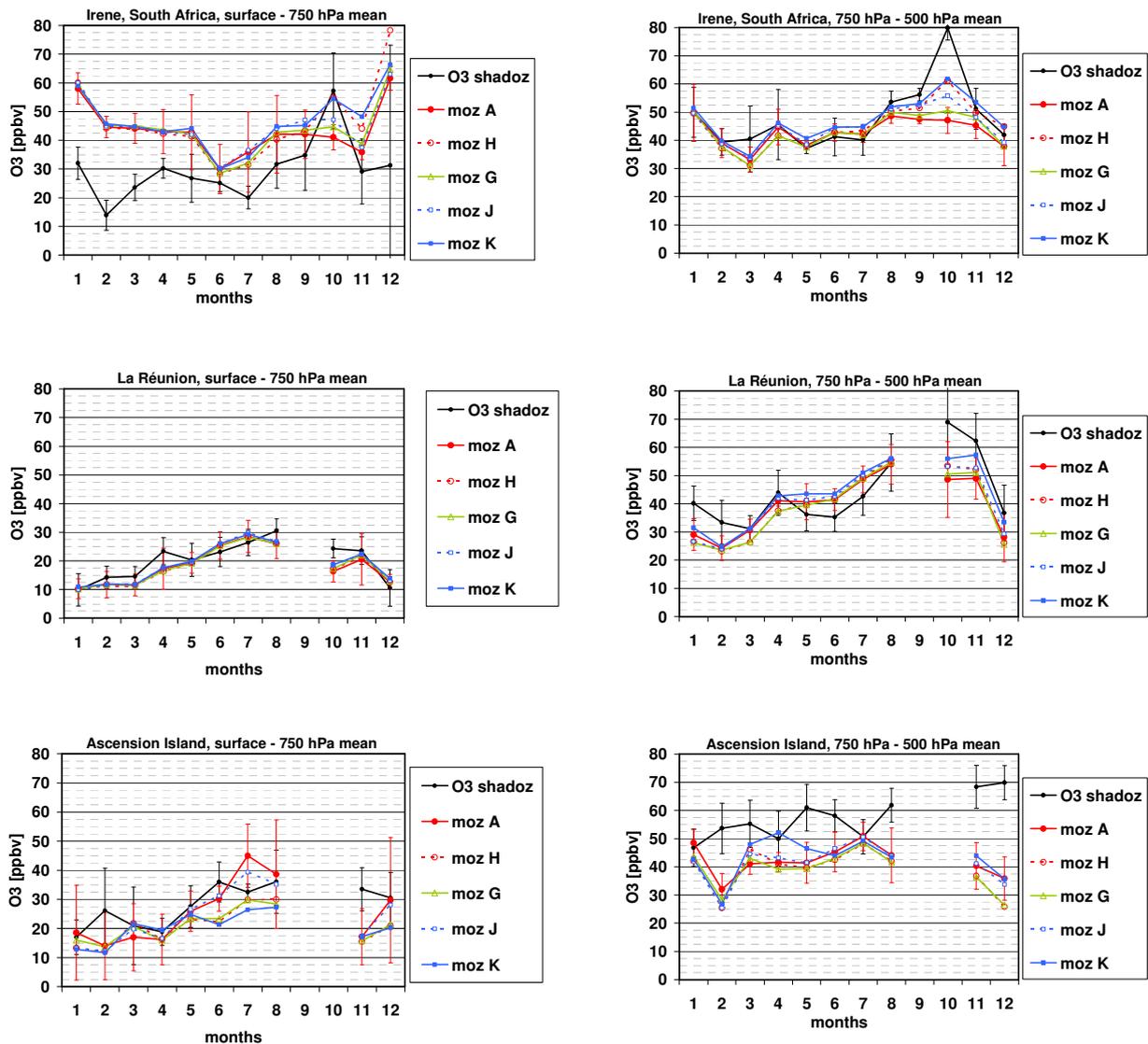
Figure 4.25: CMDL CO measurements in ppbv in the year 2000 (red dots) and available other years (black spots) at Ascension Island, South Atlantic, and Gobabeb, Namibia. Interannual variability is shown in the upper panel, year 2000 seasonality in the lower panel. The lower panel also shows MOZART-2 results for the main runs A, J, H, G, K (solid lines), as described in section 4.3

H, MOZART yields even 2.6 times more ozone than SHADOZ observations. At higher altitudes there is a good agreement within standard deviations for all runs, only the October peak is not reached by any of the runs (K and H about 25% too low, J by 30%, and G and A by 40% lower than observations. At surface, R^2 correlations are not significant (R^2 below 0.2, see Table C4a), while at the 750 hPa layer correlations are considerably better. Run K correlates best (R^2=0.78), closely followed by run H (R^2=0.77, see Table C4b).

Off the African continent, but influenced by transport of biomass burning polluted air masses, are two more SHADOZ stations at Ascension Island in the South Atlantic and on Réunion in front of the southern African east coast (also Figure 4.26). Réunion does not reflect a high variability in simulations due to fires. Ascension Island site is missing data for September and October. In the first part of the year (January to May) and in December, MOZART ozone is generally in the standard deviation range of SHADOZ observations. There is a low bias for June. Run A and run J are still within the standard deviation range (lower end). All runs calculated a maximum in July, the most pronounced of which is provided by run A (45 ppbv), followed by run J (40 ppbv). Observations are at about 35 ppbv. All MOZART runs are about 50% lower than measurements in November. Also in the 750 hPa to 500 hPa layer a maximum is observed in July that is well reflected by all MOZART runs. November and December are strongly underestimated by all runs. R2 correlations for each MOZART run versus SHADOZ observations (Tables C4a, b) do not reveal relevant correlation patterns (all below 0.7). Run J and K at least show R^2-numbers over 0.5 for the near-surface layer.

MOZAIC data for the year 2000 are available for the airports situated in Brazzaville, Congo, in Luanda, Angola, and in Harare, Zimbabwe. In Brazzaville (Figure 4.26a) a pronounced ozone plume can be observed in all MOZAIC monthly mean profiles between 2-3 km altitude. All MOZART runs reflect this plume (except climatological run K for June and July), but with a 0.5-1 km lower maximum. This ozone plume is a result of fire activity in this region, since run D (yellow line), which excludes all fire emissions, does not yield any ozone enhancement in its vertical profile for any of the months. All MOZART simulations are improved by using their specific underlying fire emission data sets compared both to run D

Figure 4.26: Southern African SHADOZ ozone measurements in ppbv from radio soundings at Irene, South Africa, on La Réunion in the Indian Ocean, and on Ascension Island in the South Atlantic in the year 2000 and corresponding MOZART-2 graphs of the five main runs A, J, H, G, and K. Seasonalities of monthly mean ozone are averaged from the surface level to 750 hPa on the left-hand side and for 750 - 500 hPa on the right-hand. Error bars are standard deviations

without fire emissions, but also compared to run K, based on the climatological fire emissions, for most months. In June, run A and run J severely overestimate ozone, while in July ozone is well represented by run J. While still severely overestimating in July, run A shows the best ozone representation in August, compared to all other runs. There is a good agreement for June ozone concentrations of runs G and H in the lowest 2 km.

Also in Luanda, all MOZART runs are improved by including fire emissions (compared to run D). Run K fails to represent the fire-related ozone plumes during the fire season (here July and August). The profile of July shows too elevated concentrations for run A and J near the surface (run A: 45% more ozone than in observations, run J: 25% more ozone). If fire emissions were lifted up higher into the troposphere in MOZART, the ozone plume in August as simulated by run A and J would match the MOZAIC measurements within their standard deviation.

Finally, further south in Harare, Zimbabwe, some influences from fire activity on the ozone budget can be observed and the different MOZART simulations show some discrepancies: in
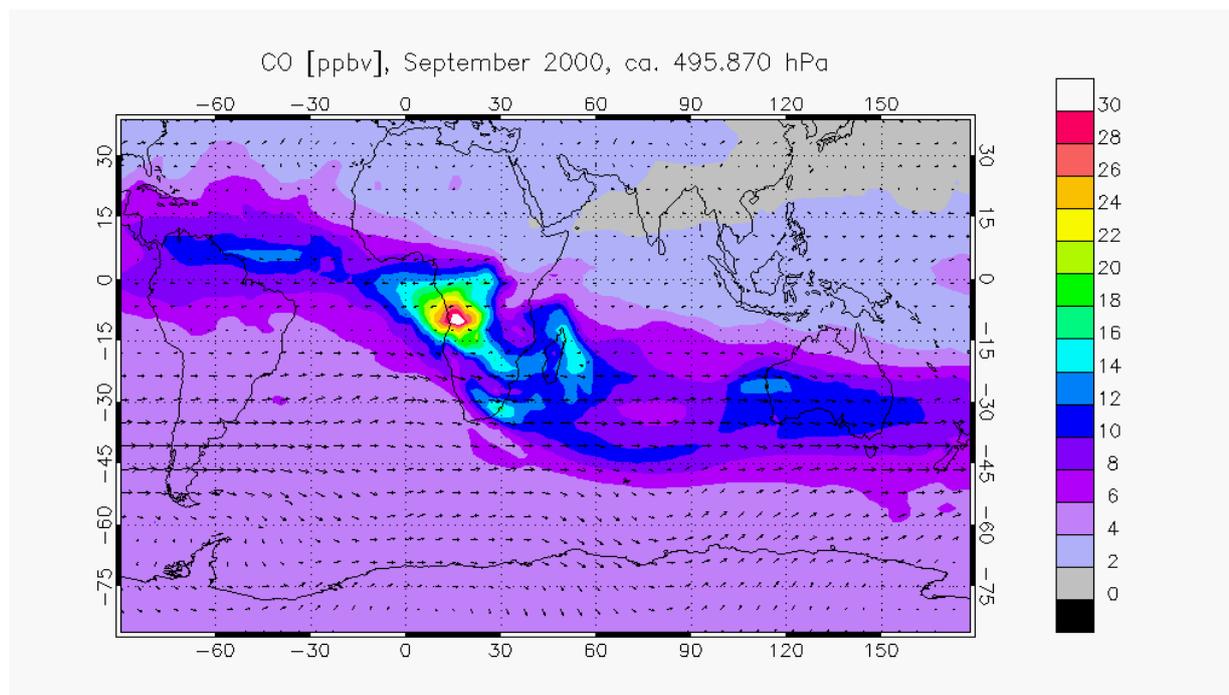
Figure 4.27: Mean CO concentrations of MOZART run A–E for September 2000 in ppbv at ~500 hPa. CO concentrations result exclusively from fires in southern hemispheric Africa

January, the upper troposphere over Harare (4 km - 9 km) is strongly influenced by fire-related ozone production, which provokes some divergence in the different MOZART ozone profiles. Since January is outside the typical fire-season in the middle of Southern Africa and the plume is highly above the boundary layer, this indicates that the observed and modeled ozone was transported from other regions.

An inspection of the MOZART simulations reveals that the ozone stems from the typical ozone plume over the southern Atlantic and was transported over southern hemispheric Africa. Thus, this ozone occurrence is also a child of fire emission precursors, although stemming from remote regions in northern hemispheric Africa and South America (see the "ozone-paradoxon" description in northern hemispheric African discussion above). In this specific case, the conclusion is that close to all of the ozone over Southern Africa emerged from emissions produced from Northern African fires, because there is almost no discrepancy in run A (GWEM based fire emissions) and run J (GFED based fire emissions): the GWEM model yields very low fire emissions in South America, while the GFED inventory presents considerably higher fire emissions in this region. If the ozone over southern Africa in January were to be produced by Southern American fire emissions, a large discrepancy between MOZART run A and run J would be encountered.

 Compared to the "no-fire-simulation" run D, all MOZART simulations improve the model performance with their different fire emissions. However, run G and H do not show a pronounced ozone plume in about 6 km height, as reflected in the MOZAIC measurements. Run A and J are close to the climatological run K, which surprisingly reflects the best ozone concentrations compared to measurements with a pronounced plume. Still, ozone concentrations are about 20 ppbv too low. In August all MOZART simulations show a small plume within the boundary layer that is not observed by MOZAIC aircrafts. In September, a small ozone enhancement at about 2.5 km altitude is well reflected by run A, G and H, overestimated by run J and K, and neglected by run D, and thus also fire-related.

For most cases the two runs G and H that are based on ATSR-scaled fire emission inventories show similar performances both in the simulation of carbon monoxide as of ozone. Surprisingly, in many situations this is also the case for the two runs A and J that are based

on completely different fire emission data that rely on different satellite fire information. All MOZART simulations A, J, G, and H are better than the "no-fire" run D and also than climatological run K. Run G and H have the tendency of yielding too low CO and ozone concentrations. This can be traced back to the fact that the nighttime-observed ATSR fire pixels used for the underlying fire emission estimates miss many fire occurrences in regions where short daytime fire-practices are common (e.g. tropical deforestation fires and savanna maintenance fires). In contrary, run A and J have a tendency of overestimating CO and ozone concentrations, which is especially evident in the MOZAIC ozone profiles (e.g. Luanda in July, Brazzaville in June, Figures 4.28a and b). Overestimates by run A are stronger and are due to the overestimate in burned biomass in wooded savanna ecosystems for fire emission calculations, as already mentioned for northern hemispheric Africa. According to Chapter 3, Figure 3.10, CO emissions from fires as calculated by the GWEM model (used in run A) are higher than those from all other inventories in the southern African sub regions 1, 3, and 5 located along the west coast (Figure 3.8). These defined regions include the cities of Brazzaville and Luanda of the MOZAIC profiles.

Sinha et al. (2004) conclude in a transport study of biomass burning emissions from Southern Africa that during a direct and consequent anticyclonic circulation eastward transport event (entitled "river of smoke" by Annegarn et al. (2002)) in September 2000, enhanced CO concentrations over the Indian Ocean and even Australia could be observed. As reflected in Figure 4.27, the MOZART model also reproduces these results. The figure presents a CO concentration difference plot in the midtroposphere of MOZART run A (using the GWEM-1.3 fire emissions) and run E that excludes emissions from fires in southern hemispheric Africa. Over the subtropical Indian Ocean, CO concentrations are enhanced by 4-14 ppbv by the transport of CO resulting only from fires in Southern Africa. Over Melbourne, Australia, Figure 4.27 shows CO abundances from 8-10 ppbv that are also exclusively a product of Southern African fires. These CO enhancements are in excellent agreement with the range of values found by Sinha et al. (2004) and evaluated with in-situ measurements. Further, Figure 4.27 shows elevated CO concentrations over northern South America, transported by westwards winds from Southern Africa. The CO enhancement is in the same order as CO abundances over Australia (6-14 ppbv), which highlights the role of long-range transport and thus, intercontinental impacts of biomass burning emissions on the chemical composition of the atmosphere.

a)

b)
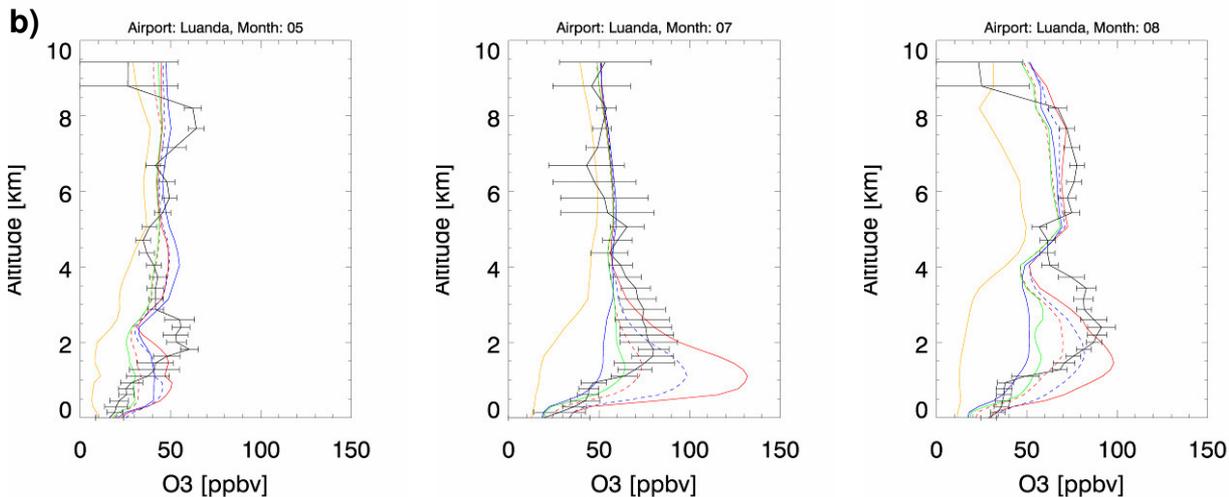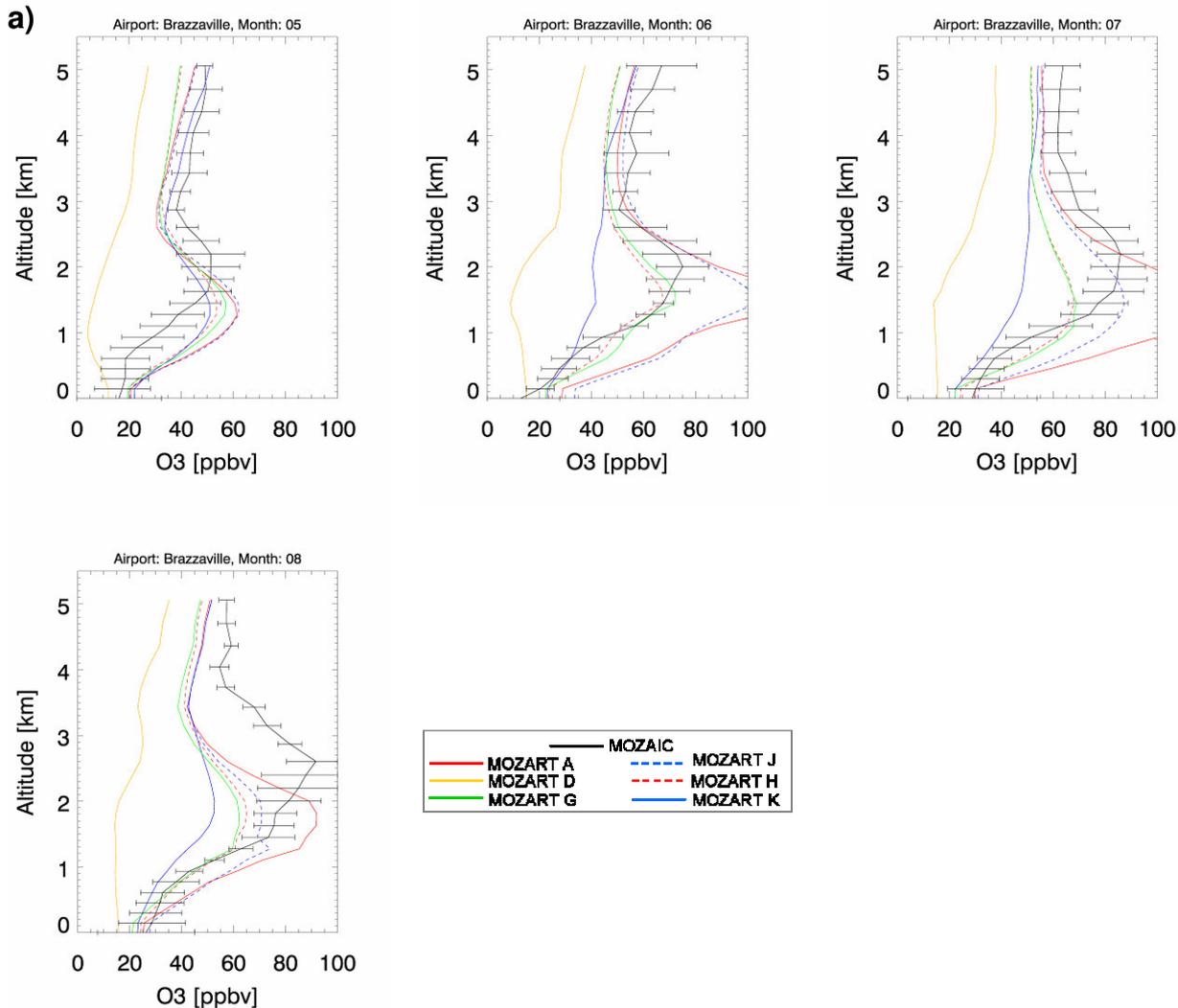
Figures 4.28a,b: MOZAIC monthly mean ozone aircraft measurements (black) and corresponding MOZART simulations in ppbv at **a)** Brazzaville, Congo airport from May to August 2000 and **b)** Luanda, Angola airport for May, July and August. MOZART runs: A (red solid), D (orange), G (green), H (red, slashed), J (blue, slashed), and K (blue solid). Scales in a) and b) differ
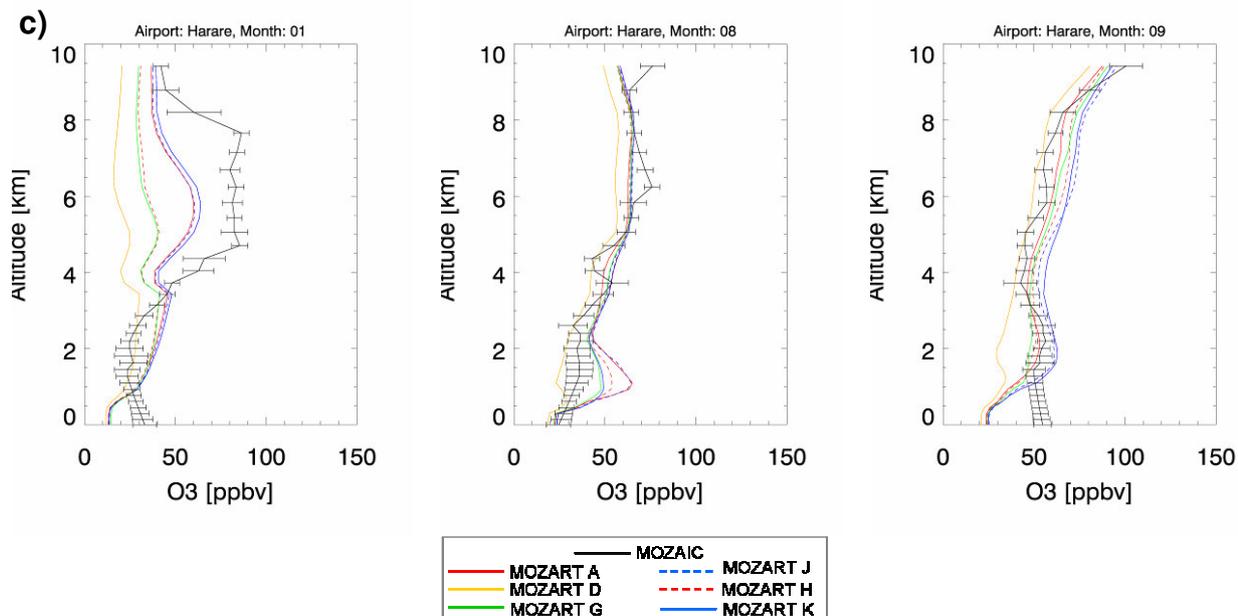
Figures 4.28c: MOZAIC monthly mean ozone aircraft measurements (black) and corresponding MOZART simulations in ppbv at Harare, Zimbabwe airport for January, August and September 2000

Synthesis for Southern Hemispheric Africa

The chemistry of the lower troposphere over Southern Hemispheric Africa, as expected, was strongly influenced by emissions from fires in the months from May to October 2000. This impact can well be observed in CO and ozone measurements at the surface but also from aircrafts and satellite. The effect of the burning season on CO but also for ozone concentrations is also well reflected in all MOZART simulations. CO in 700 hPa altitude compared to CO from the MOPITT instrument was best represented by run A and run J, based on the new bottom-up inventories GWEM and GFED, respectively. This is valid for the early burning season from May to August. Later, for the months of September and October 2000, all runs considerably underestimate CO compared to MOPITT with run J producing somewhat more elevated CO concentration from fires than run A. The October ozone maximum observed at the only ozone measurement site from SHADOZ on the Southern African continent (Irene, South Africa), agrees temporarily well with the CO maximum observed by MOPITT. Compared to ozone observations from MOZAIC, no clear MOZART run favorite could be determined. However, it can be said that run G and H are most times somewhat too low in their ozone concentrations, to the same extent that run A and J overestimate ozone. In some months, run A severely overestimates ozone quantitatively (by over 50%), but in other occasions run A represents the measured ozone observations rather well. All MOZART simulations reduce the model-observation discrepancy compared to the model run that excluded all fire emissions (run D) and also mostly with regard to the climatological run K. As in the northern hemisphere, most of the times the height of the simulated ozone plumes was too low in MOZART.

A comparison of MOZART run A results with a published model analysis over Southern Africa (Sinha et al., 2004) reveals a very good agreement of remote CO concentrations of the studies over the Indian Ocean and Australia, which were a product of fires in Southern Africa.

4.5.2 South America

**South American CO emission source partitioning
for MOZART run J (gfed)**
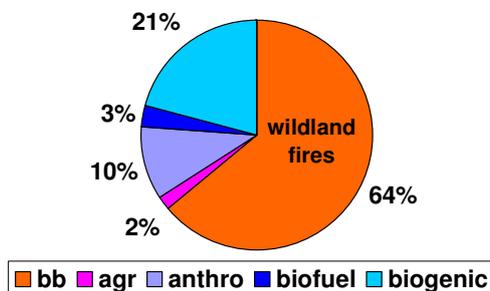
Figure 4.29: CO emission source partitioning in MOZART run J for South America in the year 2000

South America has been chosen as second region to discuss as it is the second major player in terms of global fire emissions. About 2/3 of emitted CO over South America during the year 2000 can be attributed to fires (Figure 4.29) followed by biogenic emissions, which contribute with about 1/5 to the CO budget.

A large amount of deforestation and maintenance fires take place on a regular basis every year in primary and secondary forests but also in wooded savanna (Cerrado) mainly in the Amazonian region and Central Brazil. These fires serve the purpose of conversion of vegetated areas for cattle-ranching i.e. to promote fresh grass growth during the dry season (Coutinho, 1990 and Mistry, 1998) and extended plantations of crops (Potter et al., 2002; Cardoso et al., 2003 and Cochrane 2003), such as soybean, rice, beans and cassava (Klink et al., 1993 and Mistry, 1998). Burning takes place during the southern hemispheric winter from May to October, with a maximum at the end of the dry season from August-September (Mistry, 1998). The annual area burned by fires is in the order of 40 000 km^2 for South America. These anthropogenic controlled fires are responsible for the emission of a significant amount of trace gases and aerosols (e.g. Artaxo et al., 1998). Their emitted smoke plumes that are distributed by atmospheric transport regularly cover an area of around 4-5 million km^2 (Freitas et al., 2005b). On the continent during the dry season, fires dominate the emission scenarios outside the mega-cities. The trace gas composition of the atmosphere changes significantly during this time of the year, altering the regulating mechanisms of atmospheric composition (Longo et al., 1999).

Many times fire emissions are transported over long distances over the Southern Atlantic or over the tropical Pacific by the prevailing wind systems (Freitas et al., 1997), which turn South America into an important fire emission -and thus ozone precursor- export continent.

Large differences in the existing fire emission inventories for chemical transport studies over South America reinforce the need of an intercomparison and seek for reasons. The year 2000 under investigation was a year with lower fire activity due to enhanced precipitation on the South American continent, compared to earlier and subsequent years (P. Artaxo, K. Longo, pers. communication, 2004).

In this study, comparisons to MOPITT CO retrievals show large discrepancies between the different MOZART simulations over South America (Figure 4.30). MOZART run A with the underlying GWEM-1.3 fire emissions for South America fails to reflect a realistic carbon monoxide distribution for the year 2000. The very low fire emissions from GWEM-1.3 that
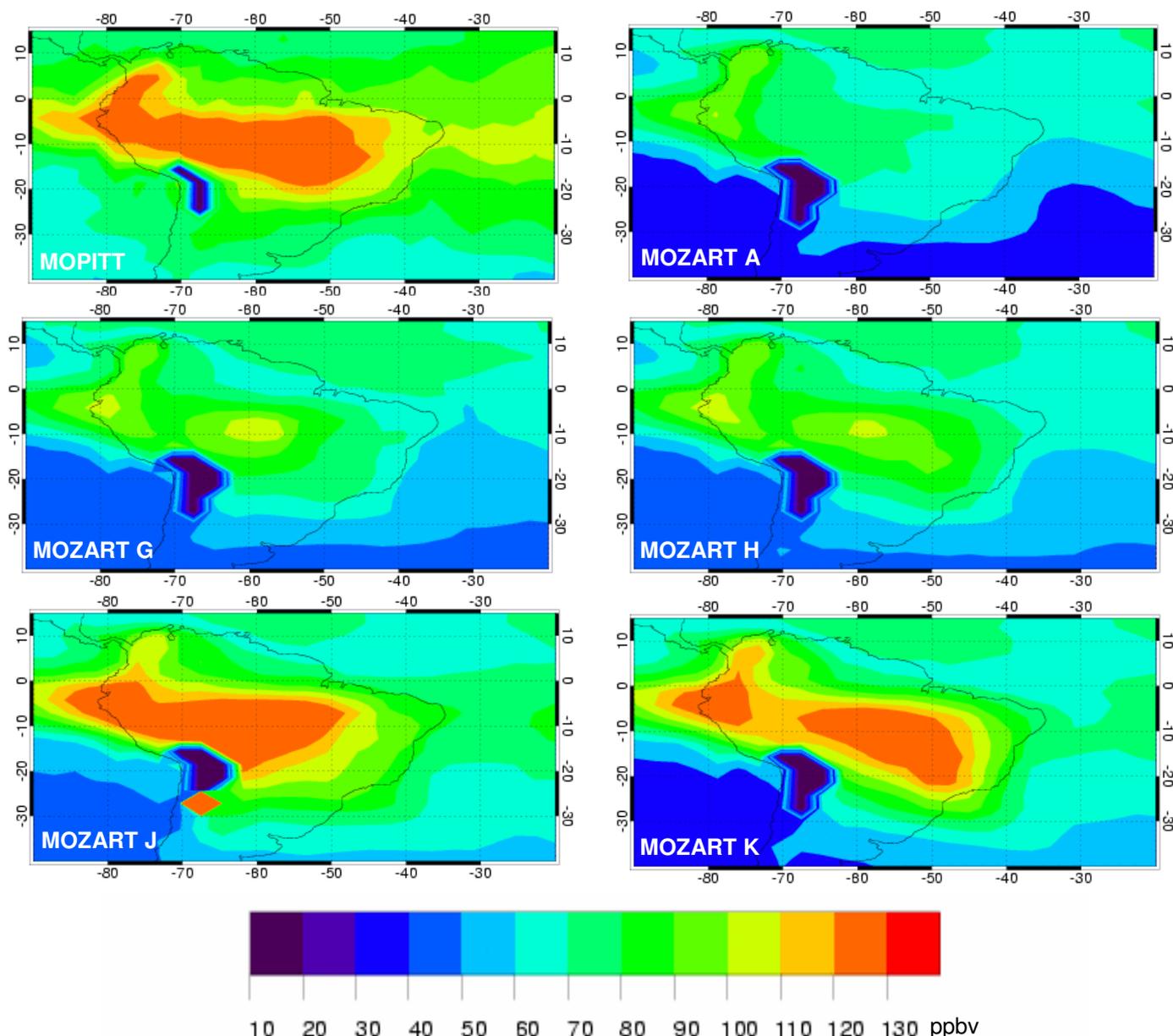
Figure 4.30: South American MOPITT and MOZART CO in ppbv for simulations A, G, H, J, and K in September 2000 at 700 hPa

are additionally located outside the regular fire regions and season, are a result of deficiencies of the underlying GBA2000 area burnt product that has been used in this GWEM version. In Brazil for example, an excess of cloud cover and small burnt areas lead to a strong underestimate of burnt areas. Many fires additionally occur only beneath the canopy and a therefore not visible from space. Further, the mountain topography of the Andes causes shadows that lead to some false detections. (http://www-gvm.jrc.it/TEM /Disturbance%5Fby%5Ffire/products/burnt_areas_/global2000/gba2000_data.htm). In more recent GWEM versions (see GWEM-1.4 presented in Appendix A) the GBA2000 product has been replaced by a compilation of various satellite fire products from the Centro de Previsão de Tempo e Estudos Climáticos (CPTEC/INPE) in Brazil (see http://www.cptec.inpe.br/queimadas/).

A slightly better, but still considerably too low CO scenario can be seen for both the figures of run G and H for the month of September in Figure 4.30. The maxima of these two runs are found in September (northwest of South America) and October (Amazonia). According to MOPITT, a clear maximum of CO concentrations at 700 hPa is found in October, followed by

September and then November. This seasonal and quantitative feature is fully reflected by run J and surprisingly, by run K. Obviously, the simpler temperature-threshold based fire pixel detections that were used to calculate the emission inventories of runs H, G, and J are able to reflect the real emission situation in Southern America better than the global area burned product GBA2000 used for the run A fire emissions. This problem persists also with the new generation products from MODIS, when comparing active fire pixels to the real area burned product (presentation by David Roy, on the 5th International Workshop on Remote Sensing and GIS Applications to Forest Fire Management: Fire Effects Assessment, in Zaragoza, June 16-18th, 2005, entitled: Global mapping of fire-affected area using multi-temporal MODIS data). However, also the ATSR fire pixel product used for fire emission estimates in run G and H are considerably too low, as only nighttime detections of fires are possible with this sensor.

Unfortunately, there is no CMDL station in the Amazonian region, where almost all of the fires in South America occur. There is only one site northeast of South America at Ragged Point, Barbados and another at the opposite end in the south at Tierra del Fogo, Argentina. Time series at both stations are practically smooth and do not reveal any major influence from biomass burning. Only in the month of August, at Ragged Point, Barbados, run A has about 10 ppbv higher CO concentrations than the other MOZART simulations and therewith matches well the monthly mean CO observations. Only the CMDL site at Ascension Island (Figure 4.25) is located in the Southern Atlantic outflow region of South America and shows enhanced CO concentrations from July to October. This CO increase is a combined effect of Southern African and South American fire emissions (see discussion in previous section).

There are three SHADOZ sites in South America (Figure 4.31): one is located in Brazil in Natal and two further north in Paramaribo, Suriname and in the Pacific on San Cristóbal Island. At Natal in the boundary layer (averaged from the surface to 750 hPa), MOZART values are within the range of the standard deviation of SHADOZ ozone for January to April. The same holds for November and December. In May and June however, ozone concentrations are overestimated by all runs, especially runs A and J (about 15 ppbv higher than measured values). From August to October all runs underestimate SHADOZ ozone by up to 50% (10-15 ppbv lower). In higher altitudes (750-500 hPa layer) the behavior is similar. Paramaribo and San Cristóbal observatories yield similar features in the model: run A and J highly overestimate ozone in June to August (50% more ozone in June). Other runs also overestimate by 20–25%. Since this is a general observation of all MOZART runs, regardless of the underlying fire emission inventory, this feature is apparently not related to fire activities. The seasonality of both observatories is different from the modeled data. For example, average observations in the 750-500 hPa levels at San Cristóbal show a very slight ozone maximum in October, where most model runs have a minimum that yields only 40% of the observed ozone concentrations. At these higher levels, the average MOZART ozone concentrations all show a maximum earlier in July. Along the season, monthly ozone model values lie within the range from 30 to over 50 ppbv, while the SHADOZ ozone concentrations are between 20-40 ppbv. The different MOZART simulations agree in their general seasonality, except for the climatological run K in higher altitudes (Figure 4.31).

Measurements from MOZAIC aircrafts starting and landing on South American airports are available for Rio de Janeiro and São Paulo in Brazil, from Bogotá, Columbia and from Caracas, Venezuela (Figure 4.32). In south eastern Brazil influence from fire emissions can typically be observed from July through September. For the year 2000 there are mainly measurements outside the burning season that do no reveal any influence from fires on the ozone budget over Rio de Janeiro and São Paulo. Relevant discrepancies between the different MOZART simulations could only be found for November (Rio) and December (São Paulo). The simulated ozone concentrations over Rio de Janeiro are better in all MOZART runs that include a fire inventory, compared to the "no-fire" run D (Figure 4.32a). However,
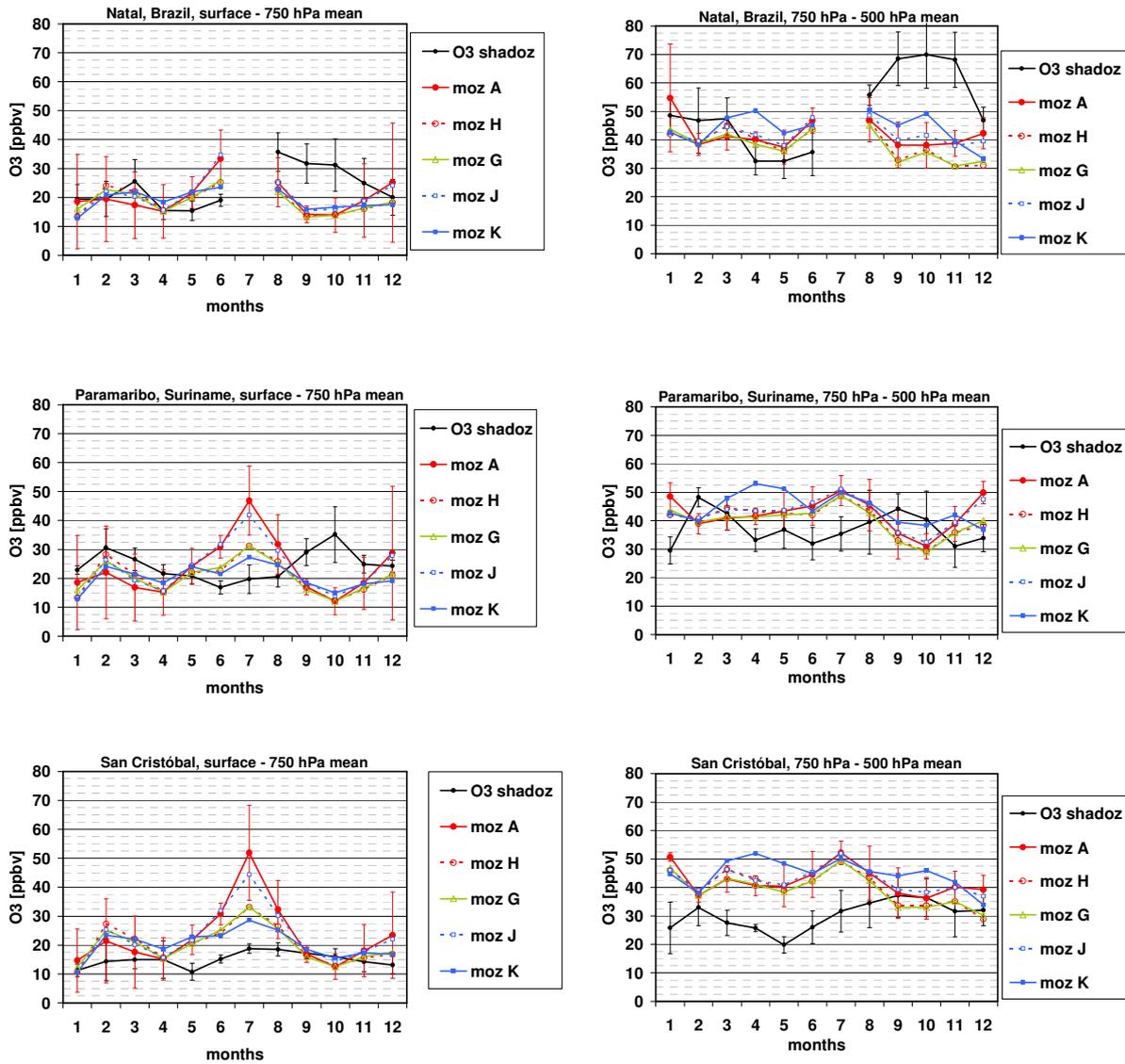
Figure 4.31: Southern American SHADOZ ozone measurements in ppbv from radio soundings in the year 2000 and corresponding MOZART-2 graphs of the five main runs A, J, H, G, and K. Seasonalities of monthly mean ozone are averaged from the surface level to 750 hPa on the left-hand side and for 750 - 500 hPa on the right-hand. Error bars are standard deviations

the old climatological fire emission based run K remains closest to the measurements for Rio de Janeiro, followed by run H, one of the ATSR-scaled fire emission inventories (mgs_scal). Still, the ozone peak in about 1.5 km height is underestimated by about 15 ppbv (20%). An inspection of the MOZART simulations reveals that the fire emission-related ozone loaded air is transported from the states of southern Mato Grosso, northern Mato Grosso do Sul, and eastern Goiânia across the south eastern coast of Brazil where fire activity at this time of the year can still be abundant.

Figure 4.32b shows the ozone situation over São Paulo in December 2000: since the different MOZART ozone simulations were diverging at about 5 km height, the scale has been extended to almost 10 km altitude. Until about 3 km from surface the atmosphere over the city of São Paulo was mainly not perturbed by fire emissions. All MOZART runs show a very similar behaviour.

Remarkably, the simulation without fires (run D) performs best in the free troposphere, followed pair-wise by run G and H and then by run A and J. Climatological run K yields the highest ozone concentrations, which are more than doubled compared to the MOZAIC
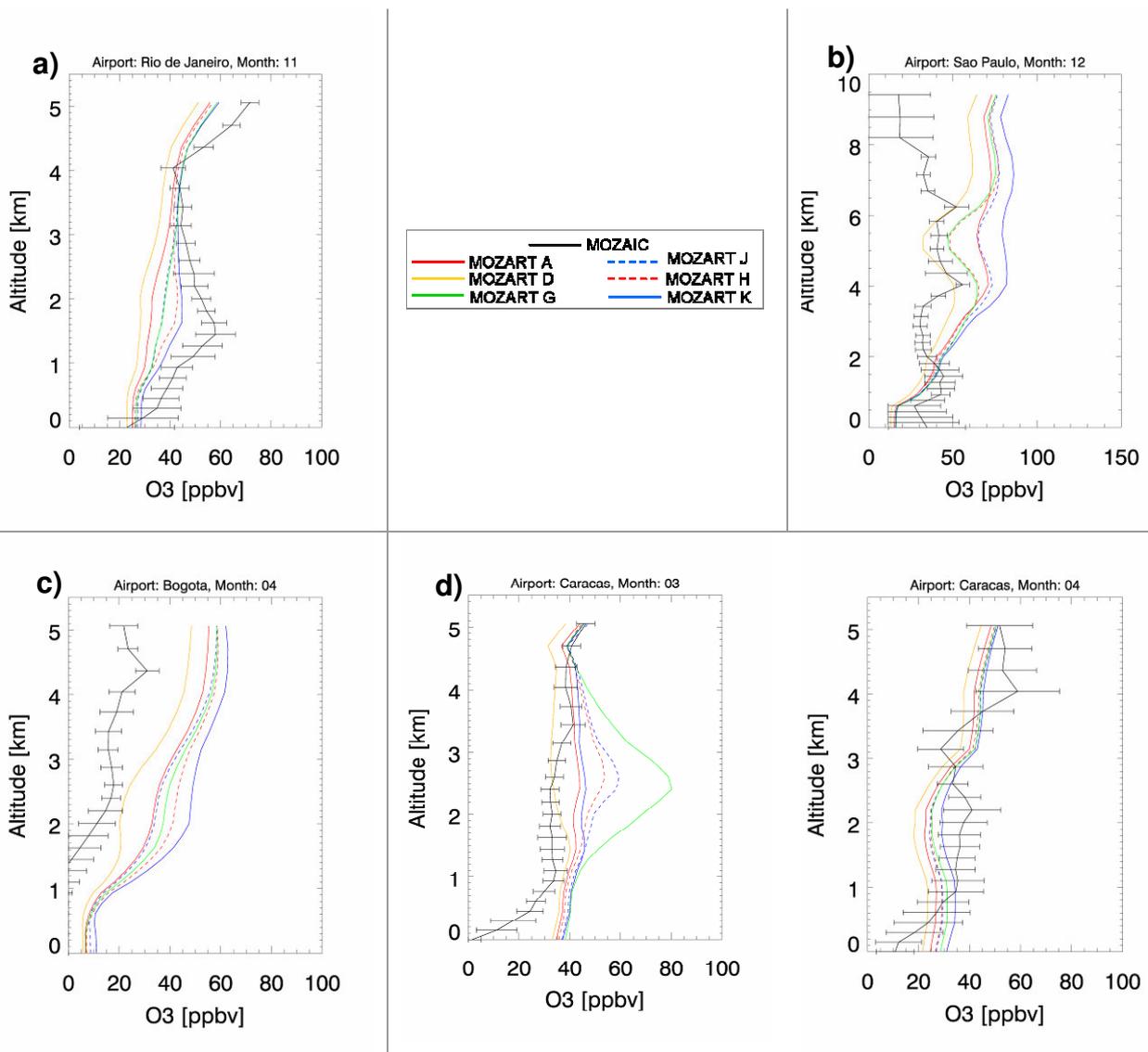
Figure 4.32: MOZAIC monthly mean ozone aircraft measurements (black) and corresponding MOZART simulations in ppbv at a) Rio de Janeiro airport in November, b) São Paulo airport in December (different scale!), c) at Bogotá airport in Colombia, and d) at Caracas, Venezuela airport in the year 2000

observations in about 5 km height. As over Rio de Janeiro this feature is an effect of transported air masses from the state of Mato Grosso do Sul and does not have local origins. In Bogotá, Columbia ozone concentrations were measured only in April 2000 and are best matched by run A, however all runs overestimate MOZAIC observations throughout the vertical profile. Also run D, without any influence from fires, still overestimates ozone concentrations, but to a lesser extent than all other MOZART runs.

The good agreement of run D, without any fires, in South America is a recurring feature for this continent and is also reflected in the MOZAIC ozone in March over Caracas, Venezuela. Only at a height from 3 km on, the MOZART runs including fire emissions improve the ozone result compared to run D and matches the observations within the error bars. Run G shows an extremely high ozone maximum of 80 ppbv at about 2.7 km altitude that is not measured by the MOZAIC aircrafts (around 35 ppbv). A little maximum is also reflected in run H and run J. Only run A, based on the GWEM fire inventory and climatological run K yield a similar behaviour as the ozone observations. In April, run A also simulates ozone concentrations somewhat better than the other fire emission based runs up to an altitude to 1.7 km. Again, run D is closest to the MOZAIC ozone observations. In higher altitudes, the situation is

reversed and all MOZART runs have closer values to the observation profile, with climatological run K performing best (between 1–2.8 km). It remains unclear, whether one of the discrepancy reasons may be the lack of uplifting fire emissions into higher MOZART model levels.

Synthesis for South America

The chemical scenario over South America presented by diverse measurements and the different MOZART simulations cannot be easily resumed. According to MOPITT carbon monoxide satellite measurements, MOZART run J, based on the GFED fire emission inventory, yields the most similar CO concentrations quantitatively and in its seasonal distribution. Also, the climatological MOZART run K performs reasonably well compared to MOPITT data of the year 2000. All other fire emission inventories used in MOZART runs A, G and H seem to have difficulties to represent a realistic chemical scenario over South America. The reason is the performance of the GBA2000 area burnt product (in case of run A) and ESA´s ATSR active fire pixel product (used in runs G and H), which only monitors fire during night. Most deforestation and savanna maintenance fires are lit and extinguished during one day and can therefore not be captured by overnight satellite overpass. In case of the GBA2000 product, the arising detection problems are related to the small extension of fires in South America (compared to large wildland fires), the overpass frequency, and a small change in surface albedo when conversion from dark green tropical forest to burned area takes place. Additionally, temporarily water-covered vegetation types (swamps, e.g. the Pantanal in Brazil) and areas covered with dark stones (e.g. in the Andes) lead to severe commission errors of the satellite fire product (see also Chapter 2). However, it should also be noted that considerable uncertainties remain by using MOPITT CO to evaluate modeled CO concentrations over South America. For example, two different inversion studies based on the same MOPITT data arrive at estimates for South American fire emisons which differ by a factor of four (Pétron et al., 2004; Arrellano et al., 2004).

According to an intercomparison with SHADOZ ozone radiosondes, MOZART seems to overestimate ozone in the north of South America, regardless of the fire emission inventory used. Closer to the surface the MOZART simulations A and J based on the new bottom-up inventories GWEM and GFED, respectively, present the strongest overestimates from June to August 2000. From a strictly statistical point of view, Tables C4a and b in Appendix C reveal no relevant R^2-correlations between model runs and ozone observations for any of the stations in South America.

The four MOZAIC aircraft ozone profiles allow the conclusion that essentially none of the new fire emission inventories substantially improves the MOZART ozone simulation. In most cases MOZART run D that excludes fire emissions shows the best performance compared to the measurements. Many times even the climatological fire emissions-based run K is better than the other MOZART simulations.

In summary, it can be said that a better fire emission inventory for MOZART is not the ultimate solution for a better model performance in terms of ozone concentrations in South America. Since the airports where MOZAIC aircraft measurements were carried out are located in or close to large cities, a complex combination of NO_x and VOC´s from local pollution combined with transported pollution from industry and also fires from elsewhere are responsible for the formation and depletion of ozone in the surrounding atmosphere.

However, the MOPITT-MOZART intercomparison also suggests that the concentration of directly emitted species, such as CO, can in fact be improved on a regional and intercontinental scale by the inclusion of more adequate fire emissions in the model.
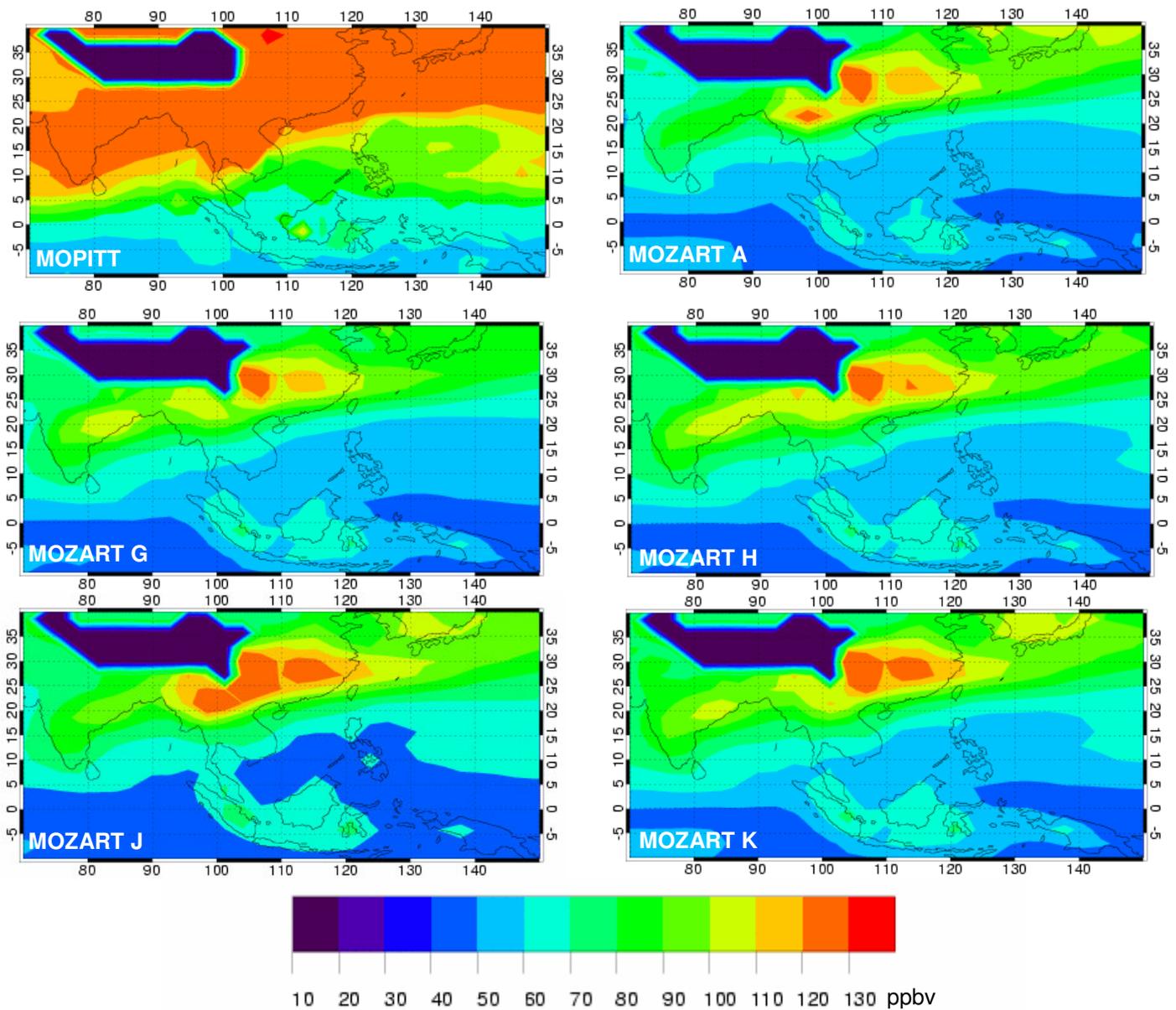
4.5.3 Southern Asia and Australia
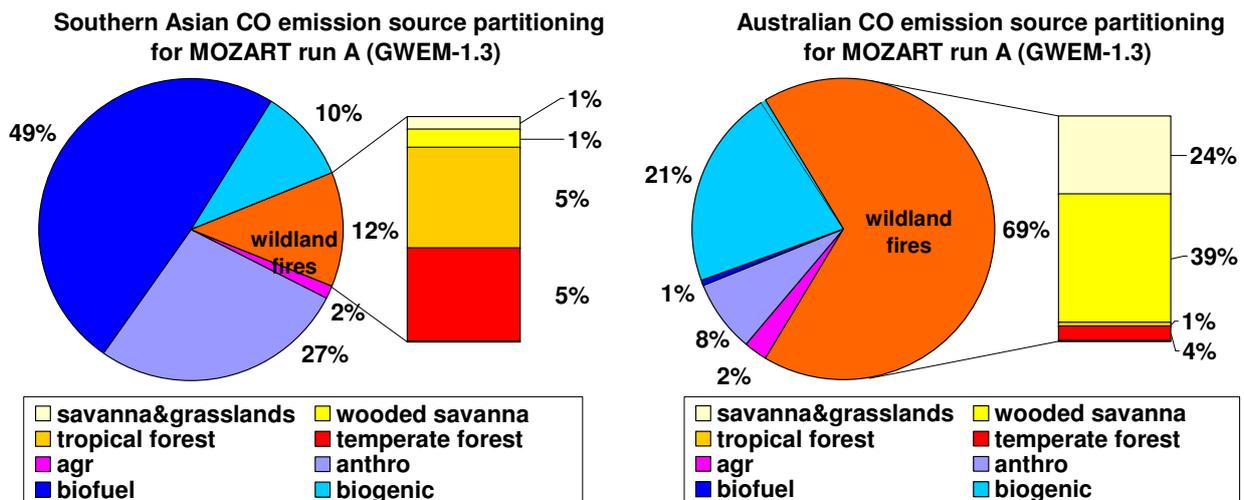
Figure 4.33: CO emission source partitioning in MOZART run A for Southern Asia (left) and Australia (right). Sub-categories as in Chapter 3

Southern Asia is a region highly influenced by a variety of emission sources (Figure 4.33, left). Especially biofuel emissions are the main contributor to abundant CO concentrations (~50% of total). The appearance of satellite fire products in recent years however, has revealed that fires sometimes also play an important polluting factor, -not only in Indonesia but also on the Asian continent. Since a number of publications in recent years have focused on Indonesian peat and forest fires and their impacts (e.g. Hauglustaine et al., 1999; Page et al., 2002, Heil et al., 2005), comparably little is still known about burning practices in other Southern Asian countries. According to Schultz et al. (2005) there are strong indications that fires in Southern Asia might be related to deforestation processes and also involve the burning of peat layers.

On the Southern Asian continent, fires occur during northern hemispheric spring (from March to May) and to a smaller extent again in September/October, as can be verified by the fire emission inventories for the year 2000 used within this work (see Figure 3.7, Chapter 3). This is also confirmed by Streets et al. (2003) who have based the seasonality of their fire emission estimates on a fourth fire satellite product from the NOAA Advanced Very High Resolution Radiometer (AVHRR) of the World Fire Web (WFW). Streets et al. (2003) also state that the year 2000 was a regular year with regard to burning occurrences.

In Indonesia, globally relevant fire activity occurs on an annual very irregular basis and is strongly related to the El Niño event. Controlled land-clearing and land-conversion fires are regularly set during the dry season from June to October (Olson et al., 1999) and cease with the start of the raining season. During an El Niño period the rain is suppressed which leads to prolonged drought periods in Indonesia and thus results in more anthropogenic burning processes that under these conditions may get out of control (Heil and Goldammer, 2001) In addition, the drying of peat swamps caused by e.g. drought or human selective logging processes (or both) leads to a fire susceptibility of ground layers that under undisturbed conditions would not contribute to the carbon release of fires. Once setting the vegetation on top of these several meter deep layers on fire, the peat is partly combusted by the initial surface fire on top. Once ignited, peat fires in the ground cannot be easily traced or extinguished. This process causes a release of enormous amounts of trace gases and aerosols into the atmosphere. (e.g. Levine, 1999; Page et al. 2002) Since combustion occurs under oxygen-poor smoldering conditions, an enhanced fraction of the incomplete combustion product CO is emitted. A detailed investigation of Indonesian peat fires and their effect on the atmosphere has been studied by Heil et al. (2005) and Heil (2006, PhD thesis in preparation at the Max Planck Institute for Meteorology, Hamburg, Germany).

Figure 4.34: Southern Asian MOPITT and MOZART CO in ppbv for simulations A, G, H, J, and K in April 2000 at 700 hPa

In contrast, most Australian fires occur regularly every year with strongest emissions being observed in the savannas of the northern part of the continent during the months from June to November, during the dry season. Fires occur also in central Australian grasslands from September to March, in forests along the eastern coast (September to January), and during drought periods also in forests situated in the south-east and south-west (Bradstock et al., 2002).

Compared to MOPITT CO, all MOZART runs show very low CO concentrations over Southern Asia and North Australia. Simulated CO concentrations are in the order of 30 % lower than MOPITT observations over large areas (Figures 4.34 and 4.35). According to MOPITT, whole continental Southern Asia is covered by CO concentrations between 120-130 ppbv in April 2000. This is not the case for all of the MOZART simulations, which uniformly only yield 80-100 ppbv CO. This low-bias in the northern hemisphere has been discussed earlier in this chapter in the global discussion (see section 4.2.2). Differences in the MOZART runs, and thus related to the difference in fire emissions can be observed over Central China occurring in a large area stretching from the southwest over to the northeast towards Shanghai. All of
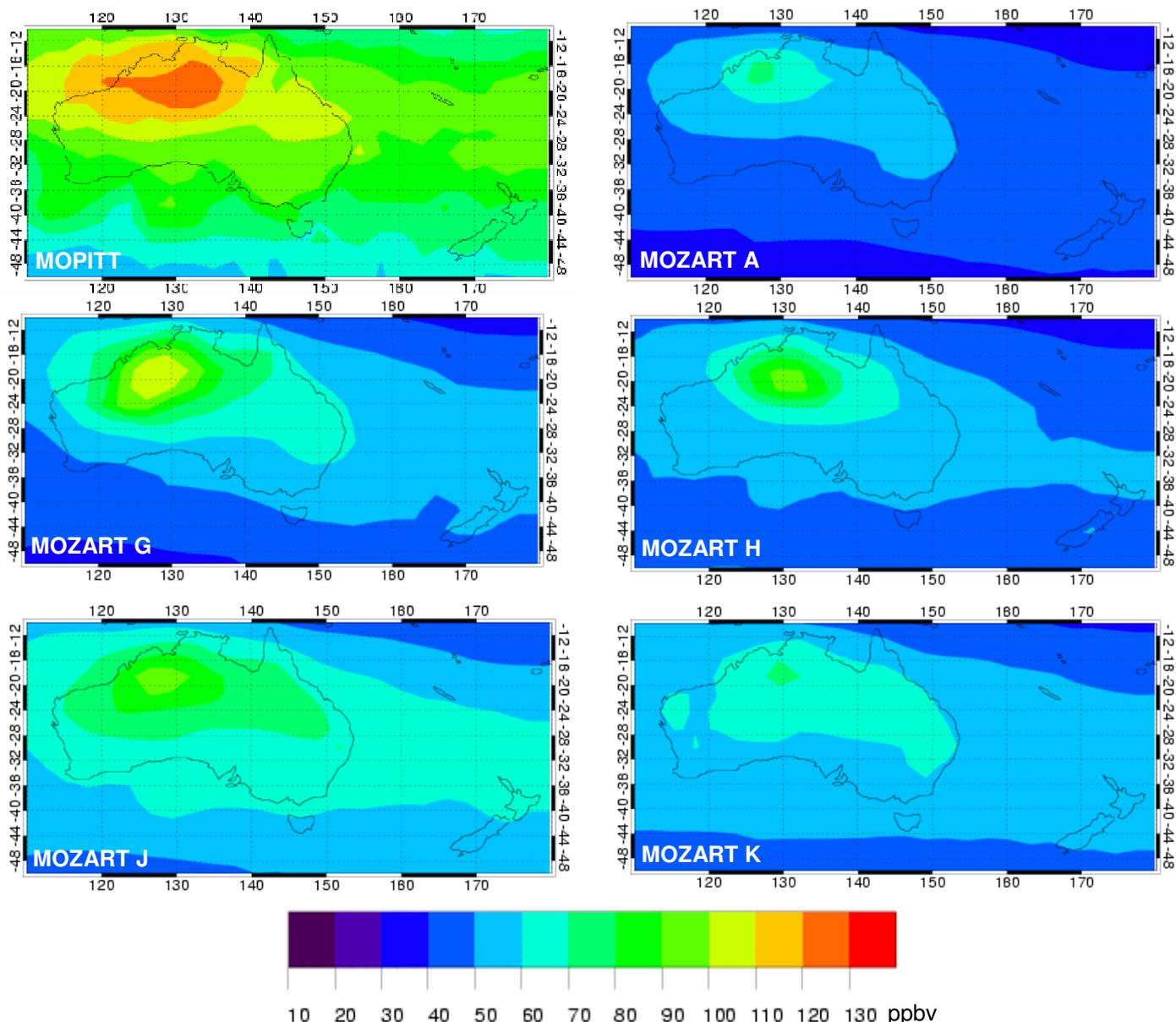
Figure 4.35: Australian MOPITT and MOZART CO in ppbv for simulations A, G, H, J, and K in October 2000 at 700 hPa

the MOZART runs show enhancements of CO concentrations in this region that reach the MOPITT CO maximum concentrations, but they are somewhat differently shaped. MOZART run J yields the largest area with maximum CO concentrations around 120 ppbv.

Over Indonesia, all runs yield CO concentrations around 60-70 ppbv. According to MOPITT, there were enhanced CO concentrations in April over Borneo, which is not reflected by any of the MOZART runs. A small CO enhancement of about 10 ppbv in MOPITT over Sulawesi is partly reflected by simulations except for run A. Over Sumatra, also all simulations but run A show a little more CO, however no similar enhancement can be found in the MOPITT data.

Over Australia, a CO maximum over the Northern Territory is observed by MOPITT in October 2000 (Figure 4.35). All MOZART simulations quantitatively yield considerably lower CO concentrations but all of them show a maximum in the same area. Largest CO enhancements are found for run G, followed by run H and run J.

No CMDL sites exist for continental Southern Asia and Indonesia within areas of fire activity. In Australia, one CMDL station exists in the far south, in Cape Grim, Tasmania (Figure 4.36). This station presents higher estimates of run A for some months than for the other model runs (about 20% more CO), but in all three cases without improving the performance, when

comparing these concentrations to the CMDL measurements.

The SHADOZ network has two observatories in Southern Asia: one in Malaysia, Kuala Lumpur and one at Watukosek on Java, Indonesia. Further, there are two Pacific observatories (Samoa and Fiji) that are located in the Asian pollution outflow region of the Pacific and are therefore discussed in the Southern Asian section. No SHADOZ measurements are available on the Australian continent.

At Kuala Lumpur three maxima in February, June and September are observed and also modeled by all MOZART runs (Figure 4.37). Run J clearly overestimates all maxima, while all other runs only show too elevated values for the June maxima. In higher altitudes there is no big impact from biomass burning and all runs take a very uniform course, although with a low-bias ranging from less than 5 up to 15 ppbv for the individual months.

Further to the south ozone simulations over Java, Indonesia, also do not yield a noticeable impact from fires for the first part of the year (January to July). SHADOZ shows a distinct peak of 55 ppbv ozone in September that is not very distinct in the MOZART runs that are around 15-20 ppbv lower for that month. Again, higher altitudes at this site are not influenced by biomass burning in this year, but present a low-bias between 5 and 15 ppbv monthly.
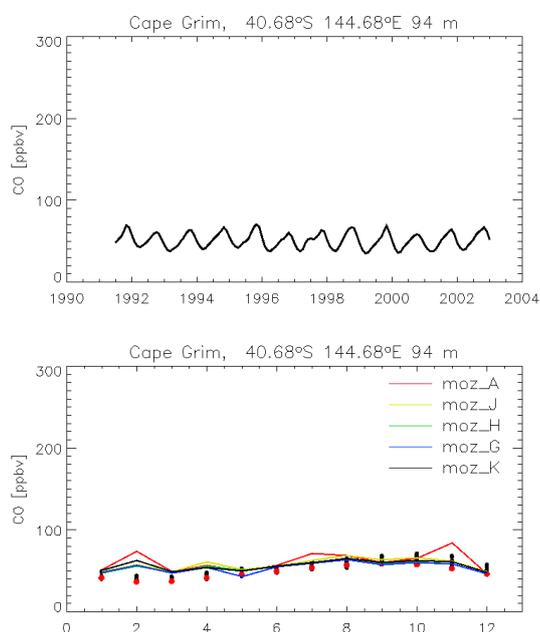
Figure 4.36: CMDL CO measurements in the year 2000 (red dots) and available other years (black spots) in ppbv at Cape Grim, Tasmania. Interannual variability is shown in the upper panel, the year 2000 seasonality in the lower panel. The lower panel also shows MOZART-2 results for the main runs A, J, H, G, K (solid lines), as described in section 4.3

In Samoa, far away eastwards in the Pacific Ocean, ozone model predictions overestimate measured values throughout the whole year. Close to the surface, overestimates for July and August are strongest for run A and run J. Nevertheless, the overall correlation is a bit higher for run J than for all other MOZART runs (R^2 = 0.73) (see Table C4a and b, in Appendix C).

For Fiji, there is data missing in October. No features due to different fire emissions in the model runs can be observed near the surface and also not higher up. There is a general underestimate of the model towards observations, but the peak in June is well represented by all runs. All MOZART runs present relevant R^2 correlations (see Table C4a and b in Appendix C), with the highest for run G at R^2 = 0.81.

Generally, MOZART is able to follow the seasonality given by the SHADOZ radio soundings
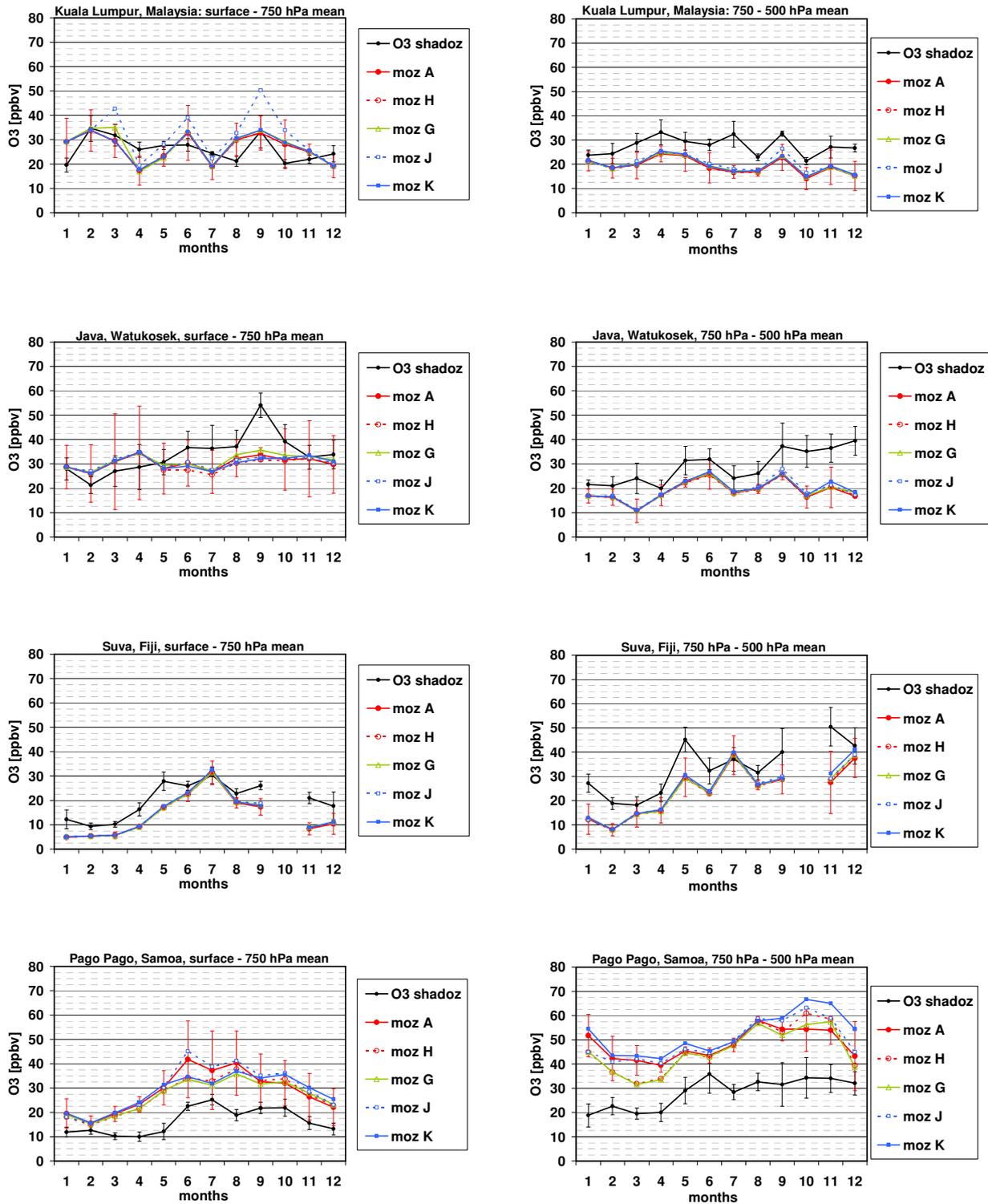
Figure 4.37: Asian SHADOZ ozone measurements from radio soundings in year 2000 and corresponding MOZART-2 graphs in ppbv of the five main runs A, J, H, G, and K. Seasonalities of monthly mean ozone are averaged from the surface level to 750 hPa on the left-hand side and for 750 - 500 hPa on the right-hand. Error bars are standard deviations

and matches the observations quantitatively within their standard deviations. Higher tropospheric ozone over Southeast Asia (at 750 – 500 hPa) is underestimated by MOZART for the whole year 2000 and is not influenced by fire emissions. Much further east in the Pacific at Samoa the situation is inversed and ozone is overestimated by all MOZART runs, both close to the surface as well as in the free troposphere. In this area influence from fires is stronger and the different MOZART runs show a higher variability.

MOZAIC ozone profiles are available for several airports in Asia. The southernmost airports with noticeable impact from fires on local air masses are located in Colombo, Sri Lanka and Bombay, India. Enhancement of ozone concentration can be observed in northern hemispheric spring in April and May. April profiles at Colombo (Figure 4.38a) are only weakly influenced by fire emissions. In May, there is a uniform overestimate of ozone near the surface and no influence from fires can be observed. In 1-4 km height, run A, H, and J seem to slightly reduce the model-observation discrepancy. Compared to the "no-fire" run D, ozone concentrations are improved by the inclusion of fire emissions in the MOZART model. In higher altitudes (> 4 km) there is still a noticeable impact from fires on the ozone formation and all MOZART simulations A, G, H, J, and K improve the model performance.
In Bombay in May (Figure 4.38b), none of the MOZART runs improves the model performance and run D without any fire emissions is closest to the observations through all altitudes.
Further to the northeast in Hong Kong in April (Figure 4.38c), the monthly mean ozone profile shows discrepancies in the different MOZART runs above 1 km height and a small ozone plume is formed between 2-3 km. All runs improve the model performance compared to run D without fire emissions, but still underpredict ozone by 15% (run J) and 35% (run H and run K).
Already in Shanghai in May, further to the north, all fire emission based MOZART runs improve the model simulations. Run A shows clearly more elevated ozone concentrations and therewith further improves the model performance. However, at these latitudes air masses are already influenced by northwestern air masses and will therefore be discussed together with Seoul and Tokyo ozone profiles in the North Central Asian section.
Apart from Shanghai, the Southern Asian profiles show influence from fires in higher altitudes. Fire emission-prone air masses are therefore not a local product but are transported over the airports within the free troposphere.
Generally, CO concentrations over Southern Asia are not primarily related to fires but are mainly a product of CO fossil fuel emissions. Due to the general underestimate of these emissions in MOZART, simulations show low CO concentrations over Southern Asia, especially for the winter months. This is evident from an evaluation with MOPITT satellite data at 700 hPa. All inventories show similar features at this altitude with only small differences. In Indonesia, CO emissions from fires play a bigger role in the formation of the atmospheric CO budget. However, all MOZART runs underestimate CO concentrations over Borneo/Kalimantan that are present in the MOPITT figure. The GBA2000 product used for the calculation of fire emissions in MOZART run A is not suitable to detect burned areas in Indonesian forest and peat lands, due to a combination of different effects: an elevated cloud coverage inhibits the detection of good observations of burned areas. Second, albedo changes from unburned to burned areas are often minor in tropical forests, when understorey and ground fires are predominant and leave the top vegetation layer (e.g. tree crowns) unaltered. Also, temperature thresholds are often not reached by smoldering peatland-fires burning at low temperatures. The latter argument also holds for the ATSR sensor, used for fire emissions in MOZART run G and H.

Over Northern Australia in October, where most fires of this continent occur, MOPITT shows a distinct CO maximum that is also underestimated by all MOZART runs. However, run G (cg_scal) and run J (gfed) perform somewhat better with more elevated CO concentrations than the other simulations. The GBA2000 area burnt product used for fire emissions in run A underestimates the true areas burnt by fire in Australia due to an increase in reflectance
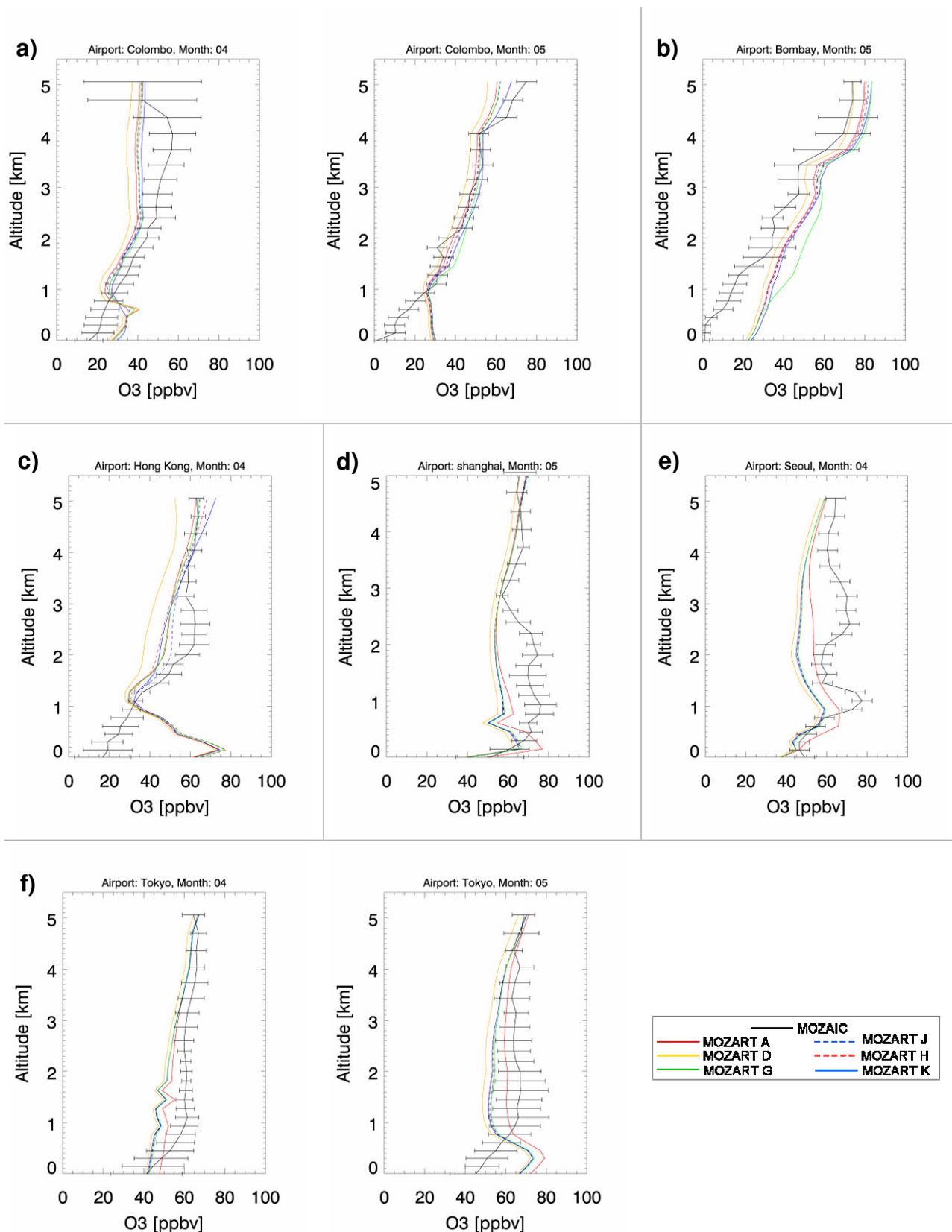
Figure 4.38: Asian MOZAIC monthly mean ozone aircraft measurements in ppbv at **a)** Colombo, Sri Lanka in April and May, 2000, **b)** Bombay, India airport in May 2000, **c)** Hong Kong, in April 2000, **d)** Shanghai airport in May 2000, **e)** Seoul, Korea, in April, and **f)** Tokyo, Japan in April and May, 2000

caused by certain types of burning activities (the GBA2000 product defines burned areas by changes in reflectance) (http://www-gvm.jrc.it /TEM/Disturbance%5Fby%5Ffire/products /burnt_areas/global2000/gba2000_data.htm).

The generally too low CO concentrations modeled by MOZART do not necessarily preclude a reasonable ozone simulation of the model, as the SHADOZ and MOZAIC ozone intercomparison demonstrate: at Fiji and also much further east in the Pacific, at Samoa reasonable R^2-correlations are found between most MOZART simulations and SHADOZ ozone. At Fiji, impact from fire emissions is low throughout the year and thus, MOZART simulations are very similar. At Samoa, the ozone seasonality is well represented however ozone is systematically overpredicted by the model.

In the MOZAIC profiles on the Southern Asian continent, discrepancies are found between surface ozone concentrations of model versus measured quantities. Above the boundary layer MOZART simulations with fire emissions mostly improve the model performance compared to run D without any fire emissions. No clear favorite can be identified and also the simulations based on new fire emissions are not necessarily better than the climatological MOZART run K.

Synthesis for Southern Asia and Australia

In summary, for the broader Southern Asian region none of the inventories was able to substantially improve the MOZART performance for CO and ozone. None of the MOZART runs performs clearly better or worse than the others.

In Australia, MOZART run G and run J CO estimates are higher than those from the other simulations, however they still underestimate MOPITT observations by about 15-25%.
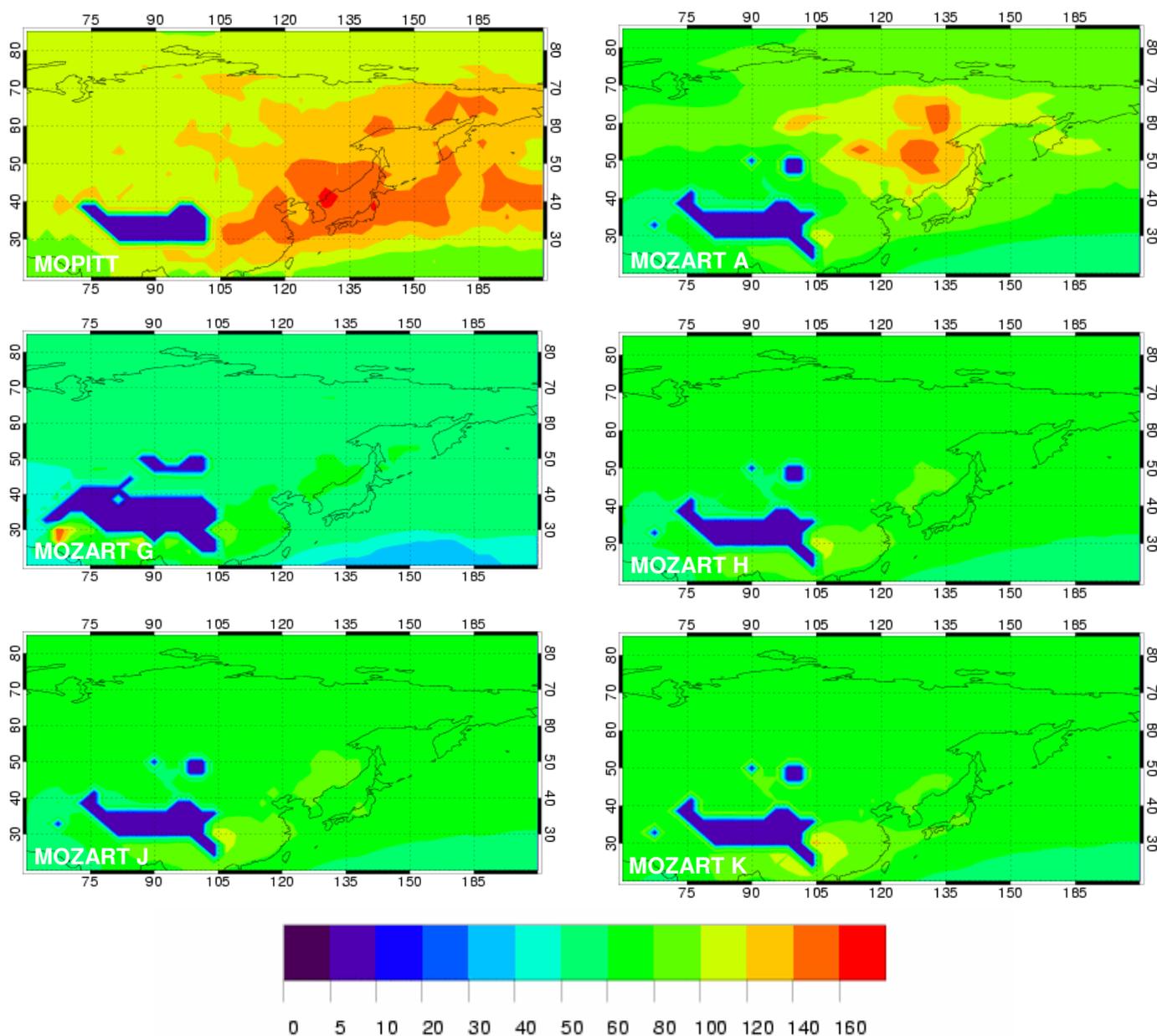
4.5.4   North Central Asia
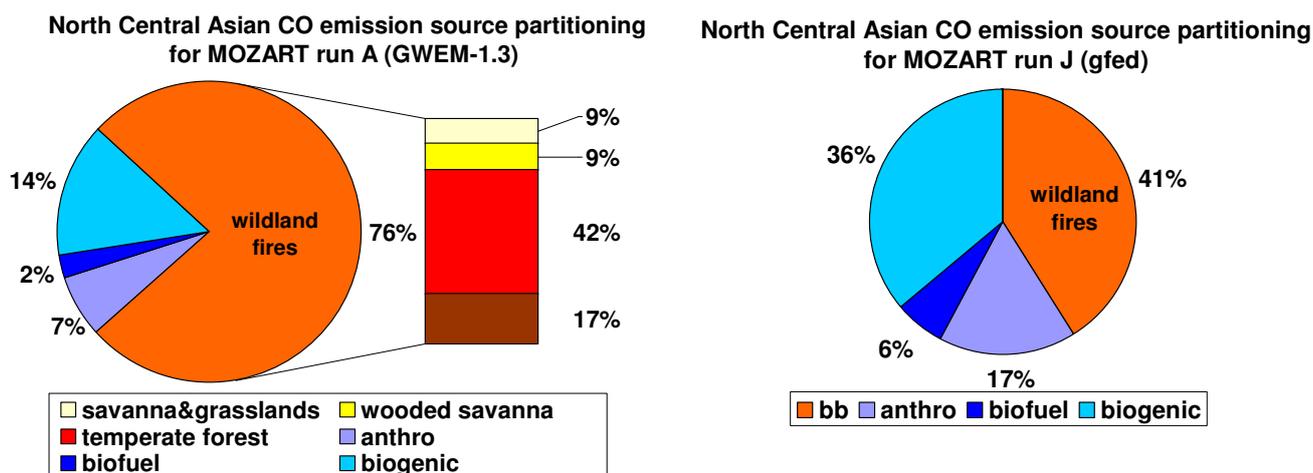
Figure 4.39: CO emission source partitioning in MOZART run A (left) and run J (right) for North Central Asia. Sub-categories as in Chapter 3

Over the large region of North Central Asia, emissions from fires play a predominant role throughout the burning season. Fires in North Central Asia occur in northern hemispheric spring and summer with a progression from south to north during the burning season (Kasischke et al., 2005). In some years the fire season peaks in April or May, when human-caused pasture management fires get out of control. In other years a maximum of fires as a result of lightning activity can be observed later in June or July. The fires with the largest area burnt are uncontrolled wildland fires, which account for more than 90% of the annually burned areas (Kajii et al., 2002). Apart from the forest stands and their organic ground-layer, peatlands burn under drought conditions (Kajii et al., 2002) and emit relevant amounts of gaseous compounds and aerosols. Since many of the large fires occur in near-to unpopulated areas, especially in the eastern part of the region, fires are mostly not extinguished and can burn uncontrolled until natural extinction takes place (e.g. by precipitation). Before the satellite fire product era, a large part of the fires were not recorded or known to exist and, therefore, only in recent years it has been recognized that North Central Asia is an important fire-related contributor of carbon monoxide and other emittants to atmospheric chemical composition. However, large discrepancies exist between the different area burned estimates (e.g. Boschetti et al., 2004), active fire pixel products (e.g. Kasischke et al. 2005), statistics (e.g. country statistics from Russia, available by the Global Fire Monitoring Center (GFMC)), or a combination of those (Conard et al., 2002; Goldammer, 2003; Soja et al, 2004; and Sukhinin et al., 2004). The differences are sometimes up to a factor of five and lead to high uncertainties in therefrom derived fire emission estimates (see Figure 4.39).

In May, in the rise of the burning season, eastwards from 100°W, MOPITT concentrations at 700 hPa range between 120-140 ppbv, with CO maxima at 140-160 ppbv (Figure 4.40). The intercomparison with MOZART simulations reveals that all MOZART runs clearly underestimate the background CO concentrations over North Central Asia throughout the year, but most strongly during the winter months (about 30-40 ppbv). This phenomenon is not fire-related but could be traced back to the fossil fuel emissions (sub-group of anthropogenic emissions in POET data base) used in MOZART and will therefore not be further investigated here (for a more detailed discussion on this topic see section 4.2.2).
Figure 4.40 however, reveals that there are also differences in the fire emission inventories applied to the different MOZART runs. MOZART run A is the only run that presents enhanced CO concentrations over the eastern part of North Central Asia (see also Figure 4.39). Fire

Figure 4.40: North Central Asian MOPITT and MOZART CO in ppbv for simulations A, G, H, J, and K in May 2000 at 700 hPa

emissions of the underlying emission inventory from GWEM-1.3 in this part of the region are much more abundant than for all other runs (120-160 ppbv). All other simulations (G, H, J, and K) remain at background concentrations of about 60-100 ppbv without any distinct CO maxima (Figure 4.40). According to the GBA2000 area burnt product (which was used in run A to calculate fire emissions, http://www-gvm.jrc.it/TEM/Disturbance%5Fby%5Ffire /products /burnt_areas/global2000/gba2000_data.htm), North Central Asia yields a few regions with commission of burned areas in forest-type ecosystems and a small amount of omitted pixels in grassland ecosystems. Especially the CO abundances north of 45°N are believed to stem from fires and not from Southern Asian fossil fuel emission sources (see section 4.5.3).

Also according to CMDL data, the burning season from April to September yields considerably more CO concentrations for run A (Figure 4.41). In Sary Taukum , Kazakhstan (Figure 4.41), model simulation of run A is improved in comparison to all other runs, by increasing CO concentrations by about 20-40 ppbv during the fire season. Another measurement site at Plateau Assy in Kazakhstan (Figure E1, Appendix E) shows improved
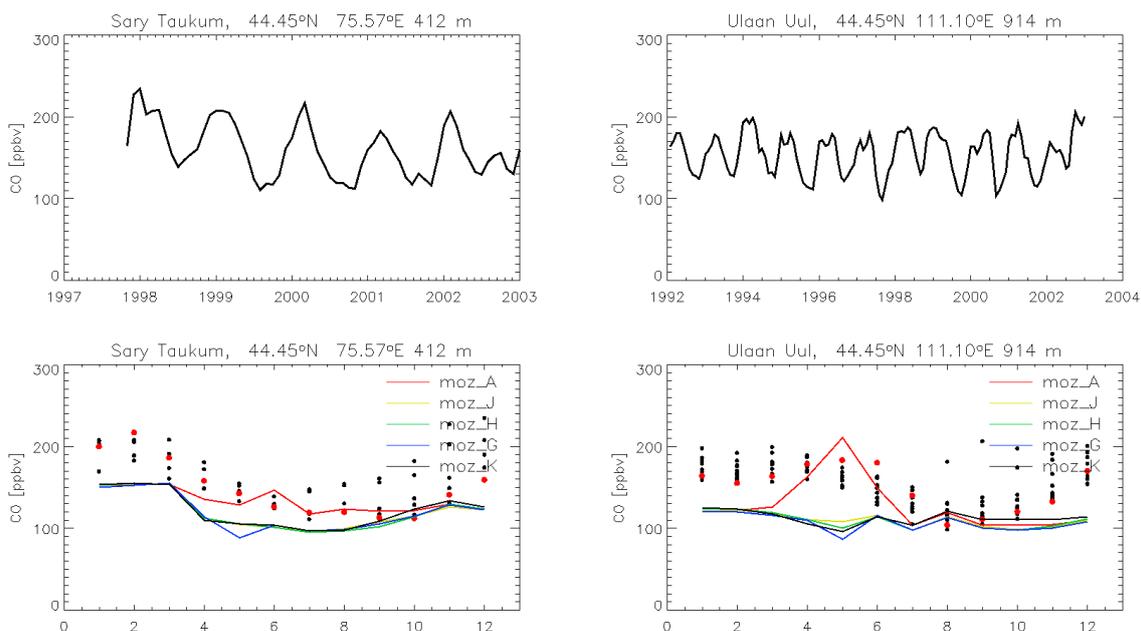
Figure 4.41: CMDL CO measurements in the year 2000 (red dots) and available other years (black spots) at Sary Taukum, Kazakhstan and Ulaan Uul, Mongolia Interannual variability is shown in the upper panel, year 2000 seasonality in the lower panel. The lower panel also shows MOZART-2 results for the main runs A, J, H, G, K (solid lines), as described in section 4.3

model performance in the early burning season in run A but overestimates CO concentrations in later months. In Ulaan Uul, Mongolia (Figure 4.41) a distinct peak of run A overestimates measured CO quantities by 20 ppbv. Still, the observation/model discrepancy is reduced from April to June compared to runs G, H, J, and K.

No data is available from SHADOZ in the northern hemispheric mid and high latitudes. In the North Central Asian region at least MOZAIC aircrafts gathered some ozone profiles for the year 2000 for some Asian airports (see Figure 4.38). A smaller impact from biomass burning emissions was observed, compared to the more fire-dominated regions. Nevertheless a few results are presented where a different model performance could be noticed. The general feature in these profiles is that run A yields higher ozone concentrations, due to much higher fire emissions from the underlying GWEM-1.3 fire emission model. In Tokyo (Figure 4.38f), April and May profiles show similar features. Run A has 5-10 ppbv higher ozone concentrations. Close to the surface this leads to an overestimate in ozone. In higher levels however, the model-observation bias is reduced by 50% using GWEM-1.3 fire emissions for MOZART. MOZART run A improves the model performance compared to the "no-fire" run D and also compared to climatological run K. The same counts for Seoul in April (Figures 4.38e). In Shanghai (Figure 4.38d), as mentioned in the previous section, the general picture is the same, only that ozone is additionally improved by MOZART run A at the surface.

Synthesis for North Central Asia

Both the evaluation with CO satellite (MOPITT) and surface (CMDL) observations as well as the ozone aircraft measurements from MOZAIC uniformly show that MOZART run A (based on GWEM-1.3 fire emissions) was submitted to more elevated fire emissions. Thus, more CO but also more ozone concentrations were modeled in this simulation, compared to all other runs.
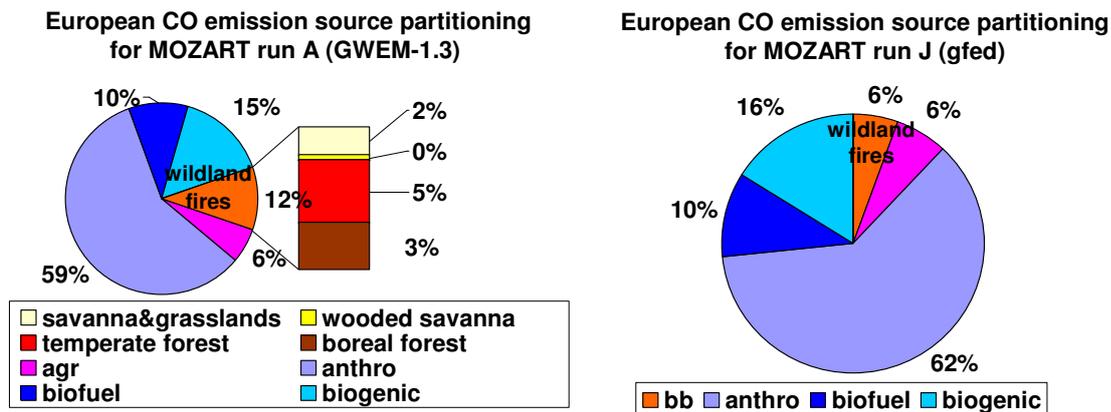
The MOPITT/MOZART intercomparison shows that the modeled CO of run A clearly improves the simulation, however the maxima are not exactly in the same locations as shown in the correspondent MOPITT plot in Figure 4.40. This is partly explained by fossil fuel emission produced CO in the MOPITT data, which is missing in MOZART in the same abundances.

Also CMDL surface CO measurements indicate that indeed enhanced CO stemming from fires is the solution for missing spring and summertime CO in MOZART. Here, MOZART run A improves the CO seasonality, with sometimes a few overestimates. All other MOZART simulations are uniformly equipped with a low-bias. The gap between observed and modeled wintertime CO however, is not related to fires but could be corrected with an updated fossil fuel emission inventory (see section 4.2.2) inserted into the MOZART model.

A clear impact from the elevated fire emissions in MOZART run A could also be observed in the ozone production of the model: run A yields overall higher ozone concentrations than all other simulations G, H, J, and K. MOZAIC ozone profiles (e.g. Hong Kong, Shanghai, Seoul) show that ozone-prone air masses produced by fire emitted precursors are transported over the East Asian cities in altitudes from 1-4 km. The fire emission inventories used in MOZART, reveal that many fires in the year 2000 were located in South Eastern Russia and built an ozone plume extending southwards at its limits over Tokyo, Seoul, and even further south over Shanghai.

The modeled ozone of run A mainly improves the model performance in higher altitudes but not close to the surface (with exception of Shanghai). In most Asian mega-cities the local ozone production caused by urban pollution close to the surface is predominant.

4.5.5 Europe

European CO emission source partitioning
for MOZART run A (GWEM-1.3)

European CO emission source partitioning
for MOZART run J (gfed)

Figure 4.42: CO emission source partitioning in MOZART run A (left) and run J (right) for Europe. Sub-categories as in Chapter 3

Fires in Europe occur mainly in forests and shrublands of the Southern European countries during summer. During the arid summer period the onset of the burning season is around May and ends in September, with the start of the raining season. The countries that are most affected by these uncontrolled wildland fires are located in Southern Europe: Portugal, Spain, Southern France, Italy and Greece. But also in some of the Eastern European countries, fires take place (see e.g. Forest Fires in Europe – 2003 fire campaign, report no 4, European Commission). The year 2000 can be considered an average fire year with no major reported or satellite observed fire hazards. In total, Figure 4.42 demonstrates that emissions from fires are in the order of a factor of 5-10 smaller than anthropogenic emissions (mainly fossil fuel), and are therefore not one of the main contributors to the chemical composition of the atmosphere over Europe.

As over North Central Asia, MOPITT shows higher wintertime CO concentrations at 700 hPa over Europe than MOZART (Figure 4.3). Concentrations range between mainly 120-140 ppbv, especially in higher latitudes. In May, in the rise of the early European burning season CO concentrations range between 100-120 ppbv with maxima over 140 ppbv (Figure 4.43). The intercomparison with all MOZART simulations reveals that all MOZART runs clearly underestimate CO concentrations over Europe throughout the year, but most strongly during the winter months (about 30-40 ppbv). This phenomenon is not fire-related but could be traced back to the fossil fuel emission inventory used in MOZART and will therefore not be further investigated here. For a more detailed discussion on this topic see section 4.2.2. Figure 4.43 reveals almost no impacts of fires on the CO concentration at 700 hPa over Europe in May, only run A yields higher CO concentrations over Europe. Run A has by about 20 ppbv enhanced CO concentrations over northern Russia (centered at 55°W), compared to all other MOZART simulations. The underlying area burnt product to calculate fire emissions for run A yields some difficulties to estimate the true area burnt for the small fire sizes in Europe.

Northern European CMDL measurement sites reflect a comparable CO picture as MOPITT: run A shows a distinct higher CO scenario during burning season from May to July, with maxima in May at the boreal stations (Figure 4.44 a and b. All other runs take a uniform course with 10-30 ppbv lower concentrations. Simulations at the high-latitude stations Ny-Alesund and Ocean station M are considerably improved for run A. The underestimate of CO
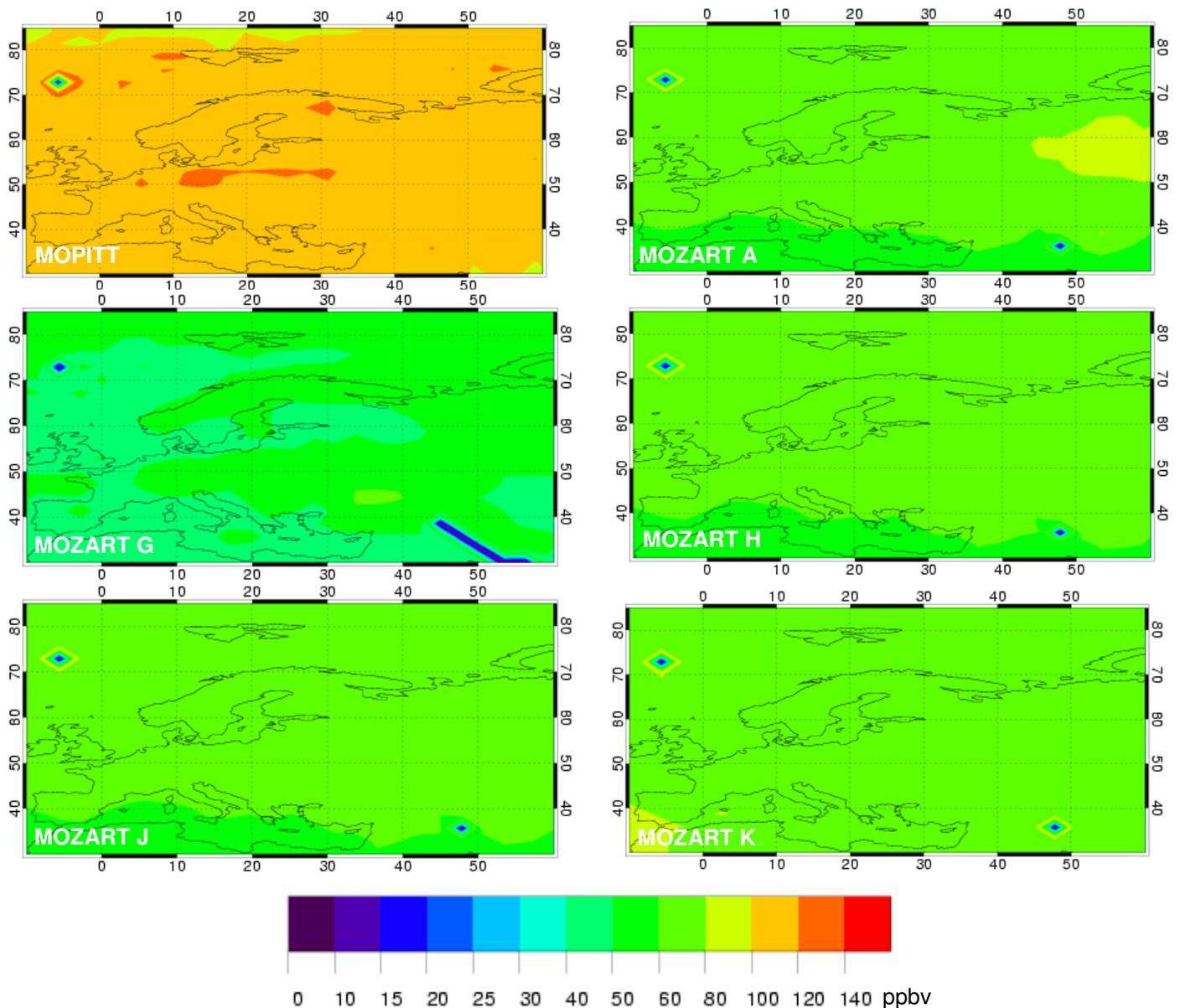
Figure 4.43: European MOPITT and MOZART CO in ppbv for simulations A, G, H, J, and K in May 2000 at 700 hPa

for the winter months in higher latitudes is also evident here. An actualization of those CO emissions would considerably enhance wintertime CO concentrations but almost maintain the present CO concentrations during summer (confer in Figure 4.6, section 4.2.2). At moderate latitudes , such as in Mace Head (Figure 4.44c), CO simulations of run A are improved for the month of May by the underlying GWEM-1.3 emissions, but they seem to overestimate CMDL observations in June and July by 20 ppbv. The correcting effect of run A as described for the boreal latitudes still persists although with a lower amplitude.

MOZART simulations at European MOZAIC airports show minimal influence of fires on ozone in European air masses. Nevertheless, differences in the ozone model simulations of up to 5 ppbv can be observed (Figure 4.45). In Vienna (May), Brussels and Frankfurt (June), run A shows about 2 ppbv higher ozone concentrations up to 3 km altitude. Until reaching 1.5 km however, model performance is not improved by that fact. Concentrations at Hamburg are
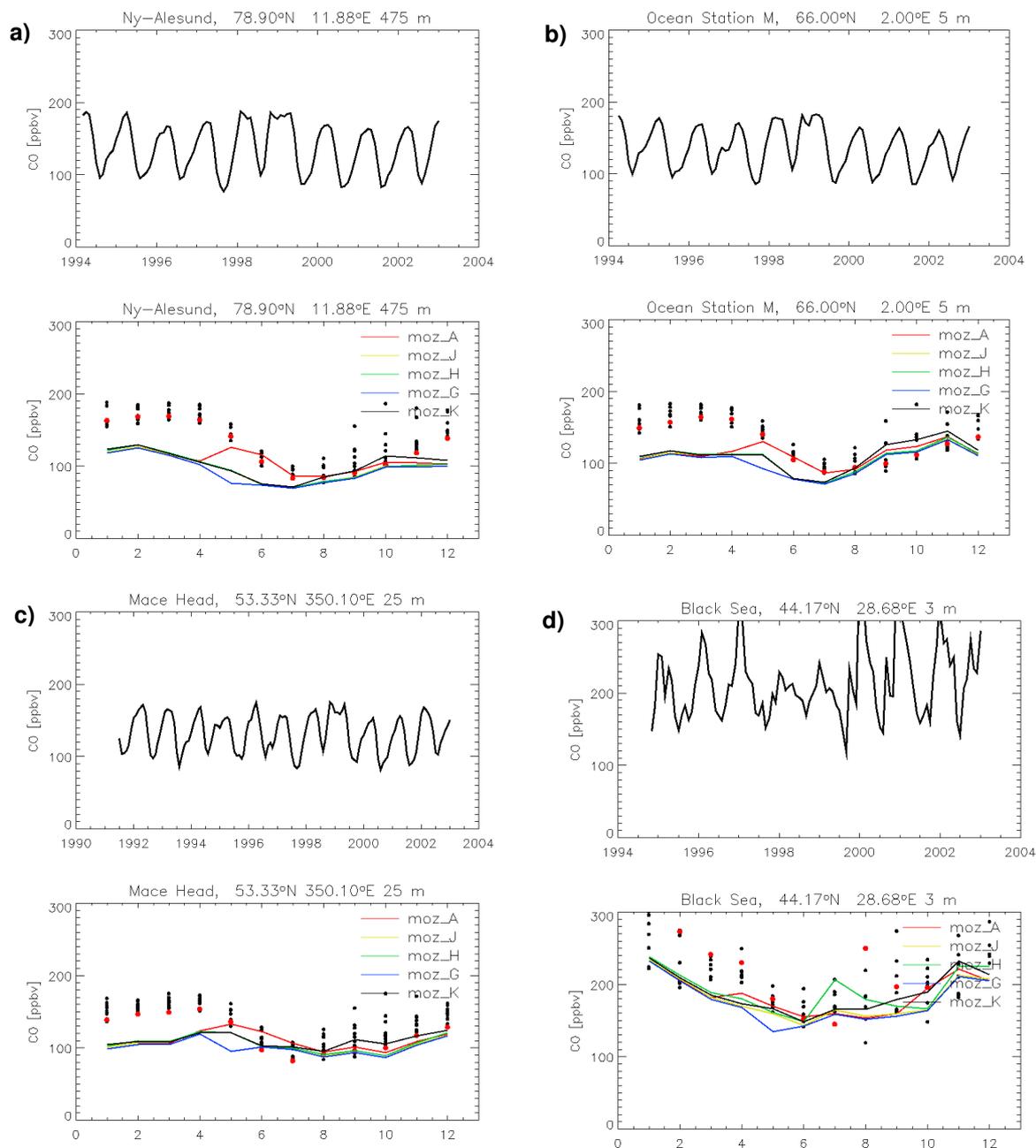
Figure 4.44: European CMDL CO measurements in ppbv for the year 2000 (red dots) and available other years (black spots) **a)** at Ny-Alesund, Sweden/Norway, **b)** at Ocean Station M, Norway, **c)** at Mace Head, Ireland, and **d)** at the Black Sea, Romania. Interannual variability is shown in the upper panel, year 2000 seasonality in the lower panel. The lower panel also shows MOZART results for the main runs A, J, H, G, K (solid lines), as described in section 4.3

even 5 ppbv higher, with an overestimate of run A from the surface up to 2 km.

All MOZART simulations but run A are near-to identical and generally slightly improve the model performance, compared to run D that contains no fire emissions.

Wind is coming from southwest close to the surface, changing to west wind in altitudes above 1 km. A comparison of the different MOZART runs shows a small discrepancy in magnitude from a fire emission source in northwestern Italy and another small one in northwestern Germany. These differences induce the somewhat variable ozone concentrations in the different MOZART simulations.
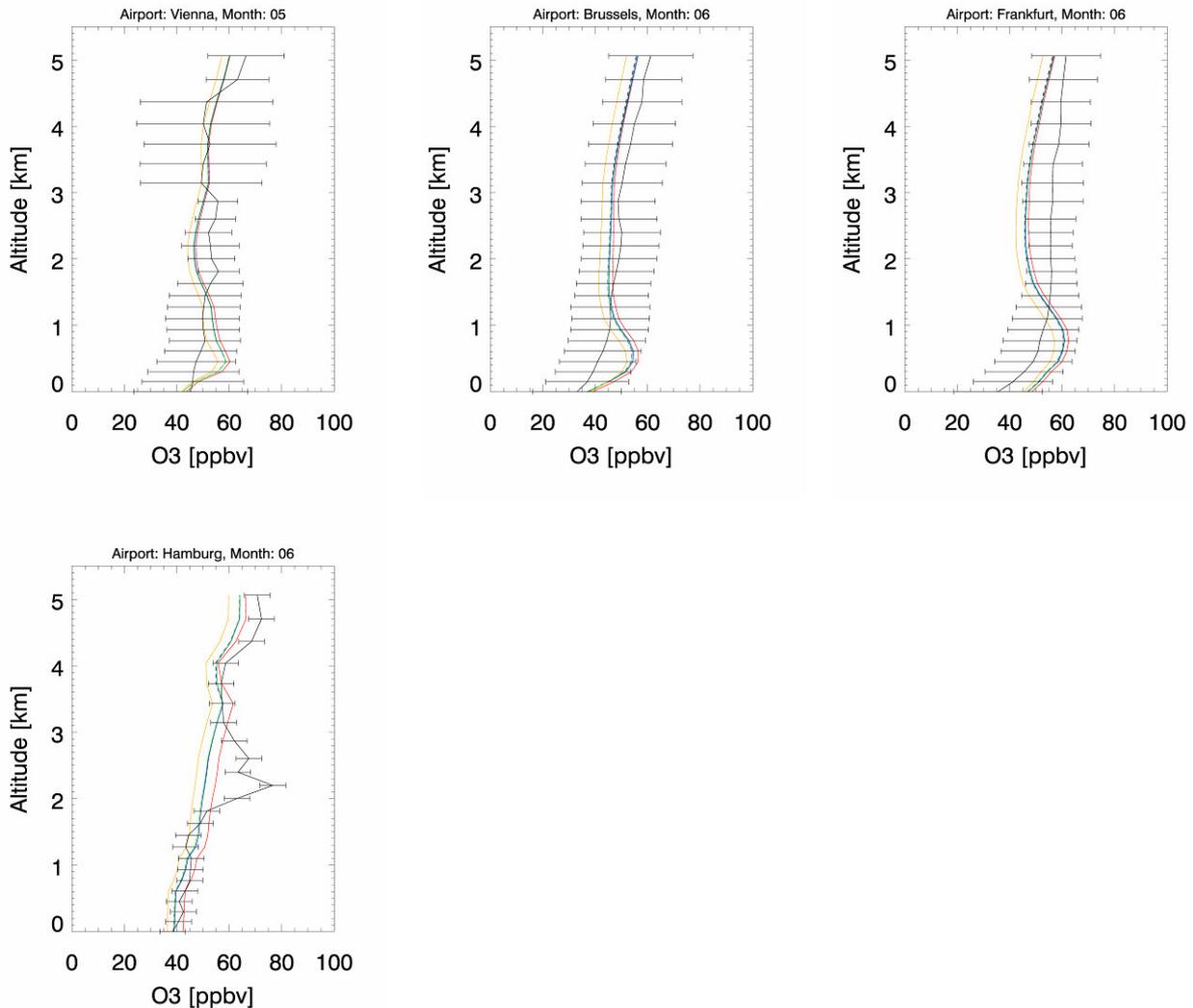
Figure 4.45: Europe, MOZAIC monthly mean ozone aircraft measurements in ppbv at Vienna, Austria airport for May, Brussels, Hamburg and Frankfurt airports for June 2000. MOZAIC ozone: solid black line, MOZART-2 run A: red solid line, run J: blue dashed line, run H: red dashed line, run G: green line, run K: blue solid line

Synthesis for Europe

In summary, all MOZART runs yield very low CO concentrations over Europe, as is reflected by both the satellite measurements from MOPITT and the CMDL surface stations. This systematic underestimate is related to very low northern hemispheric wintertime fossil fuel emissions used in the MOZART model and thus, not related to wildland vegetation fires. In section 4.2.2 it has been demonstrated that a more suitable fossil fuel emission data set would increase CO concentrations in winter as expected from the observations, while maintaining current CO concentrations during summer.

Concerning the differences provoked by the use of different fire emissions, the only differently acting MOZART simulation is run A, based on the GWEM-1.3 fire emission inventory. All other MOZART runs are near-to identical. MOZART run A showed enhanced CO and also, to a small extent, elevated ozone concentrations. In most cases this enhancement led to an improved model performance.

4.5.6 North America
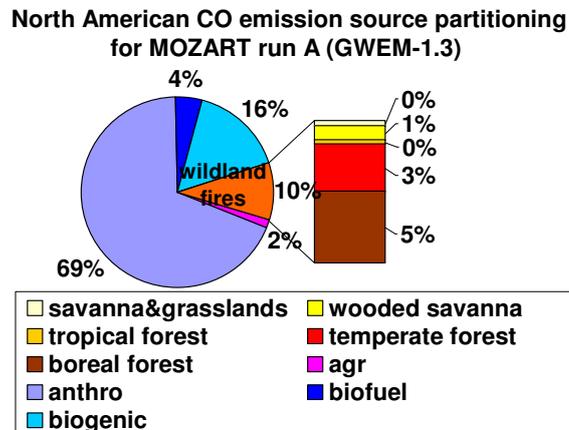
Figure 4.46: CO emission source partitioning in MOZART for North America. Sub-categories as in Chapter 3

In North America, fires take place during the northern hemispheric summer and have different reasons: in Canada and Alaska the majority of severe wildland fires are ignited by lightning (Stocks et al., 2003). These large fires (>200 ha) are responsible for 97% of the area burned, although they only represent 3% of the total quantity of fires (Stocks, 1991). According to the Canadian Large Fire Database (LFDB, see http://fire.cfs.nrcan.gc.ca/ research/climate_change /lfdb_e.html), fires occur between April and August with a maximum of area burned in June or July (Stocks et al., 2003).
Further to the south, in the United States, fires occur in the eastern and northwestern forests, in the western shrublands in California and in the prairies in the central plains (Lavoué et al., 2000). Fires throughout all states, in terms of their burned area, are almost equally caused by humans and lightning (see National Interagency Coordination Center, http://www.nifc.gov/stats/lightning_human_fires.html). For individual states, the ratio may differ, depending mostly on population density and natural lightning activity. The year 2000 was a year with an exceptionally high fire activity in the northwestern US and in the Rocky Mountains (Lamarque et al., 2003). The most affected states were Idaho and Montana. However, as is demonstrated by Figure 4.46 on the continental scale, wildland fires only contributed to about 10% to the North American CO budget.

A continental overview on the CO distribution at 700 hPa is provided in Figure 4.47 by MOPITT CO satellite data and the simulations of MOZART runs A, G, H, J, and K in May 2000. Clearly, MOPITT observations yield considerably more CO in May than calculated by all MOZART runs. The background ranges from 100-120 ppbv, while over a large area concentrations of 120-140 with peaks at over 140 ppbv domain the scenario at 700 hPa. All MOZART runs, except run A, look very alike with monotonously 60–80 ppbv CO, not showing any local CO emission events. Run A yields somewhat higher CO concentrations, especially in the north-west centered over Alaska. The reason of this clear general underestimate of CO concentrations has been discussed in the previous northern hemispheric regional discussions and is not related to emissions from fires.

At CMDL measurement sites in boreal regions (Alaska and Canada), run A shows higher CO concentrations (up to 50 ppbv) for the burning season from April to September than the other four MOZART runs (Figure 4.48). Seasonality of runs J, H, G, and K take a very similar course. The latter has 5-10 ppbv higher CO concentrations in fall. At the two stations Alert

and Mould Bay in Canada that are located at latitudes higher than 75° (Figure E2, Appendix E), run A concentrations match better with CO measurements from CMDL during the biomass burning season than the other MOZART runs. Also for lower latitudes the model/measurement discrepancies are reduced. CMDL station Shemia Island (Figure 4.41b) that is located in North Pacific between Alaska and easternmost Russia, is strongly influenced by emissions from Siberian fires from April to July. The overall northern hemispheric CO low-bias observed in the global MOPITT comparisons is also clearly reflected by the CMDL model/measurement comparison. It is strongest in northern hemispheric winter and in the range of 30-60 ppbv at surface, which is also about the range observed in the MOPITT comparison (20 – 60 ppbv) at the 700 hPa level.

Comparisons with CMDL measurement stations at temperate latitudes of North America show a less pronounced low bias (10–40 ppbv) and a generally uniform behavior of all performed MOZART runs at most stations in the eastern USA an off the east coast (Figure E3, Appendix E). Run K yields more elevated CO concentrations in fall in the east (5-10 ppbv). In the western USA, Wendover in Utah (Figure 4.41c) yields quite different seasonalities driven by the fire emissions. Run H and run K feature distinct seasonalities from June to August and from July to October 2000, respectively. For both runs CO is clearly overestimated in these months (about 60 ppbv overestimation by run H and about 30 ppbv by run K). The other runs do not show a clear enhancement of CO concentrations due to biomass burning. In Park Falls (Figure 4.41d) run K also overestimates considerably for late summer and fall, while run A shows a CO enhancement in May that reduces the model/observation low-bias by 50% compared to all other simulations. North American CMDL measurement sites reflect a similar CO pattern as stations in North European high latitudes with run A showing a distinct higher CO scenario during the burning season.
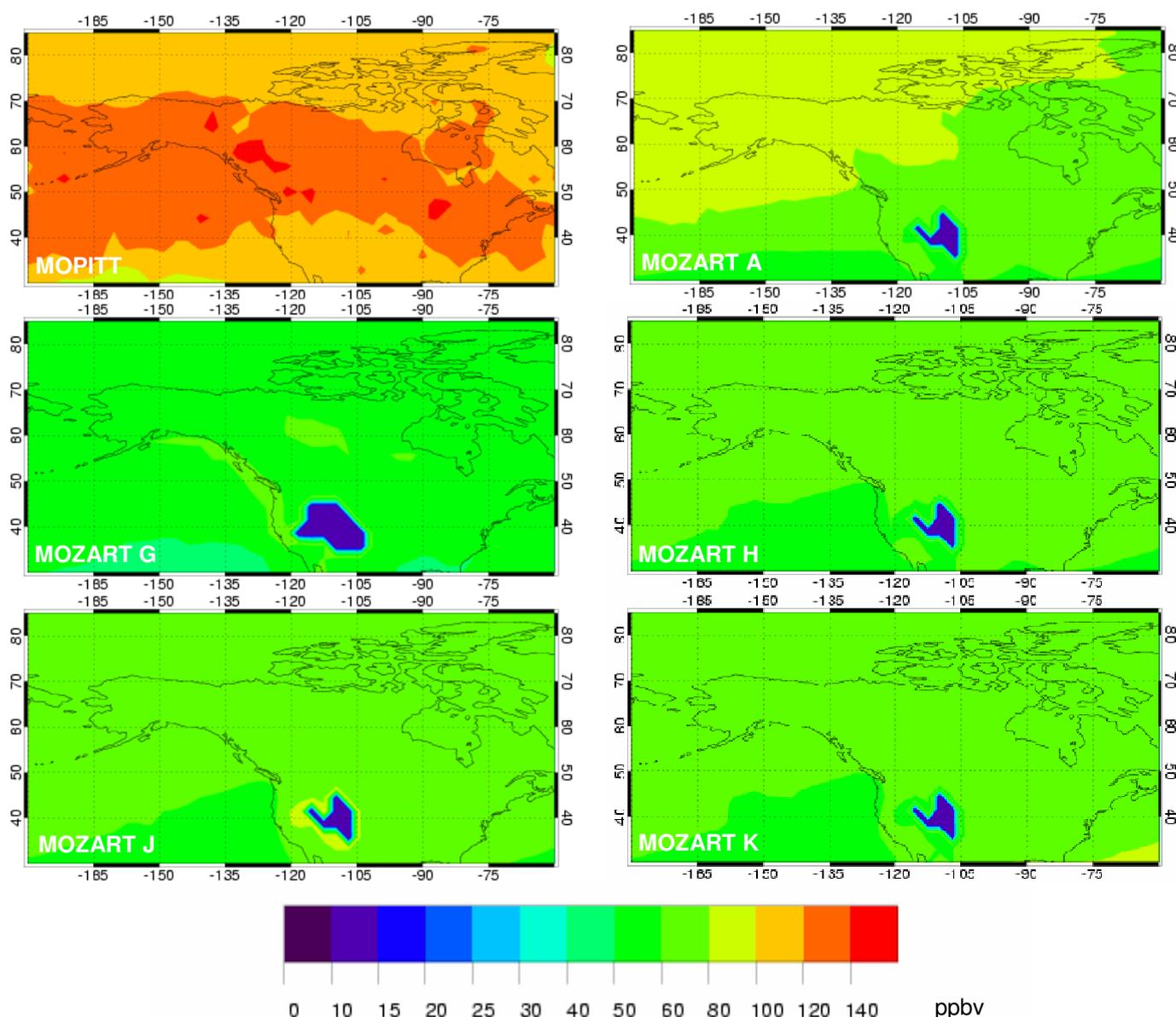
Figure 4.47: North American MOPITT and MOZART CO in ppbv for simulations A, G, H, J, and K in May 2000 at 700 hPa

In the Pacific there are two further CMDL measurement sites that experienced influence from pollution stemming from fires. CO emission loaded air is transported over the islands from north-east/east, i.e. North America. On Sand Island (Figure E4, Appendix E), run A has higher CO concentrations for May (15%) and June (30%) than all other MOZART runs. For the month of June CMDL CO observations are matched well with this enhancement, while for May there is still a considerable low-bias of about 30% less CO. Exactly the same feature is observed further south in Cape Kumukahi, Hawaii, although a bit smoother (also Figure E4, Appendix E).

The CO emissions released by fires that are used in MOZART run A may still be conservative as the GBA2000 (area burnt product used for fire emission calculations for run A) website states that there are underestimates of burned areas in Canadian forests.
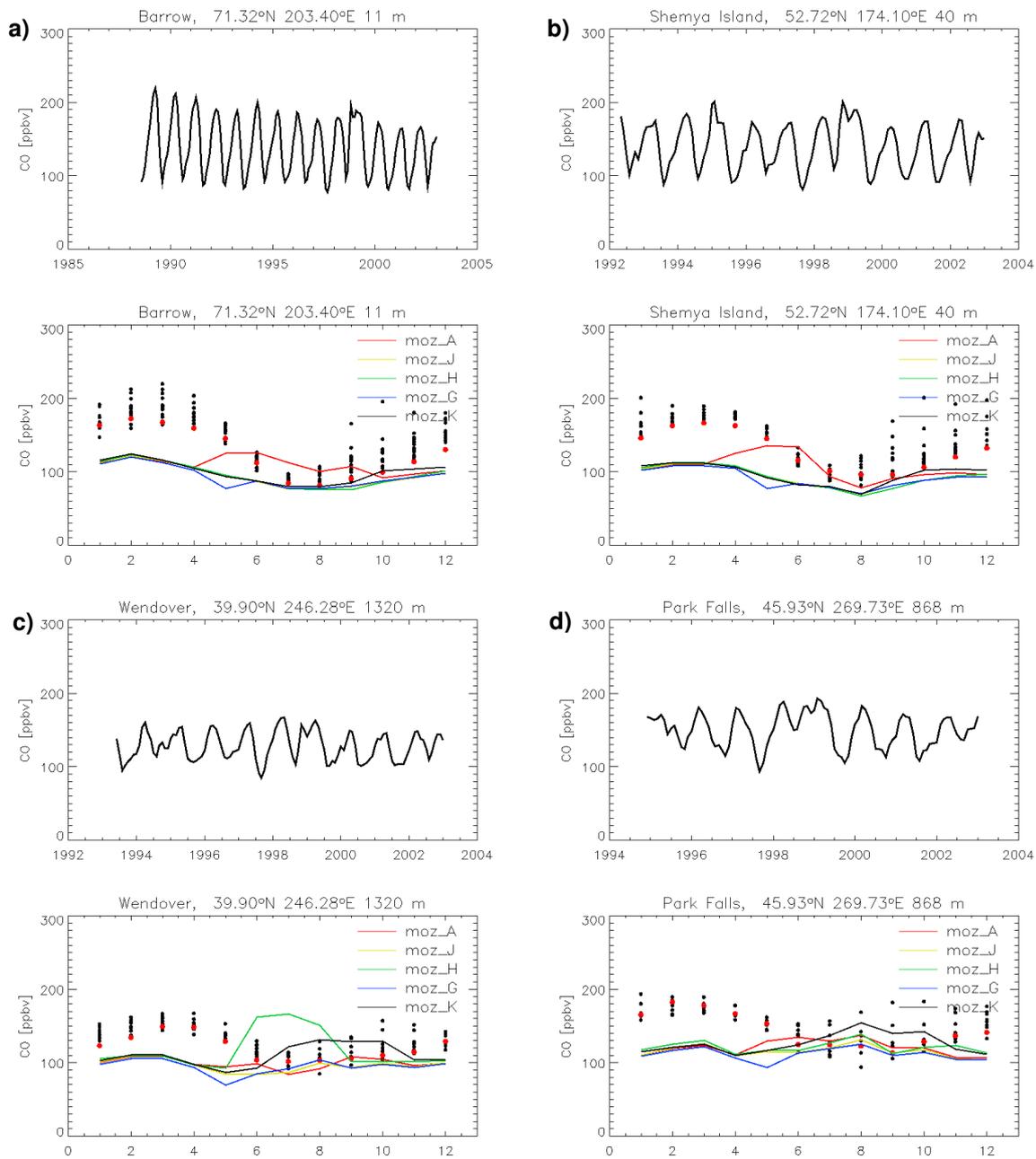
Figure 4.48: CMDL CO measurements in ppbv for the year 2000 (red dots) and available other years (black spots) **a)** at Barrow **b)** at Shemya Island, Alaska, **c)** at Wendover, Utah, USA and **d)** at Park Falls, Wisconsin, USA. Interannual variability is shown in the upper panel, year 2000 seasonality in the lower panel. The lower panel also shows MOZART results for the main runs A, J, H, G, and K described in section 4.3

The low CO concentrations discussed above do not preclude a reasonable ozone simulation: at some North American MOZAIC airports, model ozone simulations are influenced only to a small extent by biomass burning. In Boston in July 2000 for example, all MOZART runs with new fire emissions slightly improve the performance in the lowest levels by 2-7 ppbv, compared to the climatological fire run K. The same is the case for Chicago in July and Washington in August. All simulations that included fire emissions improve the performance of the model compared to MOZART run D without any fire emission sources.
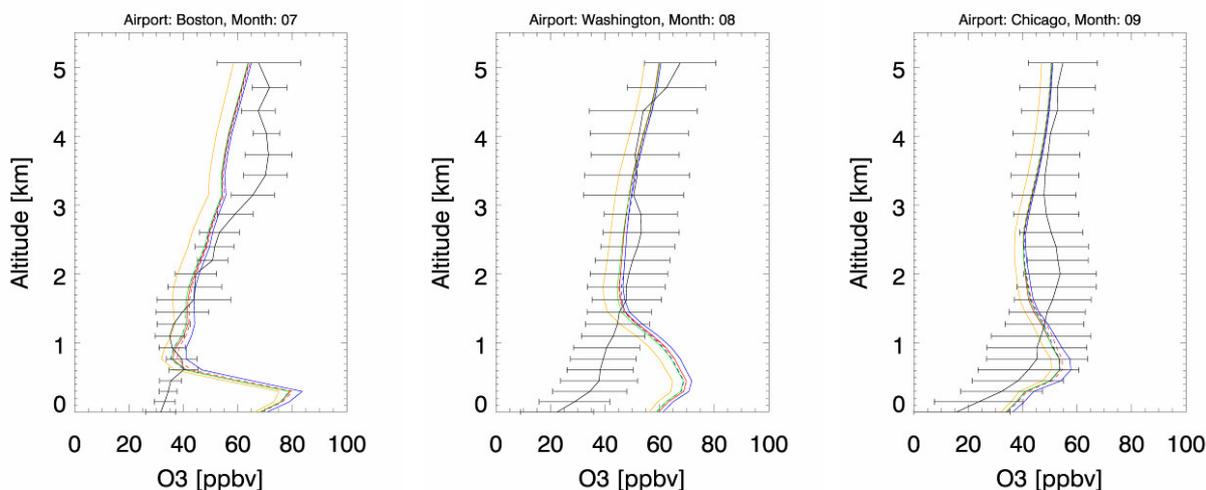
Figure 4.49: North America, MOZAIC monthly mean ozone aircraft measurements in ppbv at Boston, USA airport for July, Washington, USA, airport in August, and Chicago, USA airport in September 2000. MOZAIC ozone: solid black line, MOZART-2 run A: red solid line, run J: blue dashed line, run H: red dashed line, run G: green line, run K: blue solid line

Synthesis for North America

In general, the overall low-bias related to low winter fossil fuel emissions in MOZART is also reflected in all North American CO model/observation intercomparisons. Some differences due to the use of different fire emission inventories in MOZART could be observed, the most apparent of which is the enhanced CO concentrations by run A. In some cases, CO concentrations in MOZART are improved by run A, in others the CO seems to be too high for some months. Since the area burnt GBA2000 product that is used for the fire emissions in run A (generated by the GWEM model) seem to be inclined towards underestimating the real area burnt sizes in some regions, probably the fuel loads for some biomes are overestimated in GWEM-1.3. This is also reinforced by Figure 2.5b in Chapter 2, where boreal forest fuel load estimates for the GWEM model are considerably higher than the range of literature values provided by Reid et al (2005a,b). A new study by Poulter et al. (2006) indicates that emissions from some fires in the temperate zone of the US may be considerably underestimated, because of peat burning in the ground layer. Poulter et al. (2006) showed that during a case-study a temperate peat fire emitted less trace gases and aerosols into the atmosphere than a peat fire in tropics, but emissions were higher than from boreal peat fires. In future studies of fire emission estimates the enhanced available fuel load due to peat may need to be taken into account.

As to the ozone concentrations, only a very small impact from fire emissions on the ozone budget over North America could be derived from the intercomparison with MOZAIC. Generally all fire emission data sets improve the MOZART performance compared to the no-fire run D and also compared to climatological run K.

4.5.7 Boreal CO Fire Emission Partitioning – North America versus Eurasia

In this section a brief intercomparison between boreal CO fire emissions strengths from North America and Eurasia and their impact on atmospheric CO concentrations is performed. Some of the fire emission inventories presented in Chapter 3 and used here in the MOZART model show large differences in the two boreal regions. GWEM-1.3 for example, yields CO emissions that are about a factor of five higher in Eurasia than in North America (Table 4.3). Other inventories, such as GFED, show values of the same order for both regions (Table 4.3).

Emission source	North America [Tg CO]	Eurasia [Tg CO]	Total [Tg CO]
GWEM-1.3	12 (16%)	64 (84%)	76
GFED	13 (48%)	14 (52%)	27
Mgs_scal	16 (62%)	10 (38%)	26
Cg_scal	6 (29%)	15 (71%)	21
Hao&Liu	34 (68%)	16 (32%)	50
Soja et al., 2004	-	64 [a]	-
Kasischke et al., 2005	27 [b] (61%)	17 [b] (39%)	44

[a] boreal Siberia only

[b] extrapolated from total CO emissions and carbon ratio in boreal North America and boreal Eastern Russia

Table 4.3: CO emissions in Tg in the year 2000 from North America and Eurasia from the inventories in this study and as published in literature

Wotawa et al. (2001) concluded that according to their statistical model on CO concentrations, burned areas in Russia must be considerably higher than reported by the local authorities' statistics. Since then, a number of emission studies have either scaled their burnt areas for this region or, if available, have recently used satellite fire information on fire pixels or burnt area in order to derive emission estimates. For example, Kasischke et al. (2005) constructed the Boreal Wildland Fire Emission Model (BWEM-1) and found that for the period of 1995-2003 in average about three times more area was burned in boreal Eurasia than in boreal North America. However, this assertion needs to be handled with care, because Kasischke et al. (2005) also state that there was a very high interannual variability associated with this ratio. For individual years the percentage of burned area was found to be considerably higher in North America than in Eurasia (e.g. 92% in 1995). Overall, Kasischke et al. (2005) calculate higher average carbon emissions for boreal Eurasia than for boreal North America, which the authors attributed to higher above-ground biomass loads and deeper organic soil layers (that can also be partly combusted during a fire) in boreal Eurasia. However, for the year 2000, only 39% of the boreal carbon emissions are associated with Eurasian fires (Table 4.3).

On the other hand, Wooster and Zhang (2004) investigated the differences in fire intensity on both continents and found a much smaller mean burning intensity for fires in Russia than in North America. According to their study, this fact may compensate the much higher fire pixels and burned areas found by all satellite fire products over Russia and likely leads to equal emissions from fires on both continents, if the different burning intensity is taken into account.

The emission inventories for the year 2000 used in this work (Table 4.3) show large discrepancies in the CO emission partitioning between boreal North America and Eurasia. 84% of the CO produced by GWEM-1.3 stems from Eurasian fires, while the climatological Hao&Liu emission data set only attributes 32% of its boreal CO emissions to this region. Total CO emissions from GWEM-1.3 are identical with those from the study of Soja et al. (2004), however all other inventories present a better agreement in total CO emissions with

the much lower estimates from Kasischke et al. (2005) for Eurasia. Generally, two of the inventories show higher emissions in Eurasia than in North America (GWEM-1.3 and cg_scal), another two have opposite tendencies with considerably more emissions in North America (mgs_scal and hao&liu, in agreement with the study of Kasischke et al. (2005)). One of the fire emission inventories yields equal CO emission amounts for both boreal regions (gfed). Three of these inventories rely on ATSR fire count data at temperate and boreal latitudes (mgs_scal, cg_scal and gfed). As this product is known to ommit many fires in the boreal regions (Kasischke et al., 2003b; Arino and Plummer, 2001), it is questionable to which extent emission estimates at these latitudes are reliable based on this source. It is also unknown, if the ATSR omissions in boreal North America and Eurasia are exposed to the same bias and therefore, whether derived emission estimates can be qualitatively compared (percentual contribution by region). Further, the climatological hao&liu inventory also relies on incomplete information of the 1970's and 1980's in the boreal regions, due to the data situation at the time this part of the inventory was compiled (in 1992, by Müller). Finally, the GWEM-1.3 estimates yield very elevated fuel loads for boreal Eurasia according to literature intercomparison (see Chapter 2, Figure 2.5b) Further, for the sake of global consistency the model does not distinguish between regional burning efficiencies (they only differ between ecosystems), as recommended by Wooster and Zhang (2004). The intercomparison of model and observations in the regional discussion of North Central Asia (section 4.5.4) however show that the elevated CO emissions by GWEM-1.3 improve the MOZART CO simulation.

MOPITT CO observations at 700 hPa (see Figures 4.40 and 4.47 above and the NCAR-MOPITT web-page for a global intercomparison at various levels: http://www.eos.ucar.edu/mopitt/data/plots/mapsv3_mon.html) qualitatively show similar CO concentrations in both boreal regions for the year 2000. However it has to be kept in mind that CO concentrations in the northern hemisphere are generally dominated by other sources than biomass burning (anthropogenic emissions i.e. fossil fuels and industrial pollution sources). As CO has a lifetime between weeks and months (Brasseur, 1999), it can also be transported from anthropogenic polluted areas over to remote regions with fire activity. Additionally, the MOPITT instrument is not very sensible to CO within the boundary layer. As remarked by Edwards et al. (2004), MOPITT might therefore not be such a reliable indicator of exact wildland fire locations, but be more adequate for the long-range transport studies.

According to the results available in published literature and the present work, obviously a more profound investigation is needed to arrive at a final conclusion concerning the fire emission partitioning between boreal North America and Eurasia. A study including the best available emission data for various years to account for the high interannual variability (e.g. BWEM-1 estimates by Kasischke et al., 2005) and satellite observations that allows for a (i) better detection of fire emitted species within the boundary layer (ii) distinction of fire and industrial emission sources (e.g. MODIS fine mode Aerosol Optical Depth (AOD), see Edwards et al. (2004)) would provide a detailed picture of the fire emission contributions from both boreal regions. At present neither the BWEM-1 fire emission data nor any other data set specialized on boreal fire emissions is available for further investigation of boreal North American and Eurasian fire emission partitioning.

5 Conclusions and Outlook

5.1 Approach

The primary goal of this thesis was to improve the existing fire emission data bases for use in global Chemistry Transport Models (CTM's), which play an important role to correctly reflect the chemical state of the lower atmosphere. The standard fire emission inventories that until today are still used in some atmospheric chemistry transport modeling studies, are based on incomplete data of the 1970's and 1980's originating from subjective and scattered country based reports of varying quality and operate on a very coarse spatial (5° X 5°) and temporal (1 yr) resolution.

The chosen approach was based on a new global area burnt satellite product with the aim to build a transparent, globally consistent, partly satellite-derived fire emission data set that delivers a high spatial and temporal resolution. From this initial approach evolved the Global Wildland Fire Emission Model (GWEM) (Hoelzemann et al., 2004) that today can make use of a variety of different landcover data sets (IGBP, MODIS, GLC2000), area burnt satellite information (GLOBSCAR, GBA20000, or other made available area burnt datasets), a Global Dynamic Vegetation Model (Lund-Potsdam-Jena Model (LPJ)), and burning efficiencies as well as emission factors from published literature. GWEM calculates monthly emissions from wildland fires on a 0.5° x 0.5° global resolution to account for the high intra-annual and spatial variability of fire occurrence. In this study, GWEM was tested specifically for the year 2000. Until today this is the only year for which globally consistent area burnt satellite products exist. The perspective of GWEM has been the future availability of multi-year area burnt products such as the GLOBCARBON product from ESA, which was expected for 2003, however is still under development.

The first study with GWEM also served as a testing tool to investigate the skill of these new area burnt satellite products (see Hoelzemann et al., 2004). Later, in the framework of the European RETRO project another global area burnt product for various years was tested with GWEM.

After numerous impact tests of the various input variables and parameters of GWEM-1.3 (based on GBA2000, see Chapter 2) and an intercomparison of the GWEM-1.3 fire emissions with other available global fire emission data sets (Chapter 3), a global impact study of these fire emission inventories on the atmospheric chemical composition was conducted with the Chemistry Transport Model MOZART-2 (Chapter 4). The outcome of these model simulations were compared and evaluated with in-situ and satellite derived measurements of the primary emitted species carbon monoxide (measurements from CMDL surface sites and the MOPITT satellite instrument) and the secondary chemical product ozone (observations from SHADOZ radiosondes and MOZAIC aircrafts). This transport study permitted new insights on the variability induced in modeling studies by the use of different fire emission inventories and on the skill of the individual fire emission data sets.

5.2 Main Findings and Conclusions

The Global Wildland Fire Emission Model GWEM allowed for several new insights on location, season and strength of wildland fire emissions in the year 2000. Large fire variability and pronounced regional fire seasons could be observed owing to the new global area burnt products used in this model. GWEM is the first fire emission model making use of globally consistent area burnt satellite data. Emissions are calculated for various chemical species and carbonaceous aerosols. Globally, the resulting emissions are at the lower end of previous estimates (see Chapter 2 and 3). A detailed inspection of the individual factors contributing to the emission estimates indicates that there is an underestimation in the

GBA2000 burnt areas for regions where small but intense deforestation fires dominate. For other regions however, the GBA2000 product works reasonably well for the needs of global modeling studies. GWEM presents higher estimates in the Northern Hemisphere, especially for Siberia, than many other inventories. Some recently published emission estimates for this region also yielded comparable higher estimates than previous studies (Soja et al., 2004). Others however, show lower numbers for the year 2000 (Kasischke et al. (2005) and highlight the remaining uncertainties for this boreal region.

A quantitative evaluation of the fire emission calculated by GWEM-1.3 and other available global fire emission inventories for the year 2000 required a sensitivity and evaluation study with the Chemistry Transport Model MOZART-2 to allow for final conclusions (Chapter 4).

With no exception, all MOZART simulations using the fire emission inventories GWEM-1.3, cg_scal, mgs_scal, gfed, and hao&liu (see Chapter 3 for details) showed a very significant impact of fire emissions on atmospheric chemistry, particularly on the ozone precursors carbon monoxide (CO) and nitrogen oxides (NO_x) and consequently on ozone. All fire emission inventories were generally able to improve the CTM simulations compared to a model run without any emissions from fires (except for the climatological fire emissions hao&liu, in some cases).

A general feature reflected by all MOZART simulations was the low injection height of fire emissions. In comparison to measurements, the simulated fire plume was systematically located in lower model levels. MOZART distributes its fire emissions in the surface model layer, which has a considerable impact on transport patterns of the fire plumes. The injection height of fires is a complex interaction of fire temperature, burning material and meteorological conditions (winds, convective patterns, etc.) and it is therefore not possible to insert this parameterization in a CTM in a straight forward manner (computational costs still are a constraining factor here).

Overall the performed MOZART simulations showed that none of the applied fire emission inventories was clearly superior in improving the model simulations globally, compared to the others. However there were distinct regional differences in performance that can be summarized as follows: in Africa, CO and ozone concentrations are best represented by the new bottom-up inventories GWEM-1.3 and gfed. The ATSR-scaled climatological fire emission inventories (cg_scal and mgs_scal) mainly follow the seasonal behavior as of the bottom-up inventory based simulations, but fail to reach the quantitative concentrations as given by the observations.

South American carbon monoxide concentrations are quantitatively and seasonally best represented by the gfed fire emission inventory, according to the intercomparison with MOPITT satellite observations. All other fire emission inventories used in MOZART seem to have difficulties to represent a realistic chemical scenario over South America. GWEM-1.3 yields erroneous emissions in this region due to the above mentioned failing of the GBA2000 area burnt product (see GWEM correction (v1.4) in Appendix A). The evaluation with monthly mean ozone observations did not allow for a valid conclusion. By the experience gained with fire emission modeling, a detailed evaluation of daily fire emissions in a CTM is required to account for the high variability of emissions and to be able to completely understand the ozone formations over South America (K. M. Longo, pers. comm., 2005).

For the broader Southern Asian region none of the inventories was able to substantially improve the MOZART performance for CO and ozone. None of the MOZART runs performs clearly better or worse than the others.

There is an overall underestimation of CO concentrations in the northern hemisphere (see section 4.3). This underprediction is not related to fire emissions, but to the Asian inventory on residential fossil fuel use, as described in section 4.2. Over Europe, Eurasia, and North America only the MOZART run with GWEM-1.3 fire emissions shows enhanced concentrations of carbon monoxide during the burning season and also minor enhancements of ozone, which improves the model performance compared to all other MOZART simulations.

Overall, the evaluation of the MOZART runs showed that a reasonable CO simulation does

not necessarily lead to a good representation of ozone. This is for example the case close to the South American mega-cities, where a combination of urban pollution and transported biogenic and fire emissions lead to a complex chemical scenario. On the other hand in remote areas or urban regions that are influenced by non-urban air masses a good CO simulation may go in hand with a good ozone performance of the model (e.g. as observed for Africa).

The new bottom-up fire emission inventories generally showed a superior performance compared to the ATSR-scaled inventories. The ATSR active fire counts often underestimate fire occurrence due to the night-time overpass (many fires are only lit and burn during day). At the same time commission errors occur related to hot spots that are not related to wildland fires but to warm surfaces, gas flares, and city lights. Mota et al. (2006) filtered the ATSR fire counts and found that only between 70-80% of the annual reported hot spots are associated with vegetation fires. However useful and important this additional information on the ATSR-data certainly is, it reinforces the need of an additional regional bias correction to account for the numerous fire underdetections of this product for its application in future studies.

Further, the intercomparison of GWEM with other global fire emission estimates showed that global satellite area burnt products cannot be directly compared to a combination of active fire satellite products with attributed constant burnt area to each fire pixel: if the relation of burnt area per spotted fire changes with time, a bias is inferred in the emission calculations. In presently existing emission inventories based on these different products to localize fires and derive their extension, a clear shift in the seasonality can be observed. Many studies make use of fire emissions derived from active fire pixels, because these simpler fire pixel satellite products exist for more than one year and thus, allow for a multi-year study with interannual variability of fire emissions. However, large uncertainties persist as to the real extension of the detected fires by these simpler algorithms.

5.3 Outlook

This work has considerably contributed to a better understanding of presently available satellite fire data and the implications of various biogeochemical and geophysical properties on fire emission calculations. It has also demonstrated the necessity of further improving the observations and the modeling of wildland fire emissions to meet future needs of the global atmospheric modeling community: on the one hand, climatological modeling studies need consistent global fire emission data sets for various years (or even decades) to be able reproduce and thus understand the climate and its inter-relationships of past years. On the other hand, higher spatial and temporal resolution of fire emissions are required as near real-time (NRT) operating Chemistry Transport Models become computationally feasible to produce daily chemical weather forecasts.

The GWEM model in its present form produces off-line fire emissions for Chemistry Transport Models and relies on pre-processed satellite (fire information), model (fuel load), and published literature input data to produce monthly estimates of emissions that can be used for studies of past years. Future developments of GWEM should include (i) improved fuel load estimates, and (ii) emissions from peat fires. Improved estimates of the available fuel load can either be achieved by the insertion of recently improved data of the vegetation model LPJ that now includes anthropogenic agricultural influences on vegetation by newly introduced Crop Plant Functional Types (L. Criscuolo, PhD-thesis at the International Max Planck Research School on Earth System Modelling (IMPRS) at MPI-M, defended in February 2006). Another option to additionally account for the intra-annual change of fuel loads is the recurrence to satellite products of the Normalized Difference Vegetation Index (NDVI) that is a measure for plant growth. This would allow a deduction on fuel moisture and thus on seasonal dependent burning efficiencies and emission factors. However, according to Barbosa et al. (1999) the derivation of available fuel loads from NDVI requires validation.

Further, the burning of peatlands is not considered in GWEM, since many peat fires cannot be detected by satellite fire products. This is related to their low-temperature burning characteristics and minor changes in the earths' surface properties. Little is still known on the global systematic assessment of peatland fires. A recent extensive study by Kasischke et al. (2005) presented the Boreal Wildland fire Emission Model (BWEM) that calculated fire emissions, including those from peatlands, in the boreal regions. It may be hoped that these data will be available to the atmospheric modeling community to enrich future research. An even more recent study by Poulter et al.(2006) found that peat layers may also be regularly attained by fires in temperate forests and that consequent emissions of fires in these latitudes may be higher than assumed. More insights on emissions from tropical peat fires may be expected from another IMPRS/MPI-M PhD thesis by A. Heil, in preparation (2006).

In addition, more campaigns in different ecosystems that derive burning efficiencies directly from the on-site biomass by assessment of pre-burning and post-burning biomass amounts would avoid the interim step of calculating the available fuel load from the total biomass, which infers another uncertainty in fire emission estimates. Another approach to avoid calculation of the available fuel load was found by Wooster et al. (2003): some satellites are able to measure the Fire Radiative Power (FRP) emitted by a fire. The FRP, integrated over time (called Fire Radiative Energy then) is close-to linearly correlated with the amount of biomass burnt by a fire. This method eliminates three major uncertainty sources in one step, as neither the available fuel load, the area burned, nor the burning efficiencies are required anymore.

Apart from the proposed further developments, GWEM relies on the availability of globally available burnt area data sets. In the framework of the European RETRO project a 20-year area burnt data set derived from the Advanced Very High Resolution Radiometer (AVHRR) with 8km resolution was developed and a preliminary version of it was tested with GWEM. A final version of is still under development (J.M.C. Pereira, pers. comm., 2005). The availability of this product will allow investigating the interannual variability of fire emissions of the 1980's and the 1990's.

Since this and also all previous mentioned area burnt products do not yet fulfill earlier expectations, active fire pixel products from satellites are an integral aspect of developing area burnt estimates. For these products however, more field work and statistical analyses for validation purposes such as presented in Cardoso et al. (2005) and screening for false alarms (Mota et al. 2005) is highly required. From the point of view of an end-user of satellite fire pixel products (such as atmospheric chemistry modelers) it is crucial to obtain detailed information as given in those studies directly by the data provider as the product is released to the public. This has also been stated in a comment by Giglio and Kendall (2004) on a paper by Generoso et al. (2003), where they clarified the considerable discrepancies of two different fire pixel products both derived from the Visible and Infrared Sensor (VIRS).

Satellite derived fire pixels are also a prerequisite for identification of fire locations and extension for the purpose of Chemical Weather Forecast. Recent research is heading toward near-real-time applications, which rely on fast-forward operational estimates of fire emissions estimates. These are only feasible using the simpler hot spot surface-temperature based algorithms. An ecosystem dependent average area burnt size derived from literature and burning campaigns is then attributed to each fire pixel.

Every fire pixel product delivers unique and valuable information, due to different overpass times and frequencies of the different satellites, differences in temperature or other parameter sensitivities. To make best use of all this information, a multi-sensor approach guarantees the most complete fire monitoring.

The first operational near real-time Chemical Weather Forecast Model making use of such an approach is the CPTEC/INPE emission model (Freitas et al., 2005a) that calculates daily fire emissions by using satellite fire pixels from the polar orbiting satellites NOAA/AVHRR (Advanced Very High Resolution Radiometer), and TERRA and AQUA/MODIS, both products from INPE (http://www.cptec.inpe.br/queimadas), as well as data from the geostationary

GOES/VAS (Visible Infrared Spin Scan Radiometer) of the WFABBA system http://cimss.ssec.wisc.edu/goes/burn/abba.html.

The outcome of this emission model is operationally fed to the CATT-BRAMS Chemistry Transport Model (Coupled Aerosol and Tracer Transport to the Brazilian developments on the Regional Atmospheric Modeling System, described in Freitas et al. (2005a)) which produces maps of CO and aerosols on three different grids: the coarsest grid includes Africa and South America, a finer grid operates on South America only, and the grid with the highest resolution (12.5 km x 12.5 km) operates over the Brazilian state of São Paulo. Daily results are made publicly available on: (http://www.cptec.inpe.br/ meio_ambiente).

A recent adaptation of GWEM (version 1.4) based on multi-sensor satellite fire data for South America provided by CPTEC/INPE for the year 2000, shows a considerable improvement in regional locations and seasonality of emissions by fires (see Appendix A).

To establish global fire emission estimates, the Brazilian approach could be extended by including more fire pixel products that cover the remaining globe.

However, the attribution of the burnt area extension to the fire pixels still remains a major uncertainty, even constrained to the tropical and subtropical latitudes (K. Longo, pers. comm., 2005). An extension to the temperate and boreal zones will even be more challenging, since fire patterns highly differ from the tropics.

The development of the GWEM model has shown that a regionalized approach is needed to account for the highly differing fire behavior on different continents, latitudes and ecosystems. In tropical deforestation areas, a higher resolution may help to further improve emission estimates. Recently Giglio et al. (2006) have presented a new global area burnt product, where a quantitative relationship was established between AQUA/TERRA MODIS fire pixels and available MODIS area burnt tiles from various regions. By these means a further step is taken to reduce the uncertainty of the area burnt parameter.

The effort of a multi-sensor approach is also being focused by the European GEMS project (Global and Regional Earth-System Monitoring using Satellite and In-Situ Data, EC 6th Framework Project under leadership of the European Centre for Medium-range Weather Forecast (ECMWF), see http://www.ecmwf.int/research/EU_projects/GEMS), therein entitled "Fire Assimilation of Wildfire Emissions". The outcome of the GWEM model development also provided an incentive to these recent efforts. It is planned to implement GWEM in the ECMWF model to serve as a basis of the new fire assimilation system.

A further improvement still needed in CTM's is the integration of fire injection heights. Most CTM's insert fire emissions in the lowermost model level. In more recent studies some modelers have adopted a constant database with different injection heights per latitude and ecosystem based on a compilation of literature values by Lavoué (pers. comm. 2003) (e.g. in the Aerosol Inter Comparison project AeroCom (http://nansen.ipsl. jussieu.fr/AEROCOM/, Dentener et al., 2006). In reality, if meteorological conditions are favorable, smoke plume heights of fires are highly variable and may be injected into altitudes above the planetary boundary layer (PBL) (e.g. Fromm and Servranckx, 2003; and Andreae et al., 2001). From there they can even be transported over thousands of kilometers on an intercontinental scale. These processes are driven initially by fire heat and fuel moisture, depending later on meteorological conditions mainly (wind, temperature, precipitation), and can therefore only be correctly calculated if data from the meteorological module of the CTM is used for its parameterization. Freitas et al. (2006) have adopted a new parameterization of shallow and deep cumulus by Grell (1993) and Grell and Devenyi (2002) in CATT-BRAMS that calculates the plume-rise from fires. It considers the quantity of biomass, burnt area and fire temperature and is coupled with a microphysics parameterization. The study by Freitas et al. (2006) report a major improvement of the simulated pollution transport patterns by the introduction of the plume-rise parameterization.

Finally, advanced data assimilation of fire relevant chemical species and aerosols into CTM's will help to further constrain

fire emission bottom-up inventories and highlight regions or specific ecosystems where emissions from fires still remain highly uncertain. Simpler inversion methods have been applied earlier to evaluate the skill of fire inventories and other emission sources (e.g. Arellano et al., 2004; Pétron et al., 2004, and Van der Werf et al., 2004), however with some regional contradictions between inversions of the same observational data. Pétron et al. (2004) conclude that the discrepancies may be associated with differences in the applied inversion techniques, specification and number of regions, errors assigned to emissions and observations and finally, the selection and filtering of observations.

Appendix A - GWEM-1.4 Description

The Global Wildland Fire Emission Model version 1.3 that was used throughout this study was improved for South America. The global area burnt product GBA2000 used in GWEM presents some major flaws for the South American continent. For this reason, a new version of GWEM, version 1.4, was created for future applications that makes use of two pre-compiled satellite fire pixel products from the Brazilian Center of Weather Forecast and Climate Studies at the National Institute for Space Research (CPTEC/INPE, K. M. Longo, pers. comm. 2005). One of the satellite fire pixel product is from the AVHRR/NOAA series (Advanced High Resolution Radiometer from the National Oceanic & Atmospheric Administration, US) series received by CPTEC/INPE, Brazil (http://www.cptec.inpe.br/queimadas). The other is from the GOES satellite (Geostationary Operational Environmental Satellite) (Prins and Menzel, 1992 and Prins, et al. 1998; available at http://www.nrlmry.navy.mil/flambe/index.html). This new compilation of fire pixels assumes a representative average burnt area for each fire pixel and almost doubled the burnt area in South America for the year 2000 from 119100 km^2 (GWEM-1.3) to 213 021 km^2 (GWEM1.4). CO emissions however, are only enhanced by 30% to the amount of 20 Tg CO. Qualitative results of the temporal evolution (Figure A1) and the spatial distribution (Figure A2) of this multi-tier approach are quite satisfactory, albeit still with some systematic underestimation in quantities, resulting partly from the coarse resolution of the GOES fire satellite data that provides the area burnt location and extension. However it represents a large improvement compared to the earlier GWEM-1.3 version for South America.
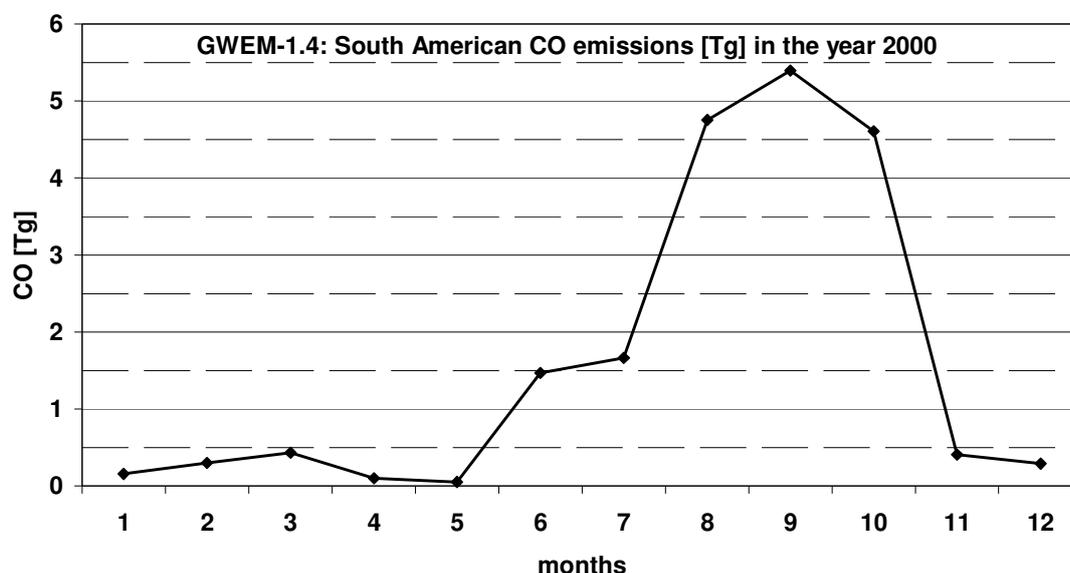
Figure A1: GWEM-1.4 monthly CO evolution in [Tg] during the year 2000 in South America
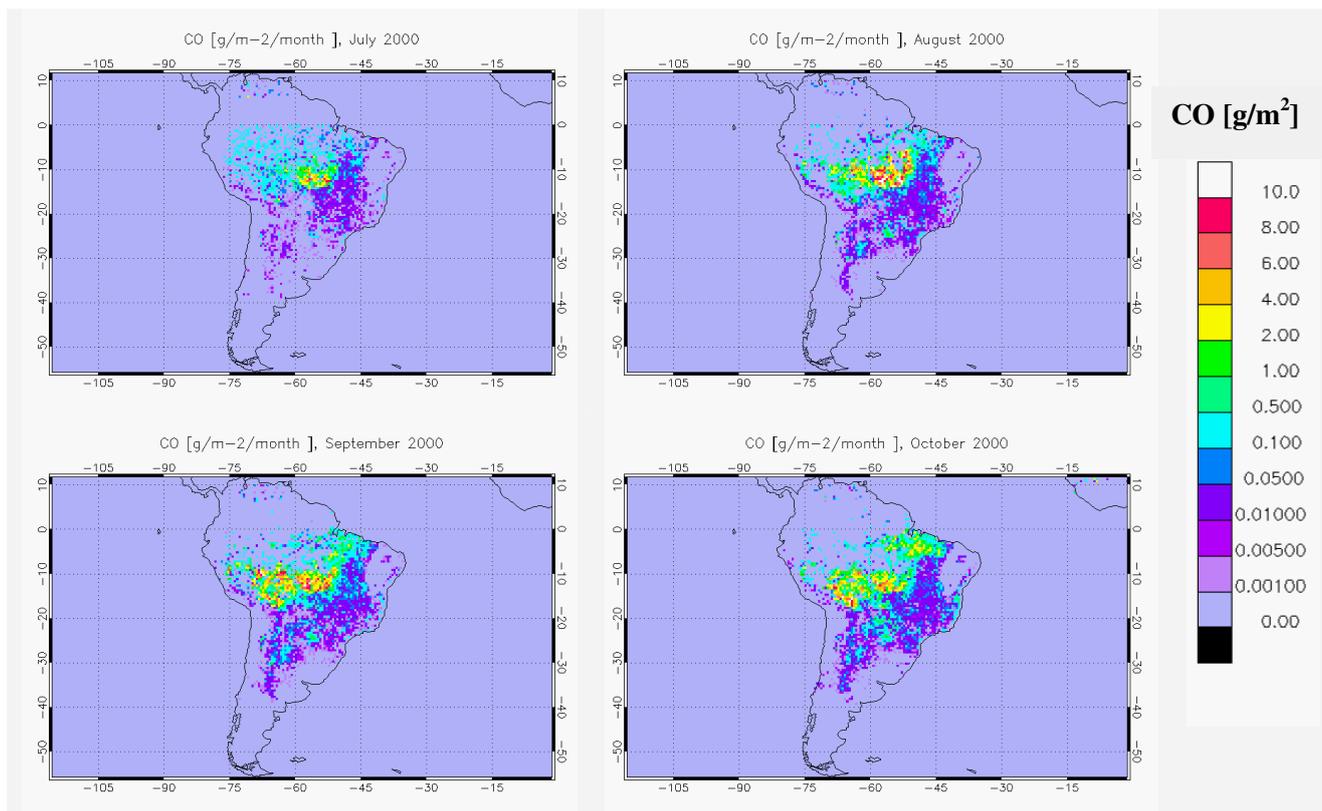
Figure A2: GWEM-1.4 monthly CO distribution in [g/m²] during the burning season in South America for the year 2000

Appendix B – Global MOZART Figures of All Simulations
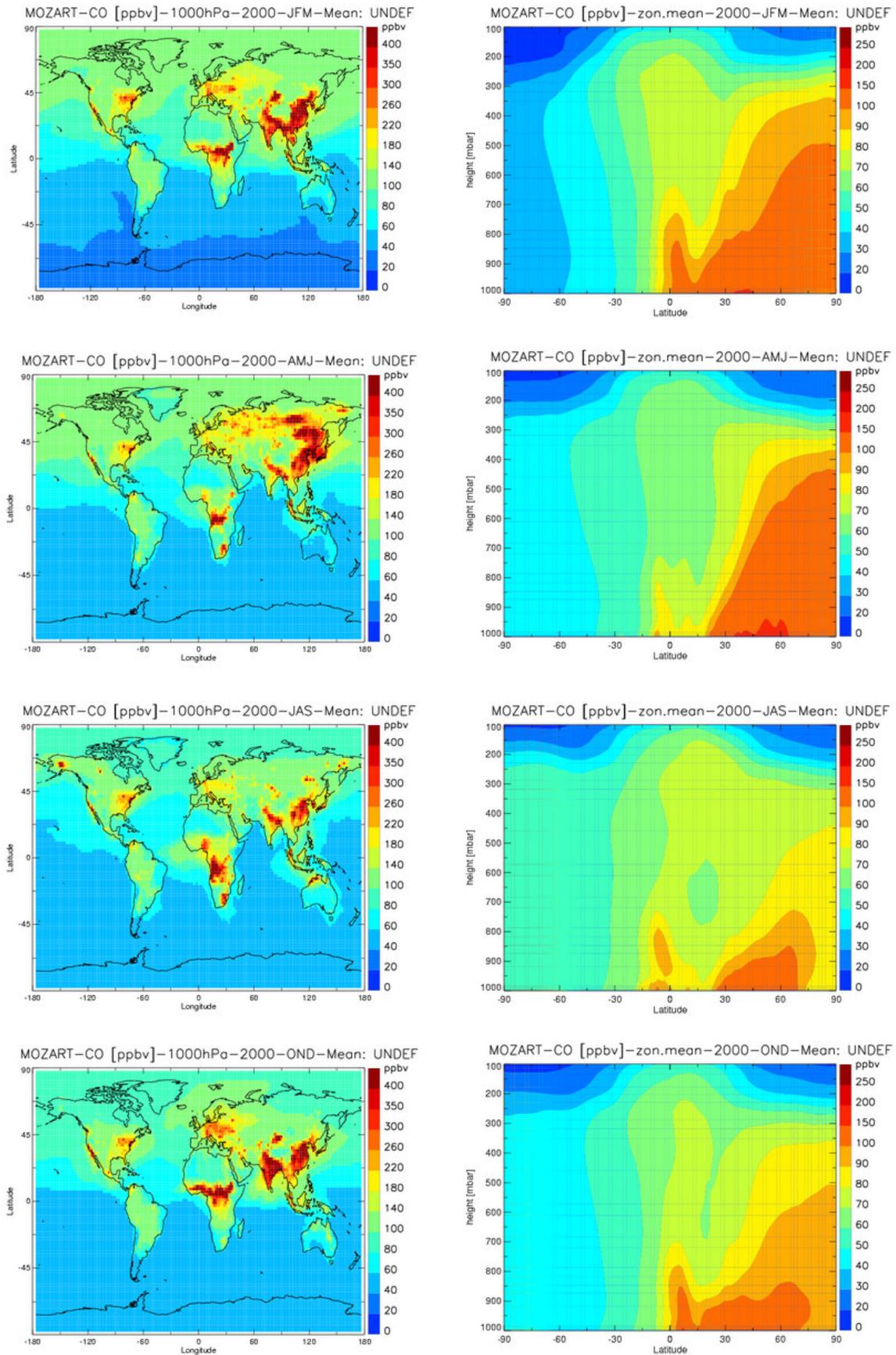
Figure B1: MOZART run A global seasonal carbon monoxide (CO) concentrations in ppbv of the year 2000, using GWEM-1.3 fire emissions. On the left hand side are seasonal CO concentrations at surface level, on the right hand side seasonal zonal means (note the different scales)
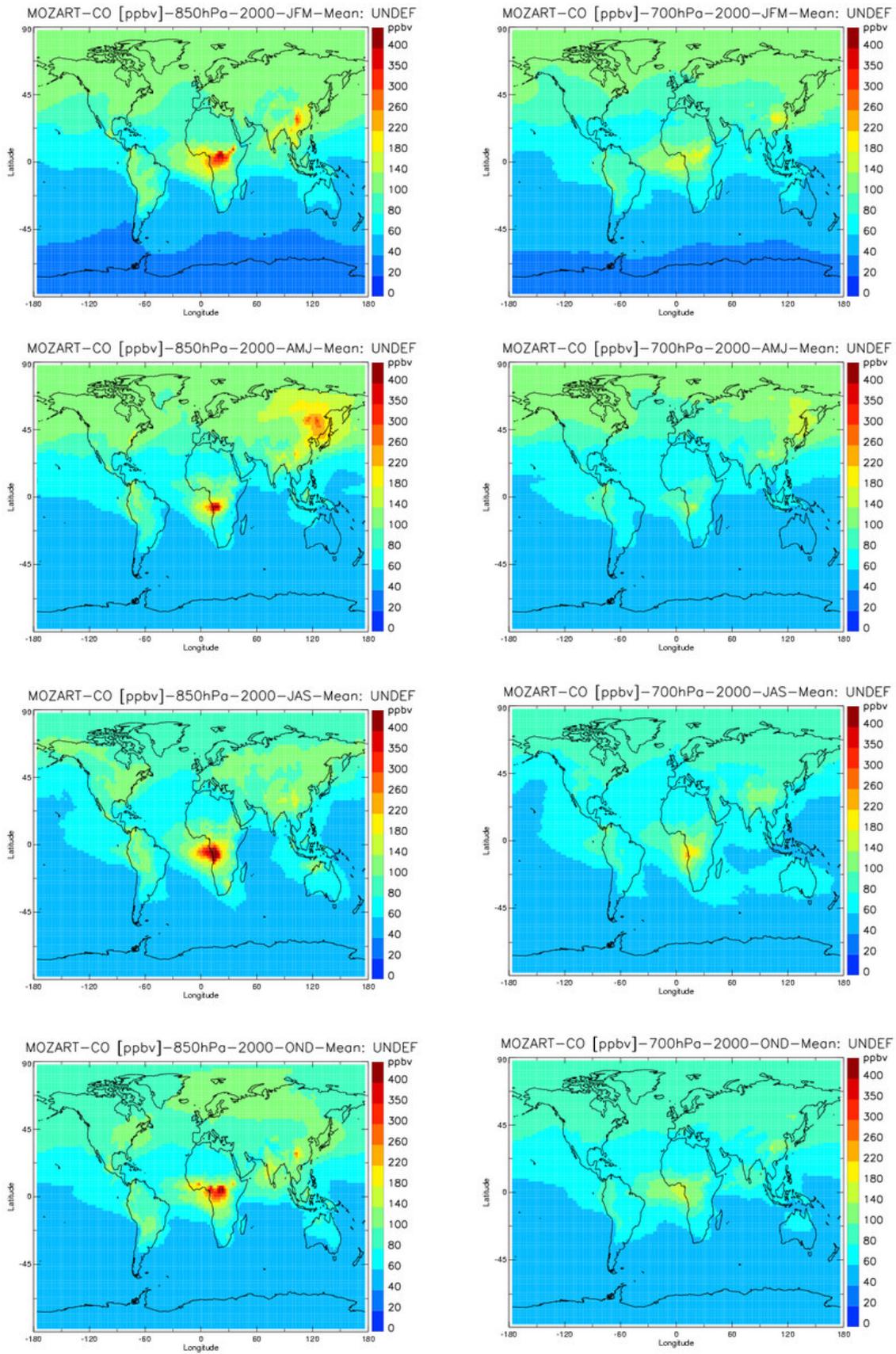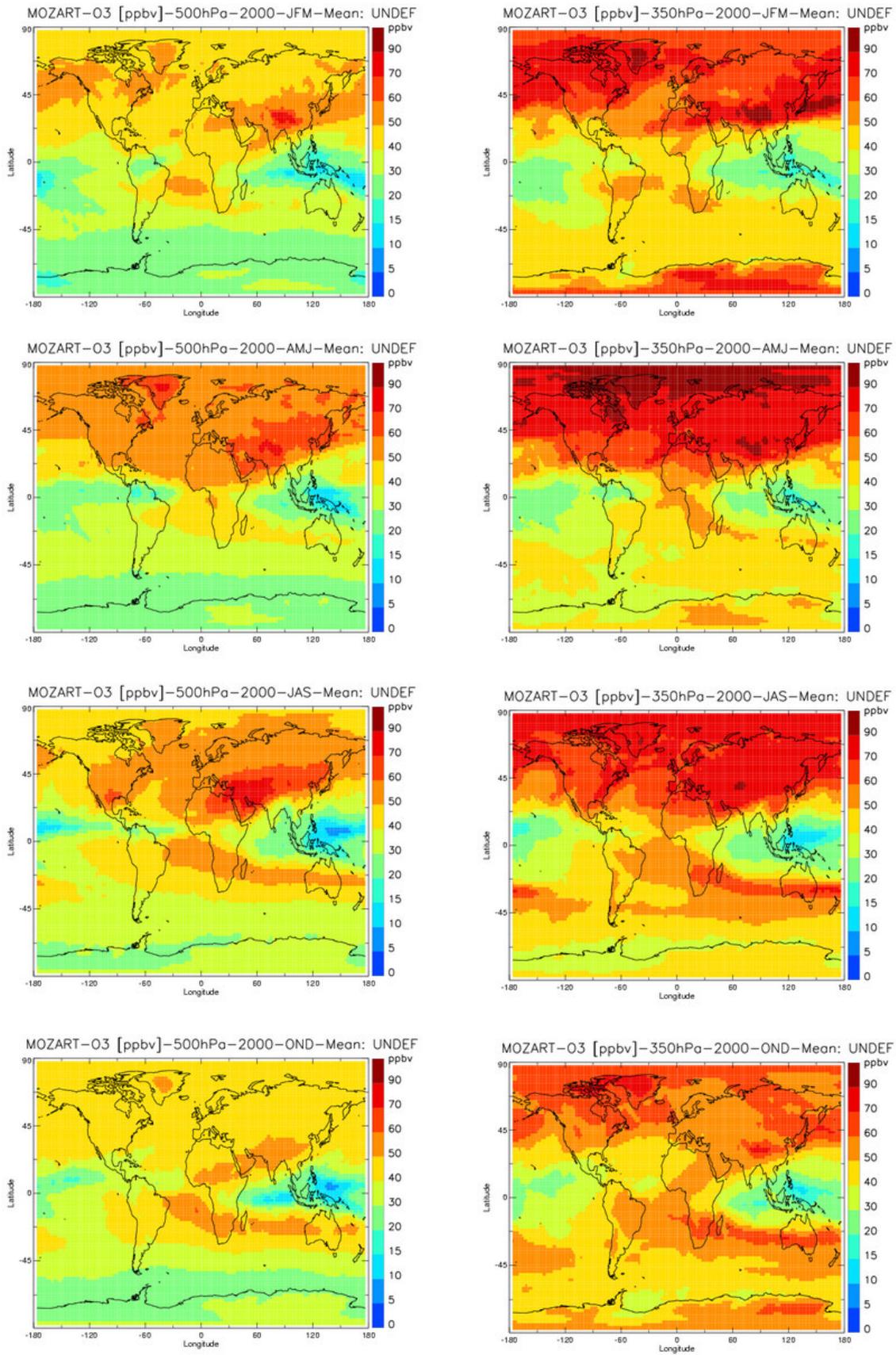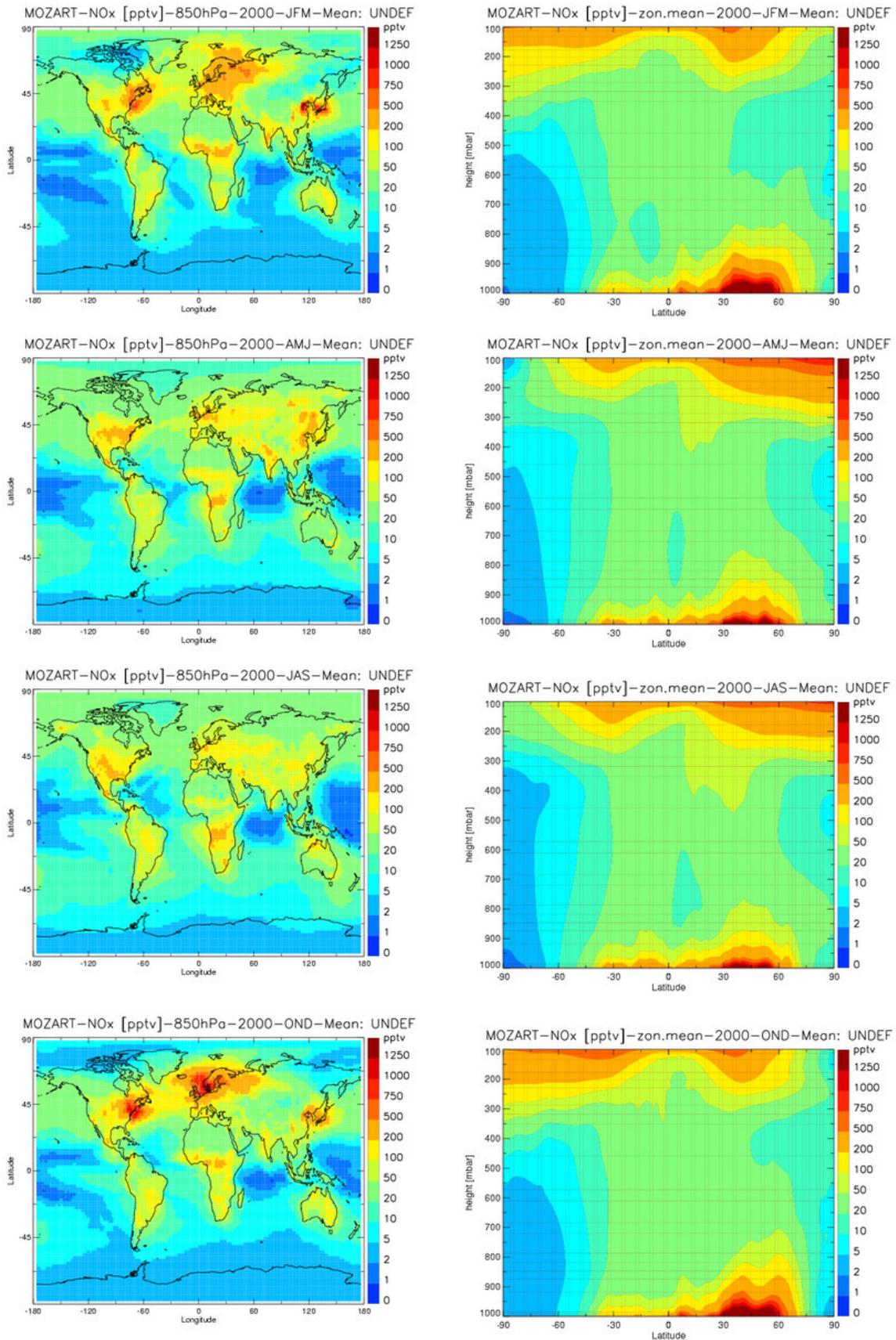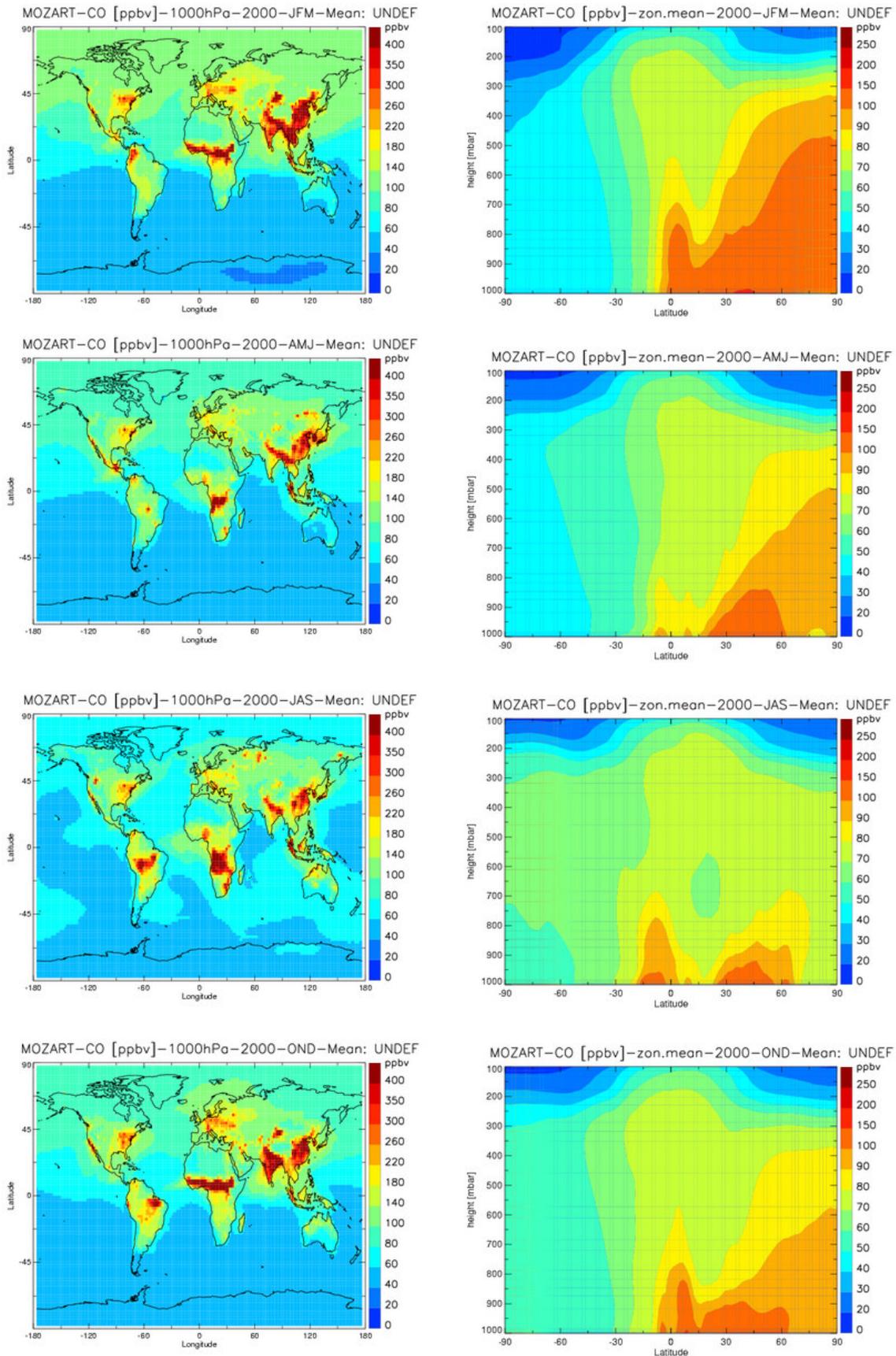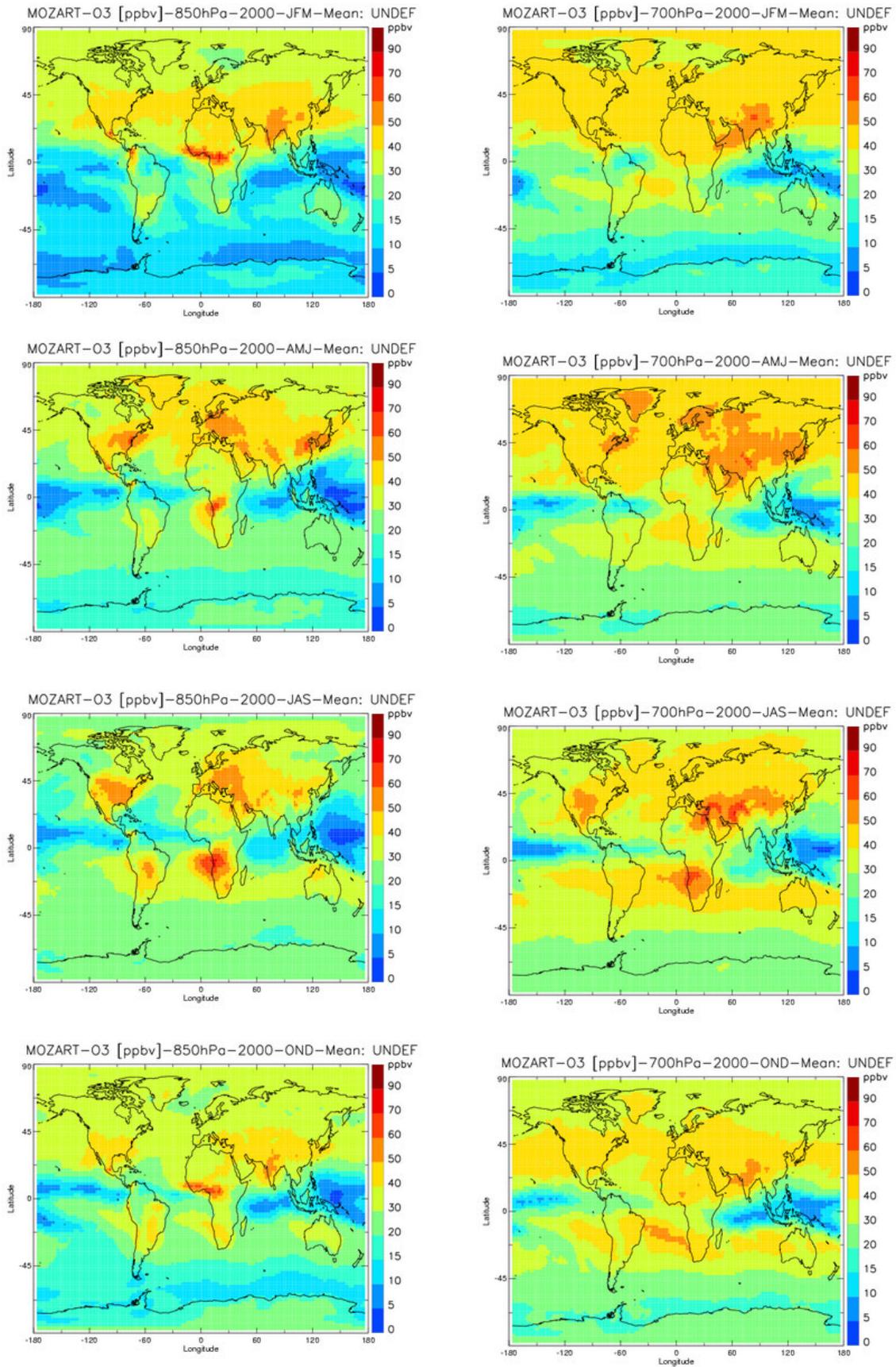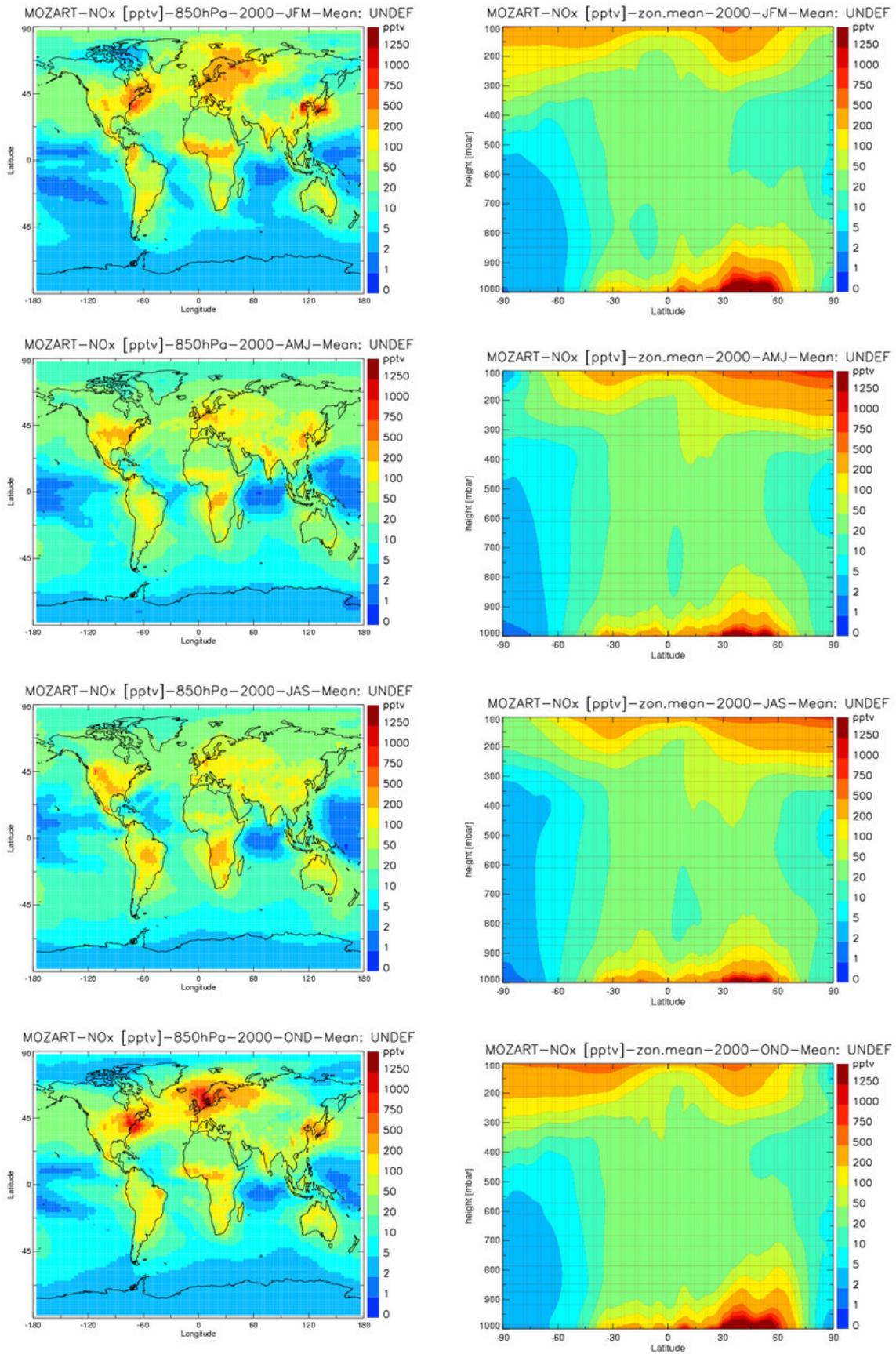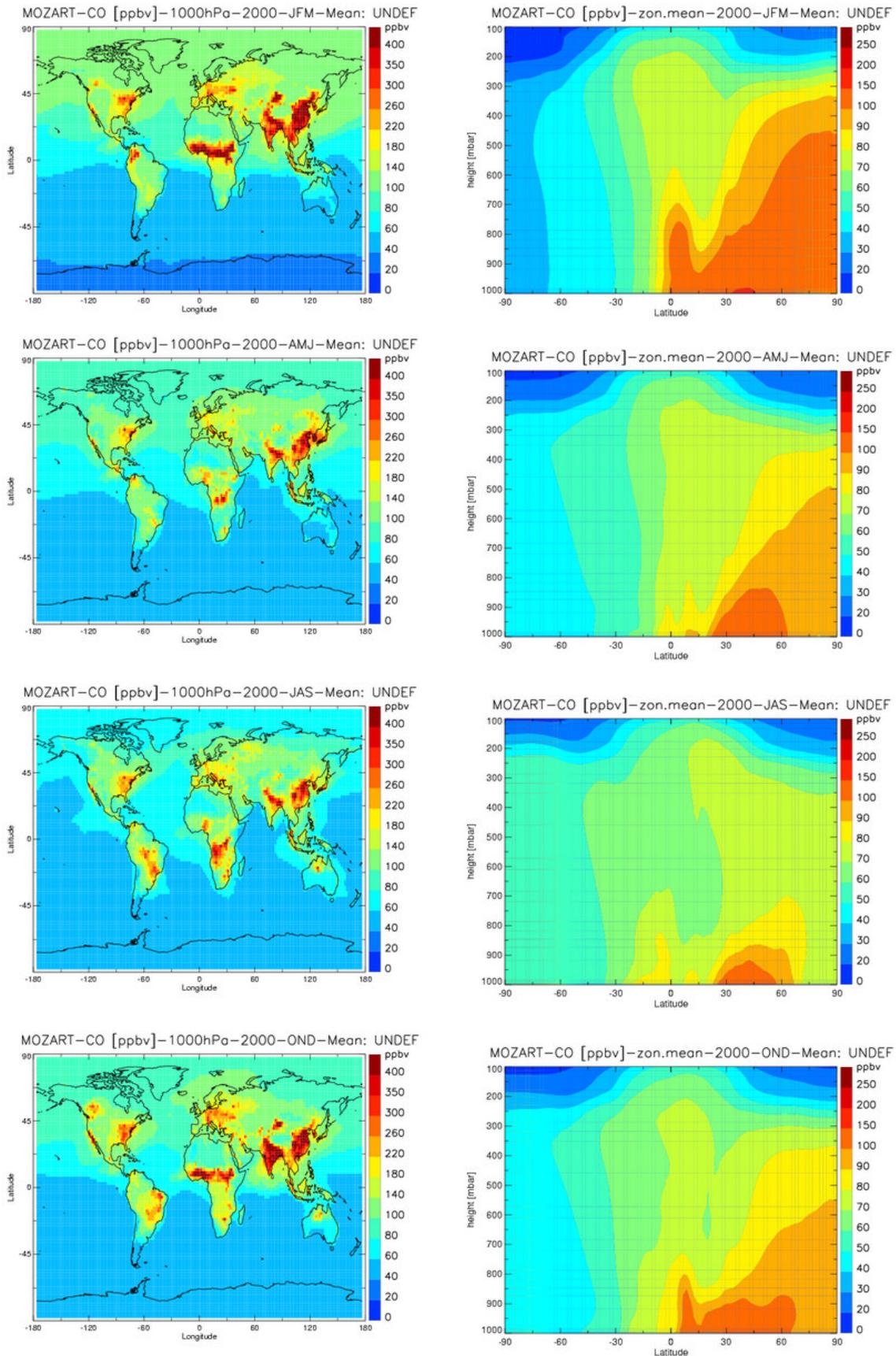
Figure B2: MOZART run A global seasonal carbon monoxide (CO) concentrations in ppbv of the year 2000 at 850 hPa and 700 hPa, using GWEM-1.3 fire emissions
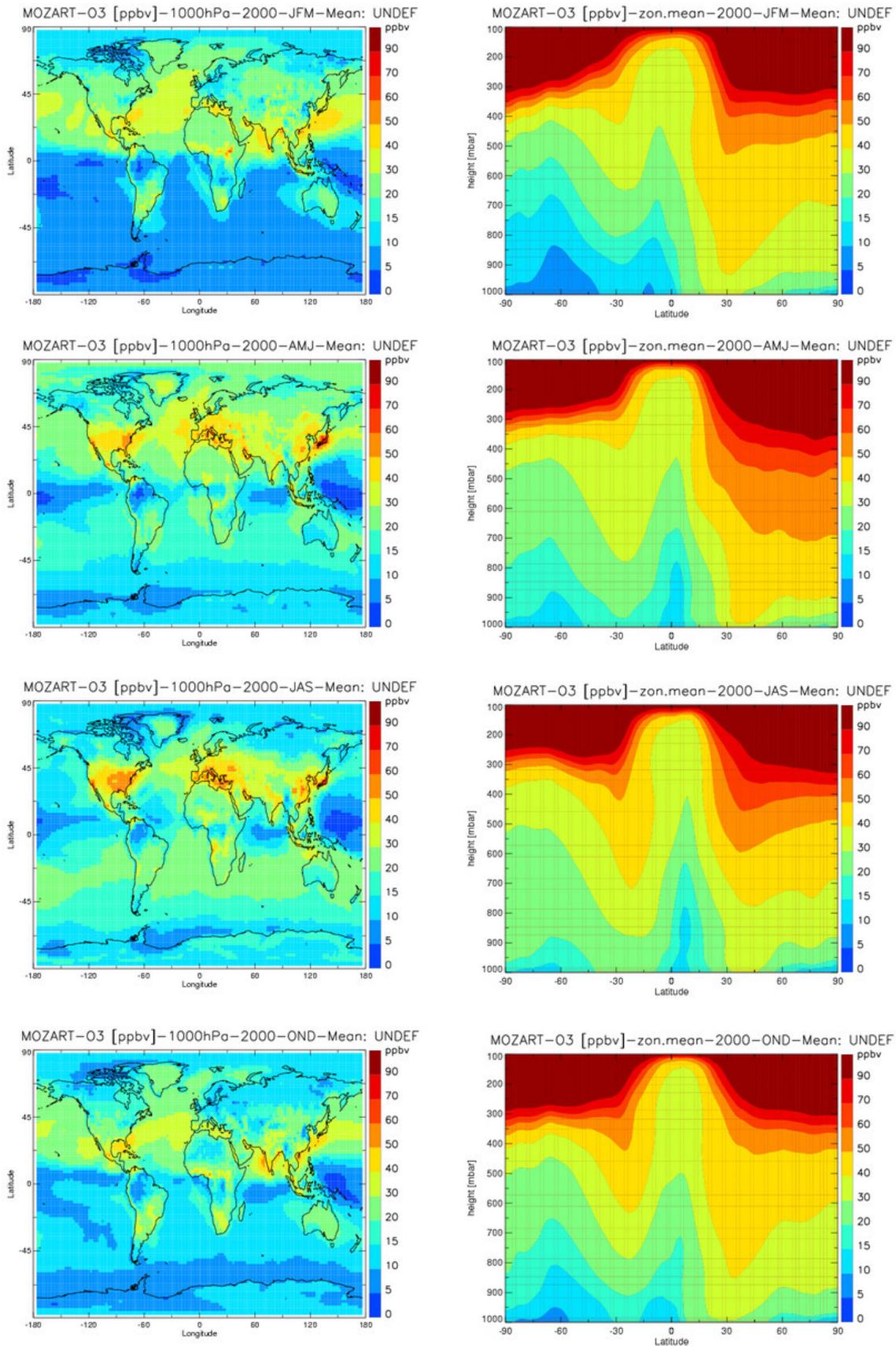
Figure B3: MOZART run A global seasonal ozone concentrations in ppbv of the year 2000, using GWEM-1.3 fire emissions. On the left hand side are seasonal ozone concentrations at surface, on the right hand side seasonal zonal means
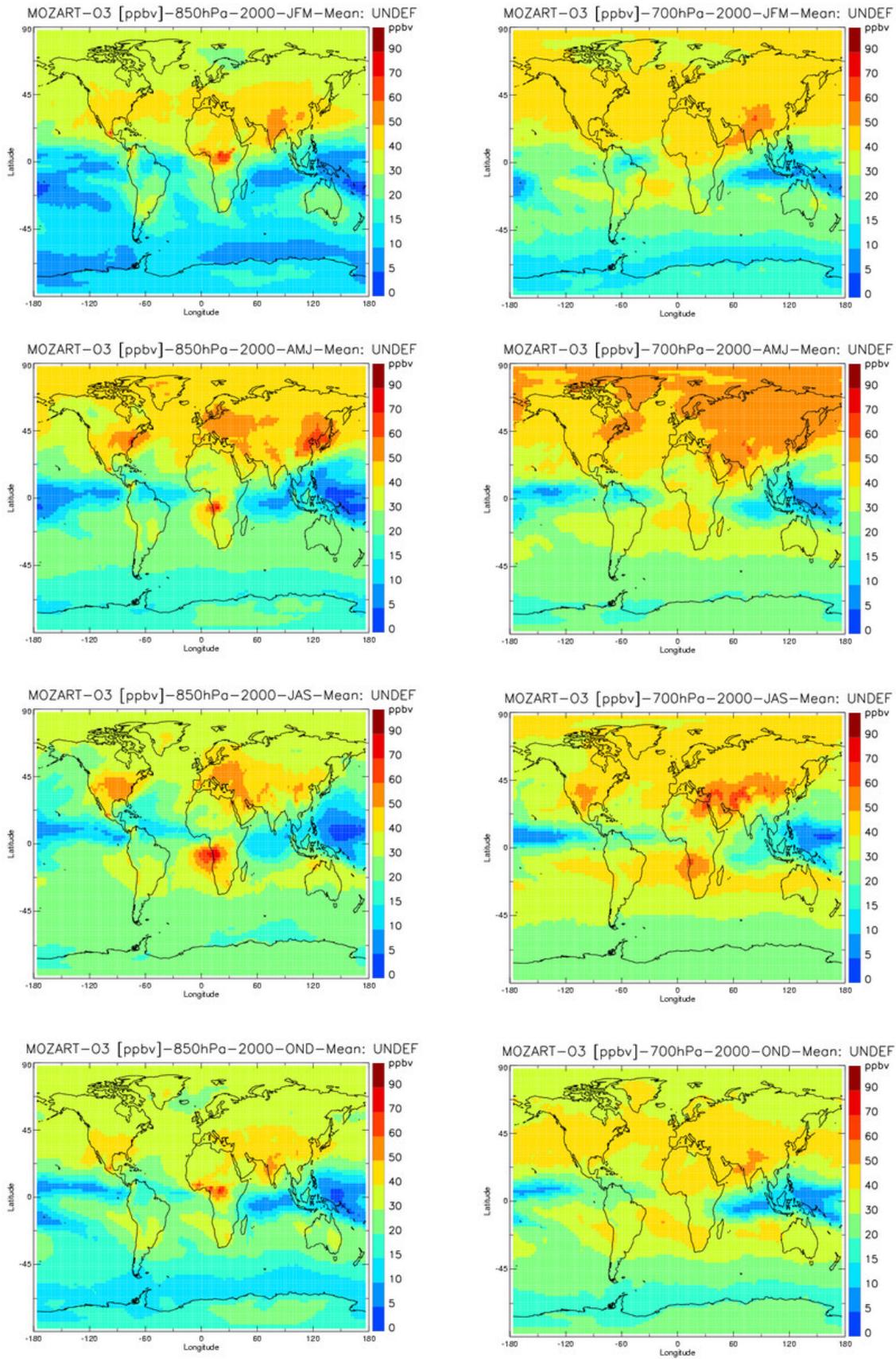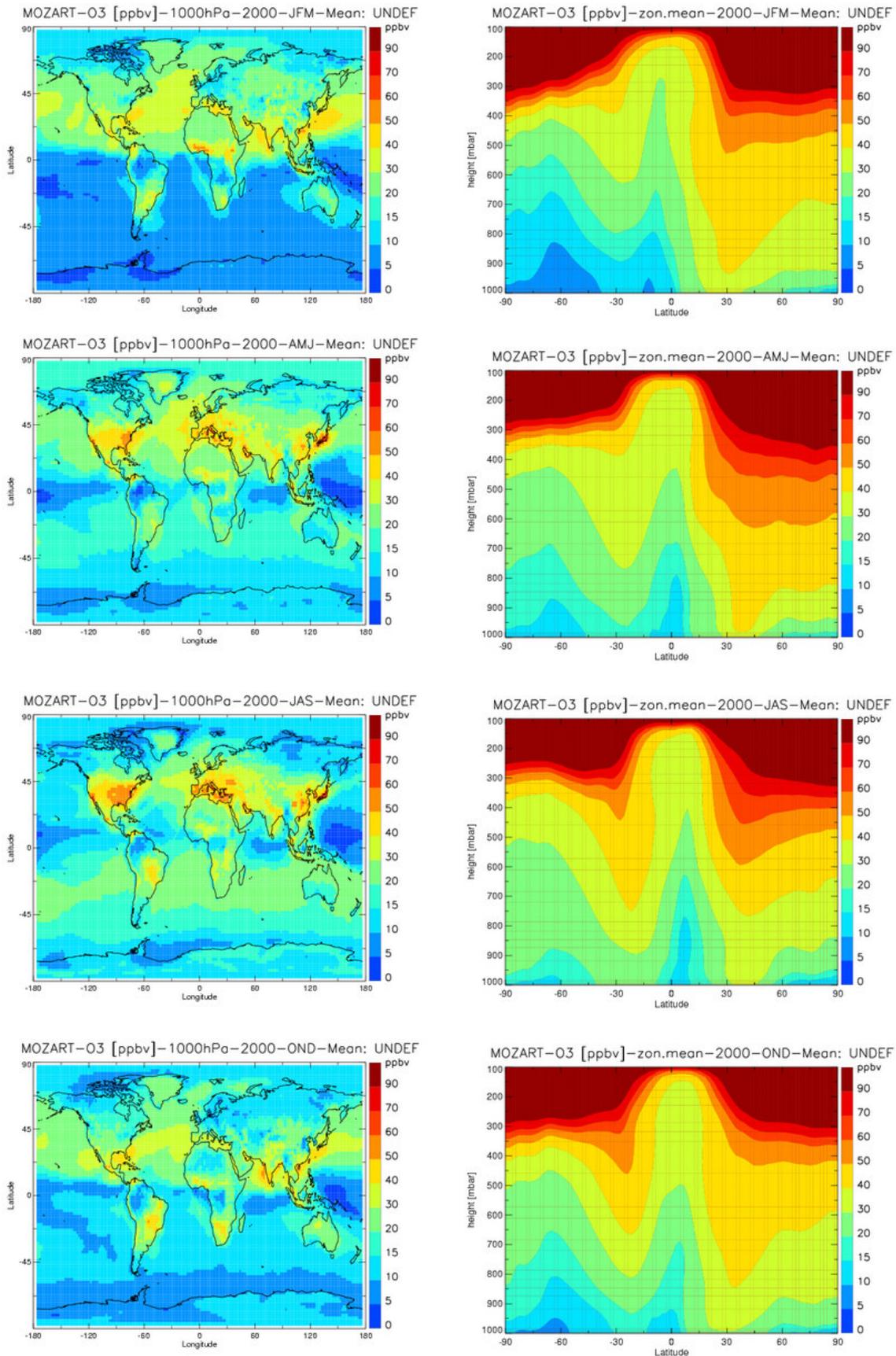
Figure B4: MOZART run A global seasonal ozone concentrations in ppbv at 850 hPa and 700 hPa of the year 2000, using GWEM-1.3 fire emissions

Figure B5: MOZART run A global seasonal ozone concentrations in ppbv at 500 hPa and 350 hPa of the year 2000, using GWEM-1.3 fire emissions
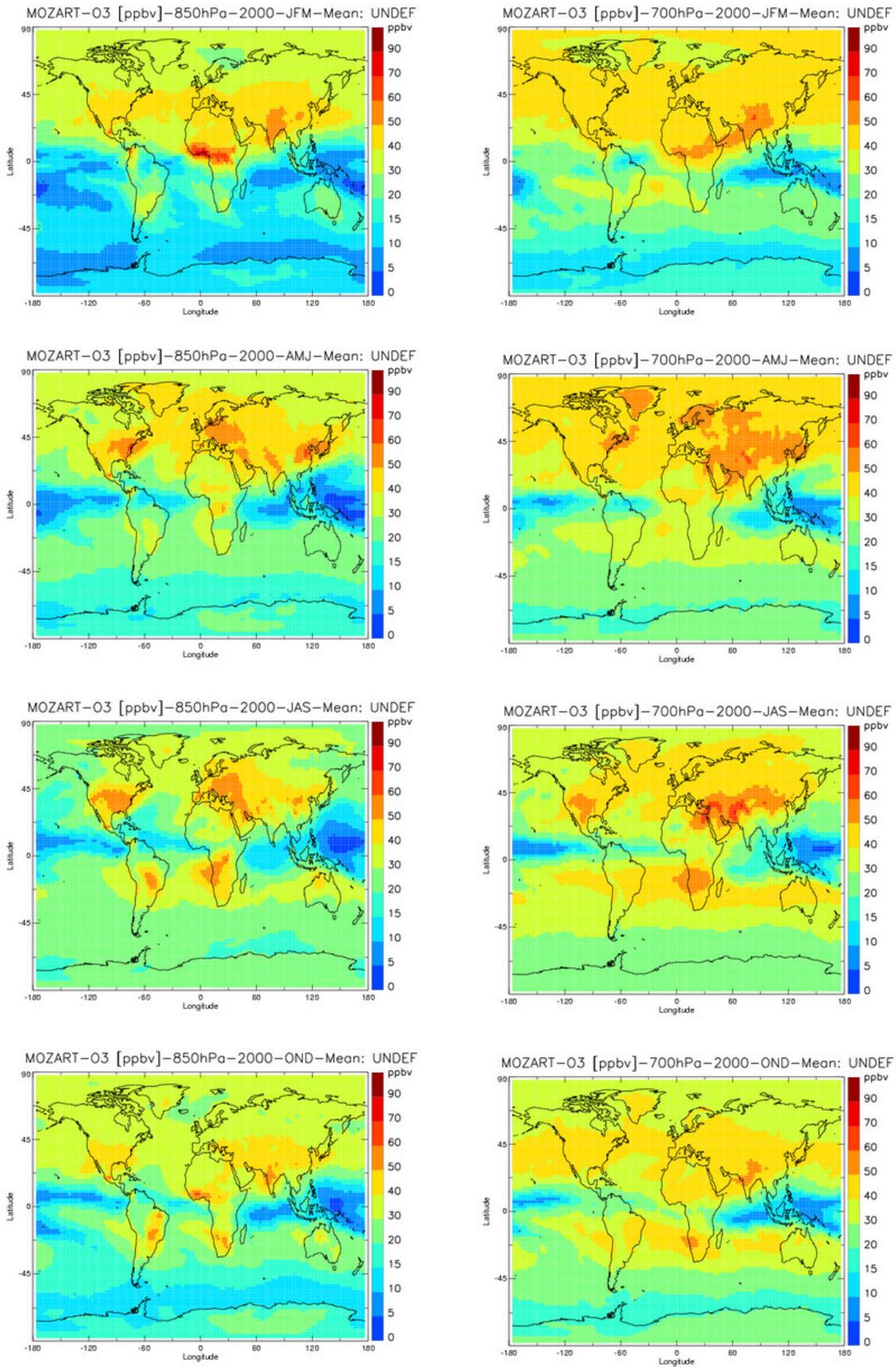
Figure B6: MOZART run A global seasonal nitrogen oxide concentrations in ppbv of the year 2000, using GWEM-1.3 fire emissions. On the left hand side are seasonal nitrogen oxide concentrations at 850 hPa, on the right hand side seasonal zonal means
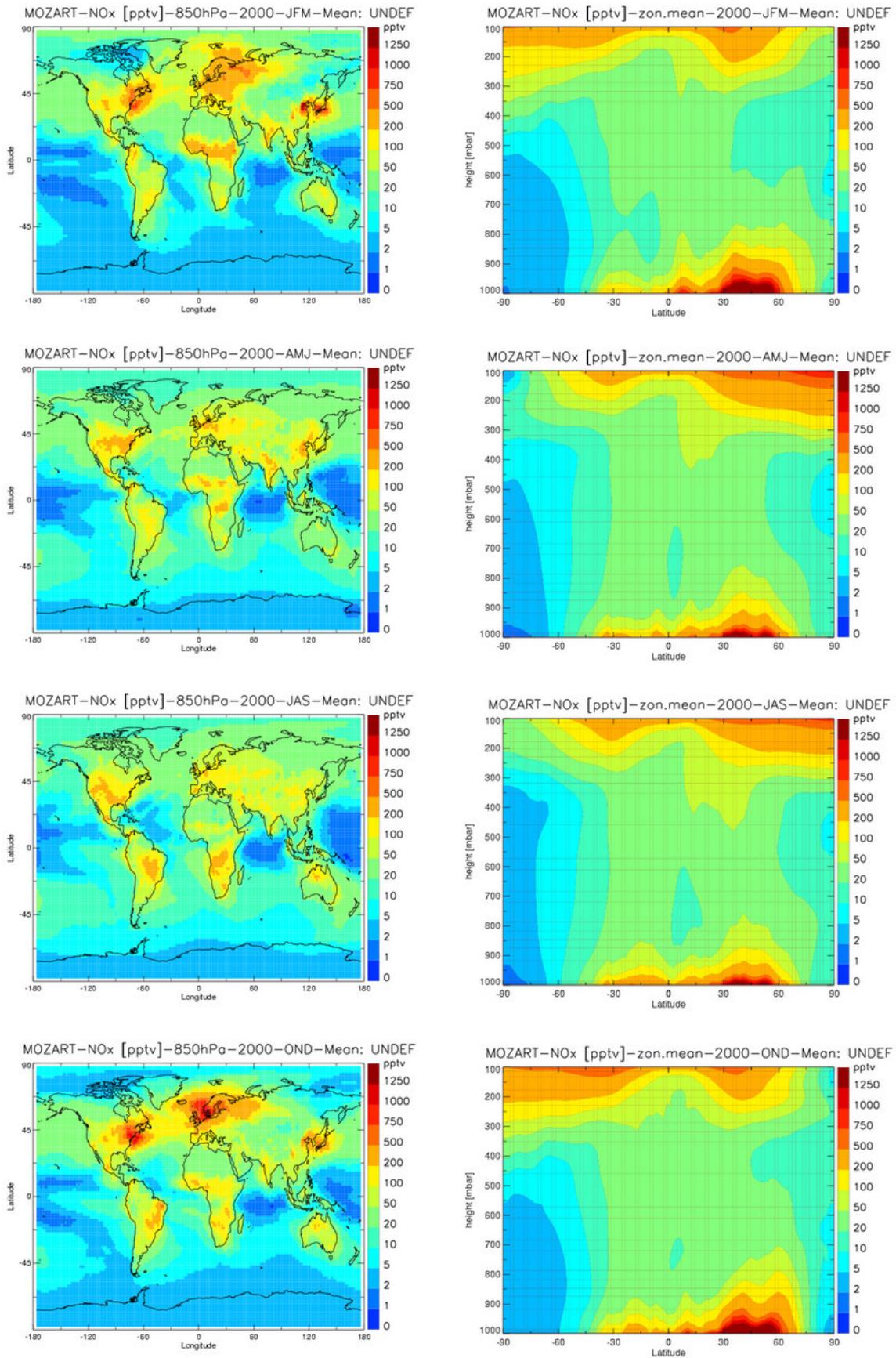
Figure B7: MOZART run J global seasonal carbon monoxide (CO) concentrations in ppbv of the year 2000, using gfed fire emissions. On the left hand side are seasonal CO concentrations at surface level, on the right hand side seasonal zonal means (note the different scales)
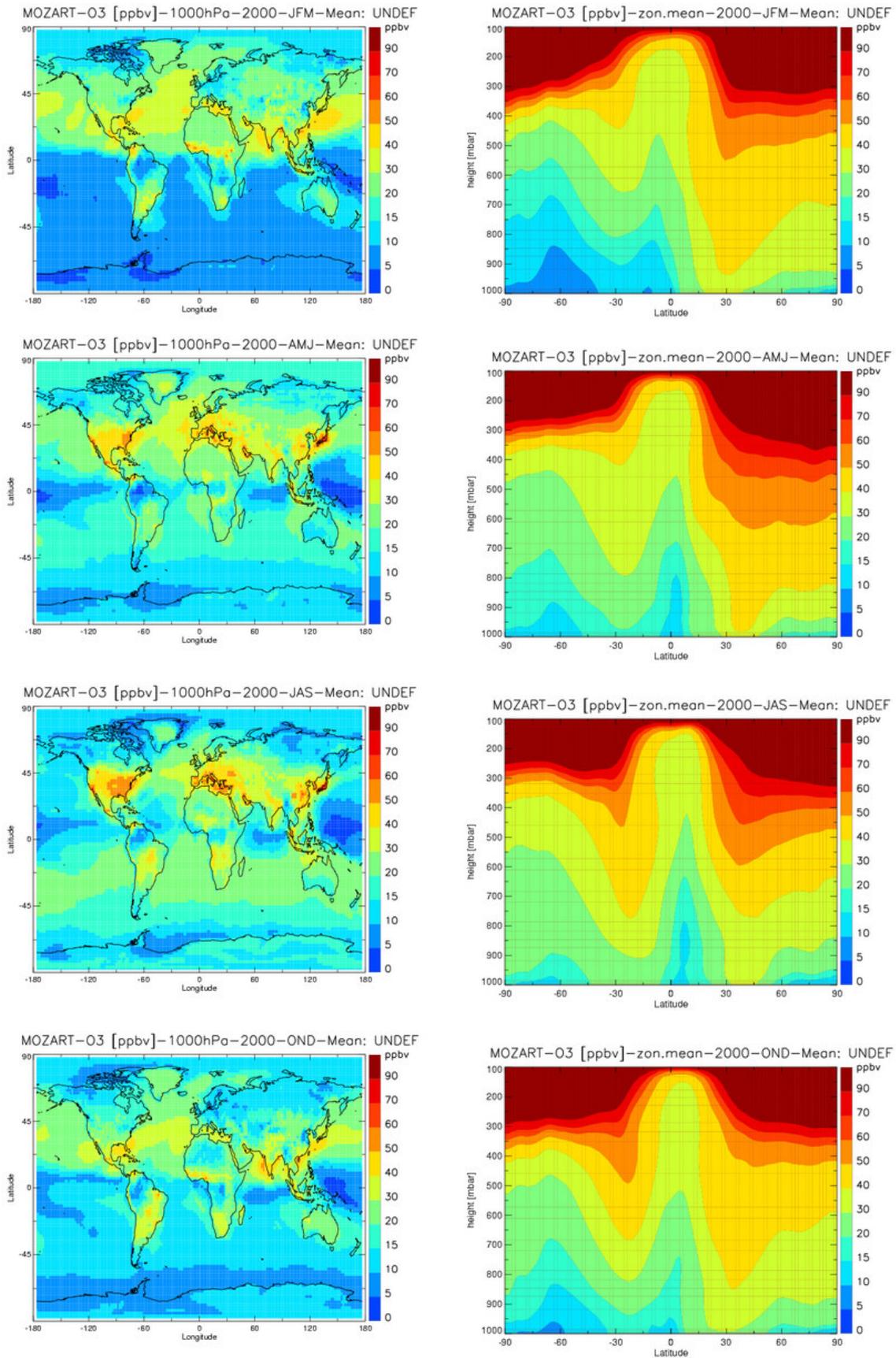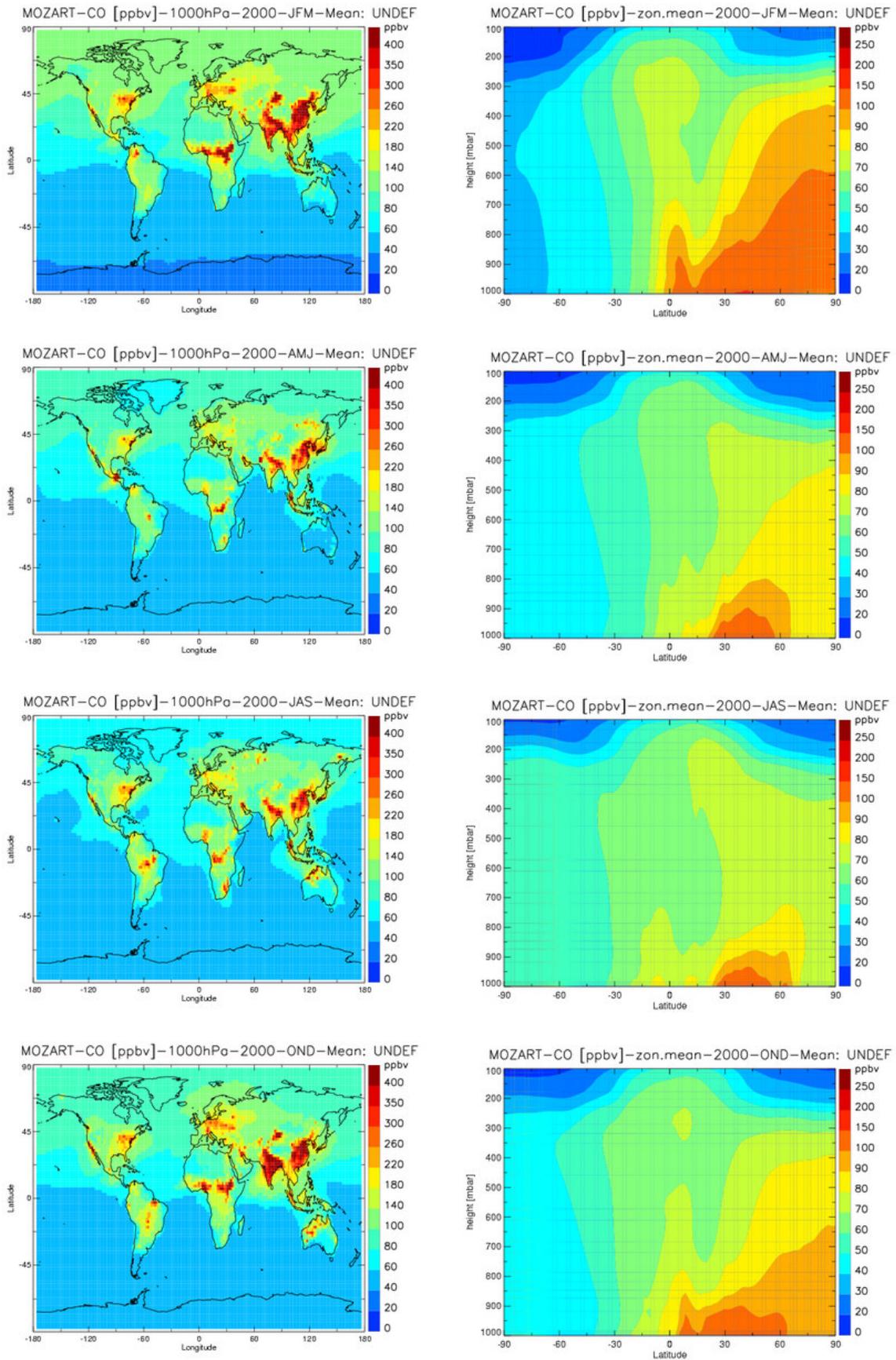
Figure B8: MOZART run J global seasonal ozone concentrations in ppbv of the year 2000, using gfed fire emissions. On the left hand side are seasonal ozone concentrations at surface, on the right hand side seasonal zonal means

Figure B9: MOZART run J global seasonal ozone concentrations in ppbv at 850 hPa and 700 hPa of the year 2000, using gfed fire emissions

Figure B10: MOZART run J global seasonal nitrogen oxide concentrations in ppbv of the year 2000, using gfed fire emissions. On the left hand side are seasonal nitrogen oxide concentrations at 850 hPa, on the right hand side seasonal zonal means

Figure B11: MOZART run H seasonal carbon monoxide (CO) concentrations in ppbv of the year 2000 using ATSR scaled Hao&Liu fire emissions (mgs_scal) fire emissions. On the left hand side are seasonal CO concentrations at surface level, on the right hand side seasonal zonal means (note the different scales)

Figure B12: MOZART run H seasonal ozone concentrations in ppbv of the year 2000, using ATSR scaled Hao&Liu fire emissions (mgs_scal) fire emissions. On the left hand side are seasonal ozone concentrations at surface, on the right hand side seasonal zonal means
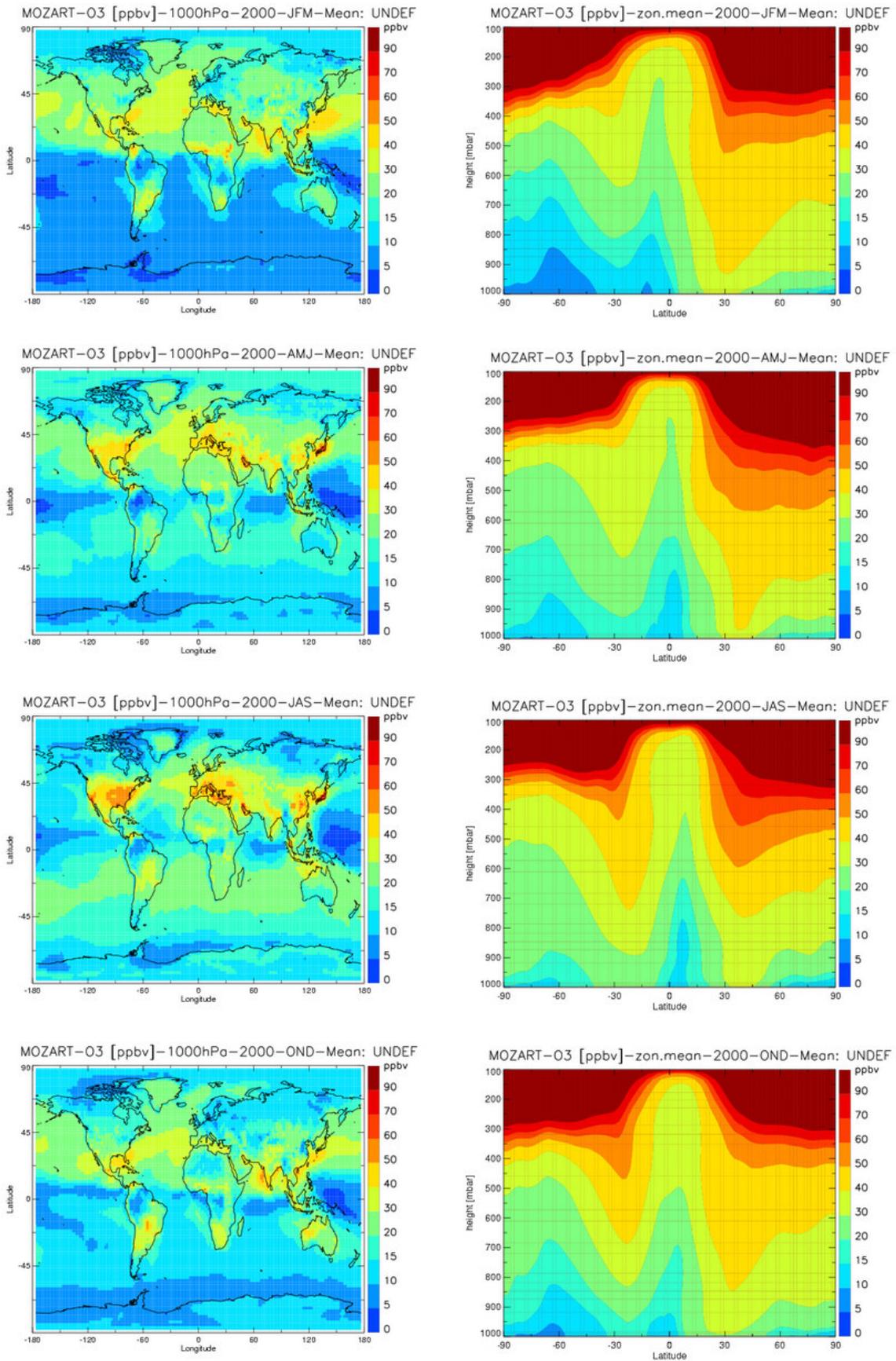
Figure B13: MOZART run H seasonal ozone concentrations in ppbv at 850 hPa and 700 hPa of the year 2000, using ATSR scaled Hao&Liu fire emissions (mgs_scal) fire emissions

Figure B14: MOZART run H seasonal nitrogen oxide concentrations in ppbv of the year 2000, using ATSR scaled Hao&Liu fire emissions (mgs_scal). On the left hand side are seasonal nitrogen oxide concentrations at 850 hPa, on the right hand side seasonal zonal means

Figure B15: MOZART run G seasonal carbon monoxide (CO) concentrations in ppbv of the year 2000, using ATSR scaled Hao&Liu fire emissions (cg_scal). On the left hand side are seasonal CO concentrations at surface level, on the right hand side seasonal zonal means (note the different scales)

Figure B16: MOZART run G seasonal ozone concentrations in ppbv of the year 2000, using ATSR scaled Hao&Liu fire emissions (cg_scal) fire emissions. On the left hand side are seasonal ozone concentrations at surface, on the right hand side seasonal zonal means
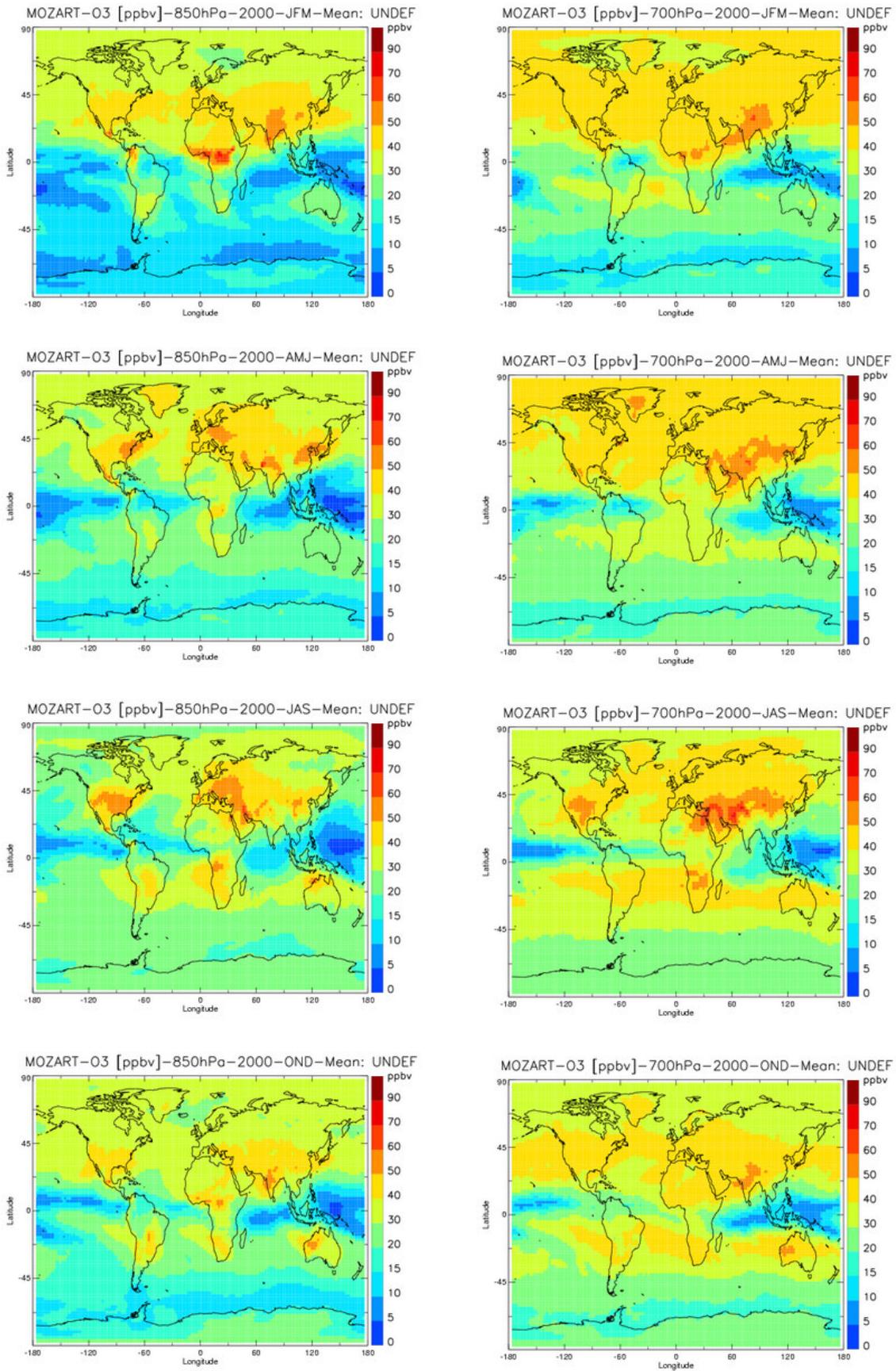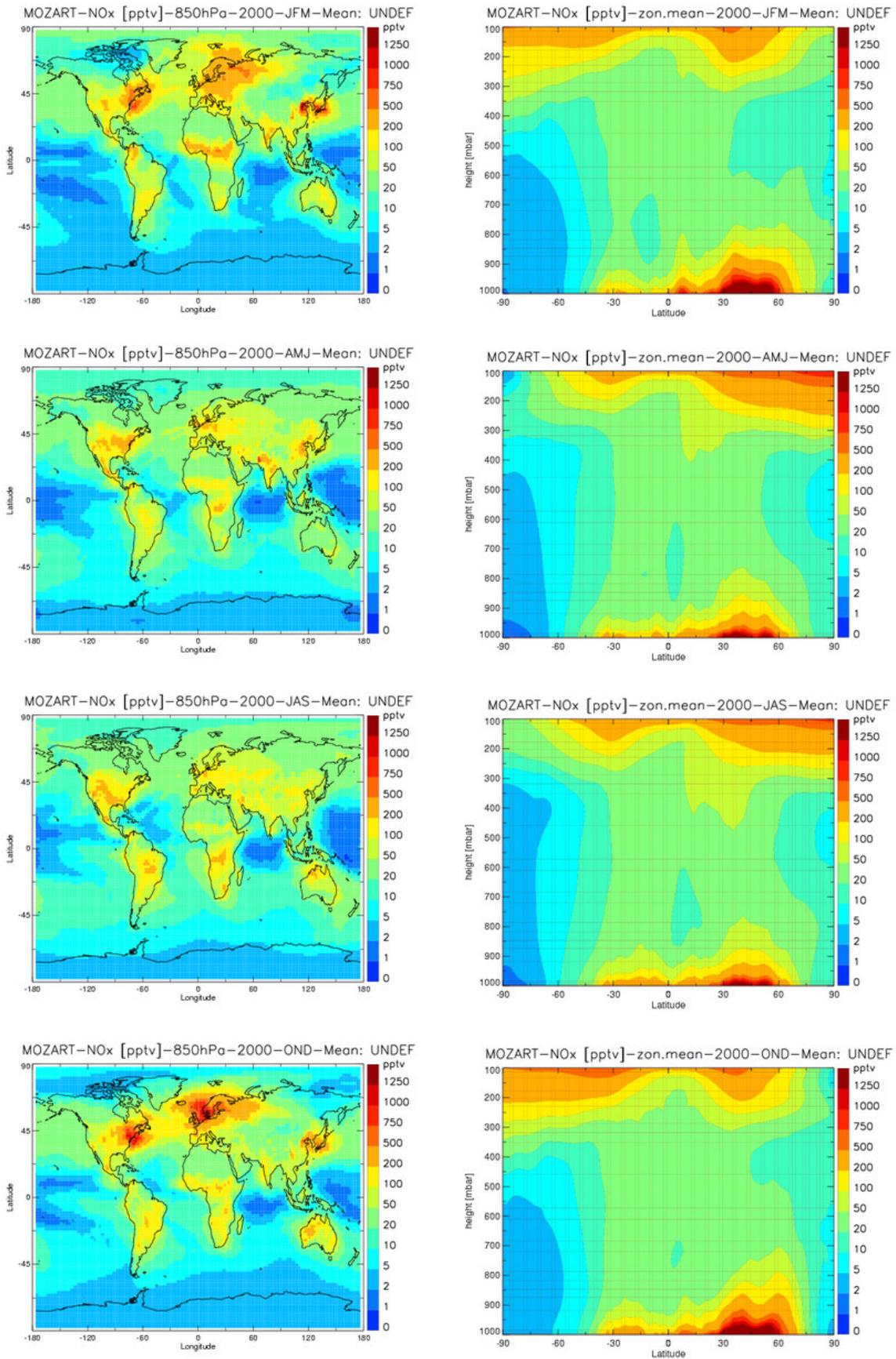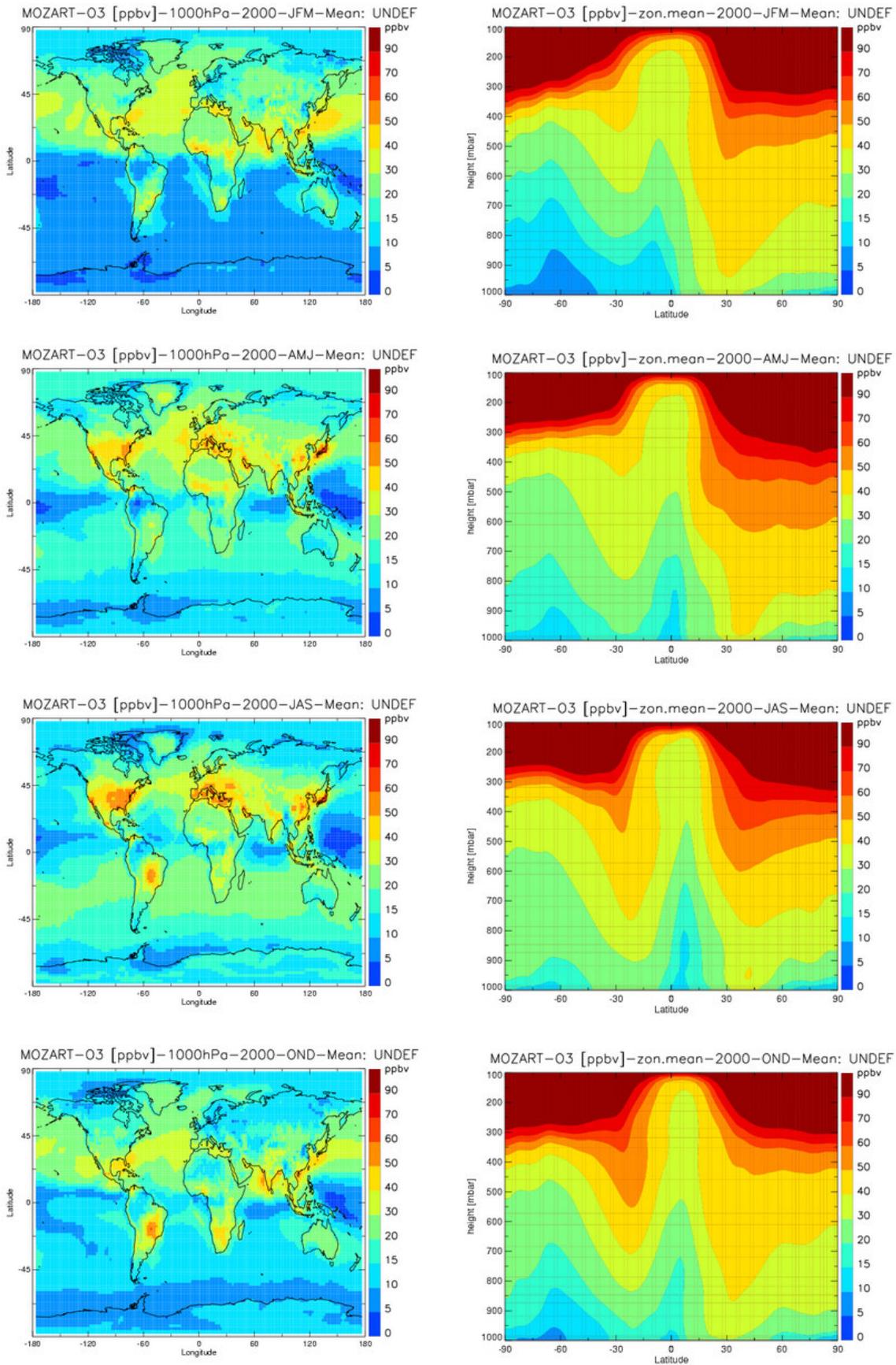
Figure B17: MOZART run G seasonal ozone concentrations in ppbv at 850 hPa and 700 hPa, using ATSR scaled Hao&Liu fire emissions (cg_scal) fire emissions

Figure B18: MOZART run G seasonal nitrogen oxide concentrations in ppbv of the year 2000, using ATSR scaled Hao&Liu fire emissions (cg_scal) fire emissions. On the left hand side are seasonal nitrogen oxide concentrations at 850 hPa, on the right hand side seasonal zonal means
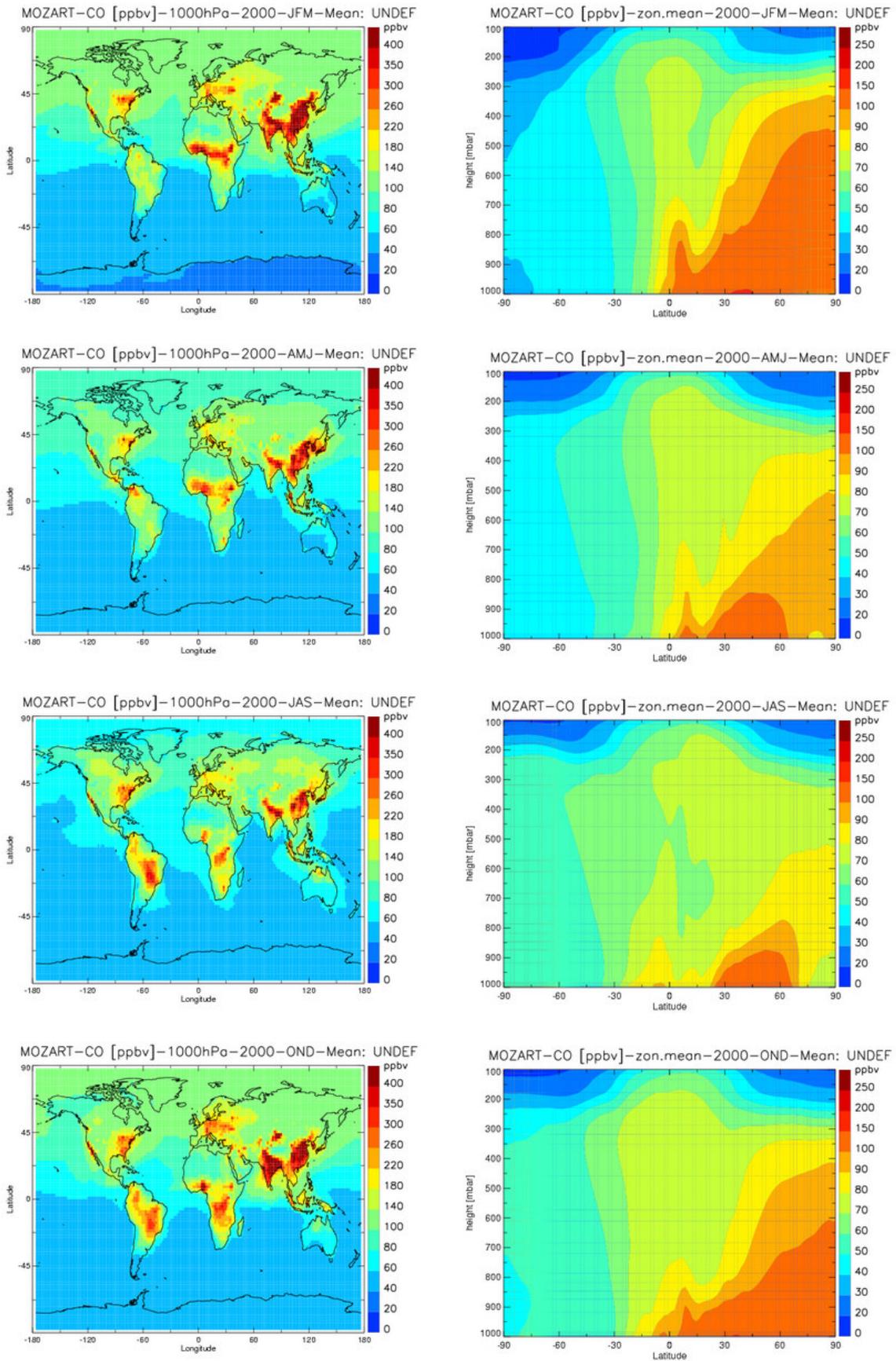
Figure B19: MOZART run K seasonal carbon monoxide (CO) concentrations in ppbv of the year 2000, using Hao&Liu climatological fire emissions. On the left hand side are seasonal CO concentrations at surface level, on the right hand side seasonal zonal means (note the different scales)

Figure B20: MOZART run K seasonal ozone concentrations in ppbv of the year 2000, using Hao&Liu climatological fire emissions. On the left hand side are seasonal ozone concentrations at surface, on the right hand side seasonal zonal means
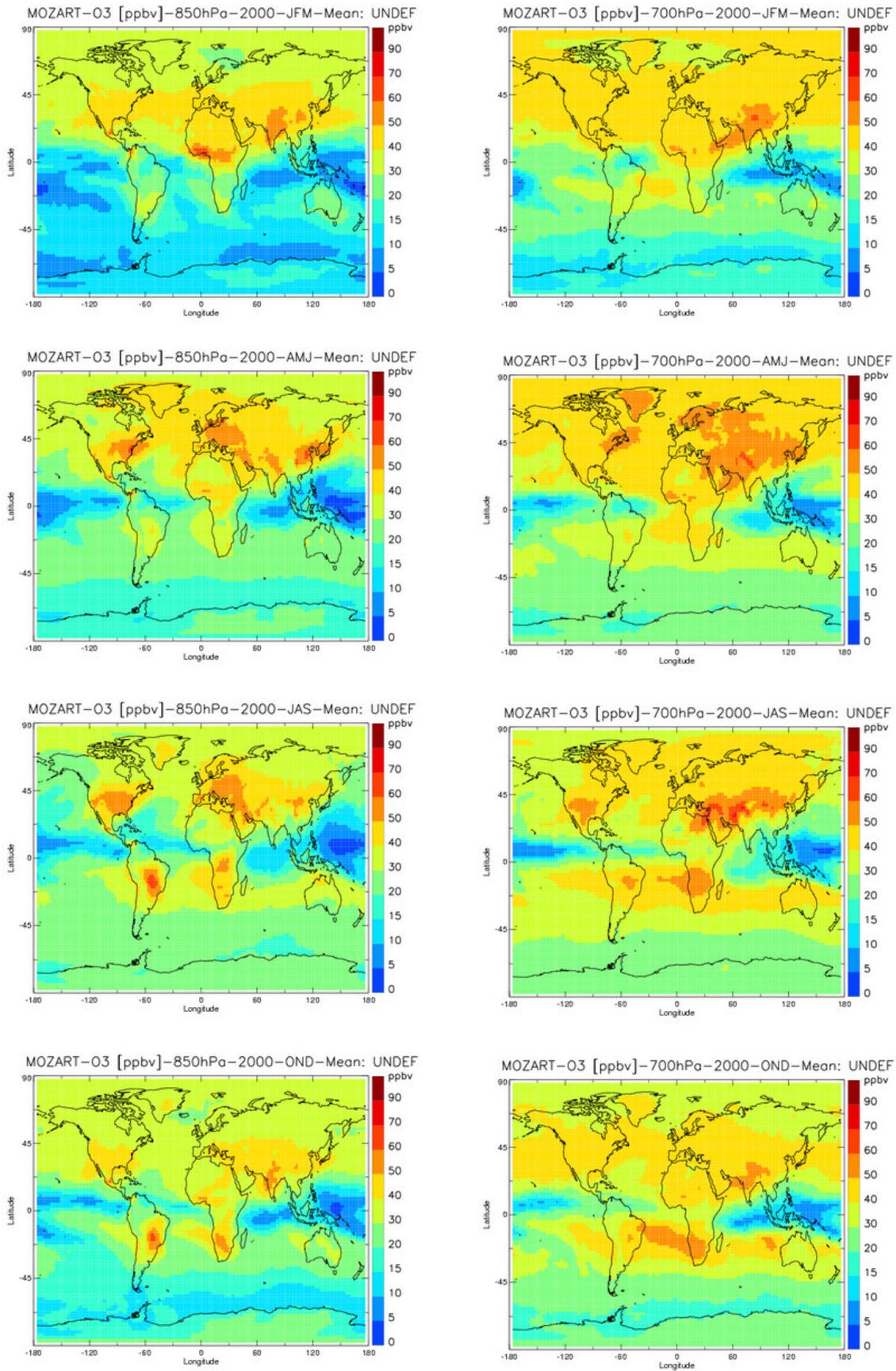
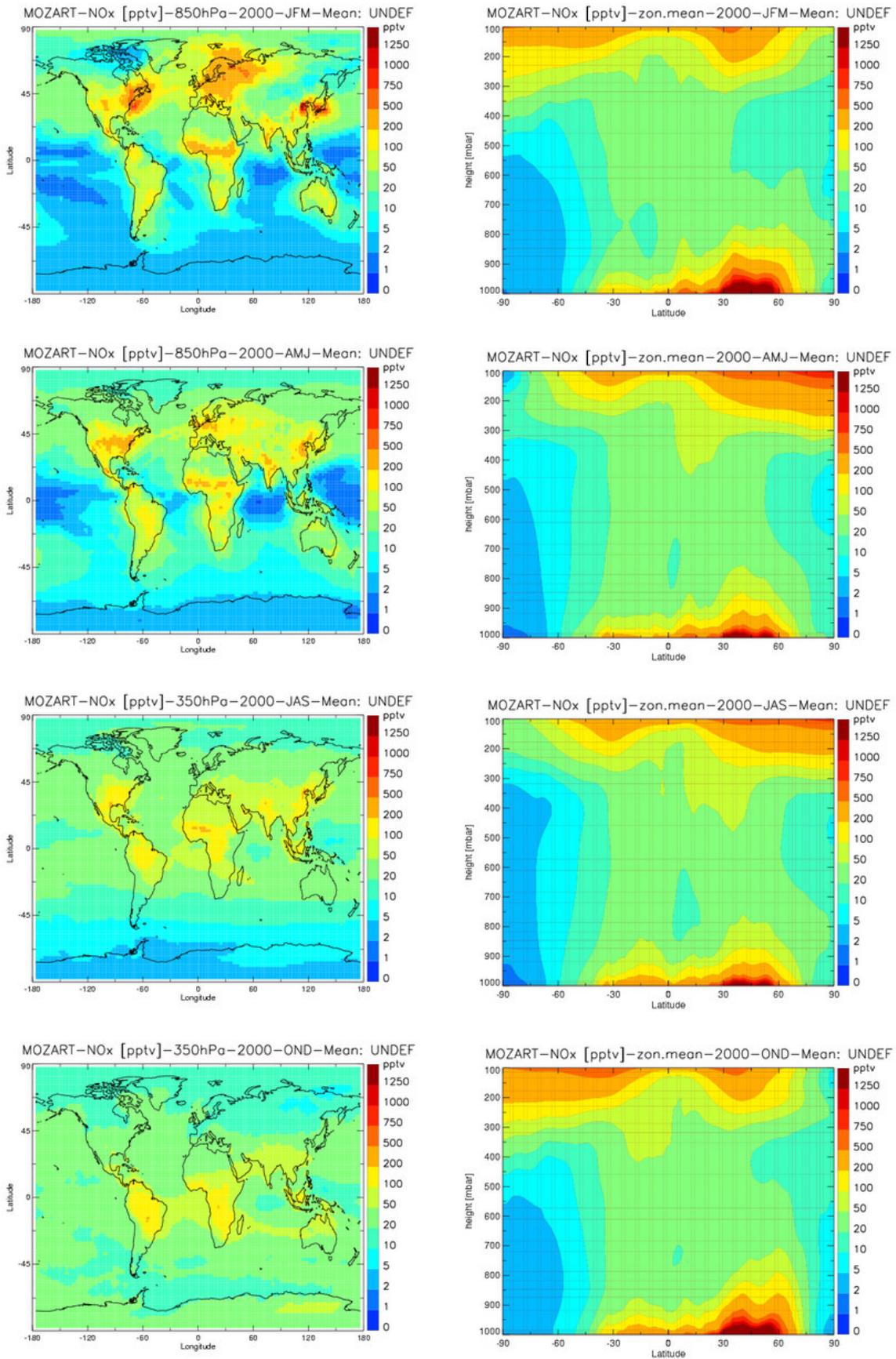**Figure B21:** MOZART run K seasonal ozone concentrations in ppbv at 850 hPa and 700 hPa of the year 2000, using Hao&Liu climatological fire emissions

Figure B22: MOZART run K seasonal nitrogen oxide concentrations in ppbv of the year 2000, using Hao&Liu climatological fire emissions. On the left hand side are seasonal nitrogen oxide concentrations at 850 hPa, on the right hand side seasonal zonal means

Appendix C - Tables

station code	station name	location / country	latitude			longitude			altitude
CMDLALT	Alert	Canada	82	27	0 N	62	31	12 W	210
CMDLASC	Ascension Island	South Atlantic, UK	7	55	12 S	14	25	12 W	54
CMDLASK	Assekrem	Algeria	23	10	48 N	5	25	12 E	2728
CMDLAZR	Terceira Island	Azores, Portugal	38	46	12 N	27	22	48 W	40
CMDLBAL	Baltic Sea	Poland	55	25	12 N	17	4	12 E	28
CMDLBME	St. Davids Head	Bermuda, UK	32	22	12 N	64	39	0 W	30
CMDLBMW	Tudor Hill	Bermuda, UK	32	16	12 N	64	52	48 W	30
CMDLBRW	Barrow	Alaska, USA	71	19	12 N	156	36	0 W	11
CMDLBSC	Black Sea	Romania	44	10	12 N	28	40	48 E	3
CMDLCBA	Cold Bay	Alaska, USA	55	12	0 N	162	43	12 W	25
CMDLCGO	Cape Grim	Tasmania	40	40	48 S	144	40	48 E	94
CMDLCHR	Christmas Island	Republic of Kiribati	1	42	0 N	157	10	12 W	3
CMDLCMO	Cape Meares	Oregon, USA	45	28	48 N	123	58	12 W	30
CMDLCRZ	Crozet Island	France	46	27	0 S	51	51	0 E	120
CMDLEIC	Easter Island	Chile	27	9	0 S	109	27	0 W	50
CMDLGMI	Mariana Islands	Guam	13	25	48 N	144	46	48 E	6
CMDLGOZ	Dwejra Point	Gozo, Malta	36	3	0 N	14	10	48 E	30
CMDLHBA	Halley Station	Antarctica	75	34	48 S	26	30	0 W	33
CMDLHUN	Hegyhatsal	Hungary	46	57	0 N	16	39	0 E	344
CMDLICE	Storhofdi	Vestmannaeyjar, Iceland	63	20	24 N	20	17	24 W	127
CMDLITN	Grifton	Carolina, USA	35	21	0 N	77	22	48 W	505
CMDLIZO	Tenerife	Canary Islands, Spain	28	18	0 N	16	28	48 W	2360
CMDLKEY	Key Biscayne	Florida, USA	25	40	12 N	80	12	0 W	3
CMDLKUM	Cape Kumukahi	Hawaii, USA	19	31	12 N	154	49	12 W	3
CMDLKZD	Sary Taukum	Kazakhstan	44	27	0 N	75	34	12 E	412
CMDLKZM	Plateau Assy	Kazakhstan	43	15	0 N	77	52	48 E	2519
CMDLLEF	Park Falls	Wisconsin, USA	45	55	48 N	90	16	12 W	868
CMDLMBC	Mould Bay	Canada	76	15	0 N	119	21	0 W	58
CMDLMHD	Mace Head	Ireland	53	19	48 N	9	54	0 W	25
CMDLMID	Sand Island	Midway, USA	28	12	36 N	177	22	48 W	7
CMDLMLO	Mauna Loa	Hawaii	19	31	48 N	155	34	48 W	3397
CMDLNMB	Gobabeb	Namibia	23	34	48 S	15	1	48 E	461
CMDLNWR	Niwot Ridge	Colorado, USA	40	3	0 N	105	34	48 W	3475
CMDLPSA	Palmer Station	Antarctica	64	55	12 S	0	38	24 W	10
CMDLRPB	Ragged Point	Barbados	13	10	12 N	59	25	48 W	45
CMDLSEY	Mahe Island	Seychelles	4	40	12 S	55	10	12 E	7
CMDLSHM	Shemya Island	Alaska, USA	52	43	12 N	174	6	0 E	40
CMDLSMO	Tutuila	American Samoa	14	14	24 S	170	34	12 W	42
CMDLSPO	South Pole	Antarctica	89	58	48 S	24	48	0 W	2810
CMDLSTM	Ocean Station M	Norway	66	0	0 N	2	0	0 E	5
CMDLSYO	Syowa Station	Antarctica	69	0	0 S	39	58	0 E	11
CMDLTAP	Tae-ahn Peninsula	South Korea	36	43	48 N	126	7	48 E	20
CMDLTDF	Tierra Del Fuego	Argentina	54	52	12 S	68	28	48 W	20
CMDLUTA	Wendover	Utah, USA	39	54	0 N	113	43	12 W	1320
CMDLUUM	Ulaan Uul	Mongolia	44	27	0 N	111	6	0 E	914
CMDLWIS	Sede Boker	Negev Desert, Israel	31	7	48 N	34	52	48 E	400
CMDLWLG	Mt. Waliguan	Peoples Republic of China	36	17	24 N	100	54	0 E	3810
CMDLZEP	Ny-Alesund	Ny-Alesund, Norway, Sweden	78	54	0 N	11	52	48 E	475

Table C1: CMDL measurement stations with carbon monoxide measurements in the year 2000

station	latitude	longitude	altitude [m]
Pago Pago, American Samoa	- 14.23	-170.56	77
Ascension Island	-7.98	-14.42	91
Suva, Fiji	-18.13	-178.40	6
Irene, South Africa	-25.90	-28.22	1524
Kuala Lumpur, Malaysia	2.73	101.7	17
La Réunion	-21.06	55.48	24
Malindi, Kenya	-2.99	40.19	-6
Nairobi, Kenya	-1.27	36.8	1795
Natal, Brazil	-5.42	-35.38	42
San Cristóbal	-0.92	-89-60	8
Paramaribo, Suriname	5.81	55.21	25
Watukosek, Java	-7.57	11.65	50

Table C2: SHADOZ stations with ozone radio soundings in the year 2000

	months											
station	1	2	3	4	5	6	7	8	9	10	11	12
Pago Pago, Am. Samoa	4	4	5	3	3	2	4	4	3	1	4	3
Ascension Island	4	1	5	3	2	4	4	3	0	0	4	1
Suva, Fiji	4	4	5	4	1	4	2	4	3	0	3	3
Irene, South Africa	1	3	5	2	4	2	3	4	8	3	4	1
Kuala Lumpur, Malaysia	2	1	2	1	2	1	2	2	3	2	2	2
La Réunion	4	3	2	3	5	3	3	4	0	1	5	2
Malindi, Kenya	3	1	0	0	0	0	0	1	1	1	0	1
Nairobi, Kenya	4	2	0	0	3	4	4	5	4	3	6	4
Natal, Brazil	4	4	4	3	2	2	0	2	2	4	3	4
San Cristóbal	2	4	9	3	4	5	4	5	5	4	3	0
Paramaribo, Suriname	4	4	5	3	3	4	3	5	4	4	3	2
Watukosek, Java	1	1	2	4	4	4	4	5	4	4	4	7

Table C3: Number of SHADOZ radio soundings per month at each station in the year 2000

a.)

station	moz A	moz H	moz G	moz J	moz K
Africa:					
Ascension	0.434	0.335	0.346	**0.510**	**0.510**
La Reunion	0.745	0.760	0.758	**0.781**	**0.781**
Malindi	0.761	0.826	0.800	**0.880**	0.380
Nairobi	**0.214**	0.035	0.036	0.091	0.091
Irene	0.011	**0.142**	0.049	0.079	0.079
Southern America:					
Natal	**0.042**	0.041	**0.042**	0.012	**0.042**
Paramaribo	**0.396**	0.138	0.246	0.283	0.157
San Cristobal	0.281	0.269	0.244	**0.327**	0.287
South Eastern Asia:					
Samoa	0.671	0.677	0.639	**0.729**	0.577
Fiji	0.798	0.797	**0.812**	0.806	0.800
Kuala Lumpur	0.139	0.147	0.187	**0.299**	0.137
Java	0.234	0.058	**0.339**	0.148	0.088

b.)

station	moz A	moz H	moz G	moz J	moz K
Africa:					
Ascension	0.196	0.207	**0.272**	0.051	0.058
La Reunion	0.524	0.621	0.572	0.581	**0.668**
Malindi	0.816	0.830	0.835	**0.840**	0.802
Nairobi	**0.434**	0.312	0.375	0.379	0.406
Irene	0.393	0.772	0.517	0.678	**0.780**
Southern America:					
Natal	0.042	0.042	0.042	0.042	0.042
Paramaribo	**0.280**	0.042	0.119	0.124	0.042
San Cristobal	0.090	**0.168**	0.167	0.071	0.146
South Eastern Asia:					
Samoa	0.230	**0.482**	0.478	0.459	0.355
Fiji	0.630	0.650	0.655	0.644	**0.679**
Kuala Lumpur	0.363	0.365	0.391	**0.431**	0.364
Java	0.211	0.238	0.274	0.264	**0.295**

Table C4: R^2 correlation of MOZART runs A, H, G, J, and K ozone concentrations versus SHADOZ measurements. a.) Averages from surface to 750 hPa, b.) Averages from 750 to 500 hPa

airport location	country	latitude	longitude	altitude m
Abidjan	Cote d'Ivoir	5,15	3,56	7
Accra	Ghana	5,36	-0,12	65
Bogota	Colombia	4,6	-74,083	2576
Bombay	India	18,967	72,833	35
Boston	USA	41,278	-73,408	177
Brazzaville	Congo	-4,25	15,28	296
Brussels	Belgium	50,83	4,33	62
Budapest	Hungary	47,26	19,15	102
Caracas	Venezuela	9,083	-69,833	236
Chicago	USA	41,85	-87,65	178
Colombo	Sri Lanka	6,932	79,848	1
Dakar	Senegal	14,44	-17,3	23
Dallas,Texas	USA	32,783	-96,8	137
Frankfurt	Germany	50,11	8,68	113
Harare	Zimbabwe	-17,55	31,08	1427
Hong Kong	China	22,283	114,15	89
Houston	USA	29,763	-95,363	15
Johannesburg	South Africa	-26,2	28,16	1740
Lagos	Nigeria	6,45	3,38	3
Libreville	Gabun	0,27	9,25	12
Luanda	Angola	-8,49	-13,13	45
London	UK	51,5	-0,105	18
Madras	India	13,083	80,283	7
New York	USA	40,714	-74,006	2
Osaka	Japan	34,667	135,5	5
Paris	France	48,87	2,31	1
Rio de Janeiro	Brazil	-22,9	-43,233	1
San Francisco	USA	37,775	-122,418	60
Sao Paulo	Brazil	-23,55	-46,63	860
Seoul	South Korea	37,567	127	34
Shanghai	China	31,222	121,458	6
Tokyo	Japan	35,7	139,767	20
Vancouver	Canada	49,25	-123,133	72
Vienna	Austria	48,2	16,367	169
Washington	USA	38,895	-77,037	11
Windhoek	Namibia	-23,36	27,66	1728

Table C5: MOZAIC airport locations with ozone aircraft measurements in the year 2000

# Appendix D – Global MOZART Difference Plots
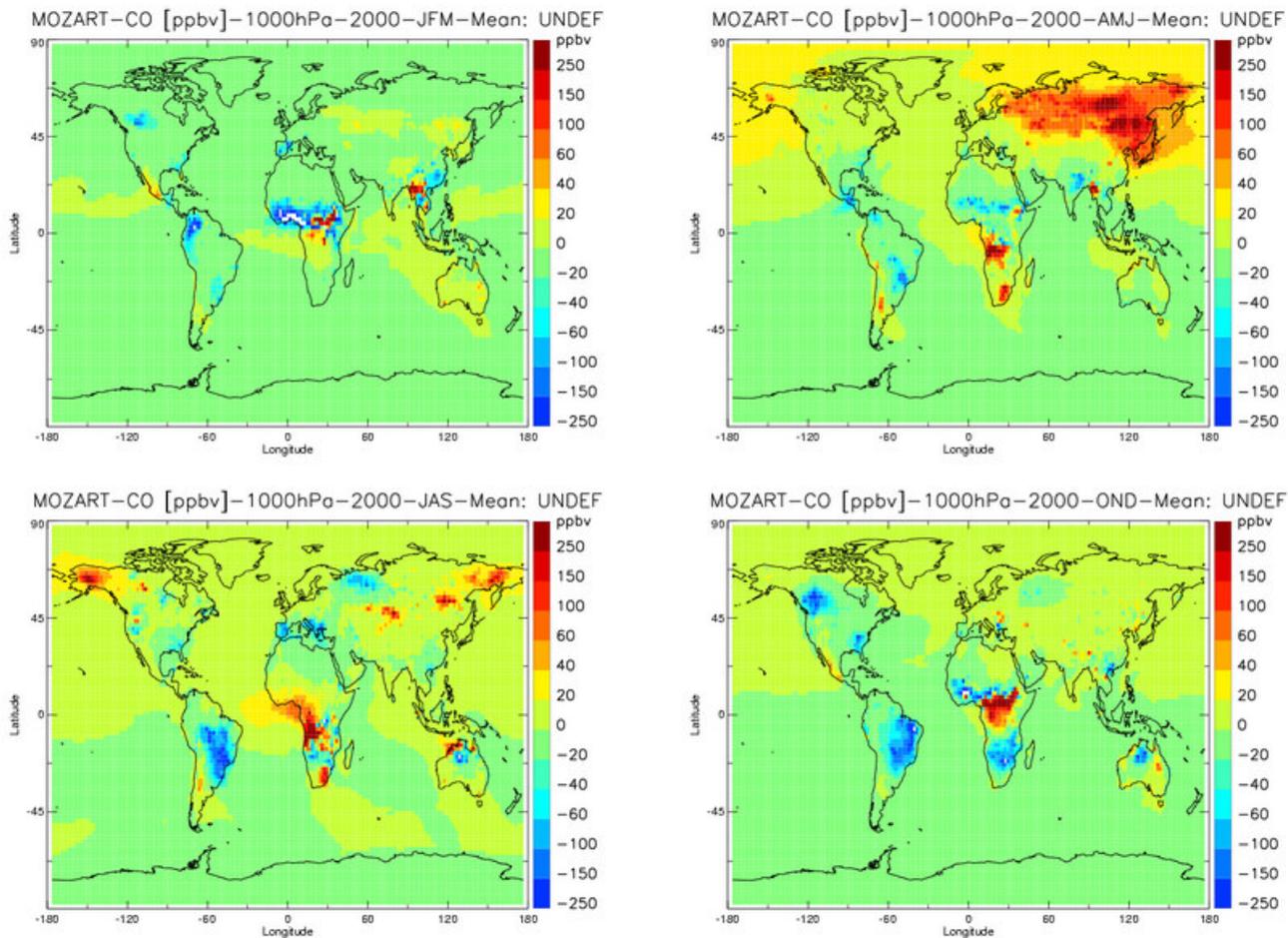
Figure D1: MOZART run A – H: difference of global seasonal surface carbon monoxide concentrations in ppbv in year 2000. Run A uses GWEM-1.3 fire emissions and run H uses mgs_scal fire emissions (ATSR scaled)
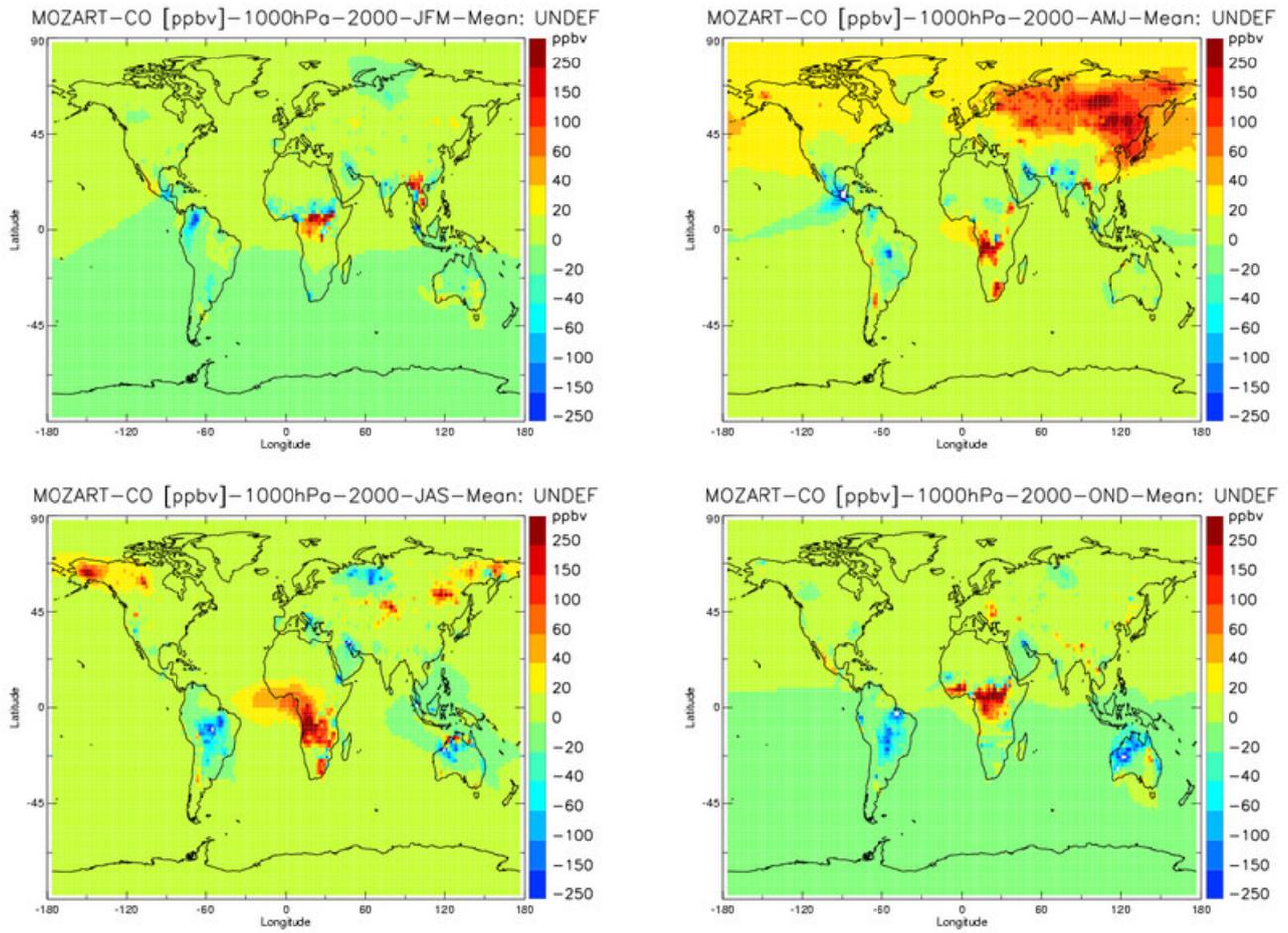
Figure D2: MOZART run A – G: difference of global seasonal surface carbon monoxide concentrations in ppbv in year 2000. Run A uses GWEM-1.3 fire emissions and run G uses cg_scal fire emissions (ATSR scaled)
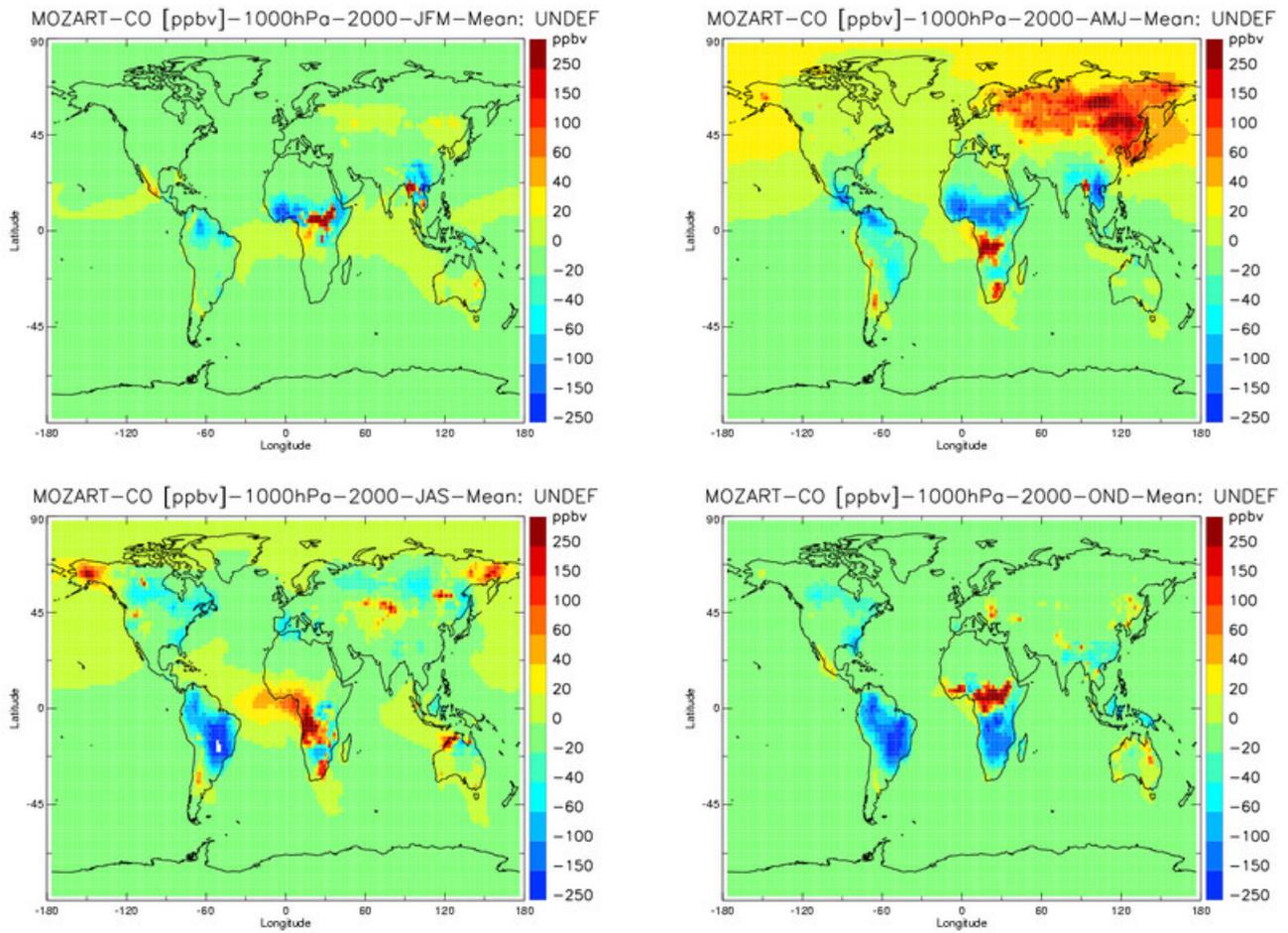
Figure D3: MOZART run A – K: difference of global seasonal surface carbon monoxide concentrations in ppbv in year 2000. Run A uses GWEM-1.3 fire emissions and run K uses the climatological Hao&Liu fire emissions

Appendix E – CMDL Figures

North Central Asia
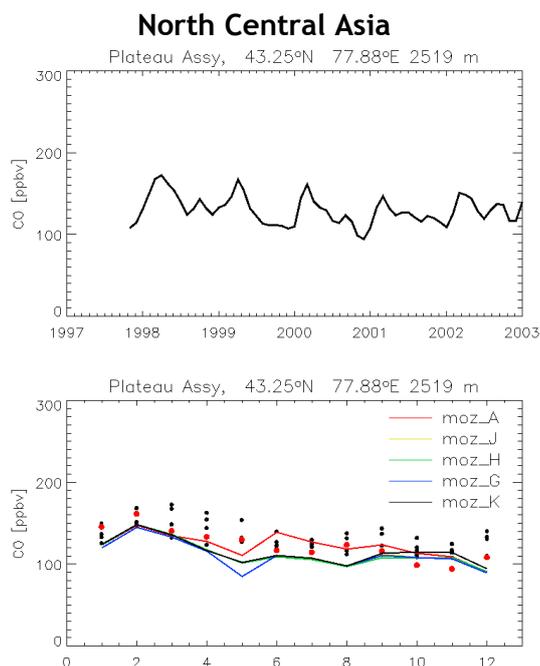
Figure E1: CMDL CO measurements in ppbv for the year 2000 (red dots) and available other years (black spots) at Plateau Assy, Kazhakhstan. Interannual variability is shown in the upper panel, year 2000 seasonality in the lower panel. The lower panel also shows MOZART results for the main runs A, J, H, G, and K described in section 4.3

Boreal North America
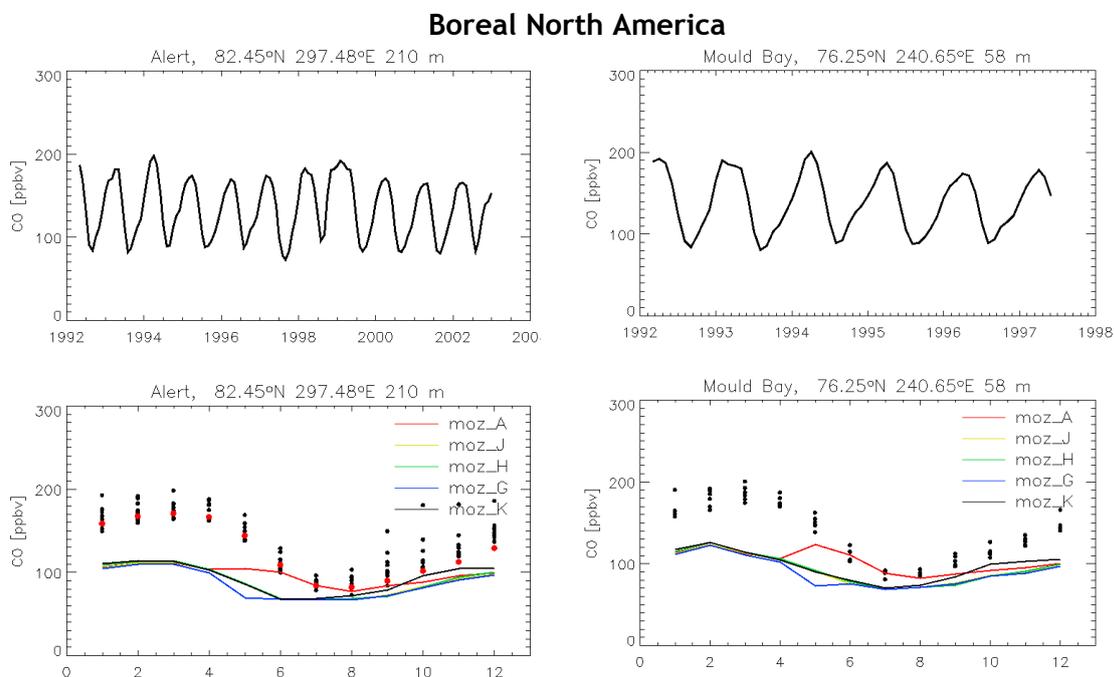
Figure E2: CMDL CO measurements in ppbv for the year 2000 (red dots) and available other years (black spots) at Alert and Mould Bay, Canada. Interannual variability is shown in the upper panel, year 2000 seasonality in the lower panel. The lower panel also shows MOZART results for the main runs A, J, H, G, and K described in section 4.3

North America - East
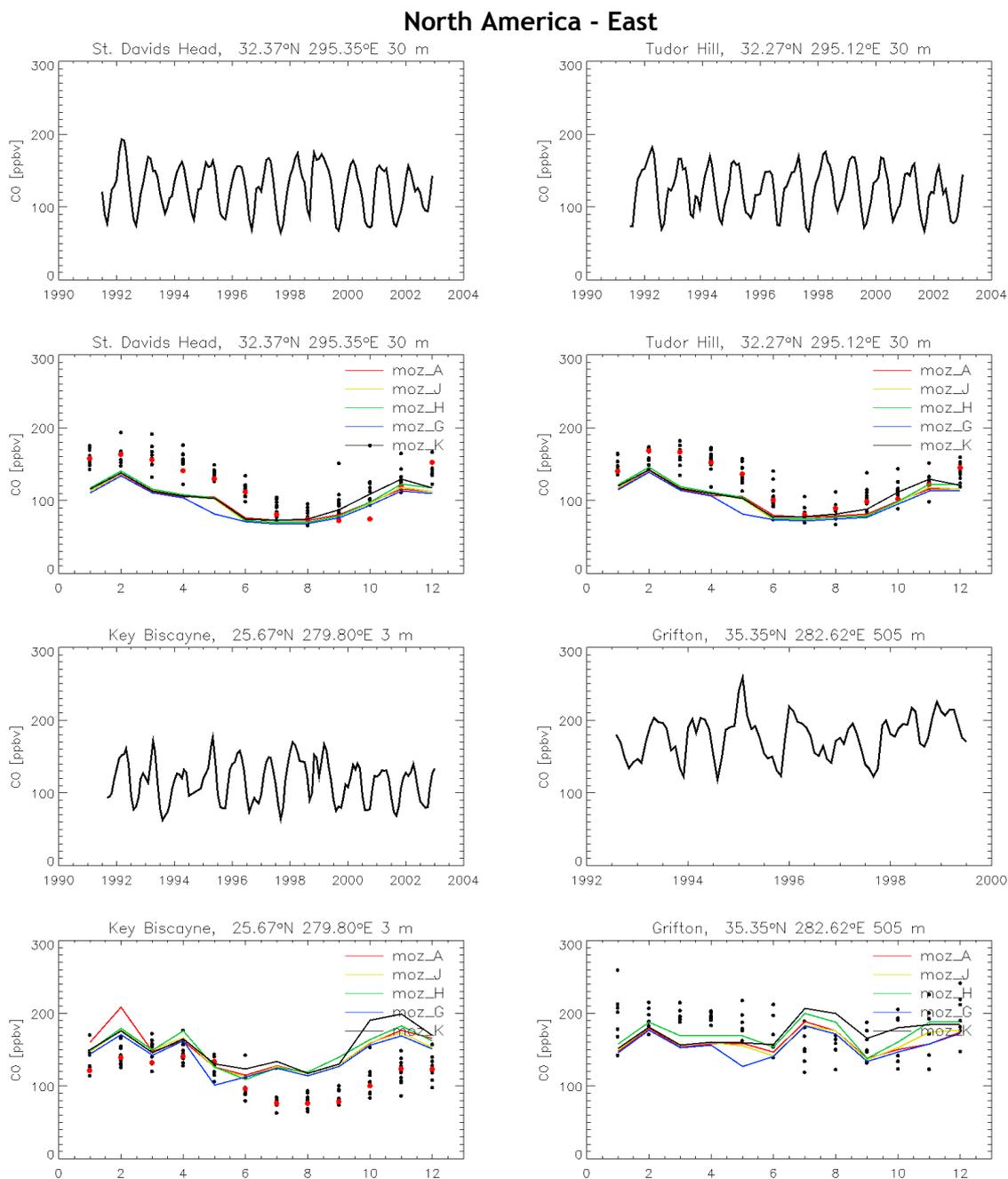
Figure E3: CMDL CO measurements in ppbv for the year 2000 (red dots) and available other years (black spots) at Bermudas, UK (top) and in the eastern USA (bottom). Interannual variability is shown in the upper panel, year 2000 seasonality in the lower panel. The lower panel also shows MOZART results for the main runs A, J, H, G, and K described in section 4.3

Pacific
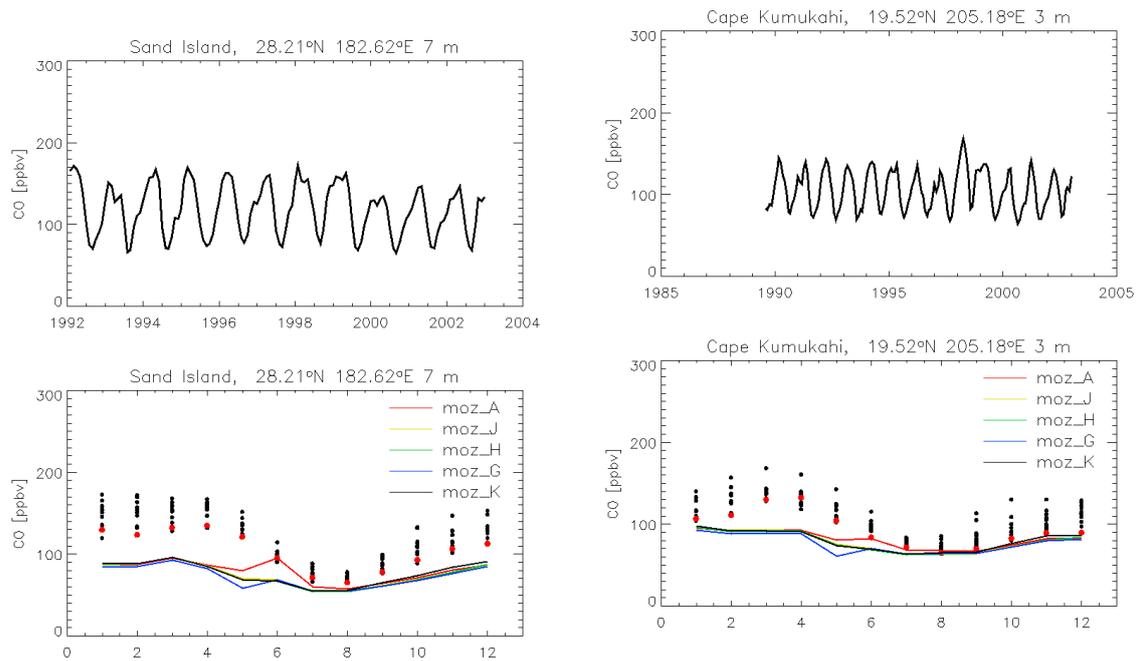
Figure E4: CMDL CO measurements in ppbv for the year 2000 (red dots) and available other years (black spots) in the Pacific. Interannual variability is shown in the upper panel, year 2000 seasonality in the lower panel. The lower panel also shows MOZART results for the main runs A, J, H, G, and K described in section 4.3

Bibliography

Aardenne, J. A. van, Uncertainties in emission inventories, PhD thesis, Wageningen University, The Netherlands, 2002.

Aber, J. D. and J. M. Melillo, Terrestrial Ecosystems, 2nd edition, *Saunders College Publishing*, 2001.

Albuquerque, L. M. M., K. M. Longo, S. R. Freitas, T. Tarasova, A. Plana Fattori , C. Nobre, L. V. Gatti, Sensitivity studies on the photolysis rates calculation in the Amazonian atmospheric chemistry Part I: The impact of the direct radiative effect of biomass burning aerosol particles. *Atmospheric Chemistry and Physics Discussions*, 5, 9325-9353, 2005.

Andreae, M.O., Biomass burning: Its history, use, and distribution, and its impact on environmental quality and climate, In: J.S. Levine (ed.), *Global biomass burning, Atmospheric, climatic, and biospheric implications*, pp. 3-21, MIT Press, Cambridge, MA, 1991.

Andreae M. O., J. Fishman, and J. Lindesay, The Southern Tropical Atlantic Experiment (STARE): Transport and Atmospheric Chemistry near the Equator-Atlantic (TRACE A) and Southern African Fire-Atmosphere Research Initiative (SAFARI): An introduction, *J. Geophys. Res*. 101 (D19), p. 23,519-23,520, 1996.

Andreae M. O. and P. Merlet, Emission of trace gases and aerosols from biomass burning, *Global Biogeochem. Cycles* 15 (4), 955-966, 2001.

Andreae M. O., P. Artaxo, H. Fischer, S. R. Freitas, J.-M. Grégoire, A. Hansel, P. Hoor, R. Kormann, R.Krejci, J. Lelieveld, W. Lindinger, K. Longo, W. Peters, M. de Reus, B. Scheeren, M. A. F. Silva Dias, J. Ström, P. F. J. van Velthoven, and J. Williams, Transport of biomass burning smoke to the upper troposphere by deep convection in the equatorial region, *Geophys. Res. Let*. 28, 6, p. 951-954, 2001.

Andreae, M. O., P. Artaxo, C. Brandão, Carswell, F. E., Ciccioli, P., Costa, A. L., et al., Biogeochemical cycling of carbon, water, energy, trace gases, and aerosols in Amazonia: The LBA-EUSTACH experiments. *J. Geophys. Res.,* 107(D20), p. 8066, 2002.

Andreae, M. O., D. Rosenfeld, P. Artaxo, A. A. Costa, G. P. Frank, K. M. Longo, and M. A. F. Silva-Dias, Smoking rain clouds over the Amazon, *Science*, 303, 1337-1342, 2004.

Andreae, M. O., C. D. Jones, and P. M. Cox, Strong present-day aerosol cooling implies a hot future, *Nature*, 435, 1187-1190, 2005.

Annegarn, H. J., L. otter, R. J. Swap and R. J. Scholes, Southern Africa's ecosystem in a test-tube: A perspective on the Southern African Regional Science Initiative (SAFARI 2000), *S. Afr. J. Sci.*, 98, p111-113, 2002.

Arino O., I. Piccolini, and J. M. Rosaz, Development and Testing of Algorithms for a Global Burned Area Product from ERS ATSR-2, *IGARSS Symposium*, Honolulu, July 2000.

Arino O. and S. Plummer, The Along Track Scanning Radiometer World Fire Atlas Detection of Night-Time Fire Activity, Validation Report, *IGBP-DIS Working Paper # 23*, May 2001.

Arino O., M. Simon, I. Piccolini, J.M. Rosaz, The ERS-2 ATSR-2 World Fire Atlas and the ERS-2 ATSR-2 World Burned Surface Atlas projects, *Proceedings of the 8th ISPRS conference on Physical Measurement and Signatures in Remote Sensing, International Society for Photogrammetry and Remote Sensing*, Aussois, 8-12 January 2001.

Artaxo, P., E. T. Fernandes, J. V. Martins, M.A. Yamasoe, P. V. Hobbs, W. Maenhaut, K. M. Longo, A. Castanho, Large Scale Aerosol Source Apportionment in Amazonia, *J. Geoph. Res.*, 103 (D24), p. 31837-31848, 1998.

Artaxo, P.; J. V. Martins, M. A. Yamasoe, A. S. Procópio, T. M. Pauliquevis, M. O. Andreae, P. Guyon, L. V. Gatti, A. M. Cordova Leal, Physical and chemical properties of aerosols in the wet and dry season in Rondônia, Amazonia. *J. Geophys*. Res., 107 (D20) , 2002.

Artaxo, P., V. G. Gatti, A. M. C. Leal, K. M. Longo, S. R. de Freitas, L. L. Lara, T. M. Pauliquevis, A. S. Procópio, and L. V. Rizzo, Química atmosférica na Amazônia: A floresta e as emissões de queimadas controlando a composição da atmosfera amazônica, *Acta Amazonica*, Vol. 35(2), p. 191-208, 2005.

Barbosa P. M., D. Stroppiana, and J.-M. Grégoire, An Assessment of vegetation fire in Africa (1981-1991): Burned areas, burned biomass, and atmospheric emissions. *Global Biogeoch. Cycles* 13 (4), 933-950, 1999.

Barbosa, P. M., J. S.-M. Ayanz, G. Libertà, M. Gimeno, and G. Schmuck, Forest fire emissions in Southern Europe. First estimates from 2000, submitted to *J. Geophys. Res.*, 2003.

Bartholomé E., A. S. Belward, F. Achard, S. Bartalev, C. Carmona Moreno, H. Eva, S. Fritz, J.-M. Grégoire, P. Mayaux, H.-J. Stibig, Global Land Cover mapping for the year 2000 – Project status November 2002, *EUR 20524*, Joint Research Centre of the European Commission, 2002.

Beringer, J., L. B. Hutley,N. J. Tapper, A. Coutts, A. Kerley, and A. P. O'Grady, Fire impacts on surface heat, moisture and carbon fluxes from a tropical savanna in northern Australia, *International Journal of Wildland Fire, 12*, 333-340, 2003.

Bondeau, A., P. Smith, S. Zaehle, D. Gerten, S. Schaphoff, B. Schröder, B. Smith, Accounting for agriculture within a Dynamic Global Vegetation Model, *Poster at the Land Open Science Conference*, Morelia, Mexico, 2-5 Dec 2003.

Boschetti, L., H. D. Eva, P. A. Brivio, andJ. M. Grégoire, Lessons to be learned from the comparison of three satellite-derived biomass burning products, *Geophys. Res. Lett., 31,* L21501, doi:10.1029/2004GL021229, 2004.

Bradstock, R., J. Williams, and A.M. Gill, Flammable Australia: Fire regimes and biodiversity of a continent, 486 pp., Cambridge University Press, Cambridge, UK, 2002.

Brasseur, G. P., D. A. Hauglustaine, S. Walters, P. J. Rasch, J.-F. Müller, C. Granier, X. X. Tie, MOZART, a global chemistry transport model for ozone and related chemical tracers: 1. Model description, *J. Geophys. Res.*, 103, 28,265-28,289, 1998.

Brasseur, G. P., J. J. Orlando, and G. S. Tyndall, Atmospheric Chemistry and Global Change, Oxford Univ. Press, New York, 1999.

Brasseur, G. P., M. Schultz, C. Granier, M. Saunois, T. Diehl, M. Botzet, E. Roeckner, and S. Walters, Impact of Climate Change on the Future Chemical Composition of the Global Troposphere, to be submitted to J. of Climate, 2005.

Browell, E. V., M. A. Fenn, C. F Butler, W. B. Grant, M. B. Clayton, J. Fishman, A. S. Bachmeier, B. E. Anderson, G. L. Gregory, H. E. Fuelberg, J. D. Bradshaw, S. T. Sandholm, D. R. Blake, B. G. Heikes, G. W. Sachse, H. B. Singh, and R. W. Talbot, Ozone and aerosol distributions and air mass characteristics over the South Atlantic basin during the burning season, *J. Geophys. Res.* 101(19):24,043, 1996.

Cardoso, M. F., G.C. Hurtt, B. Moore III, C. A. Nobre, and E. M. Prins, Projecting future fire activity in Amazonia, *Global Change Biology*, 9, 656-669, 2003.

Cardoso M. F., Fire Dynamics in Amazonia. *Ph.D. Thesis*, University of New Hampshire, USA, 2004.

Cardoso, M. F., G. C. Hurtt, B. Moore III, C. A. Nobre, H. Bain, Field work and statistical analyses for enhanced interpretation of satellite fire data, *Remote Sensing of Environment*, 96, 212–227, 2005.

Chédin, A., S. Serrar, N. A. Scott, C. Pierangelo, and P. Ciais, Impact of tropical biomass burning emissions on the diurnal cycle of upper tropospheric CO_2 retrieved from NOAA 10 satellite observations, *J. Geophys. Res.,* 110, D11309, doi:10.1029/2004JD005540, 2005.

Cochrane, M.A., Fire science for rainforests, *Nature*, 421, 913-919, 2003.

Conard, S. G., and G. A. Ivanova, Wildfire in Russian boreal forests -Potential impacts of fire regime characteristics on emissions and global carbon balance estimates, *Environ. Pollut.*, 98, 305– 313, 1998.

Cooke W.F., J. J. N. Wilson, A global black carbon aerosol model, *J. Geophys. Res.* 101, p. 19395-19409, 1996.

Cotton, W. R., R. A. Pielke, Human impacts on weather and climate, *Cambridge University Press*, New York, 1996.

Coutinho, L. M., Fire in the Ecology of the Brazilian Cerrado, *In: Fire in the Tropical Biota*, J. G. Goldammer (ed.), Springer Verlag, p82-105, 1990.

Criscuolo, L., Assessing the agricultural system and the carbon cycle under climate change in Europe using a Dynamic Global Vegetation Model, PhD thesis at the International Max Planck Research School on Earth System Modelling (IMPRS) at MPI-M, 2006.

Crutzen P. J. and M. O. Andreae, Biomass Burning in the tropics: impact on atmospheric chemistry and biogeochemical cycles. *Science*, 250, p. 1669-1678, 1990.

Crutzen P. J., and J. Lelieveld, Human impacts on atmospheric chemistry, *Ann. Rev. of Earth and Planetary Sciences*, 29, 17-45, 2001.

Culf, A. D., J. L. Esteves, A. O. M. Filho, and H. R. Rocha, Radiation, temperature and humidity over forest and pasture in Amazonia, *in: J Gash; C A Nobre; J M Roberts; R. Victoria. (Org.), Amazon deforestation and climate. 1st ed. Chichester*, John Wiley and Sons, p. 175-192, 1996.

Daly, C., D. Bachelet, J. M. Lenihan and R. P. Neilson, Dynamic simulation of tree-grass interactions for global change studies, *Ecological Applications,* 10(2), p. 449-469, 2000.

Deeter, M. N., et al., Evaluation of operational radiances for the Measurements of Pollution in the Troposphere (MOPITT) instrument CO thermal band channels, *J. Geophys. Res.,* 109, D03308, doi:10.1029/2003JD003970, 2004.

Dentener F., S. Kinne, T. Bond, O. Boucher, J. Cofala, S. Generoso, P. Ginoux, S. Gong, J.J. Hoelzemann, A. Ito, L. Marelli, J. Penner, J.-P. Putaud, C. Textor, M.Schulz, G.R. Van der Werf and J. Wilson, Emissions of primary aerosol and precursor gases in the years 2000 and 1750 prescribed data-sets for AeroCom, *Atmos. Chem. Phys. Discuss.,* 6, 2703-2763, 2006.

Duncan, B. N., R. V. Martin, A. C. Staudt, R. Yevich, and J. A. Logan, Interannual and seasonal variability of biomass burning emissions constrained by satellite observations, *J. Geophys. Res.* 108 (D2), 4040, doi:10.1029/2002JD002378, 2003.

Drummond, J. R., Measurements of Pollution in the Troposphere (MOPITT), *In: The Use of EOS for Studies of Atmospheric Physics,* edited by J. C. Gille and G. Visconti, pp. 77–101, North-Holland, New York,1992.

Dwyer, E., S. Pinnock, J.-M. Grégoire, Global spatial and temporal distribution of vegetation fire as determined from satellite observations, *Int. J. Remote Sensing* 21, 6, 7, p. 1289 - 1302, 2000.

Edwards, D. P., C. Halvorson, and J. C. Gille, Radiative transfer modeling for the EOS Terra Satellite Measurement of Pollution in the Troposphere (MOPITT) instrument, *J. Geophys. Res.,* 104, 16,755– 16,775, 1999.

Edwards, D. P. et al., Tropospheric ozone over the tropical Atlantic: A satellite perspective, *J. Geophys. Res.,* 108(D8), 4237, doi:10.1029/2002JD002927, 2003.

Edwards, D. P., et al. , Observations of carbon monoxide and aerosols from the Terra satellite: Northern Hemisphere variability, *J. Geophys. Res.,* 109, D24202, doi:10.1029/2004JD004727, 2004.

Emmons, L. K., et al., Validation of Measurements of Pollution in the Troposphere (MOPITT) CO retrievals with aircraft in situ profiles, *J. Geophys. Res.,* 109, D03309, doi:10.1029/2003JD004101, 2004.

FIRESCAN Science Team, Fire in Ecosystems of Boreal Eurasia: The Bor Forest Island Fire Experiment Fire Research Campaign Asia-North (FIRESCAN), *in Biomass Burning and Global Change, Vol. 1,* ed. by J. S. Levine, pp. 848-873, 1996.

Fishman J., J. M. Hoell Jr., R. D. Bendura, R. J. McNeal, V. W. J. H. Kirchhoff, NASA GTE TRACE A Experiment (September-October 1992): Overview, *J. Geophys. Res.* 101 (D19), p. 23,865-23,879, 1996.

Fishman, J. and V. G. Brackett, The climatological distribution of tropospheric ozone derived from satellite measurements using version 7 Total Ozone Mapping Spectrometer and Stratospheric Aerosol and Gas Experiment data set, *J. Geophys. Res.,* 102, 19275-19278, 1997.

Folkins, I., R. Chatfield, D. Baumgardner, and M. Proffitt , Biomass burning and deep convection in southeastern Asia: Results from ASHOE/MAESA, *J. Geophys. Res.*, 102(D11), 13,291–13,300, 1997.

Forest Fires in Europe – 2003 fire campaign, *Report no 4,* European Commission, 2004.

Forster, C., U. Wandinger, G. Wotawa, P. James, I. Mattis, D. Althausen, P. Simmonds, S. O'Doherty, S.G. Jennings, C. Kleefeld, J. Schneider, T. Trickl, S. Kreipl, H. Jaeger, and A Stohl, Transport of boreal forest fire emissions from Canada to Europe. *J. Geophys. Res. A*, 106(D19):22887–22906, 2001.

Freitas, S. R., K. M. Longo, M. A. F. Silva Dias, P. Artaxo, Numerical modelling of air mass trajectories from the biomass burning areas of the Amazon Basin, *Annais da Academia Brasileira de Ciências*, 68, p193-206, 1997.

Freitas, S. R., K. M. Longo, M. A. F. Silva Dias, P. L. Silva Dias, R. Chatfield, E. Prins, P. Artaxo, G. Grell, and F. S. Recuero, Monitoring the Transport of Biomass Burning Emissions in South America, *J. Env. Fluid Dyn.,* 5, p.135 -167 , 2005a.

Freitas, S. R., K. M. Longo, M. A. F. Silva Dias, P. L. Silva Dias, Emissões de Queimadas em Ecosistemas da América do Sul: Efeitos Climáticos e Biogeoquímicos e Distribuição Regional da Fumaça, *Estudos Avançados* 19, 53, 2005b.

Freitas, S. R., K. M. Longo, and M. O. Andreae, The impact of including the plume rise of vegetation fires in numerical simulations of associated atmospheric pollutants, submitted to Geoph. Res. Let., 2006.

Friedl, M. A., D. K. McIver, J. C. F. Hodges, X. Y. Zhang, D. Muchoney, A. H. Strahler, C. E. Woodcock, S. Gopal, A. Schneider, A. Cooper, A. Baccini, F. Gao, and C. Schaaf, Global land cover mapping from MODIS: algorithms and early results, *Int. J. Remote Sensing* 83, p. 287-302, 2002.

Fromm, M. D., and R. Servranckx, Transport of forest fire smoke above the tropopause by supercell convection, *Geophys. Res. Lett.,* 30(10), 1542, doi:10.1029/2002GL016820, 2003.

Galanter, M., H. Levy II, G. R. Carmichael, Impacts of biomass burning on tropospheric CO, NO_x, and O_3, *J. Geophys. Res.* 105 (D5), 6633-6653, 2000.

Garstang, M., P. D. Tyson, R. Swap, M. Edwards, P. Kallberg, and J. A. Lindsay, Horizontal and vertical transport of air over southern Africa, *J. Geophys. Res.,* 101, 23,721-23, 736, 1996.

Geist, H. and E. Lambin, What drives tropical deforestation?, *Land-Use and Land-Cover Change (LUCC) Report Series*, Vol. 4, 2001.

Generoso S., F. M. Bréon, Y. Balkanski, O. Boucher, and M. Schulz, Improving the seasonal cycle and interannual variations of biomass burning aerosol sources, *Atmos. Chem. Phys.* 3, p. 1211-1222, 2003.

Giglio, L. and J. D. Kendall, Commentary on "Improving the seasonal cycle and interannual variations of biomass burning aerosol sources" by Generoso et al., *Atmos. Chem. Phys.*, 4, 585–587, 2004.

Giglio L., G. R. Van der Werf, J. T. Randerson, G. J. Collatz, and P. Kasibhatla, Global estimation of burned area using MODIS active fire observations, *Atmos. Chem. Phys.*, 6, 957–974, 2006.

Goldammer, J. G. Tropical Wild-land Fires and Global Changes: Prehistoric Evidence, Present Fire Regimes, and Future Trends, *in: J.S. Levine (ed.), Global biomass burning, Atmospheric, climatic, and biospheric implications*, pp. 3-21, MIT Press, Cambridge, MA, 1991.

Goldammer, J. G., and C. Price, Potential impacts of climate change on fire regimes in the Tropics based on MAGICC and a GISS GCM-derived lightning model, *Climatic Change*, 39, p. 273-296, 1998.

Goldammer, J. G., Forests on Fire, *Science* 284, p. 1782-1783,1999.

Goldammer, J. , Russian Federation Fire 2002 Special, Part I: The wildland fire season 2002 in the Russian Federation, An assessment by the Global Fire Monitoring Center (GFMC), *Int. Forest Fire News*, 28, 2-14, 2003.

Govaerts, Y. M., J. M. Pereira, B. Pinty, and B. Mota, Impact of fires on surface albedo dynamics over the African continent, *J. Geophys. Res.* 107 (D22), p. 4629, doi: 10.1029/2002JD002388, 2002.

Granier, C., J.-F. Müller, and G. P. Brasseur, The impact of biomass burning on the global budget of ozone and ozone precursors, *In: Biomass Burning and its Inter-relationships with the Climate System, ed. Innes, Beniston, and Verstraete, Advances in Global Change Research,* Kluwer Academic Publishers, The Netherlands, 2000.

Granier C., M. Kanakidou, P. Kasibhatla, et al., Modelling, *In: Atmospheric Chemistry in a Changing World, ed.: G. P. Brasseur, R. G. Prinn, and A. P. Pszenny, IGBP Series*, Springer-Verlag Berlin, 2003.

Grégoire, J.-M., K. Tansey, and J. M. N. Silva, The GBA2000 initiative: Developing a global burned area database from SPOT-VEGETATION imagery, *Int. J. Remote Sensing* 24, 6, p. 1369 – 1376, 2003.

Grell, G. A. Prognostic Evaluation of Assumptions used by Cumulus Parameterization, *Mon. Wea. Rev.,* 121, 1993.

Grell, G. A. and D. Devenyi, A generalized approach to parameterizing convection combining ensemble and data assimilation techniques. *Geophysical Research Letters*, Vol. 29, NO. 14, 2002.

Guild L. S., J. B. Kauffman, L. J. Ellingson, D. L. Cummings, E. A. Castro, R. E. Babbitt, and D. E. Ward, Dynamics associated with total aboveground biomass, C, nutrient pools, and biomass burning of primary forest and pasture in Rondonia, Brazil during SCAR-B, *J. Geophys. Res.* 24, 32,091-32,100, 1998.

Gupta, S., S. Saksena, V. R. Shankar, and V. Josni, Emission factors and thermal efficiencies of cooking biofuels from five countries, *Biomass and Bioenergy*, 14, p. 547-560, 1998.

Hao W. M., M. H. Liu, and P. J. Crutzen, Estimates of annual and regional releases of CO_2 and other trace gases to the atmosphere from fire in the tropics, based on FAO statistics for the period 1975-1980, *in: Fire in the Tropical Biota, J. G. Goldammer (ed.),* Springer Verlag, 440-462, 1990.

Hao, W. M. and M.-H. Liu, Spatial and temporal distribution of tropical biomass burning, *Global Biogeochem. Cycles* 8(4), 1994.

Hauglustaine, D. A., G. P. Brasseur, and J. S. Levine, A sensitivity simulation of tropospheric ozone changes due to the 1997 Indonesian fire emissions, *Geophys. Res. Lett.*, 26, 3305–3308, 1999.

Heil, A., and J. G. Goldammer, Smoke-haze pollution: A review of the 1997 episode in Southeast Asia, *Reg. Environ. Change*, 2, 24–37, 2001.

Heil, A., B. Langmann, and E. Aldrian, Indonesian peat and vegetation fire emissions: Study on factors inuencing large-scale smoke haze pollution using a regional atmospheric chemistry model, *Mitigation and Adaptation Strategies for Global Change*, in press, 2005.

Heil, A., Atmospheric Implications of Indonesian Peat and Forest Fires, *PhD thesis of the International Max Planck Research School on Earth System Modelling*, Max Planck Institute for Meteorology, Hamburg, Germany, in preparation, 2006.

Hély C., P. R. Dowty, S. Alleaume, K. K. Caylor, S. Korontzi, R. J. Swap, H. H. Shugart, and C. O. Justice, *J. Geophys. Res.* 108 (D13), 8475, doi:10.1029/2002JD002341, 2003a.

Hély, C., K. Caylor, S. Alleaume, R. J. Swap, and H. H. Shugart, Release of gaseous and particulate carbonaceous compounds from biomass burning during the SAFARI 2000 dry season field campaign, *J. Geophys. Res.* 108 (D13), 8470, doi:10.1029/2002JD002482, 2003b.

Hobbs, P. V., and L. F. Radke, Cloud Condensation Nuclei from a Simulated Forest Fire, *Science* 163, p. 279-280, 1969.

Hobbs P. V., J. S. Reid, J. A. Herring, J. D. Nance, R. E. Weiss, J. L. Ross, D. A. Hegg, R. D. Ottmar, and, C. Liousse, Particle and trace-gas measurements in smoke from prescribed burns of forest products in the Pacific Northwest, *In: Biomass Burning and Global Change*, Vol. 1, ed. by J. S. Levine, p. 697-715, 1996.

Hoelzemann, J. J., M. G. Schultz, G. P. Brasseur, and C. Granier, Global Wildland Fire Emission Model (GWEM): Evaluating the use of global area burnt satellite data, *J. Geophys. Res.*, 109, D14S04, doi:10.1029/2003JD003666, 2004.

Hoffa E. A., D. E. Ward, W. M. Hao, R. A. Susott, and R. H. Wakimoto, Seasonality of carbon emissions from biomass burning in a Zambian savanna, *J. Geophys. Res.* 104 (D11), p. 13,841-13,853, 1999.

Holdsworth, A. R. and C. Uhl, Fire in eastern Amazonian logged rain forest and the potential for fire reduction, *Ecological Applications*, 7, 713-725, 1997.

Horowitz L., S. Walters, D. L. Mauzerall, L. K. Emmons, P. J. Rasch, C. Granier, X. Tie, J.-F. Lamarque, M. G. Schultz, G. S. Tyndall, J. J. Orlando, and G. P. Brasseur, MOZART, A global simulation of tropospheric ozone and related tracers: Description and evaluation of MOZART, version 2, *J. Geophys. Res.*, 108 (D24), 4784, doi:10.1029/2002JD002853, 2003.

Hudson R.D. and A.M. Thompson, Tropical tropospheric ozone from total ozone mapping spectrometer by a modified residual method, *J. Geophys. Res.*, 103, 22129-22145, 1998.

Hurst, D.F., D.W.T. Griffith, and G.D. Cook, Trace gas emissions from biomass burning in tropical Australian savannas, *J. Geophys. Res.*, 99(D8), 16,441-16,456, 1994.

IPCC, Climate Change 2001: The Scientific Basis. *Contribution of Working Group I to the Third Assessment Report of the Intergovernmental Panel on Climate Change, [Houghton, J. T., Y. Ding, D. J. Griggs, M. Noguer, P. J. Van der Linden, X. D. K. Maskell, and C. A. Johnson (eds.)]*, Cambridge University Press, Cambridge, United Kingdom and New York, NY, USA, 2001.

Ito, A., and J. E. Penner, Global estimates of biomass burning emissions based on satellite imagery for the year 2000, *J. Geophys. Res.*, 109, D14S05, doi:10.1029/2003JD004423, 2004.

Ito, A., and J. E. Penner, Estimates of CO emissions from open biomass burning in southern Africa for the year 2000, *J. Geophys. Res.*, 110, D19306, doi:10.1029/2004JD005347, 2005.

Jacobson, M. Z., Strong radiative heating due to the mixing state of black carbon in atmospheric aerosols, *Nature*, 409, 695-697, 2001

James, S. R., Hominid Use of Fire in the Lower and Middle Pleistocene: A Review of the Evidence, *Current Anthro.*, 30, p. 1-26, 1989.

Jaeglé, L., R. V. Martin, K. Chance, L. Steinberger, T. P. Kurosu, D. J. Jacob, A. I. Modi, V. Yoboue, L. Sigha-Nkamdjou,and C. Galy-Lacaux, Satellite mapping of rain-induced nitric oxide emissions from soils, *J. Geophys. Res.*, 109, D21310, doi:10.1029/2004JD004787, 2004.

Jaeglé, L., R. V. Martin, L. Steinberger et al., Global partitioning of NO_x sources using satellite observations: Relative roles of fuel combustion, biomass burning and soil emissions, *Faraday Discussions*, 130, 407-423, 2005.

Jain, A. K., Z. Tao, X. Yang, and C. Gillespie, Estimates of global biomass burning emissions for reactive greenhouse gases (CO, NMHCs, and NOx) and CO2, *J. Geophys. Res.*, 111, D06304, doi:10.1029/2005JD006237, 2006.

Jost, H.-J., et al., In-situ observations of mid-latitude forest fire plumes deep in the stratosphere, *Geophys. Res. Lett.*, 31, L11101, doi:10.1029/2003GL019253, 2004.

Kajii, Y., et al., Boreal forest fires in Siberia in 1998: Estimation of area burned and emissions of pollutants by advanced very high resolution radiometer satellite data, *J. Geophys. Res.*, 107(D24), 4745, doi:10.1029/2001JD001078, 2002.

Kasischke, E. S. and L. P. Bruhweiler, Emissions of carbon dioxide, carbon monoxide, and methane from boreal forest fires in 1998, *J. Geophys. Res.*108 (D1), 8146, 2003.

Kasischke et al., The use of ATSR active fire counts for estimating relative patterns of biomass burning, a study from the boreal forest region, *Geophys. Res. Let.*, Vol. 30, No. 18, 1969, doi:10.1029/2003GL017859, 2003.

Kasischke, E.S., E.J. Hyer, P.C. Novelli, L.P. Bruhwiler, N.H.F. French, A.I. Sukhinin, J.H. Hewson, and B.J. Stocks, Influences of boreal fire emissions on Northern hemisphere atmospheric carbon and carbon monoxide, *Global Biogeoch. Cycles*, 19, GB1012, doi:10.1029/2004GB002300, 2005.

Kauffman, J. B., D. L. Cummings, D. E. Ward, and R. Babbitt, Fire in the Brazilian Amazon: Biomass, nutrient pools, and losses in slashed primary forest, *Oecologia* 104, p. 397-408, 1995.

Kauffman, J. B., D. L. Cummings, D. E. Ward, Fire in the Brazilian Amazon, 2: Biomass, nutrient pools, and losses in cattle pastures, *Oecologia*, 113, p. 415-427, 1998.

Kaufman, Y., Remote sensing of direct and indirect aerosol forcing, *in: Aerosol Forcing of Climate, edited by R. J. Charlson and J. Heintzenberg,* pp. 297-332, John Wiley, New York, 1995.

Kaufman, Y. J. and R. S. Fraser, the effects of smoke particles on clouds and climate forcing, *Science*, 277, p. 1636-1639, 1997.

Klink, C. A., A. G. Moreira, and O. T. Solbrig, Ecological impact of agricutural development in the Brazilian cerrado, in The Worlds Savannas. Economic driving forces, ecological constraints and policy options for sustainable land use. *Man and the Biosphere,* Vol. 12, Paris: UNESCO, 259-282, 1993.

Koren, I., Y. Kaufman, L. A. Remer, J. V. Martins, Measurement of the effect of Amazon smoke on inhibition of cloud formation, *Science*, 303, 1342-1345, 2004.

Korontzi, S., D. E. Ward, R. A. Susott, R. J. Yokelson, C. O. Justice, P. V. Hobbs, E. A. H. Smithwick, and W. M. Hao, Seasonal variation and ecosystem dependence of emission factors for selected trace gases and PM2.5 for southern African savanna fires, *J. Geophys. Res.*, 108(D24), 4758, doi:10.1029/2003JD003730, 2003.

Lamarque, J.-F., et al., Identification of CO plumes from MOPITT data: Application to the August 2000 Idaho-Montana forest fires, *Geophys. Res. Lett.,* 30(13), 1688, doi:10.1029/2003GL017503, 2003.

Lavoué D., Transport vers la région arctique de l'aerosol carbone emis par les feux de biomasse des régions boréale et temperée, *PhD thesis*, University Paris VII, UFR de Chimie, 2000.

Lavoué D., C. Liousse, H. Cachier,B. J. Stocks, and J. G. Goldammer, Modeling of carbonaceous particles emitted by boreal and temperate wildland fires at northern latitudes, *J. Geophys. Res.*105 (D22), 26,871-26,890, 2000.

Levine, J. S., The 1997 fires in Kalimantan and Sumatra, Indonesia: Gaseous and particulate emissions, *Geophys. Res. Lett.*, 26, 815– 818, 1999.

Lin, S.-J., and R. B. Rood, Multidimensional flux-form semi-langrangian transport schemes., *Mon. Weather Rev.*, 124, 2046-2070, 1996.

Liousse C., J. E. Penner, C. Chuang, J. J. Walton, and H. Eddleman, A global three-dimensional model study of carbonaceous aerosols, *J. Geophys. Res.* 101 (D14), p. 19,411-19,432, 1996.

Lobert, J. M., W. C. Keene, J. A. Logan, and R. Yevich, Global chlorine emissions from biomass burning: Reactive chlorine emissions inventory, *J. Geophys. Res.*, 104(D7), 8373–8389, 1999.

Longo K. M., A. M. Thompson, V. W. Kirchhoff, L. Remer, S. R. Freitas, M. A. F. Silva Dias, P. Artaxo, W. Hart, J. D. Spinhirne, M. A. Yamasoe, Correlation between smoke and tropospheric ozone concentrations in Cuiabá during Smoke Clouds and Radiation – Brazil (SCAR-B), *J. Geophys. Res.*, 104 (D10), p12113-12129, 1999.

Longo K. M., S. R. Freitas, et al., Numerical modelling of the transport of biomass burning emissions - Part II: Aerosol direct radiative effects on the thermodynamic structure of the atmosphere and precipitation, *submitted manuscript*, 2006.

Loveland T. R. and A. S. Belward, The IGBP-DIS global 1-km land cover data set, DIScover: first results, *Int. J. Remote Sensing* 65, 9, p. 1,021-1,031, 1997.

Loveland T. R., B. C. Reed, J. F. Brown, D. O. Ohlen, J. Zhu, L. Yang, and J. W. Merchant, Development of a Global Land Cover Characteristics Database and IGBP DISCover from 1-km AVHRR Data, *Int. J. Remote Sensing* 21, 6/7, p. 1,303-1,330, 2000.

Marenco, A., V. Thouret, P. Nedelec, H. G. Smit, M. Helten, D. Kley, F. Karcher, P. Simon, K. Law, J. Pyle, G. Poschmann, R. Von Wrede, C. Hume, and T. Cook, Measurement of ozone and water vapor by Airbus in-service aircraft: The MOZAIC airborne program, an overview, *J. Geophys. Res.*, 103, 25 631–25 642, 1998.

Mistry, J., Fire in the cerrado (savannas) of Brazil: an ecological review, *Progress in Phys. Geography*, Vol. 22, 2, 1998.

Mota, B. W., J. M. C. Pereira, D. Oom, M. J. P. Vasconcelos, and M. Schultz, Screening the ESA ATSR-2 World Fire Atlas (1997–2002), *Atmos. Chem. Phys.*, 6, 14091424, 2006.

Mueller-Dombois D. and J. G. Goldammer, Fire in Tropical Ecosystems and Global Environmental Change: An Introduction, *In: Fire in the Tropical Biota, J. G. Goldammer (ed.)*, Springer Verlag, p82-105, 1990.

Müller, J.-F., Geographical distribution and seasonal variation of surface emissions and deposition velocities of atmospheric trace gases, *J. Geophys. Res.*, 97, 3787-3804, 1992.

Nepstad D. C., C. R. de Carvalho, E. Davidson, P. Jipp, P. Lefebvre, P., G. H. Negreiros, E. D. da Silva, T. Stone, S. Trumbore, and S. Vieira, the role of deep roots in water and carbon cycles of Amazonian forests and pastures, *Nature*, 372, p. 666-669, 1994.

Nepstad D. C., P. Jipp, P. Moutinho, G. Negreiros, and S. Vieira, Forest recovery following pasture abandonment in Amazônia: Canopy seasonality, fire resistance and ants, *in: Evaluating and monitoring the health of large-scale ecosystems, ed.: Rapport D., C. Gander, and P. Calow, NATO ASI series*, Springer Verlag, New York, p. 339-349, 1995.

Nepstad, D. C., A. Verissimo, A. Alencar, C. Nobre, E. Lima, P. Lefebvre, P. Schlesinger, C. Potter, P. Moutinho, E. Mendonza, M. Cochrane, V. Brooks, Large-scale impoverishment of Amazonian forests by logging and fire, *Nature*, 398, p. 505-508, 1999.

Novelli, P.C., L.P. Steele, and P.P. Tans, Mixing ratios of carbon monoxide in the troposphere, *J. Geophys. Res.*, 97, 20,731-20,750, 1992.

Novelli, P.C., K.A. Masarie, and P.M. Lang, Distributions and recent changes in carbon monoxide in the lower troposphere, *J. Geophys. Res.*, 103, 19,1015- 19,033, 1998.

Novelli, P. C., K. A. Masarie, P. M. Lang, B. D. Hall, R. C. Myers, and J. W. Elkins, Reanalysis of tropospheric CO trends: Effects of the 1997–1998 wildfires, *J. Geophys. Res.*, 108(D15), 4464, doi:10.1029/2002JD003031, 2003.

Olivier, J.G.J. and J.J.M. Berdowski, Global emissions sources and sinks, *in Berdowski, J., Guicherit, R. and B.J. Heij (eds.) "The Climate System"*, A.A. Balkema Publishers/Swets & Zeitlinger Publishers, Lisse, The Netherlands, pp. 33-78., 2001.

Olivier, J. G. J., J. J. M. Berdowski, J. A. H. W. Peters, J. Bakker, A. J. H. Visschedijk, and J. P. J. Bloos, Applications of EDGAR, Including a description of EDGAR V3.0: reference database with trend data for 1970 – 1995, *RIVM, Bilthoven, report no. 773301001 / NRP report 410200051*, 2001.

Olivier, J.G.J. , Part III: Greenhouse gas emissions: 1. Shares and trends in greenhouse gas emissions; 2. Sources and Methods; Greenhouse gas emissions for 1990 and 1995. *In: "CO$_2$ emissions from fuel combustion 1971-2000", 2002 Edition*, pp. III.1-III.31. International Energy Agency (IEA), Paris. ISBN 92-64-09794-5, 2002.

Olivier, J., J. Peters, C. Granier, G. Pétron, J. F. Müller, and S. Wallens, Present and future emissions of atmospheric compounds, *POET Report #2*, EU project EVK2-1999-00011, 2003.

Olson, J. R., B. A. Baum, D. R. Cahoon, and J. H. Crawford, Frequency and distribution of forest, savanna, and crop fires over tropical regions during PEM Tropics A, *J. Geophys. Res.*, 104, 5865– 5876, 1999.

Page, S. E., F. Siegert, J. O. Rieley, H.-D. V. Boehm, A. Jaya, and S. Limin, The amount of carbon released from peat and forest fires in Indonesia during 1997, *Nature*, 420, 61– 65, 2002.

Palacios, A., E. Chuvieco, and C. Carmona-Moreno , Trace gas emission estimation in biomass burning: State of the art, *Publ. EUR 20376 EN, Eur. Commun.,* Brussels, 2002.

Palacios-Orueta, A., A. Parra, E. Chuvieco, and C. Carmona-Moreno, Remote sensing and geographic information systems methods for global spatiotemporal modeling of biomass burning emissions: Assessment in the African continent, *J. Geophys. Res.*, 109(D14S09), doi:10.1029/2004JD004734, 2004.

Pan, L., J. C. Gille, D. P. Edwards, P. L. Bailey, and C. D. Rodgers, Retrieval of tropospheric carbon monoxide for the MOPITT experiment, *J. Geophys. Res.*, 103, 32,277– 32,290, 1998.

Penkett, S. A., K. S. Law, T. Cox, P. Kasibhatla, Atmospheric Photooxidants, *In: Atmospheric Chemistry in a Changing World,* Chapter 3, The IGBP series, eds. G. P. Brasseur, R. G. Prinn, and A. P. Pszenny, Springer Verlag, 2003.

Pereira, J. M. C., B. Pereira, P. Barbosa, D. Stroppiana, M. J. P. Vasconcelos, and J.-M. Grégoire, Satellite monitoring of fire in the EXPRESSO study area during the 1996 dry season experiment: Active fires, burned area, and atmospheric emissions, *J. Geophys. Res.*, 104 (D23), p. 30,701-30,712, 1999.

Pétron G., C. Granier, B. Khattatov, V. Yudin, J. F. Lamarque, L. Emmons, J. Gille, D. Edwards, Monthly CO surface sources inventory based on the 2000-2001 MOPITT satellite data, *Geophys. Res. Let.*, Vol. 31, L21107, doi:10.1029/2004GL020560, 2004.

Potter, C., V. Brooks-Genovese, S. Klooster, and A. Torregrosa, Biomass burning emissions of reactive gases estimated from satellite data analysis and ecosystem modeling for the Brazilian Amazon region, *J. Geophys. Res.*, 107(D20), 8056, doi:10.1029/2000JD000250, 2002.

Poulter, B., N. L. Christensen Jr., and P. N. Halpin, Carbon emissions from a temperate peat fire and its relevance to interannual variability of trace atmospheric greenhouse gases, *J. Geophys. Res.*, 111, D06301, doi:10.1029/2005JD006455, 2006.

Prather, M., et al., Fresh air in the 21st century?, *Geophys. Res. Lett.,* 30(2), 1100, doi:10.1029/2002GL016285, 2003.

Price, C. and D. Rind, What determines the cloud-to-ground lightning fraction in thunderstorms?, *Geophys. Res. Lett.* 20, 463-466, 1993.

Prins, E. and W. Menzel, Geostationary satellite detection of biomass burning in South America, *Int. J. Remote Sensing*, 13, 15, 2783 2799, 1992.

Prins, E., J. Feltz, W. Menzel, and D. Ward, An overview of GOES-8 diurnal fire and smoke results for SCAR-B and 1995 fire season in South America, *J. Geophys. Res.* 103, D24, 31821 31835, 1998.

Pyne, S. J. and J. G. Goldammer, The Culture of Fire: An Introduction to Anthropogenic Fire History, *In: Sediment Records of Biomass Burning and Global Change*, ed. Clark, J. S., H. Cachier, J. G. Goldammer, and B. Stocks, NATO ASI Series, Vol., 151, Springer-Verlag, Berlin Heidelberg, 1997.

Ramanathan V., P. J. Crutzen, J. T. Kiehl, and D. Rosenfeld, Aerosols, climate, and the hydrological cycle, *Science,* 294, p. 2119-2124, 2001.

Randerson, J. T., G. R. Van der Werf, G. J. Collatz, L. Giglio, C. J. Still, P. Kasibhatla, J. B. Miller, J. W. C. White, R. S. DeFries, and E. S. Kasischke, Fire emissions from C3 and C4 vegetation and their influence on interannual variability of atmospheric CO2 and d13CO2, *Global Biogeochem. Cycles,* 19, GB2019, doi:10.1029/2004GB002366, 2005.

Reid J. S., R. Koppmann, T. F. Eck, and D. P. Eleuterio, A review of biomass burning emissions part II: intensive physical properties of biomass burning particles, *Atmos. Chem. Phys.,* 5, 799 825, 2005a.

Reid, J. S., T. F. Eck , S. A. Christopher , R. Koppmann, O. Dubovik, and D. P. Eleuterio, B. N. Holben, E. A. Reid, and J. Zhang , A review of biomass burning emissions part III: intensive optical properties of biomass burning particles, *Atmos. Chem. Phys.,* 5, 827 849, 2005b.

Rosenfeld D., TRMM observed first direct evidence of smoke from forest fires inhibiting rainfall, *Geophys. Res. Lett.,* Vol. 26, N. 20, 3101, 1999.

Russel-Smith, J., A.C. Edwards, and G.D. Cook, Reliability of biomass burning estimates from savanna fires: Biomass burning in Northern Australia during the 1999 Biomass Burning and Lightning Experiment B field campaign, *J. Geophys. Res.,* 108(D3), 8405, doi:10.1029/2001JD000787, 2003.

Sauvage, B., V. Thouret, J.-P. Camma, F. Gheusi, G. Athier, and P. Nédélec, tropospheric ozone over Equatorial Africa: regional aspects from the MOZAIC data, *Atmos. Chem. Phys.,* 5, 311-335, 2005.

Scholes R. J., J. Kendall, and C. O. Justice, The quantity of biomass burned in southern Africa, *J. Geophys. Res.*101, p. 23,667-23,676, 1996.

Scholes, M. C., P. A. Matrai, M. O. Andreae, K. A. Smith,and M. R. Manning et al., Biosphere-Atmosphere Interactions, in: *Atmospheric Chemistry in a Changing World, ed.: G. P. Brasseur, R. G. Prinn, and A. P. Pszenny*, IGBP Series, Springer-Verlag Berlin, 2003.

Seiler W. and P. J. Crutzen, Estimates of gross and net fluxes of carbon between the biosphere and the atmosphere from biomass burning, *Climatic Change* 2, p. 207-247,1980.

Schultz, M. G., On the use of ATSR fire count data to estimate the seasonal and interannual variability of vegetation fire emissions, *Atmos. Chem. Phys.* 2, 387-395, 2002.

Schultz, M. G., T. Diehl, G. P. Brasseur, and W. Zittel, Air pollution and climate-forcing impacts of a global hydrogen economy, *Science*, 302, 624-627, 2003

Schultz M. G., A. Heil, J. J. Hoelzemann, A. Spessa, K. Thonicke, J. Goldammer, A. C. Held, and J. M. C. Pereira, Global Emissions from Wildland Fires from 1960 to 2000, *submitted to Glob. Biogeochem. Cycl.*, 2005.

Seiler, W., and P. J. Crutzen, Estimates of gross and net fluxes of carbon between the biosphere and the atmosphere from biomass burning, *Clim. Change*, 2, 207– 247, 1980.

Shea R. W., B. W. Shea, J. B. Kauffman, D. E. Ward, C. I. Haskins, and M. C. Scholes, Fuel biomass and combustion factors associated with fires in savanna ecosystems of South Africa and Zambia, *J. Geophys. Res.* 101, 23,551-23,568, 1996.

Simon, M., GLOBSCAR Products Qualification Report, *ESA, Technical Note*, December, 2002.

Simon M., S. Plummer, F. Fierens, J. J. Hoelzemann, and O. Arino, Burned area detection at global scale using ATSR-2: the GLOBSCAR products and their qualification, *J. Geophys. Res.*, 109, D14, 2004.

Sinha P., L. Jaeglé, P. V. Hobbs, Q. Liang, Transport of biomass burning emissions from Southern Africa, *J. Geophys. Res.* 109, D20204, doi:10.1029/2004JD005044, 2004.

Sitch S., B. Smith, I. C. Prentice, A. Arneth, A. Bondeau, W. Cramer, J. O. Kaplans, S. Levis, W. Lucht, M. T. Sykes, K. Thonicke, and S. Venevsky, Evaluation of ecosystem dynamics, plant geography and terrestrial carbon cycling in the LPJ dynamic global vegetation model, *Global Change Biol.* 9, 161-185, 2003.

Smith, K. R., Biofuels, air pollution and health: a global review. *Plenum Publishing Corporation*, New Delhi, 1987.

Smith , K. R., Indoor air pollution in India, *National Medical Journal of India*, 9, p. 103-104, 1996.

Soja, A. J.,W. R. Cofer, H. H. Shugart, A. I. Sukhinin, P.W. Stackhouse Jr., D. J. McRae, and S. G. Conard, Estimating fire emissions and disparities in boreal Siberia (1998 – 2002), *J. Geophys. Res.*, 109, D14S06, doi:10.1029/2004JD004570, 2004.

Stocks, B.J. , The extent and impact of forest fires in northern circumpolar countries. *In: Global biomass burning: Atmospheric, climatic, and biospheric implications, J.S. Levine (ed.),* The MIT press, Cambridge, MA, pp. 197-202, 1991.

Stocks, B. J., B. W. van Wilgen, W. S. W. Trollope, D. J. McRae, J. A. Mason, F. Weirich, and A. L. F. Potgieter, Fuels and fire behaviour dynamics on large-scale savanna fires in Kruger National Park, South Africa, *J. Geophys. Res.* 101, p. 23,541-23,550, 1996.

Stocks, B. J., M. A. Fosberg, B. M. Wottom, T. J. Lynham, and K. C. Ryan, Climate Change and forest fire activity in North American boreal forests, *In: Kasischke E. S. and B. J. Stocks (ed.), Fire, climate change and carbon cycling in the boreal forests,* Springer-Verlag, Berlin, p. 368-376, 2000.

Stocks, B.J., J.A. Mason, J.B. Todd, E.M. Bosch, B.M. Wotton, B.D. Amiro, M.D. Flannigan, K.G. Hirsch, K.A. Logan, D.L. Martell, and W.R. Skinner, Large forest fires in Canada, 1959-1997, *J. Geophys. Res.*, 108(D1), 8149, doi:10.1029/2001JD000484, 2003.

Stohl A., S. Eckhardt, C. Forster, P. James, and N. Spichtinger, On the pathways and timescales of intercontinental air pollution transport, *J. Geophys. Res.* 107(D23), 4684, doi: 10.1029/2001JD001396, 200

Streets, D. G., K. F. Yarber, J.-H. Woo, and G. R. Carmichael, Biomass burning in Asia: Annual and seasonal estimates and atmospheric emissions, *Global Biogeochem. Cycles*, 17(4), 1099, doi:10.1029/2003GB002040, 2003.

Sukhinin, A. I., et al., Satellite-based mapping of fires in Eastern Russia: New products for fire management and carbon cycle studies, *Remote Sens. Environ.*, 93, 546– 564, 2004.

Swap R. J., H. J. Annegarn, and L. Otter, Southern African Regional Science Initiative (SAFARI 2000): Summary of Science Plan, *S. Afr. J. Sci.* 98 (3-4), 119-124, 2002.

Tansey, K., J-M. Grégoire, D. Stroppiana, A. Sousa, J. Silva, J. Pereira, L. Boschetti, M. Maggi, P. A. Brivio, R. Fraser, S. Flasse, D. Ershov, E. Binaghi, D. Graetz, and P. Peduzzi, Vegetation burning in the year 2000: Global burned area estimates from SPOT VEGETATION data, *J. Geophys. Res.*, 109, D14, 2004.

Thompson, A. M., R. D. Diab, G. E. Bodeker, M. Zunckel, G. J. R. Coetzee, C. B. Archer, D. P. McNamara, K E. Picketing, J. Combrink, J. Fishman, and D. Nganga, Ozone over southern Africa during SAFARI-92/TRACE A. *J. Geophys. Res.*,101 (19):23,793, 1996a.

Thompson, A. M., K E. Picketing, D. P. McNamara, M. R. Schoeberl, R. D. Hudson, J. H. Kim, E. V. Browell, V W. J. H. Kirchhoff, and D. Nganga, Where did tropospheric ozone over southern Africa and the tropical Atlantic come from in October 1992? Insights from TOMS, GTE TRACE A, and SAFARI 1992. *J. Geophys. Res.* 101 (19): 24,251, 1996b.

Thompson, A.M., J.C. Witte, R.D. McPeters, S.J. Oltmans, F.J. Schmidlin, J.A. Logan, M.Fujiwara, V.W.J.H. Kirchhoff, F. Posny, G.J.R. Coetzee, B. Hoegger, S. Kawakami, T. Ogawa, B.J. Johnson, H. Vömel and G. Labow, Southern Hemisphere Additional Ozonesondes (SHADOZ) 1998-2000 tropical ozone climatology 1. Comparison with Total Ozone Mapping Spectrometer (TOMS) and ground-based measurements, *J. Geophys. Res.*, Vol. 108 No. D2, 8238, doi: 10.1029/2001JD000967, 30 January 2003a.

Thompson, A.M., J.C. Witte, S.J. Oltmans, F.J. Schmidlin, J.A. Logan, M. Fujiwara, V.W.J.H. Kirchhoff, F. Posny, G.J.R. Coetzee, B. Hoegger, S. Kawakami, T. Ogawa, J.P.F. Fortuin, and H.M. Kelder, Southern Hemisphere Additional Ozonesondes (SHADOZ) 1998-2000 tropical ozone climatology 2. Tropospheric variability and the zonal wave-one, *J. Geophys. Res.*, Vol. 108 No. D2,8241, doi: 10.1029/2002JD002241, 31 January 2003b.

Thonicke K., S. Venevsky, S. Sitch, and W. Cramer, The role of fire disturbance for global vegetation dynamics: coupling fire into a Dynamic Global Vegetation Model, *Global Ecol. & Biogeogr.*, 10, 661-677, 2001.

Thouret, V., A. Marenco, J. Logan, P. Nedelec, and C. Grouhel, Comparisons of ozone measurements from the MOZAIC airborne program and the ozone sounding network at eight locations, *J. Geophys. Res.*, 103, 25 695–25 720, 1998.

Twomey, S., and J. Warner, Comparison of Measurements of Cloud Droplets and Cloud Nuclei, *J. Atmos. Sci.*, 24, 702-703, 1967.

Twomey S., The Influence of Pollution on the Shortwave Albedo of Clouds, *J. of the Atmos. Sciences*, Vol. 34, p.1149-1152, 1977.

Trollope W. S. W. and L. A. Trollope, SAFARI-92 characterization of biomass and fire behavior in the small experimental burns in the Kruger National Park, *J. Geophys. Res.* 101, 23,531-23,539, 1996.

Uhl C. and J. B. Kauffman, Deforestation, fire susceptibility, and potential tree responses to fire in eastern Amazonia, *Ecology*, 71, p. 437-449, 1990.

Van der Werf, G. R., J. T. Randerson, G. J. Collatz, and L. Giglio, Carbon emissions from fires in tropical and subtropical ecosystems, *Glob. Chang. Biol.*, 9, p. 547-562, 2003.

Van der Werf, G. R., J. T. Randerson, G. J. Collatz, L. Giglio, P. S. Kasibhatla, A. F. Arellano, S. C. Olsen, E. S. Kasischke, continental-scale partitioning of fire emissions during the 1997 to 2001 El Nino/La Nina period, *Science*, 303, 73–76, 2004.

Ward D. E. and W. M. Hao, Air toxic emissions from burning of biomass globally-preliminary estimates, *In: Proceedings of Air & Waste Management Assoc.* 85th Annual Meeting & Exhibition, 1992.

Ward D. E., R. A. Susott, J. B. Kauffman, R. E. Babbitt, D. L. Cummings, B. Dias, B. N. Holben, Y. J. Kaufman, R. A. Rasmussen, and A. W. Setzer, *J. Geophys. Res.* 97(D13), 14,601-14,619, 1992.

Ward D. E., W. M. Hao, R. A. Susott, R. E. Babbitt, R. W. Shea, J. B. Kauffman, and C. O. Justice, Effect of fuel composition on combustion efficiency and emission factors for African savanna ecosystems, *J. Geophys. Res.* 101, 23,569-23,576, 1996.

Warner, J. and S. Twomey, Comparison of measurements of cloud droplets and cloud nuclei, *J. Atmos. Sci.*, 24, 702-703, 1967.

World Meteorological Organisation,Scientific assessment of ozone Depletion: 1998. *Global Ozone Research and Monitoring Project*, Geneva, Switzerland, 1999.

Wotawa G., P. C. Novelli, M. Trainer, and C. Granier, Inter-annual variability of summertime CO concentrations in the Northern Hemisphere explained by boreal forest fires in North America and Russia, *Geophys. Res. Let*. 28, 24, p. 4575-4578, 2001.

Wuebbles D. J., G. P. Brasseur and H. Rodhe et al., Changes in the Chemical Composition of the Atmosphere and Potential Impacts, *In: Atmospheric Chemistry in a Changing World,* ed.: G. P. Brasseur, R. G. Prinn, and A. P. Pszenny, IGBP Series, Springer-Verlag Berlin, 2003.

Yevich, R., and J. A. Logan, An assessment of biofuel use and burning of agricultural waste in the developing world, *Global Biogeochem. Cycles,* 17(4), 1095, doi:10.1029/2002GB001952, 2003.

Zhang, G. J. and N. A. McFarlane, Sensitivity of climate simulations to the parameterization of cumulus convection in the Canadian Climate Centre general circulation model, *Atmosphere-Ocean*, 33, 407-446, 1995.

Zheng, D. L., S. D. Prince, and R. Wright, NPP multi-biome, gridded estimates for selected regions worldwide, 1989 – 2001, R1, *http://www.daac.ornl.gov*, Oak Ridge Natl. Lab., Oak Ridge, Tenn., 2003.

Acknowledgements

I greatly acknowledge the excellent guidance and expertise of my supervisors Guy Brasseur and Claire Granier during my time as a PhD student. I also greatly acknowledge Martin Schultz for his interest in my work. He was always eager and willing to help throughout the whole time. This thesis has improved substantially by the corrections and suggestions from all of them.

I thank the Max Planck Institute for Meteorology in Hamburg for an over three year PhD student grant. I also thank Guy Brasseur, the Max Planck Institute for Meteorology in Hamburg and the IMPRS very much for giving me the opportunity to attend a very interesting summer school on Data Assimilation at the European Space Agency in Frascati, Italy in 2003, as well as spending almost four months at the Centro de Previsão de Tempo e Estudos Climáticos (CPTEC/INPE) in Brazil during the year 2004.
Erich Roeckner and Martin Schultz gave me the opportunity to work on the DEKLIM and RETRO projects respectively, for some months. I thank them very much for that.
Antje Weitz and Cornelia Kampmann of the IMPRS, and Bettina Diallo and Norbert Noreiks, graphic designers of the Max Planck Institute provided an extraordinary support to publish this thesis. I thank them very very much for their efforts.

I am deeply indebted to Karla Longo and Saulo Freitas, who were not only very great hosts during my visit to Brazil in 2004, but they also offered me an excellent working opportunity at CPTEC/INPE when I came to stay for good last year. I thank them very much for their support and understanding during almost the whole last year. I am also very much looking forward to my future work with both of them.
I thank the Eurad-group (Rhenish Institute for Environmental Research) of the University of Cologne and especially Hendrik Elbern, for their great support in 2005 but also for having a place to work for me anytime when I was in Cologne. It was always a bit like coming home.
I thank José Miguel Pereira, Johann Goldammer, Hans Feichter, Stefan Kinne, Ulrike Niemeyer, Kirsten Thonicke and many more for their interest in my work. I further thank José Miguel Pereira for some important hints about the use of satellite fire products and Kirsten Thonicke for providing LPJ model data and for fruitful discussions concerning their post-processing.

In this work I have used carbon monoxide data from CMDL/NOAA. I thank Claire Granier, Ulrike Niemeyer and Martin Schultz for processing tools and support. The MOPITT carbon monoxide data used in this work was provided and pre-processed by Gabrielle Pétron. I thank her very much for patiently and effectively helping with the adaptation to my needs. I thank Karla Longo for support and providing opinions concerning the SHADOZ ozone data. I thank Martin Keller, Martin Schultz, Bastien Sauvage and Valerie Thouret for making the MOZAIC ozone data available and providing support. I thank Meinrat Andreae for making unpublished data of emission factors available for this work. This work also used the global satellite fire product GLOBSCAR of the European Space Agency. I thank Muriel Simon and Stephen Plummer for support with this product. A similar data set, GBA2000, was used from the Joint Research Centre of the European Commission. I thank Karla Longo, Saulo Freitas, and Fernando Recuero to provide me with the compiled satellite fire pixel product from CPTEC/INPE for the year 2000. Also, I certainly acknowledge the institutions that have made all of these data available.

I owe many thanks for a pleasant time at MPI to my former colleagues, just to name a few of them: Katja Winger, Gabriela Santos, Angelika Heil, Philip Stier, Michael Weber, and many more. More recently here at CPTEC/INPE I thank Manoel Cardoso, Josefina Moraes Arraut, Leila Albuquerque, Renaud Laborbe, Karla Longo, Saulo Freitas, and more.

A very special thanks goes to my dear friends and family: you were very patient with me these last years! Thank you for this and also for your support, love, understanding, and some distraction from work!

Publikationsreihe des MPI-M
„Berichte zur Erdsystemforschung" , *„Reports on Earth System Science*", ISSN 1614-1199
Sie enthält wissenschaftliche und technische Beiträge, inklusive Dissertationen.